

REPORT DOCUMENTATION PAGE

Form Approved
OMB No. 0704-0188

Public reporting burden for this collection of information is estimated to average 1 hour per response, including the time for reviewing instructions, searching existing data sources, gathering and maintaining the data needed, and completing and reviewing the collection of information. Send comments regarding this burden estimate or any other aspect of this collection of information, including suggestions for reducing this burden, to Washington Headquarters Services, Directorate for Information Operations and Reports, 1215 Jefferson Davis Highway, Suite 1204, Arlington, VA 22202-4302, and to the Office of Management and Budget, Paperwork Reduction Project (0704-0188) Washington, DC 20503.

1. AGENCY USE ONLY (Leave Blank)	2. REPORT DATE 1996	3. REPORT TYPE AND DATES COVERED Final	
4. TITLE AND SUBTITLE Alloy Dependence of Electron-Phonon Interactions in Double Barrier Structures		5. FUNDING NUMBERS AFRL-SR-BL-TR-98-	
6. AUTHORS Corinne Renee Wallis			
7. PERFORMING ORGANIZATION NAME(S) AND ADDRESS(ES) Duke University			
9. SPONSORING/MONITORING AGENCY NAME(S) AND ADDRESS(ES) AFOSR/NI 110 Duncan Avenue, Room B-115 Bolling Air Force Base, DC 20332-8080		10. SPONSORING/MONITORING AGENCY REPORT NUMBER 0035	
11. SUPPLEMENTARY NOTES			
12a. DISTRIBUTION AVAILABILITY STATEMENT Approved for Public Release		12b. DISTRIBUTION CODE	
13. ABSTRACT (Maximum 200 words) See attached.			
14. SUBJECT TERMS		15. NUMBER OF PAGES	
		16. PRICE CODE	
17. SECURITY CLASSIFICATION OF REPORT Unclassified	18. SECURITY CLASSIFICATION OF THIS PAGE Unclassified	19. SECURITY CLASSIFICATION OF ABSTRACT Unclassified	20. LIMITATION OF ABSTRACT UL

DTIC QUALITY INSPECTED a

19980115 179

ALLOY DEPENDENCE OF ELECTRON-PHONON
INTERACTIONS IN DOUBLE BARRIER
STRUCTURES

by

Corinne Renee Wallis

Department of Physics
Duke University

Date: Jan. 12, 1996

Approved:

Stephen W. Teitsworth
Dr. Stephen Teitsworth, Supervisor

Horst Meyer
Dr. Horst Meyer

Michael Stroscio
Dr. Michael Stroscio

Henry Weller
Dr. Henry Weller

Theda Daniels-Race
Dr. Theda Daniels-Race

Dissertation submitted in partial fulfillment of the
requirements for the degree of Doctor of Philosophy
in the Department of Physics
in the Graduate School of
Duke University

1996

Copyright © 1996 by Corinne Renee Wallis
All rights reserved

ABSTRACT

(Physics)

ALLOY DEPENDENCE OF ELECTRON-PHONON
INTERACTIONS IN DOUBLE BARRIER
STRUCTURES

by

Corinne Renee Wallis

Department of Physics
Duke University

Date: Jan. 12, 1996
Approved:

Stephen W. Teitsworth
Dr. Stephen Teitsworth, Supervisor

Horst Meyer
Dr. Horst Meyer

Michael Stroscio
Dr. Michael Stroscio

Henry Weller
Dr. Henry Weller

Theda Daniels-Race
Dr. Theda Daniels-Race

An abstract of a dissertation submitted in partial
fulfillment of the requirements for the degree
of Doctor of Philosophy in the Department of
Physics in the Graduate School of
Duke University

1996

Abstract

We have carried out a systematic experimental study of electron-phonon interactions in a series of $\text{GaAs}/\text{Al}_x\text{Ga}_{1-x}\text{As}$ double barrier structures as a function of the alloy concentration in the barrier. We have measured current-voltage and conductance-voltage curves associated with phonon-assisted tunneling with magnetic fields from 0 to 6.8 Tesla. Fan diagrams are constructed and used to measure the energies of the contributing phonons and to compare the levels of different modes to the current. It is found that phonons with at least three different energies contribute to the phonon-assisted tunneling current in samples with $x \geq 0.5$ and with at least two different energies with $x \leq 0.4$. We also present results of a fitting routine to experimentally determine the relative strengths of contributions to the phonon-assisted tunneling current at 0 Tesla. These measurements indicate that as the aluminum concentration in the barriers decrease, the contribution decreases from modes with energies of bulk AlAs LO phonons, while the contribution increases from modes with energies of bulk GaAs TO phonons. Observations are in good qualitative agreement with theoretical calculations which incorporate the modified dielectric continuum model to estimate the phonon potentials. We review how the phonon-assisted tunneling current may be calculated for a GaAs/AlAs double barrier structure using

the dielectric continuum model to compute the localized phonon potentials. We discuss how the dielectric continuum model may be extended to describe structures made with $\text{Al}_x\text{Ga}_{1-x}\text{As}$ alloy barriers. Theoretical calculations of the relative contributions of the AlAs-like phonons and the GaAs-like phonons for the experimental samples are presented and compared to experimental results. We also derive and discuss a condition for extrinsic bistability and hysteresis in the onset of oscillations which are observed experimentally in many samples. Finally, we discuss a feature seen in the fan diagrams with energy below that for optical phonon emission which we attribute to the abrupt turn on of the phonon-assisted tunneling process as a function of voltage. Temperature dependent data of this feature and Shubnikov-de Haas measurements are also presented and discussed.

Acknowledgements

This thesis would not have been possible without the help and support of many people. First of all, I would like to thank my advisor, Dr. Stephen Teitsworth for his inspiration and guidance and for the opportunity to participate in his research here at Duke. I would also like to thank all the Duke physics faculty whom I've had the pleasure to work with during my stay. They were always willing to help or answer a question whenever I needed it. A special acknowledgement goes to Dr. Theda Daniels-Race, not only for all the samples grown for the data in this thesis, but also for all the advice and for being a mentor.

Thanks is not enough for all the support staff who have helped me immeasurably throughout the years, especially Richard Kendall. Thank you for helping to grow my samples and especially for all your rescues whenever something broke in the clean room. I would also like to thank all the computer staff, the systems administrator Eric Sessoms and faculty Dr. Palmer and Dr. Brown, whose prompt attention to problems has been greatly appreciated. I would also like to acknowledge all the guys in the shop and stockroom. To Dickey, thank you for your help and patience in teaching me how to use the equipment in the shop. To Bill Enscore, thank you for all your help in locating parts and for just being cheery whenever I saw you. A special thanks goes

to Maxine and the secretaries, Donna and Jennifer. I never would never have made it through Duke without you.

I would also like to acknowledge all the students whom I worked with through the years. A special thanks goes to Peter Turley for all his help and patience and for helping me to get started here by sharing his wealth of knowledge. A special thanks also goes to Linda Blue who spent hours growing my samples and for being a good friend. I would also like to thank Mike Bergmann for his help with my experiments and Kauser Banoo for her help and friendship. Acknowledgements also go to many others, especially Dan, Mark, Jeff, Fang, and Dave, who were always more than willing to help me with so many various technical aspects of my experiment. There are also many others and I would like to wish them all the best of luck for the future.

Most of all, I would like to acknowledge and thank the great number of people whose love and support helped me to come to this point in my life. I would like to thank my roommate Kim Juvan for being a good friend and tolerating me when I was in bad moods. A very special thanks goes to my fiance Greg Schmid whose love, support, and advice were crucial throughout my years at Duke. Greg, your friendship and understanding was especially appreciated during the last few months when I was writing this thesis. Finally, I would like to thank my family, my parents Allen and Dorothy, and my brothers, Scott and Eric. Your love and support throughout the years has been immeasurable, and without you, this thesis would not have been possible.

Acknowledgements also go to the NSF and Air Force who supported me during my years at Duke.

Contents

Abstract	i
Acknowledgements	iii
List of Figures	viii
List of Tables	xi
1 Introduction	1
2 Theory of Phonon-Assisted Tunneling in $\text{GaAs}/\text{Al}_x\text{Ga}_{1-x}\text{As}$ Double Barrier Structures	8
2.1 Energetics of Phonon-Assisted Tunneling	8
2.1.1 Introduction and Resonant Tunneling	8
2.1.2 Phonon-Assisted Tunneling with $B = 0$	12
2.1.3 Phonon-Assisted Tunneling with $B \neq 0$	15
2.2 Electronic Effects in Phonon-Assisted Tunneling	16
2.2.1 Electronic States	16
2.2.2 Effects of Space Charge in Well	21
2.3 Review of Optical Phonon Modes in Structures with Pure AlAs barriers	22
2.3.1 Introduction to Dielectric Continuum Model	22
2.3.2 Localized Phonon Potentials and Dispersion Relations	24
2.3.3 Electron-Phonon Interaction	30
2.3.4 Current Formulae	32
2.4 Optical Phonon Modes in structures with alloy barriers, $\text{Al}_x\text{Ga}_{1-x}\text{As}$ ($0 < x < 1$)	38
2.4.1 Review of Bulk $\text{Al}_x\text{Ga}_{1-x}\text{As}$ Properties	38

2.4.2	Generalization of Dielectric Continuum Model to Include Alloy Materials—Modified Dielectric Continuum Model	42
2.4.3	Dispersion Relations and Phonon Potentials	44
2.4.4	Electron-Phonon Interaction	46
3	Theory of Circuits which Incorporate DBS's	54
3.1	Introduction	54
3.2	Bifurcation Analysis	58
3.2.1	Review of Bifurcation Theory and Analytical Results	58
3.2.2	Numerical Results for Circuit Model	62
4	Experimental Techniques—Growth and Characterization	68
4.1	Introduction	68
4.2	Experimental Samples	68
4.3	MBE Growth	73
4.3.1	Introduction and Overview	73
4.3.2	RHEED	75
4.3.3	Growth of Alloy Barriers	76
4.3.4	Growth Interrupts Between GaAs and $Al_xGa_{1-x}As$ Layers	78
4.4	TEM Characterization	81
4.4.1	TEM Equipment	81
4.4.2	Sample Processing	81
4.4.3	Results	86
5	Experimental Techniques—Processing and Measurement	90
5.1	Introduction	90
5.2	Processing	90
5.2.1	Evaporation and Indium removal	91
5.2.2	Annealing	94
5.2.3	Final Etch	96
5.3	Low Temperature Systems	97
5.4	Electronics and Data Collection	102
5.5	Digital Filters	108
6	Experimental Results	111
6.1	Experimental Results of Asymmetric <i>Spacer</i> and Notch Samples	112
6.1.1	Asymmetric <i>Spacer</i> Sample	112
6.1.2	Notch Samples	114

6.2 Experimental Results of Asymmetric <i>Barrier</i> Samples	122
6.2.1 Data Under Forward Bias	123
6.2.2 Reverse Bias Data with $B = 0$	129
6.2.3 Data with $B \neq 0$	138
6.2.4 Energy Dependence of Modes on Alloy Concentration . .	151
6.2.5 Dependence of Relative Coupling Constants of AlAs-like Phonons	155
6.2.6 Low Energy Feature	161
7 Conclusions	168
A Calculational Details of Hopf Bifurcation	172
B Epilayer Schematics	175
B.1 Asymmetric <i>Spacer</i> Sample	175
B.2 Notch Samples	176
B.3 Asymmetric <i>Barrier</i> Samples	177
C Properties GaAs, AlAs, and $Al_xGa_{1-x}As$	178
D List of Symbols Used in this Thesis	179
D.1 Electron-Phonon Interaction	179
D.2 Equivalent Circuit and Hopf Bifurcation Calculation	182
D.3 Experimental Techniques	183
D.4 Digital Filter	183
Bibliography	184
Biography	205

List of Figures

2.1	Illustration of resonant tunneling of electrons in the conduction band edge	10
2.2	Illustration of phonon-assisted tunneling	13
2.3	Dispersion curves for interface modes in a symmetrical DBS with an 80 Å well and 45 Å AlAs barriers	27
2.4	Calculated phonon potentials for LO-like interface modes in a symmetrical DBS with an 80 Å well and 45 Å AlAs barriers . .	29
2.5	Calculated PAT currents for sample 1863	36
2.6	Experimental bulk phonon energies as a function of Al concentration	41
2.7	Dispersion relations for interface phonons in sample 263	45
2.8	Potentials for LO-like phonon modes in sample 263 calculated by modified mean field method	47
2.9	Calculated current densities for sample 263	49
2.10	Calculated current densities for sample 293	51
2.11	Ratios of calculated GaAs-like currents to calculated AlAs-like currents as a function of aluminum concentration	53
3.1	Experimental hysteresis due to spontaneous circuit oscillations .	55
3.2	Example of experimental current-voltage curve with intrinsic bistability	56
3.3	Typical biasing circuit for a DBS	57
3.4	Illustration of Supercritical vs. Subcritical Hopf bifurcation ($f > 0$)	60
3.5	Typical intrinsic device characteristics used in numerical simulations	63
3.6	Illustration of change of type of Hopf bifurcation by a change in circuit parameters	65

3.7	Numerically simulated voltage and current oscillations	66
4.1	Examples of conduction band edge profile of three types of samples	70
4.2	Example of trapping behavior in a sample with long growth interrupts	79
4.3	Schematic diagram for steps in processing samples for a TEM cross section	82
4.4	TEM images of DBS samples with AlAs barriers	88
5.1	Illustration of the finished processed sample with Au-Ni-Ge con- tacts	91
5.2	Schematic of phosphor bronze wire set-up for liquid nitrogen measurements	98
5.3	Schematic of helium dewar	100
5.4	Schematic of four terminal Current-voltage measurement	103
5.5	Schematic of Conductance-voltage measurement using Lock-In Amplifiers	105
5.6	Schematic of set-up for Shubnikov de Haas measurements	106
5.7	Schematic of oscillations data measurements with digital oscil- loscope	107
6.1	Experimental current-voltage curve for asymmetric <i>spacer</i> sample	113
6.2	Experimental current-voltage curve for notch sample 250	117
6.3	Phonon peaks of sample 250	118
6.4	Fan diagrams for sample 250	121
6.5	Experimental curves for sample 263 under forward bias	124
6.6	Fan diagram for sample 263 under forward bias	127
6.7	Experimental curves for sample 263 under reverse bias	130
6.8	Experimental curves for sample 293 under reverse bias	133
6.9	Experimental curves for sample 291 under reverse bias	134
6.10	Examples of current-voltage curves of sample 263 under reverse bias with an applied magnetic field	139
6.11	Examples of conductance-voltage curves of sample 263 under reverse bias with an applied magnetic field	141
6.12	Fan diagram for sample 263 under reverse bias	143
6.13	Fan diagram for sample 293 under reverse bias	146
6.14	Fan diagram for sample 291 under reverse bias	148
6.15	Fan diagrams for samples 264 , 262 , 292 , 278 , 280 , and 279 under reverse bias	150

6.16 Energy dependence of DBS phonon modes as a function of alloy concentration	152
6.17 Comparison of numerical phonon fit to experimental curve to theoretical calculation	158
6.18 Phonon ratios of asymmetric barrier samples under reverse bias versus the aluminum concentration x in the barriers	160
6.19 Temperature dependence of low energy feature of sample 293 under reverse bias	163
6.20 Experimental determination of electronic density of accumulation layer of sample 293 under reverse bias	165

List of Tables

6.1	Energies corresponding to low energy features	161
B.1	Epilayer schematic of asymmetric <i>spacer</i> sample	175
B.2	Epilayer schematics of notch samples	176
B.3	General epilayer schematic of asymmetric <i>barrier</i> samples	177
B.4	Asymmetric <i>barrier</i> sample emitter and collector barrier widths	177

Chapter 1

Introduction

Since the invention of the transistor in 1947, solid state devices have become increasingly smaller and faster. Dimensions of these structures are typically on the order of carrier de Broglie wavelengths, and classical dynamics are no longer sufficient to explain the transport properties of these devices. Much effort has been made to understand and exploit the quantum properties of these devices. In addition to silicon chips, high quality devices are also made of other semiconductor materials whose advantages in high speed applications and optoelectronics now outweigh the cost of producing them. One of the fastest growing areas in device fabrication has been in III-V materials, especially GaAs/AlGaAs heterostructures which consist of thin layers of GaAs and AlGaAs grown next to each other with abrupt interfaces.

High quality GaAs/AlGaAs heterostructures are usually grown by Molecular Beam Epitaxy (MBE) which grows films one atomic layer at a time and allows good control of layer thicknesses. The first periodic GaAs/AlGaAs structures were grown by Cho in 1971 [Cho71b], and device quality GaAs/AlGaAs structures were achieved in 1975 [CA75]. Since then, numerous studies of the

effects of growth conditions on the quality of samples have been done [Cho83, Sak89], and the quality of samples grown have vastly improved. Such structures can also be well characterized by technologies such as Transmission Electron Microscopy (TEM) which directly image the lattice [Rei89]. These characterizations then allow detailed comparisons between theoretical calculations of transport properties and experimental results.

Transport in semiconductor heterostructures often involve carriers tunneling through thin layers of semiconductor materials. In the structures described in this thesis, the carriers are all electrons. Thin layers often create potential wells in the conduction band edge in one direction which confine electron states so that electrons with energies equal to the energies of these states in the direction of confinement have an enhanced probability of being transmitted through the structure. This process, known as resonant tunneling (RT) and described in detail in the introduction in Chapter 2 for a double barrier structure (DBS) which contains one quantum well and two barriers in the conduction band potential, often produces the phenomenon of negative differential resistance (NDR). Typically, currents increase quickly with increasing applied voltage to some peak value in the current-voltage (I-V) curve. If the voltage is increased further, the current then falls to some minimum value in the valley before it begins to rise again. NDR due to RT in a semiconductor heterostructure was first demonstrated in 1974 by Chang, Esaki, and Tsu [CET74] who saw a peak in the I-V curve of a GaAs/AlGaAs DBS. However, it was not until Sollner et. al. [SGT⁺83] demonstrated that a properly designed DBS exhibited NDR at room temperatures and could detect frequencies up to 2.5 THz when interest and investigation into these devices soared. Since then, resonant tunneling has also been seen in many other material sys-

tems including structures made of GaInAs/AlInAs [CCP⁺89, AMR⁺89], and GaSb/AlSb/InAs [MOEW91]. Possible applications of these structures include high frequency oscillators [BSP⁺89, BSP⁺91] and logic devices [LC87].

In addition to the NDR, it is also important to properly characterize the I-V curve and equivalent circuit of the device and measuring apparatus. Many of the measurements of I-V curves exhibit spontaneous current oscillations in the NDR region which result from parasitic reactances in the circuit [Sol87, YWL⁺88, BMBA⁺90, JK91]. These oscillations typically show hysteresis and bistability. However, many of the equivalent circuits to explain these oscillations are also the same circuits to describe the circuits for high frequency oscillators in waveguides [GCM⁺87, BGS88]. Wallis and Teitsworth [WT94] derived a condition to determine whether hysteresis is observed in a common equivalent biasing circuit. This condition may prove useful in helping to reduce additional noise due to the presence of hysteresis. In particular, it suggests that the I-V curve may be tailored to minimize the hysteresis observed, and, hence, minimize the noise which may result.

In order to design practical devices, it is necessary to understand the additional current which is often seen in the valley of the I-V curves. This current includes contributions from elastic scattering off of ionized impurities [LC88, LM90, CV93a] and interface roughness [WLP⁺88, CH89, LRF92], and tunneling through the X states in the barriers [MCW86, Liu87, MFE⁺91, SR95]. However, a very important contribution to the valley current involves inelastic scattering of electrons off of longitudinal optical (LO) phonons. This scattering is especially important in III-V materials, because these phonons couple strongly to electrons due to the polar nature of these materials.

In 1987, Goldman et. al. [GTC87a] observed a small peak in the valley current above resonance which they attributed to phonon assisted tunneling (PAT). During this process, in which tunneling electrons have a higher energy than the quantum well state, electrons tunnel through the structure by emitting an optical phonon. It was found that by applying a magnetic field parallel to the direction of the current, the energies of the contributing phonons can then be determined [LAS⁺89]. Some structures exhibited contributions from only one phonon [LAE⁺89, BLSR⁺90, GCB91, ZYC90], while others clearly showed contributions from two phonons [LAE⁺89, YYK89, CCP⁺89, CYYW91, TWS⁺93]. Typical energies of these phonons were similar to the energy of the bulk LO modes of the different layers.

Several theories were proposed to find the current due to this scattering. However, many of these calculations involved bulk phonons and theoretical calculations compared poorly with experiments [WJW88, CV88, ZC92, CV93b, RL93]. In 1991, Turley and Teitsworth suggested that the scattering of electrons is due to localized phonon modes [TT91b]. In heterostructures which consist of thin layers and which are of practical interest, the phonon modes are localized, either in one particular layer or along the interfaces. Therefore, it is critical to understand how scattering due to these localized modes is affected. A simple theory to explain the scattering, in addition to good experimental data to compare with the theoretical calculations, is crucial to the understanding of these devices and, hence, to their eventual application.

There are many models to calculate the properties of these localized modes [HZ88, Rid89, MA89]. Some involve the microscopic calculations directly involving the forces between ions in the lattice [HZ88, Men89, LMR91, RRB⁺93]. However, the results of these calculations are often too difficult to

be directly incorporated into transport calculations. The most common way to simply model the localized phonon modes is the dielectric continuum model, which assumes that each layer maintains its bulk dielectric properties and uses electrostatic boundary conditions to find the localized modes. This model was first proposed by Fuchs and Kliewer [FK65], who were discussing optical absorption in thin slabs of ionic material. Hamiltonians describing the interaction between electrons and these localized modes were then derived by Lucas, Kartheuser and Badro [LKB70], and expanded by Licari and Evrard [LE77] to include other effects such as electronic polarizability. The dielectric continuum model has been used by many to calculate the phonon properties in III-V heterostructures [Wen85, MA89, KS90, KBS⁺92]. Although the validity of this model has been questioned and alternatives proposed [Men89, RB91], microscopic calculations have confirmed that the dielectric continuum model gives results very close to those from the microscopic calculations, especially for long wavelength modes to which electrons couple most strongly [LMR91].

Some ways to experimentally probe this interaction include exciting electron-hole pairs with a laser pulse and study the relaxation of the electron-hole gas through photoluminescence [SPGW85, YCSLW85]. The analysis of this data involves sophisticated many body techniques [DS91] and does not provide conclusive results for any electron-phonon coupling theory. There have also been time-resolved Raman scattering measurements [TJM93], and, although these are very well-suited to provide information on electron-phonon interactions in superlattices, which consist of many quantum wells, it is not sensitive enough to probe the interaction in structures with only a single quantum well.

Phonon-assisted tunneling is well suited to experimentally test theories of

the electron-localized phonon interaction, especially for a DBS which has only one quantum well. In 1993, Turley et. al. [TWT93] produced calculations based on the dielectric continuum model which demonstrated that much of the experimental valley current from an asymmetrical DBS was due to phonon assisted tunneling. These calculations were the closest to experimental data to date. Both the theoretical calculations and experimental data showed that phonons with two separate energies mostly contributed to the PAT current. These calculations and experiments, however, were for a GaAs/AlAs DBS, and although this theory should be applicable for barriers made with binary materials, most DBS's and superlattice barriers are made with ternary materials such as AlGaAs. The dielectric continuum model has been extended to properly account for the properties of these materials [KS90, KBS⁺92, TT]. These calculations show that the energies and relative contributions from different phonons vary as a function of the alloy concentration of the barriers. A systematic experimental study needs to be done as a function of the alloy concentration to provide detailed comparisons with the theory.

The purpose of this thesis is to provide a systematic experimental study of properties of localized modes in DBS samples made with AlGaAs and to compare these results with theory which includes the modified dielectric continuum model. Chapter 2 gives a general review of resonant tunneling and PAT in a DBS and how a magnetic field applied parallel to the direction of the current may help determine the energy of the contributing modes. Chapter 2 also reviews the dielectric continuum model to explain PAT in GaAs/AlAs DBS's and how the dielectric continuum model may be modified to include ternary materials such as AlGaAs. Chapter 3 present theory of circuit oscillations in the NDR region which is seen in our structures and is useful for many

high frequency applications. Chapter 4 discussed growth techniques and characterizations of our samples. Chapter 5 discusses processing and measurement techniques. Chapter 6 presents the experimental results and how they compare with the theoretical calculations employing the modified dielectric continuum model. Finally, Chapter 7 discusses the conclusions and future directions.

Chapter 2

Theory of Phonon-Assisted Tunneling in $\text{GaAs}/\text{Al}_x\text{Ga}_{1-x}\text{As}$ Double Barrier Structures

2.1 Energetics of Phonon-Assisted Tunneling

In this chapter, we review the general theory of phonon-assisted tunneling. Section 2.1 serves as an introduction to resonant tunneling and general aspects of phonon-assisted tunneling with no applied magnetic field and with an applied magnetic field which can be deduced from the energy conservation equations. Section 2.2 discusses the electronic states involved in phonon-assisted tunneling and the effects of charge build-up in the well. Section 2.3 reviews optical phonon modes in DBS samples with pure AlAs barriers and section 2.4 discusses the phonon modes in DBS samples with alloy barriers.

2.1.1 Introduction and Resonant Tunneling

Before one can understand phonon-assisted tunneling through a DBS, one needs to understand resonant tunneling. A general $\text{GaAs}/\text{Al}_x\text{Ga}_{1-x}\text{As}$ DBS

consists of a thin film of undoped GaAs sandwiched between two thin films of undoped $Al_xGa_{1-x}As$, and this whole structure is embedded in GaAs. The sample usually includes thick layers of heavily doped GaAs to serve as the contact regions and regions of undoped GaAs called spacers to separate the DBS from the contact region. For an electron in the Γ point conduction band edge, this arrangement forms a potential well between two square potential barriers as illustrated in Fig. 2.1(a). For the remainder of this thesis, we assume that the growth direction, and, hence, the quantization, of the DBS samples are in the z direction. This figure shows the one-dimensional Γ point conduction band edge in the z direction for one of the samples discussed later in this thesis which we refer to as either the $x = 0.7$ asymmetric *barrier* sample or the 263 sample, referring to the number in the MBE growth given in Appendix B. All experimental sample profiles are given in Appendix B. As illustrated in the figure, the well contains one or more quasibound energy states. These states are quasibound because an electron in one of these states in the well is able to tunnel out from either of the barriers. An electron incident on either side of the barriers has a small probability of being transmitted through the barriers. This probability peaks when the energy of the incident electron equals the energy of one of the well states.

This peak in the transmission probability can be realized experimentally by applying a potential difference across the barrier. The current through the structure is directly related to the transmission probability, and, hence, the current peaks when the voltage is such that the energy of the electrons incident on the barrier equals to the energy state in the well. The region which the electrons are incident on the DBS is referred to as the emitter, and the region to which the electrons tunnel out of the well is referred as the collector. An

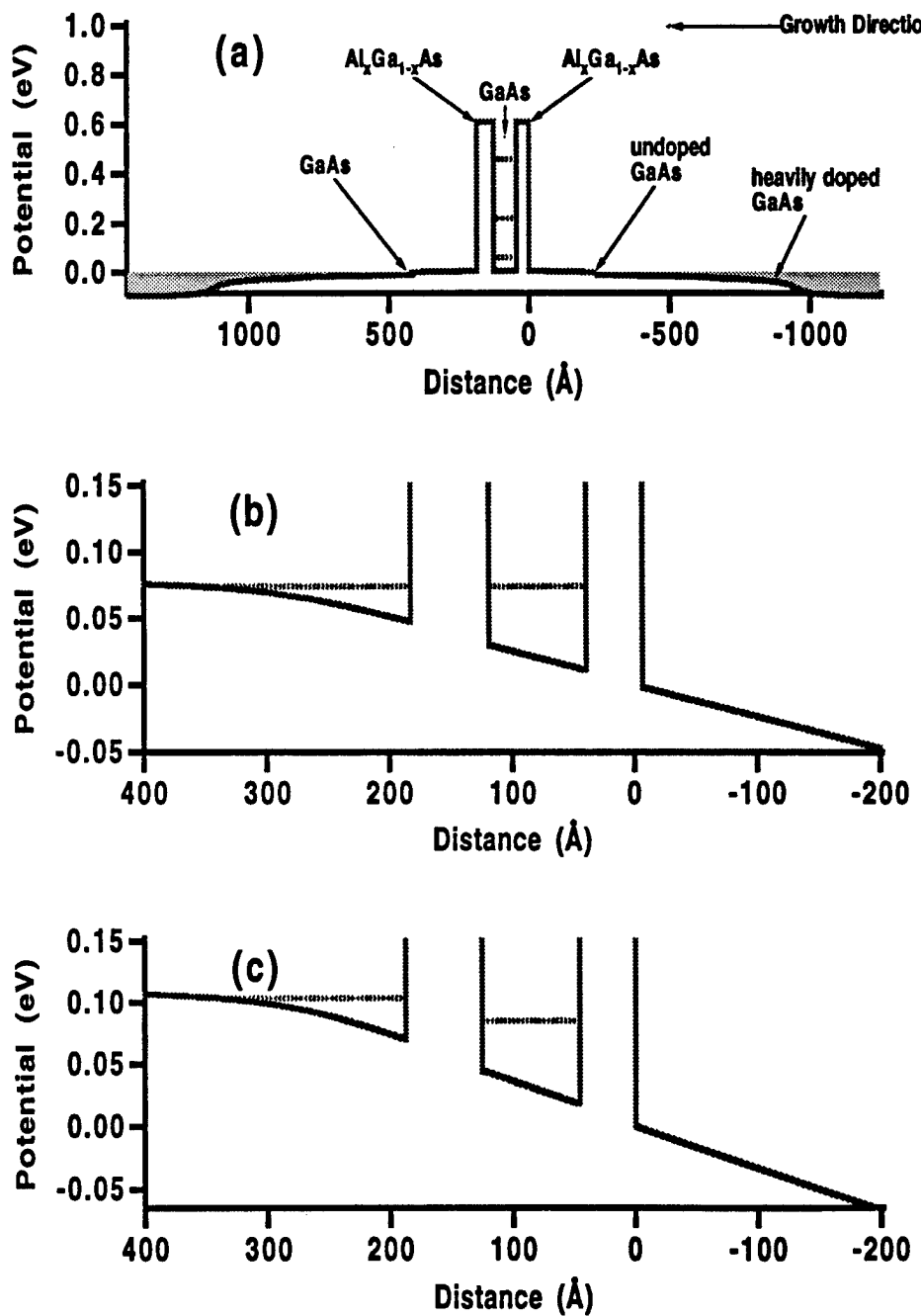


Figure 2.1: (a) Calculated Γ -point conduction band profile in the z direction with no applied voltage bias for the 263 sample. The well contains three quasibound energy states shown as the gray lines in the well. (b) Calculated conduction band profile of sample 263 focused near the DBS when biased at resonance. (c) Calculated conduction band profile of sample 263 focused near the DBS when biased above resonance.

important thing to note is that the spacer has a graded doping profile from the heavily doped contact regions to the undoped DBS. If we apply a voltage across the device, a triangular potential well forms in the emitter next to the barrier, and this potential well in the emitter contains one or more quasibound energy states in the z direction. The electrons therefore form an accumulation layer of a quasi two dimensional (2D) electron gas next to the barrier. We have chosen this doping scheme so that the electrons tunnel from one 2D gas to another in the well, and as long as the undoped layer is not too thick, the electron gas in the accumulation layer is in thermal equilibrium with the 3D electron gas in the contact [KHJ90]. These spacer layers have been found to enormously enhance the peaks in the experimental current-voltage curve [YGA90, DRY95]. This enhancement results from the accumulation layer in the emitter which narrows the range of z energies of electrons incident on the DBS, and, thus, sharpens the resonant tunneling peak. All of the structures discussed in this thesis form such a 2D accumulation layer of electrons in the emitter [Wal].

When there is only a small applied voltage, the electrons in the accumulation layer have less energy than the energy state in the well, and since the transmission probability is small, the current is also small. As we increase the applied voltage, we increase the energy of the electrons in the accumulation layer relative to the energy state in the well. At some applied voltage, the energy of the electrons in the accumulation layer will equal the energy state in the well as illustrated in Fig. 2.1(b), and, hence, we will have a peak in the current since we have a peak in the transmission coefficient. As we continue to increase the applied voltage, the energy in the accumulation layer will become greater than the energy in the well as shown in Fig. 2.1(c). The transmission coefficient decreases as does the current.

2.1.2 Phonon-Assisted Tunneling with $B = 0$

Experiments have found that the current above the resonant peak does not decrease to zero, however. Scattering allows additional pathways for an electron to tunnel through the DBS. There are various scattering mechanisms that contribute to current in the valley above resonance. Among these are scattering from interface roughness [LC88, LM90, CV93a], and Γ to X point conversion in the barriers [MCW86, Liu87, MFE⁺91, SR95]. It has been demonstrated for many of these structures, however, that one of the most important contributions to the current in the valley is the inelastic scattering from optical phonons [LAE⁺89, LKD93, TWT93].

Figure 2.2(a) illustrates the conduction band schematic of this process under no applied magnetic field. Note that an additional voltage drop of about 0.55 V occurs in the collector region which is not shown here. We show sample 263 under forward bias in this case because the phonon-assisted tunneling peak is very clear and dramatic. We assume, of course, that the structure is biased above resonance where the energy of the electrons in the accumulation layer are above the energy state in the well. Phonon-assisted tunneling occurs when the electronic state in the emitter is coupled to the electronic state in the well through the emission of an optical phonon. In many cases this process may result in an additional peak above resonance in the current-voltage characteristic of the device, as illustrated very clearly in Fig. 2.2(b). Figure 2.2(c) will be discussed in the next section.

We can obtain much information by considering energy conservation during

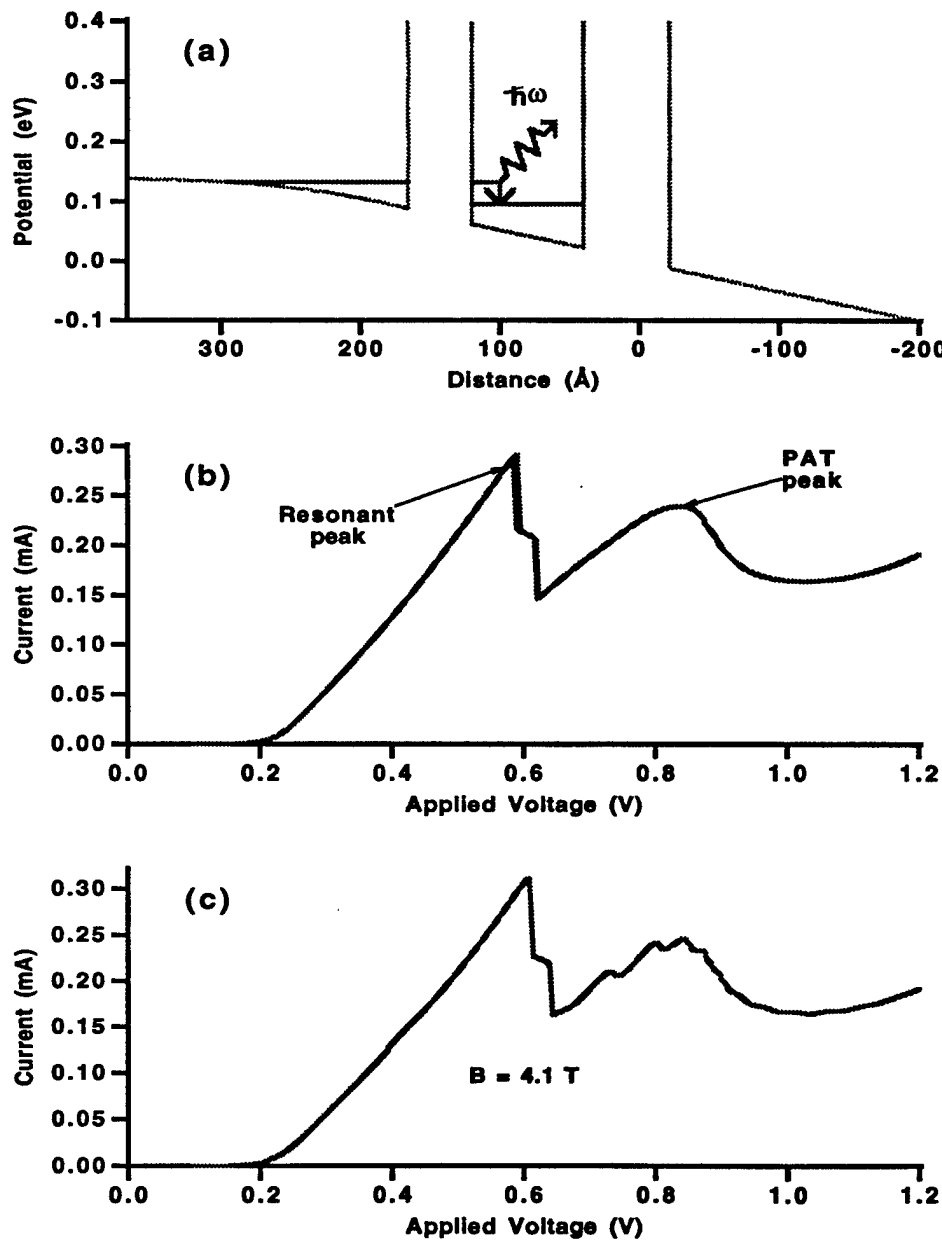


Figure 2.2: (a) Calculated potential in the Γ -conduction band edge profile for sample 263 under forward bias. (b) Current-voltage characteristic of sample 263 in the forward bias with no applied magnetic field. (c) Current-voltage characteristic of sample 263 under the forward bias with a magnetic field of 4.1 T applied parallel to the current.

this process. The energy of the electronic state in the emitter is given by:

$$E_a = E_{za} + \frac{\hbar^2 k_{||}^2}{2m^*}, \quad (2.1)$$

where m^* is the effective mass of the electron in GaAs, E_a is the total energy of the electron in the accumulation layer in the emitter, E_{za} is the energy of the electron in the emitter in the z direction, and $\hbar^2 k_{||}^2/2m^*$ is the energy of the electron in the emitter in the x - y plane parallel to the interfaces. Here, $k_{||}$ refers to the magnitude of the electron's momentum projected in the x - y plane. We can also refer to $k_{||}$ as the parallel momentum in the emitter. The energy of the electronic state in the well is given by a similar equation:

$$E_w = E_{zw} + \frac{\hbar^2 k'_{||}^2}{2m^*}, \quad (2.2)$$

where E_w is the total energy of the well state, E_{zw} is the energy of the well in the z direction, $\hbar^2 k'_{||}^2/2m^*$ is the energy of the electrons in the well in the x - y plane, and $k'_{||}$ is the parallel momentum of the electron in the well. By conservation of energy, the energy of the electron in the emitter must equal to the energy of the electron in the well plus the energy of the emitted phonon. Hence, the difference in the z energy $\Delta E_z = E_{za} - E_{zw}$ is given by:

$$\Delta E_z = \hbar\omega_{ph} + \frac{\hbar^2}{2m^*} (k'_{||}^2 - k_{||}^2), \quad (2.3)$$

where $\hbar\omega_{ph}$ is the energy of the emitted phonon.

Equation (2.3) is important because under certain circumstances, we can assume that the difference in voltage between the resonant peak and the phonon-assisted tunneling peak is directly proportional to the difference in the z energy

between the emitter and well states:

$$\Delta V \propto \Delta E_z. \quad (2.4)$$

We will discuss in Section 2.2.2 when this condition is satisfied. It would be convenient if we could combine Eqs. (2.4) and (2.3) to find the energy of the emitted phonon. However, it can be easily seen from Eq. (2.3) that, unlike the case of resonant tunneling, where the parallel momentum of the electron and hence the energy in the parallel direction must be conserved, the electron may gain or lose energy in the parallel direction. In the case of PAT, the phonon carries momentum, and by conservation of momentum,

$$\mathbf{k}_{||} = \mathbf{k}'_{||} + \mathbf{q}_{||}, \quad (2.5)$$

where $\mathbf{q}_{||}$ is the momentum of the phonon projected in the x-y plane. Hence, with no applied magnetic field, ΔE_z takes a wide range of possible values and, therefore, the phonon-assisted tunneling peak tends to be rather broad.

2.1.3 Phonon-Assisted Tunneling with $B \neq 0$

An energy scale may be determined if we apply a magnetic field parallel to the direction of current propagation. In this case, the energies of the electrons parallel to the interfaces are quantized into Landau levels. Therefore, the energy of the electronic state in the emitter is now given by:

$$E_a = E_{za} + (\nu + \frac{1}{2})\hbar\omega_c, \quad (2.6)$$

where ν is an integer and ω_c is the cyclotron frequency given by:

$$\omega_c = \frac{eB}{m^*}, \quad (2.7)$$

where B is the applied magnetic field. There is a similar equation for the energy of the electrons in the well.

During the PAT process, electrons can gain or lose energy in the parallel direction only by a change in Landau level, whose quantized energies are known. Therefore, by conservation of energy the difference in energy in the z direction is now given by:

$$\Delta E_z = \hbar\omega_{ph} + (\Delta\nu)\hbar\omega_c. \quad (2.8)$$

The phonon peak now contains many smaller peaks as illustrated in Fig. 2.2(c). The separate peaks on the main phonon peak correspond to the emission of a phonon and a change in Landau level. For a given magnetic field, we can easily calculate the the energy difference between Landau levels and then find the corresponding difference between voltage peaks. This gives us an energy scale which allows us to measure the phonon energies.

2.2 Electronic Effects in Phonon-Assisted Tunneling

2.2.1 Electronic States

In order to calculate the excess current, we need Fermi's Golden Rule to calculate the scattering rate of electrons from the optical phonons:

$$W(i \rightarrow f) = \frac{2\pi}{\hbar} |\langle i | H_{e-ph} | f \rangle|^2 \delta(E_a - E_w - \hbar\omega_{ph}), \quad (2.9)$$

where H_{e-ph} is the electron-phonon Hamiltonian, $\langle i |$ is the initial state defined as an electron in the emitter state, and $|f\rangle$ is the final state defined as an electron in the well and an emitted optical phonon. In this section we discuss

how the electronic states may be calculated for a given DBS and with no applied magnetic field, and in Section 2.2.2 we discuss how the electronic states may affect the current.

In order to find the electronic states, one must solve Schroedinger's equation for the electrons. The full three dimensional Schroedinger equation with no applied magnetic field is given by [BD66]:

$$-\frac{\hbar^2}{2}\nabla \cdot \left(\frac{1}{m^*(z)}\nabla\Psi(\mathbf{r}) \right) + U(z)\Psi(\mathbf{r}) = E\Psi(\mathbf{r}), \quad (2.10)$$

where $\Psi(\mathbf{r})$ is the three dimensional electronic wavefunction, E is the energy of the electron, $U(z)$ is the conduction band potential of the DBS, and $m^*(z)$ is the electron's effective mass as a function of z .

Since the potential and effective mass vary only in the z direction, the states in the x and y directions will simply be plane waves. Hence, we can use separation of variables to write the initial electronic state in the emitter $\Psi_a(\mathbf{r})$ and final electronic state in the well $\Psi_w(\mathbf{r})$ as:

$$\Psi_a(\mathbf{r}) = \frac{e^{i\mathbf{k}_{||}\cdot\mathbf{r}_{||}}}{\sqrt{A}}\varphi_a(z), \quad (2.11)$$

$$\Psi_w(\mathbf{r}) = \frac{e^{i\mathbf{k}'_{||}\cdot\mathbf{r}_{||}}}{\sqrt{A}}\varphi_w(z), \quad (2.12)$$

where $\varphi_a(z)$ is the electronic state in the z direction of the electron in the emitter, $\varphi_w(z)$ is the electronic state in the z direction of the electron in the well, and A is the cross sectional area of the device. The energies of these states are given by Eqs. (2.1) and (2.2). Here, $\varphi_{a,w}(z)$ both satisfy Schroedinger's equation in one dimension:

$$-\frac{\hbar^2}{2}\frac{d}{dz}\left[\frac{1}{m^*(z)}\frac{d}{dz}\varphi_{a,w}(z)\right] + U(z)\varphi_{a,w}(z) = E_{z,a,w}\varphi_{a,w}(z), \quad (2.13)$$

where $E_{z,a,w}$ refers to the energy of the electron in the z direction in either the emitter or well.

A common way to solve for the electronic states is a simultaneous solution of Schrödinger's and Poisson's equations [MH88, AES93, SR95]. This method is most convenient to use when we are determining the current resulting from electrons tunneling from a 2D gas in the emitter. It can also conveniently take into account the effects of the presence of space charge in the structure which can affect the potential by bending the conduction band edge. These effects are discussed in more detail in Section 2.2.2.

Poisson's Equation with a variable dielectric constant is given by:

$$\frac{d}{dz} \left[\kappa_0(z) \frac{d}{dz} U(z) \right] = \frac{e\rho(z)}{\epsilon_0}, \quad (2.14)$$

where $\kappa_0(z)$ is the static dielectric constant, ϵ_0 is the permittivity of free space, and $\rho(z)$ is the space charge density. This space charge density can be expressed by the Hartree approximation,

$$\rho(z) = \eta_w |\varphi_w(z)|^2 + \sum_j \eta_j |\varphi_j(z)|^2, \quad (2.15)$$

where η_w is the charge density in the well, η_j is the charge density in a bound state in the emitter, and the sum is over all bound states in the emitter $\varphi_j(z)$. We may assume the electron gas in the emitter is an ideal 2D gas at zero temperature, since most of our measurements are done at 4 K. Therefore, the η_j are given by

$$\eta_j = \frac{em^*(E_f - E_{z,j})}{\pi\hbar^2}, \quad (2.16)$$

where E_f is the Fermi energy, and $E_{z,j}$ is the energy in the z direction of the

jth bound state in the emitter. The charge density in the well depends on the tunneling rate of the collector barrier and is discussed in the next section.

We must also determine boundary conditions. The conduction band potential $U(z)$ is determined by the electric field ε , since $\varepsilon = -d(U(z)/e)/dz$. The potential is most easily calculated by using the electric field in the collector barrier ε_c as a control variable. In addition, we assume that the charge in the well and emitter totally screen the electric field in the emitter contact, so that the electric field in the contact is zero. This is ensured if

$$\epsilon_0 \kappa_0 \varepsilon_c = \eta_f + \sum_j \eta_j. \quad (2.17)$$

To determine boundary conditions for φ_a and φ_w , we note that the bound 2D electronic states in the emitter and well decay far into the emitter layer, i.e. $\varphi_{a,w} \rightarrow 0$ as $z \rightarrow -\infty$. However, the 2D electronic states in the emitter and well do not decay far into the collector region. Fortunately, except for very thin collector barriers, the amplitudes of the electronic states which do penetrate through the collector barrier are negligibly small, and thus, the outside edge of the collector barrier can be approximated by an infinite barrier [Tur94].

To numerically solve for the electronic states, we first assume no charge in the structure and numerically integrate Poisson's equation to calculate the conduction band potential $U(z)$ [AES93, Tur94]. Typically, steps for the spatial integration are about 5 Å. To find the energies of the bound states in this structure [Tur94, PFTV86], we first guess an initial energy and numerically integrate Schroedinger's equation to find the electronic wavefunction. Since we can never guess the exact energy, we note that the wavefunction will diverge far into the emitter. However, as we pass the correct energy, the state will switch from diverging to positive infinity to diverging to negative infinity. We then use

a bisection method to reach sufficient accuracy. Once the wavefunctions have been calculated, we can then use Eqs. (2.15) - (2.17) to determine the charge in the emitter and well and recalculate the potential $U(z)$. We then repeat this process until the energy from one iteration to the next is reasonably constant. Usually, it takes about 5 iterations to reach about 1 % accuracy.

For many of the DBS samples considered here, a typical electronic wavefunction in the emitter that participates in PAT usually leaks into the well, and the electronic wavefunction in the well also usually leaks into the emitter [Tur94, TT94]. In Section 2.3.4 it will be shown that the current due scattering from a phonon depends on an overlap integral which includes both the electronic wavefunctions in the emitter and well in addition to a phonon potential. It is important that this overlap integral include the emitter region of the device to properly calculate the PAT current.

During this discussion, we have assumed that the electronic wavefunctions are strictly 2D. However, because the emitter and well states are quasibound states in which electrons can tunnel from one state to the other, there will necessarily be some broadening in the z energy of these states. As it turns out, because PAT can take place for a large range of ΔE_z , the effect of broadening is minor and insensitive to how the broadening is taken into account in calculations [Tur94, TWT93]. In order to make a complete and detailed comparison with experimental data, broadening must be taken into account. However, we assume that the calculated currents which do not include broadening give a fairly accurate estimate of the PAT current [Tur94], and all calculated currents presented in this thesis do not take broadening into account.

2.2.2 Effects of Space Charge in Well

If the rate of phonon-assisted tunneling is faster than the rate of electrons tunneling out the collector barrier, a significant charge density may accumulate in the well [ZGTC88, ST88, LAS⁺89, ST92]. This usually happens when the collector barrier is larger than the emitter barrier. A build-up of charge in the well reduces the number of available states in the well because of the Pauli exclusion principle, thus reducing the tunneling rate through the emitter barrier. At the same time, the tunneling current through the collector barrier increases since there are now more electrons in the well to tunnel out. Since all the electrons in the well have the same energy in the z direction and the tunneling rate through the collector barrier is only weakly dependent on the parallel energy, we can assume that all the electrons tunnel through the collector barrier by one rate. Hence, equilibrium is reached when the charge density in the well $n_f = J/W_c$ [GTC87c, YWA⁺88, ST88], where J is the current density and W_c is the tunneling rate through the collector barrier.

This charge build-up in the well may affect the current-voltage characteristic in several ways. One significant effect is that it tends to reduce the current involved in phonon-assisted tunneling [LKD93, GRE93, TT94]. This reduction in current is the result of a reduced emission rate of electrons into the well. Calculations of the resonant tunneling current from simultaneous solutions of Schroedinger's and Poisson's equations suggest that the resonant current is similarly affected [ST88].

Another significant effect is the deflection of current peaks to higher voltages than the voltages that would be observed without charge build-up in the well [GTC87c, ST92]. The tunneling rate of the electrons from the emitter

into the well depends mostly on the ΔE_z , which is determined by the electric field across the emitter barrier. If there is a significant charge density in the well, this charge tends to screen the electric field between the emitter and well. Therefore, a large increase in the potential difference between the contacts results in only a small increase in the electric field in the emitter barrier. However, the electric field in the collector region is vastly increased, resulting in a large voltage drop, since most of the potential difference occurs across the collector region. Hence, we do not have a linear relationship between the change in applied voltage across the entire structure and ΔE_z . Most of the experimental data in this thesis are the results of samples biased so that the effects of charge build-up in the well are minimized, i.e., the tunneling rate from the emitter into the well is significantly less than the tunneling rate from the well into the collector. Therefore, Eq. (2.8) is a good approximation in our experimental data.

2.3 Review of Optical Phonon Modes in Structures with Pure AlAs barriers

2.3.1 Introduction to Dielectric Continuum Model

In polar semiconductors such as GaAs, longitudinal optical phonons can create large polarization fields which strongly interact with electrons. In bulk materials, the interaction energy of such a phonon with an electron can be found by calculating the phonon potential from the oscillating polarization field $\Phi(\mathbf{r})$. The interaction energy H_{e-ph} is then simply $H_{e-ph} = e\Phi(\mathbf{r})$, and the interaction energy is found to be proportional to $1/q$, where q is the magnitude of the phonon wavevector [BH54]. Hence, we expect that long wavelength

phonons to be preferentially emitted, and this preference should extend into heterostructures.

In heterostructures, the dielectric constant varies as a function of z , and the phonon potentials can become localized in the heterostructures. Various techniques have been developed to take into account the effects of localization on the interaction energy. Microscopic techniques calculate the phonon modes directly by looking at the forces between lattice atoms [HZ88, Men89, LMR91, RRB⁺93]. However, results from these calculations are often difficult to incorporate into transport calculations. There are also various macroscopic models which calculate the phonon potentials in terms of the bulk properties of the separate layers in the structure [Wen85, MA89, Men89, RB91]. Microscopic calculations have shown that the most commonly used macroscopic model, the dielectric continuum model, accurately approximates the electron-phonon interaction for long wavelength phonons, with which electrons couple most strongly [LMR91]. This section introduces the basic concepts of the dielectric continuum model. Section 2.3.2 describes the potentials and the dispersion relations in DBS samples made with GaAs and AlAs where the phonon modes are calculated using the dielectric continuum model. Section 2.3.3 describes the electron-phonon Hamiltonian which can be used to calculate the phonon-assisted tunneling current, and Section 2.3.4 presents formulae to calculate the currents and presents some calculations on a GaAs/AlAs DBS.

The dielectric continuum model assumes that the electric field generated by the phonons is well approximated by a scalar potential $\Phi(\mathbf{r})$. If there is no free charge, the potential must then obey Laplace's equation,

$$\nabla \cdot [\epsilon(\omega; z) \nabla \Phi(\mathbf{r})] = 0, \quad (2.18)$$

where $\epsilon(\omega; z)$ is the bulk dielectric constant in each of the layers. The dielectric continuum model also assumes electrostatic boundary conditions at the heterointerfaces are satisfied where the potential $\Phi(\mathbf{r})$ and the normal component of the electric displacement, $D_z = \epsilon(\omega; z)(\partial\Phi(\mathbf{r})/\partial z)$, must be continuous across the interfaces.

Because of translational symmetry in the direction parallel to the interfaces, the phonon potential $\Phi(\mathbf{r})$ can be expanded and written in the form [TT94]:

$$\Phi(\mathbf{r}) = \sum_{\mathbf{q}_{||}} \phi(\mathbf{q}_{||}) \frac{f(\mathbf{q}_{||}; z) e^{i\mathbf{q}_{||} \cdot \mathbf{r}_{||}}}{\sqrt{A}}, \quad (2.19)$$

where $\mathbf{q}_{||}$ is the momentum of the phonon projected in the x-y plane, and $f(\mathbf{q}_{||}; z)$ is the potential of the phonon in the z direction. The function $f(\mathbf{q}_{||}; z)$ must satisfy

$$\frac{d}{dz} \left[\epsilon(\omega; z) \frac{d}{dz} f(\mathbf{q}_{||}; z) \right] - q_{||}^2 f(\mathbf{q}_{||}; z) \epsilon(\omega; z) = 0. \quad (2.20)$$

By using an appropriate function for the dielectric constant, the phonon potentials and dispersion relations can then be found by solving Eq. (2.20).

2.3.2 Localized Phonon Potentials and Dispersion Relations

In DBS samples made with binary materials such as GaAs and AlAs, the dielectric constant $\epsilon_i(\omega)$ in each layer is given by the standard bulk semiconductor form:

$$\epsilon(\omega, z) = \epsilon_0 \kappa_\infty(z) \frac{(\omega^2 - \omega_{LO}^2(z))}{(\omega^2 - \omega_{TO}^2(z))}, \quad (2.21)$$

where κ_∞ is the high frequency dielectric constant, ω_{LO} is the longitudinal optical (LO) frequency, and ω_{TO} is the transverse optical (TO) frequency of

the corresponding bulk material. Putting this form of the dielectric constant in Eq. (2.21), and requiring the potentials to be continuous across the interfaces, we can then find the dispersion relations and phonon potentials.

In GaAs/AlAs DBS samples, there are a total of fourteen localized modes [KBS⁺92, TT92]. These modes include LO-like and TO-like confined modes in the well and barriers. The TO-like confined modes do not couple strongly with electrons and are not considered further. There are also eight interface modes, whose potentials peak at the interfaces and decay exponentially away from the interfaces. If the DBS is symmetric, there are two LO-like interface modes and two TO-like interface modes which are symmetric with respect to the center of the well and we refer to these modes as the symmetric interface modes. There are also two LO-like and two TO-like interface modes which are antisymmetric with respect to the well, and we refer to these modes as the antisymmetric interface modes. If the DBS is antisymmetric, the phonon modes are then only slightly modified.

The potential for the LO-like confined modes, in which the potentials are confined to a layer in the DBS, are found by assuming a dispersionless frequency, $\epsilon_i(\omega; z) = 0$, in the corresponding layer *i* as in the bulk case. These phonons do not penetrate beyond the confining layer and the potential in the adjacent layers must then be zero. Hence, we must have that $f(q_{||}; z) = \sin(n\pi z/d)$, where *d* is the width of the confining layer, *n* = 1,2,3,..., and *z* is measured from the left hand side of the confining region. The energies of these modes are the same as the corresponding energies in the bulk material. Hence, we have an energy of 36.2 meV for the LO confined mode in the well, and 50.1 meV for the LO confined modes in the barriers.

To solve Eq. (2.20) for the interface modes, we use the bulk dielectric constant, given by Eq. (2.21) in Eq. (2.20) and use the appropriate electrostatic boundary conditions. The corresponding LO and TO phonon energies and high frequency dielectric constants for GaAs and AlAs are given in Appendix C. In general, Eq. (2.20) can then be solved only for certain frequencies which give the dispersion relations and potential profiles for the interface phonons.

Most of the DBS samples discussed in this thesis and used in our experiments are asymmetric. Exact analytical solutions for the potential profiles and dispersion relations for the interface phonons in these structures are rather complex. There are two possible ways to deal with this problem. One way is to obtain the phonon potentials and dispersion relations from Eq. (2.20) using a numerical technique [Wen85, RLGL92, TT]. Here, we can set

$$f_i(q_{||}; z) = A_i e^{q_{||} z} + B_i e^{-q_{||} z} \quad (2.22)$$

in each layer because $\epsilon_i(\omega)$ does not vary with z inside a layer. The A_i and B_i can be found by setting the potentials equal at the interfaces and by forcing the potential to be bounded as $z \rightarrow \pm\infty$. In general, this leads to equations which can be satisfied only at certain frequencies, and a numerical root-solving method can be used to find the dispersion relation. The dispersion relations can then be used to find all the A_i and B_i to obtain the corresponding potentials.

Another way to deal with the problem of finding the potentials and dispersion relations of the interface modes in asymmetric samples is to note that neither of the electronic wavefunctions in the emitter or well penetrates much into the collector barrier [Tur94]. Hence, to calculate phonon potentials, we can model the asymmetric DBS by a symmetric DBS where the widths of both barriers are the same as the width of the emitter barrier in the actual DBS. We

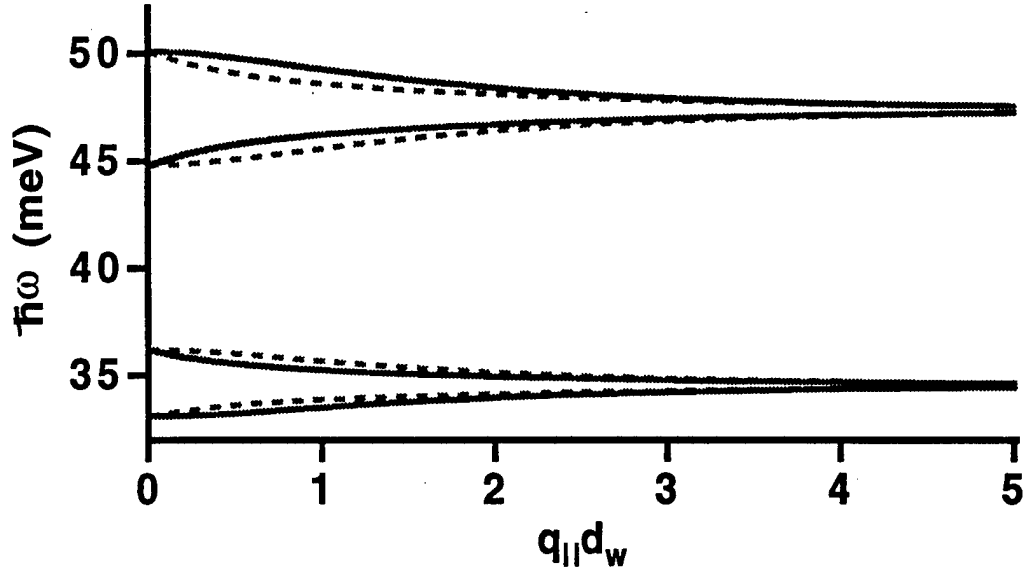


Figure 2.3: Dispersion curves for interface modes in a symmetrical DBS with an 80 Å well and 45 Å barriers. Solid lines show dispersion curves for symmetric interface modes, and dashed lines show dispersion curves for asymmetric interface modes.

assume that the scattering rates by phonon modes in the asymmetric structure are well approximated by the phonon modes in the symmetric structure. Such a symmetric structure then allows an exact solution for the dispersion relations and the potentials [KBS⁺92]. The discussion in the rest of this section assumes a symmetric DBS.

There are a total of eight interface modes for GaAs/AlAs DBS samples. Figure 2.3 plots the dispersion relations for the symmetric and antisymmetric interface modes for a DBS with an 80 Å well and 45 Å barriers. In the long wavelength limit, $q_{\parallel} \rightarrow 0$, there is a symmetrical and an asymmetrical interface phonon with the energy of a bulk AlAs LO phonon. Similarly, in the long wavelength limit, we have one symmetrical and one asymmetrical interface mode with energies of bulk AlAs TO phonons, GaAs LO phonons, and GaAs TO phonons. We can thus further classify the interface modes by the behavior

of the dispersion relation in the long wavelength limits. The modes with bulk LO energies as $q_{||} \rightarrow 0$ are referred to as LO-like and the modes with bulk TO energies as $q_{||} \rightarrow 0$ are referred to as TO-like. Furthermore, the modes converging to energies of bulk AlAs phonons are referred to as AlAs-like, and modes converging to energies of bulk GaAs phonons are referred to as GaAs-like. In the short wavelength limit, where $q_{||} \rightarrow 0$, the energies in the dispersion relations converge to the two solutions of the single interface dispersion relation: $\epsilon_w + \epsilon_b = 0$ [MA89].

Figure 2.4 shows the calculated LO-like phonon potentials for a DBS with an 80 Å well and 45 Å barriers, and with $q_{||}d_w = 0.8$, where d_w is the width of the well. The TO-like phonon potentials are very similar to these potentials. In Figs. 2.4(a) and 2.4(c), the potential peaks at the “outer” interfaces, which are the interfaces closest to the emitter and collector regions. These modes are therefore referred to as outer interface modes. Similarly, the modes illustrated in Figs. 2.4(b) and 2.4(c) are referred to as inner interface modes since their potentials peak at the “inner” interfaces, which are the interfaces adjacent to the well.

We can use a shorthand notation developed by Kim et. al. [KBS⁺92] to identify the interface modes. We label the phonon mode as “ ω ” with three subscripts. The first subscript is an “a” for an antisymmetric mode or an “s” for a symmetric mode. The second subscript is a “1” provided that the phonon has the energy of a GaAs optical phonon in the long wavelength limit, or a “2” provided that the phonon has the energy of an AlAs optical phonon in the long wavelength limit. The final subscript is a “+” which means it is an outer interface mode, or a “-” if it is an inner interface mode.

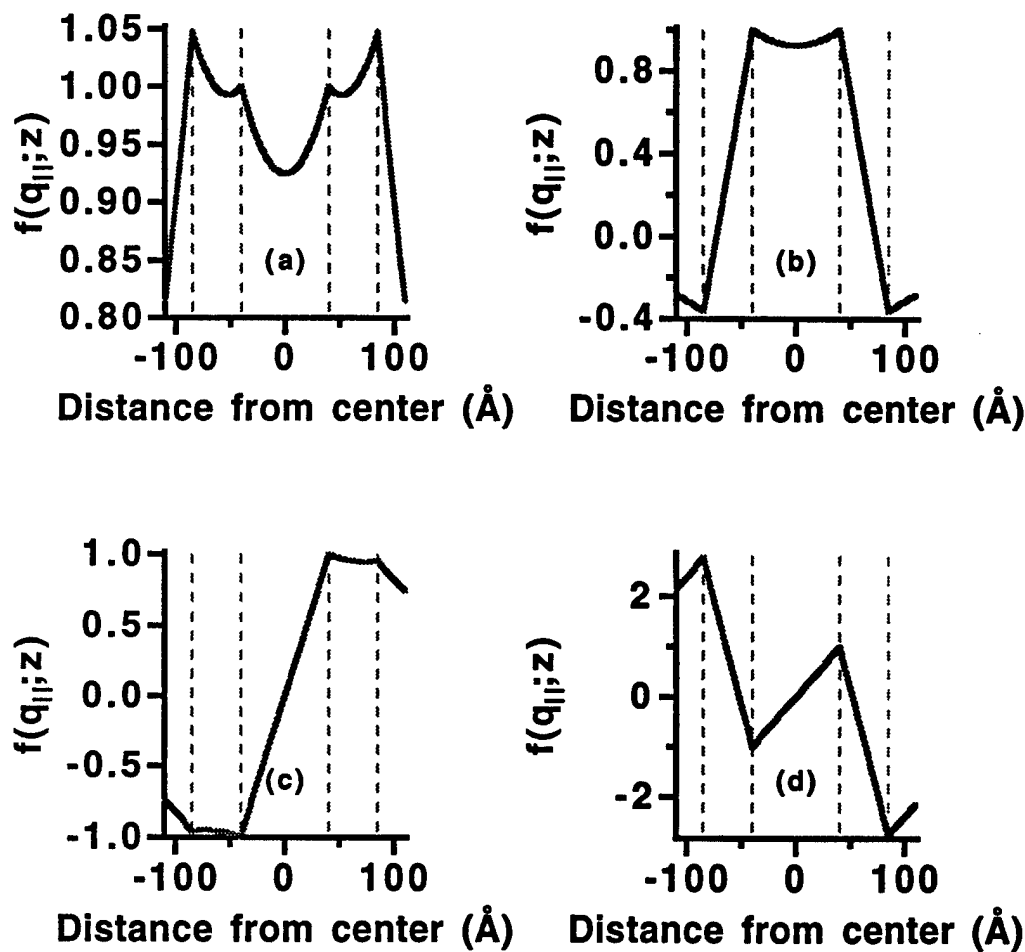


Figure 2.4: Calculated phonon potentials $f(q_{||}; z)$ with $q_{||}d_w = 0.8$ for LO-like interface modes as a function of the distance from the center of the well. Dashed lines show positions of interfaces. (a) Potential for the outer symmetric GaAs-like mode. (b) Potential for the inner symmetric AlAs-like mode. (c) Potential for inner asymmetric GaAs-like mode. (d) Potential for outer asymmetric AlAs-like mode.

Besides the localized phonons discussed above, electrons can also scatter off of bulk GaAs phonons in the emitter contact region, and the contribution of these modes must be included in any calculation of PAT current [MA89, BL94, TT94]. These phonon modes are often referred to as half space modes because they do not penetrate into the AlAs layer. It has been found that the current contribution from these modes can be well approximated by treating the half space modes as confined modes in the emitter using typical lengths of about 500 Å for the emitter confining region [TT94]. Beyond this region, where the electronic wavefunctions in the emitter and well are small anyway, these half space modes may be screened by the 3D electron gas in the heavily doped contact region [KDS78]. The bulk phonons in the collector contact are not important because the amplitude of the electronic states in the emitter and well are very small in the collector.

2.3.3 Electron-Phonon Interaction

To calculate the scattering rates, we must obtain the electron-phonon interaction Hamiltonian for heterostructures. Classically, the interaction Hamiltonian can be written as $H_{e-ph} = e\Phi(\mathbf{r})$ where $\Phi(\mathbf{r})$ is the electrostatic potential associated with phonons given by Eq. (2.19). This Hamiltonian can then be quantized, and a general expression valid for all localized phonon modes is obtained as [TT94]:

$$H_{e-ph} = \sum_{\mathbf{q}_{||}} \frac{\beta(q_{||})}{\sqrt{A}} e^{i\mathbf{q}_{||}\cdot\mathbf{r}_{||}} f(q_{||}; z) [a(\mathbf{q}_{||}) + a^\dagger(-\mathbf{q}_{||})], \quad (2.23)$$

where $a^\dagger(-\mathbf{q}_{||})$ and $a(\mathbf{q}_{||})$ are the creation and annihilation operators for phonons. The term $\beta(q_{||})$ is the coupling coefficient and is given by:

$$\beta(q_{||}) = (e^2 \hbar)^{\frac{1}{2}} \left[\int \frac{\partial \epsilon(\omega; z)}{\partial \omega} \left[q_{||}^2 f^2 + \left(\frac{df}{dz} \right)^2 \right] dz \right]^{-\frac{1}{2}}. \quad (2.24)$$

It is important to realize that the Hamiltonian in Eq. (2.23) is also valid for arbitrary heterostructures which includes DBS samples with $\text{Al}_x\text{Ga}_{1-x}\text{As}$ barriers with $x < 1$.

Since the current is roughly proportional to $\beta(q_{||})^2$, it is useful to look at the coupling coefficient $\beta(q_{||})$ for the various localized modes in the DBS, especially as $q_{||} \rightarrow 0$, since electrons couple most strongly with long wavelength phonons. It has previously been shown [MA89, TT94] that for long wavelengths, the symmetric LO-like interface mode ω_{s1+} has a very strong coupling coefficient, diverging as $(1/q_{||})$. The coupling coefficients for three other interface modes also diverge as $q_{||} \rightarrow 0$. The symmetric TO-like mode ω_{s2+} , and the two anti-symmetric LO-like modes, ω_{a2+} and ω_{a1-} diverge as $(1/q_{||})^{1/2}$. The four other interface modes have much smaller coupling coefficients at long wavelengths. Both the coupling coefficients of the symmetric LO-like mode ω_{s2-} and the anti-symmetric TO-like mode ω_{a1+} are nearly constant at long wavelengths, with ω_{a1+} being especially small throughout the range of $q_{||}$. The coupling coefficients for the TO-like symmetric mode ω_{s1-} and TO-like asymmetric mode ω_{a2-} are both proportional to $q_{||}$ as $q_{||} \rightarrow 0$. The mode ω_{s1-} is very small throughout the range of $q_{||}$, but the mode ω_{a2-} becomes rather large for large $q_{||}$. We can also look at the coupling coefficients of the confined modes too. The coupling coefficients for all the confined modes in the well and barrier are almost constant as a function of $q_{||}$, and the coupling coefficient for the well is

larger than the coupling coefficient in the barrier.

We note here that the strength of the coupling coefficients do not necessarily determine which phonons contribute most to the current. As we shall see in Section 2.3.4, the current is also roughly proportional to the square of an overlap integral between the electronic wavefunctions and the phonon potential [TT94]. This overlap integral can raise or lower a phonon's contribution to the current.

2.3.4 Current Formulae

In this section we will present formulae to calculate the PAT current for arbitrary $\text{GaAs}/\text{Al}_x\text{Ga}_{1-x}\text{As}$ DBS samples with $0 < x \leq 1$ and present results for a specific GaAs/AlAs DBS. The following calculations assume electrons tunneling from a 2D electron gas in the emitter state to a 2D gas in the well state. In our experimental structures, this is an excellent assumption because of the doping profile of the spacer layers [Wal]. We will also concentrate on calculation of currents with $B = 0$, since in Chapter 6, where we present our experimental data, we wish to try to determine the separate contributions to the current with $B = 0$ from modes of different energies.

To find the current, we first need to calculate the transmission rate of phonons via Fermi's Golden Rule Eq. (2.9). The initial state is defined as an electron in the emitter state, and the final state is defined as an electron in the well state and an emitted phonon. The initial and final electronic states are given by Eqs. (2.11) and (2.12), respectively, and the electron-phonon Hamiltonian is given by Eq. (2.23). This Hamiltonian is found by quantizing the interaction of an electron with the electrostatic potential associated with a phonon given by Eq. (2.19).

In the discussion above, we have defined $\mathbf{k}_{||}$ as the parallel momentum of an electron in the emitter state, $\mathbf{k}'_{||}$ as the parallel momentum of an electron in the well state, $\mathbf{q}_{||}$ as the parallel momentum of the emitted phonon, and ΔE_z as the difference in z energy between the emitter and well states. In addition to the total energy being conserved, the momentum in the parallel direction is also conserved. Hence, $\mathbf{k}_{||} = \mathbf{k}'_{||} + \mathbf{q}_{||}$. The magnitudes of the momentums are thus related to each other by the conservation of energy:

$$k_{||}^2 = k'^2_{||} + \frac{2m}{\hbar^2} (\hbar\omega(q_{||}) - \Delta E_z) \quad (2.25)$$

and the conservation of momentum:

$$q_{||}^2 = k'^2_{||} + k_{||}^2 - 2k'_{||}k_{||} \cos(\phi) \quad (2.26)$$

where ϕ is the angle between $\mathbf{k}_{||}$ and $\mathbf{k}'_{||}$. The energy of the emitted phonon $\hbar\omega(q_{||})$ is given by its corresponding dispersion relation which depends on the actual structure [TT94]. For a GaAs/AlAs DBS with an 80 Å well and 45 Å barriers, the dispersion relations are shown in Fig. 2.3. The dispersion relations for GaAs/Al_xGa_{1-x}As DBS samples will be discussed in Section 2.4.3.

Inserting the initial and final electronic states given by Eqs. (2.11) and (2.12) and the electron-phonon Hamiltonian given by Eq. (2.23) into Fermi's Golden Rule Eq. (2.9), we obtain the emission rate of phonons [TT92, Tur94]:

$$W(i \rightarrow f) = \frac{2\pi}{A\hbar} \beta^2(q_{||}) \left| \lambda(q_{||}) \right|^2 \delta_{\mathbf{k}_{||}-\mathbf{k}'_{||}-\mathbf{q}_{||}} \delta(E_w - E_a - \hbar\omega), \quad (2.27)$$

where $\left| \lambda(q_{||}) \right|^2$ is the overlap integral of the phonon potential with the electronic states:

$$\lambda(q_{||}) = \int \varphi_w^*(z) f(q_{||}; z) \varphi_a(z) dz \quad (2.28)$$

To find the current, we sum this emission rate over all available electronic states in the emitter and well, and over all possible phonon states. This current is thus given by [TT94]:

$$J(V) = \frac{e}{A} \sum_{\mathbf{q}_{||}} \sum_{\mathbf{k}_{||}} \sum_{\mathbf{k}'_{||}} W(i \rightarrow f) f_a(\mathbf{k}_{||}) (1 - f_w(\mathbf{k}'_{||})) , \quad (2.29)$$

where $f_a(\mathbf{k}_{||})$ is the Fermi distribution of electrons in the emitter state, and $(1 - f_w(\mathbf{k}'_{||}))$ is the available distribution of electronic states in the well. Note that this formula assumes that all electrons emitting a phonon and tunneling into the well state tunnel out of the collector barrier and thus contribute to the current. This is an excellent approximation since most of the measurements presented in this thesis are made at 4 K. At this temperature, there are few thermal phonons for the electrons to absorb and scatter back into the emitter.

Because the total momentum in the parallel direction is conserved one of the sums in Eq. (2.29) can be eliminated since the scattering rate Eq. (2.27) contains the term $\delta_{\mathbf{k}_{||} - \mathbf{k}'_{||} - \mathbf{q}_{||}}$. We can eliminate any of the momentum terms. However, the most useful result for our purposes is to eliminate the phonon momentum to obtain:

$$J(V) = \frac{e}{A} \int d\mathbf{k}'_{||} \int d\mathbf{k}_{||} W(i \rightarrow f) g_w(\mathbf{k}'_{||}) g_a(\mathbf{k}_{||}) f_a(\mathbf{k}_{||}) (1 - f_w(\mathbf{k}'_{||})) , \quad (2.30)$$

where $g_a(\mathbf{k}_{||}) = 2A/(2\pi)^2$ is the 2D density of electronic states in the emitter, and $g_w(\mathbf{k}'_{||}) = A/(2\pi)^2$ is the density of available states in the well. Electrons do not change spin during PAT, and hence the factor of 2 in the density of states in the well is dropped.

Finally, if we insert Eq. (2.27) into Eq. (2.30), and use conservation of momentum Eq. (2.26) and conservation of energy Eq. (2.25), we can then

integrate over the initial electronic states $\mathbf{k}_{||}$ to yield a general formula for the PAT current good for all localized phonon modes in all $\text{GaAs}/\text{Al}_x\text{Ga}_{1-x}\text{As}$ DBS samples [TT94]:

$$J(V) = \frac{em}{\pi^2 \hbar^2} \int_0^\pi d\phi \int_{k'_{||min}}^\infty dk' k'_{||} f_e(K_{||}) [1 - f_w(k'_{||})] \beta^2(Q_{||}) |\lambda(Q_{||})|^2. \quad (2.31)$$

The initial parallel momentum of the electron $K_{||}$ and parallel momentum of the phonon $Q_{||}$ for a given $k'_{||}$ and angle ϕ are specified by the conservation of energy and momentum equations:

$$K_{||}^2 = k'_{||}^2 + \frac{2m}{\hbar^2} (\hbar\omega(Q_{||}) - \Delta E_z) \quad (2.32)$$

$$Q_{||}^2 = k'_{||}^2 + K_{||}^2 - 2k'_{||} K_{||} \cos(\phi), \quad (2.33)$$

and the lower limit of integration $k'_{||min}$ is given by:

$$k'_{||min}^2 = \begin{cases} \frac{2m}{\hbar^2} (\Delta E_z - \hbar\omega_{ph}) & \text{if } \Delta E_z \geq \hbar\omega_{ph} \\ 0 & \text{if } \Delta E_z \leq \hbar\omega_{ph}. \end{cases} \quad (2.34)$$

Figure 2.5(a) plots the calculated current density due to each mode for a GaAs/AlAs DBS sample with an 80 Å well and 45 Å barriers. The equivalent experimental sample, which we refer to as the **1863** sample in Appendix B and is biased in the reverse direction, is a GaAs/AlAs DBS sample with an 80 Å well, a 45 Å emitter barrier and a 33 Å collector barrier. A detailed comparison between experiment and theory in this sample has been done elsewhere and has been shown to be quite good [TWT93]. The six highest modes have been labeled and include three GaAs-like modes (modes which converge to energies of bulk GaAs LO or TO phonons in the long wavelength limit), an interface mode ω_{a1-} , the confined mode in the well ω_{cw} , and the half-space modes ω_{s1+} ,

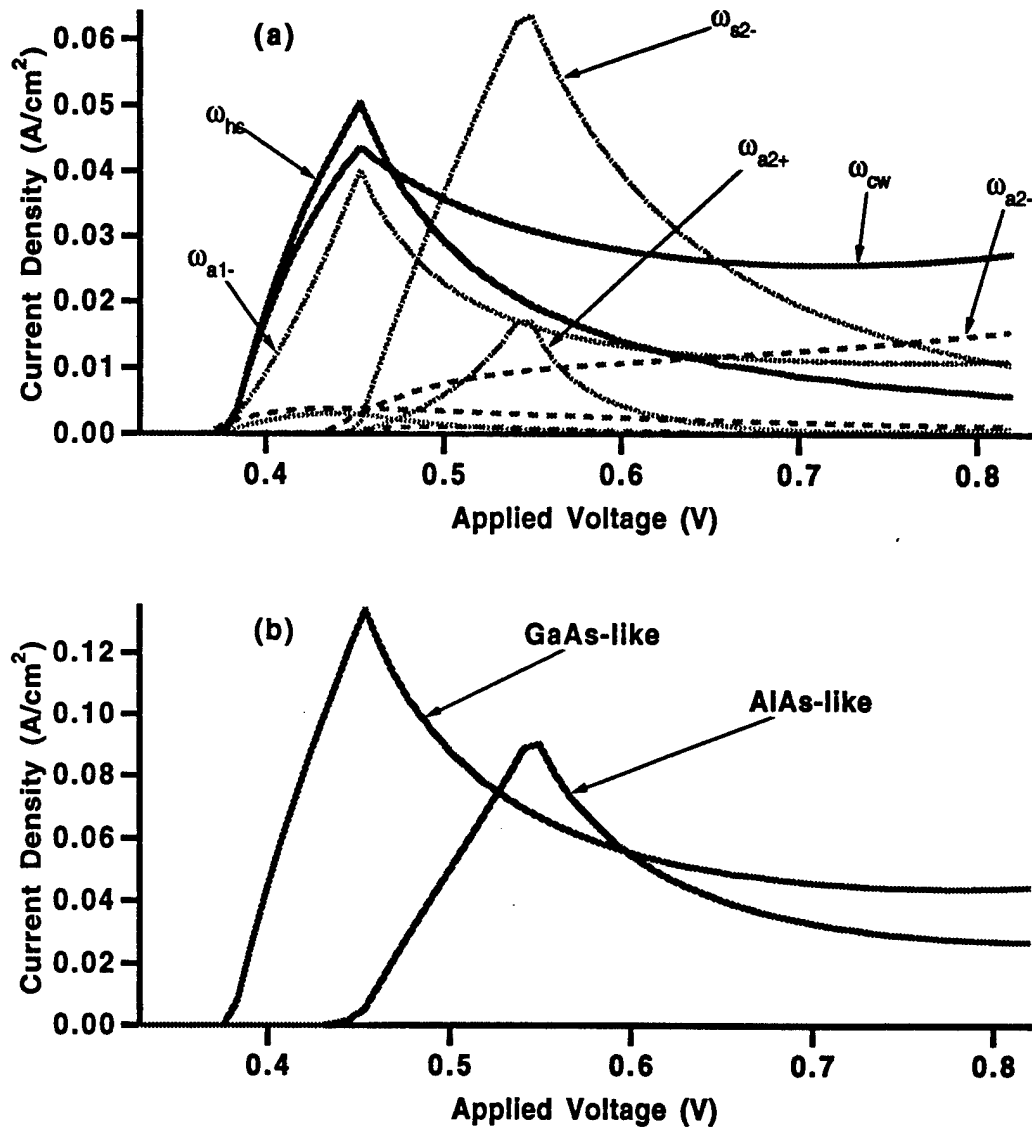


Figure 2.5: Calculated PAT currents for sample 1863. Charge build-up and broadening are not taken into account. (a) Separate current contributions due to all phonon modes. The six largest contributions are labeled. (b) Contributions from three largest GaAs-like modes and three largest AlAs-like modes. Ratio of peak currents is 0.67:1.

and three AlAs-like interface modes (modes which converge to energies of bulk AlAs LO or TO phonons in the long wavelength limit), ω_{s2-} , ω_{a2+} , and ω_{s2-} . Figure 2.5(b) plots the sum of the three highest GaAs-like modes and the three highest AlAs-like modes. As will be seen in Chapter 6, we will attempt to separate the contributions from the GaAs-like and the AlAs-like modes in the experimental data. The ratio of peak current of the AlAs-like modes to the peak current of the GaAs-like modes is 0.67:1. We will see in Section 2.3.4 how this ratio is expected to be affected by the variation in aluminum concentration in the barriers.

In order to understand why certain modes dominate the PAT current as seen in Fig. 2.5(a), it is useful to look at the overlap integral of the phonon potential with the electronic wavefunctions in addition to the relative size of the coupling constants [TT94], since the current is roughly proportional to $\beta^2(q_{||}) |\lambda(q_{||})|^2$. The modes ω_{a1+} and ω_{s1-} have very small coupling coefficients throughout the range of $q_{||}$ and, hence, do not contribute much to the current. The confined modes in the barriers also do not contribute much to the current because the electronic wavefunctions in the emitter and well states are very small in the barriers. Hence, the overlap integrals for these modes are small. Two modes which both have large coupling coefficients, but contribute negligibly to the current are the two outer symmetric modes, ω_{s1+} and ω_{s2+} . The reason these modes are so small is that the potential $f(q_{||}; z)$ for these modes is very close to the value of 1 throughout the entire range of z as shown in Fig. 2.4(a), especially for very small values of $q_{||}$. (The potential $f(q_{||}; z) \rightarrow 1$ as $q_{||} \rightarrow 0$.) Hence, the overlap integral is approximately $\langle \varphi_w(z) | \varphi_a(z) \rangle$ which must be zero since the electronic wavefunctions in the emitter and well are eigenfunctions of

the same Hamiltonian and are thus orthogonal. The other six phonon modes contribute very significantly to the current for this structure since they all have relatively large coupling coefficients and overlap integrals. The TO-like mode ω_{a2-} does not contribute much at small voltages, but contributes significantly at higher voltages. The coupling coefficient for this mode is very small for small $q_{||}$, but becomes much larger as $q_{||}$ increases, thus increasing the contribution as the applied voltage becomes larger.

2.4 Optical Phonon Modes in structures with alloy barriers, $\text{Al}_x\text{Ga}_{1-x}\text{As}$ ($0 < x < 1$)

2.4.1 Review of Bulk $\text{Al}_x\text{Ga}_{1-x}\text{As}$ Properties

The dielectric continuum model has proven quite effective in predicting currents of GaAs/AlAs DBS samples. However, many of the experimental structures studied and considered for applications include $\text{Al}_x\text{Ga}_{1-x}\text{As}$ instead of pure AlAs. Therefore, we need to extend the dielectric continuum model to include DBS structures made with GaAs/ $\text{Al}_x\text{Ga}_{1-x}\text{As}$. In this section, we review some basic properties of bulk $\text{Al}_x\text{Ga}_{1-x}\text{As}$, especially how the dielectric functions are affected as a function of the aluminum concentration. In Section 2.4.2, we discuss how we may extend the dielectric continuum model to include this alloy material. Section 2.4.3 discusses how the dispersion relations and phonon potentials are modified, and Section 2.4.4 discusses the electron-phonon interaction and the resulting currents as a function of the Al concentration.

Using $\text{Al}_x\text{Ga}_{1-x}\text{As}$ for the barriers in the DBS instead of AlAs affects both the electronic states and the phonon modes because of the variation of many of the bulk properties as a function of Al concentration x . An understanding of

these bulk properties is essential to understanding PAT in a GaAs/Al_xGa_{1-x}As DBS as a function of x, and these variations must be properly taken into account for any theory on PAT in DBS samples. A list of GaAs and Al_xGa_{1-x}As properties are given in Appendix C. One property which varies as a function of x is the effective mass m^* of the electron. In GaAs, the effective mass of the electron is approximately given by $m^* = 0.067 m_0$ where m_0 is the bare electron mass [Ada85]. For tunneling in barriers made with AlAs, the effective mass is approximately given by $m^* = 0.09 m_0$ [BdAeSS⁺90, LAW92]. It is assumed that the effective mass in Al_xGa_{1-x}As varies almost linearly between these two values with the aluminum concentration. This variation in effective mass mainly affects the electronic states in the emitter and the well. Additional properties which vary linearly as a function of x are the static and high-frequency dielectric constants [Ada85].

Another important bulk property which varies as a function of x is the band gap energy at the Γ point [CP78, Ada85]. Hence, the conduction band offset (the height of the barrier) will also change, which can affect the electronic states considerably. Experiments have shown the conduction band offset at the Γ point between GaAs and AlAs to be about 0.958 meV [CP78]. For Al_xGa_{1-x}As, this conduction band offset is approximately given by $V_0 = 0.75x$ if $x \leq 0.45$, and by $V_0 = 0.75x + 0.69(x - 0.45)^2$ if $x > 0.45$ [CP78]. As the concentration of Al decreases in the barriers (the height of the barrier decreases), the magnitude of the both emitter and well electronic wavefunctions in the barrier are expected to increase. Hence, we expect that the barrier modes will become more important. Also, if barrier widths are not varied, the emitter electronic wavefunction will have a greater magnitude in the well, and similarly for the electronic well state in the emitter. This will cause a much greater

overlap integral for all modes and much higher current levels. To compensate, we have chosen our barrier widths as a function of x to have approximately the same tunneling coefficients as the 1863 which is the 45/80/33 GaAs/AlAs structure, so that the overlap of the electronic wavefunctions in the well and emitter remains about the same throughout the aluminum concentration studied.

The energies of the bulk phonon modes are also affected, thus affecting the dielectric constant. Experiments have shown that $\text{Al}_x\text{Ga}_{1-x}\text{As}$ exhibits a two mode behavior for mixed crystals [MS87, JS81]. This means that there are a total of four optical phonon modes in $\text{Al}_x\text{Ga}_{1-x}\text{As}$ with $0 < x < 1$. There are LO and TO branches which have AlAs-like energies, and LO and TO branches which have GaAs-like energies. Figure 2.6 plots the energies of these modes versus the aluminum concentration x [MS87]. These data points, shown as the circles, are taken from Raman scattering experiments [JS81]. These energies appear to depend almost linearly on x , and the lines have been drawn in to illustrate this point more clearly. As $x \rightarrow 0$, the energies of the LO-like and TO-like GaAs-like modes converge to the corresponding bulk GaAs LO and TO phonon energies. The two AlAs-like branches converge to one energy, 42.1 meV, as $x \rightarrow 0$ which corresponds to the vibrational frequency of an Al impurity on the Ga site. Similar comments apply as $x \rightarrow 1$.

Many models have been proposed to account for these energies in the Raman data [CM71, Bon81]. Most are too complicated to be incorporated easily into the dielectric continuum model for transport calculations. Most models were proposed to explain the optical data and very little discussion of the interactions of the electron with two optical-phonon modes. A model discussing the electron-phonon Hamiltonian in a bulk ternary mixed crystal has been

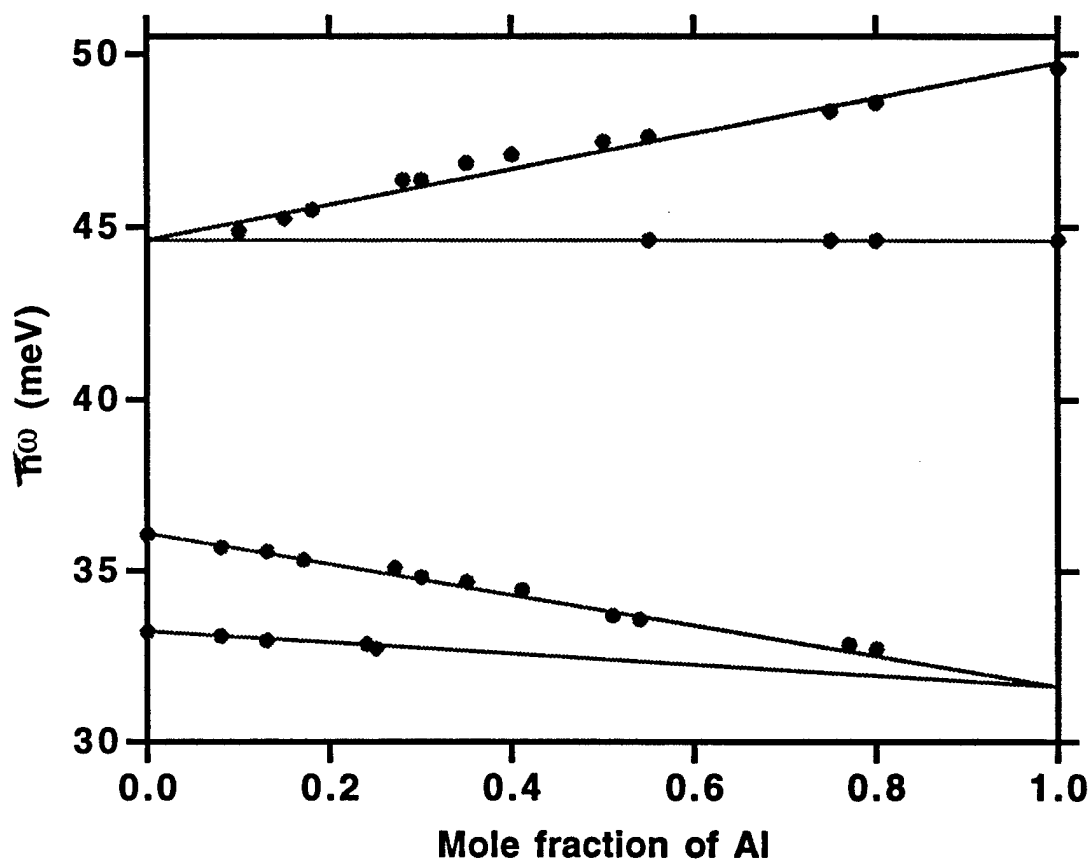


Figure 2.6: Experimental bulk phonon energies as a function of the Al concentration x [MS87]. Data points shown as circles are taken from experimental Raman scattering data [JS81] and the lines are drawn to help guide the eye.

proposed and a coupling parameter calculated [WL90]. The next section will discuss this model and how it affects the dielectric constant. We will also discuss how the model may be improved upon to obtain better agreement with experiment.

2.4.2 Generalization of Dielectric Continuum Model to Include Alloy Materials–Modified Dielectric Continuum Model

In order to apply the dielectric continuum model to $\text{Al}_x\text{Ga}_{1-x}\text{As}$, we need to model the dielectric constant of $\text{Al}_x\text{Ga}_{1-x}\text{As}$ with reasonable accuracy. One model used to derive the eigenfrequencies of a ternary mixed crystal such as $\text{Al}_x\text{Ga}_{1-x}\text{As}$ is referred to as the mean field method or the random element isodisplacement (REI) model [CM71, WL90]. This model assumes that a fraction x of the nearest neighbors of As atoms are Al atoms, and that a fraction $(1 - x)$ of the nearest neighbors of As atoms are Ga atoms. The model also assumes similar ions are displaced by the same amount by a phonon, and that the only forces on any atom are the nearest neighbor forces and the effective local field \mathbf{E}_{loc} . Hence, equations of motion similar to the Born-Huang equations [BH54] may be written as [TT]:

$$m_{\text{Al}}\ddot{\mathbf{u}}_{\text{Al}} = -\beta_1(\mathbf{u}_{\text{Al}} - \mathbf{u}_{\text{As}}) + e_{\text{Al}}\mathbf{E}_{\text{loc}}, \quad (2.35)$$

$$m_{\text{Ga}}\ddot{\mathbf{u}}_{\text{Ga}} = -\beta_2(\mathbf{u}_{\text{Ga}} - \mathbf{u}_{\text{As}}) + e_{\text{Ga}}\mathbf{E}_{\text{loc}}, \quad (2.36)$$

$$m_{\text{As}}\ddot{\mathbf{u}}_{\text{As}} = -x\beta_1(\mathbf{u}_{\text{As}} - \mathbf{u}_{\text{Al}}) - (1 - x)\beta_2(\mathbf{u}_{\text{As}} - \mathbf{u}_{\text{Ga}})e_{\text{As}}\mathbf{E}_{\text{loc}}, \quad (2.37)$$

where m_{Al} , m_{Ga} , m_{As} are the effective masses, \mathbf{u}_{Al} , \mathbf{u}_{Ga} , \mathbf{u}_{As} are the displacements, and e_{Al} , e_{Ga} , e_{As} are the effective charges of the Al, Ga, and As atoms respectively. Also, β_1 and β_2 are the nearest-neighbor force constants between

the Al and As atoms and the Ga and As atoms, respectively. By following a procedure similar to that of Born and Huang [BH54], the eigenfrequencies can be found, and a dielectric constant $\epsilon(\omega)$ can then be derived.

It can be shown that the dielectric constant found in the mean field method can be written in the form [KS90, TT]:

$$\epsilon(\omega) = \epsilon_0 \kappa_\infty(x) \frac{(\omega^2 - \omega_{LA}^2(x))(\omega^2 - \omega_{LG}^2(x))}{(\omega^2 - \omega_{TA}^2(x))(\omega^2 - \omega_{TG}^2(x))}, \quad (2.38)$$

where $\omega_{LA}(x)$ and $\omega_{TA}(x)$ are the x-dependent frequencies of the AlAs-like LO-like and TO-like phonon modes in $\text{Al}_x\text{Ga}_{1-x}\text{As}$, and $\omega_{LG}(x)$ and $\omega_{TG}(x)$ are the x-dependent frequencies of the LO-like and TO-like phonon modes in GaAs. If we were to look at the eigenfrequencies of the modes calculated using the mean field method and compare them to experiment [CM71, TT], we would find that the frequencies of the AlAs-like modes are predicted with reasonable accuracy. The GaAs-like modes are also predicted with good accuracy for low concentrations of aluminum. However, the mean field method vastly underestimates the frequencies of the GaAs-like modes near $x = 1$. This discrepancy can be understood by realizing that the Ga atom is much heavier than the Al atom, and the vibration of the Ga atom greatly perturbs the lattice around it. In Eqs. (2.35) - (2.37), we assumed that the AlAs lattice around a Ga impurity was not perturbed at all, therefore, lowering the frequency.

To improve on the mean field method, we can simply assume the dielectric constant to have the form given in Eq. (2.38) and use the experimentally obtained values for the frequencies of the phonon modes [CM71, TT]. We refer to this model as the modified mean field method. From Fig. 2.6, we can see that the frequencies vary almost linearly as a function of x. Hence, we assume

a linear dependence of each of the four phonon frequencies as a function of Al concentration. A list of these frequencies is given in Appendix C.

One final additional way to simplify finding the dielectric constant is to use the mean dielectric function [TT]:

$$\begin{aligned}\epsilon_{\text{Al}_x\text{Ga}_{1-x}\text{As}}(\omega) &= x\epsilon_{\text{AlAs}}(\omega) + (1-x)\epsilon_{\text{GaAs}}(\omega) \\ &= x\frac{\omega^2 - \omega_{LA}^2}{\omega^2 - \omega_{TA}^2} + (1-x)\frac{\omega^2 - \omega_{LG}^2}{\omega^2 - \omega_{TG}^2}\end{aligned}\quad (2.39)$$

where $\epsilon_{\text{GaAs}}(\omega)$ and $\epsilon_{\text{AlAs}}(\omega)$ are the bulk dielectric constants of GaAs and AlAs, respectively. Hence, ω_{LA} and ω_{TA} are the bulk LO and TO frequencies of AlAs, and ω_{LG} and ω_{TG} are the bulk LO and TO frequencies of GaAs. The poles of $\epsilon_{\text{Al}_x\text{Ga}_{1-x}\text{As}}(\omega)$ are simply given by the poles of $\epsilon_{\text{GaAs}}(\omega)$ and $\epsilon_{\text{AlAs}}(\omega)$, and thus, do not vary with x . However, the zeros of $\epsilon_{\text{Al}_x\text{Ga}_{1-x}\text{As}}(\omega)$ vary linearly with x , in good agreement with experiment. It has been found in most cases that by assuming this form of the dielectric wavefunction, similar results can be obtained as the modified mean field method [TT]. All of the results from the modified dielectric continuum model which are presented in this thesis have used dielectric constants found from either the modified mean field method or the mean dielectric function method.

2.4.3 Dispersion Relations and Phonon Potentials

Now that we have dielectric functions, we can solve for the dispersion relations and find the phonon potentials. We still have confined modes in the well and barriers, and these can be found as described in Section 2.3.3. We also have interface modes. The modified mean field method gives a total of twelve interface modes, while the mean dielectric function method gives only eight

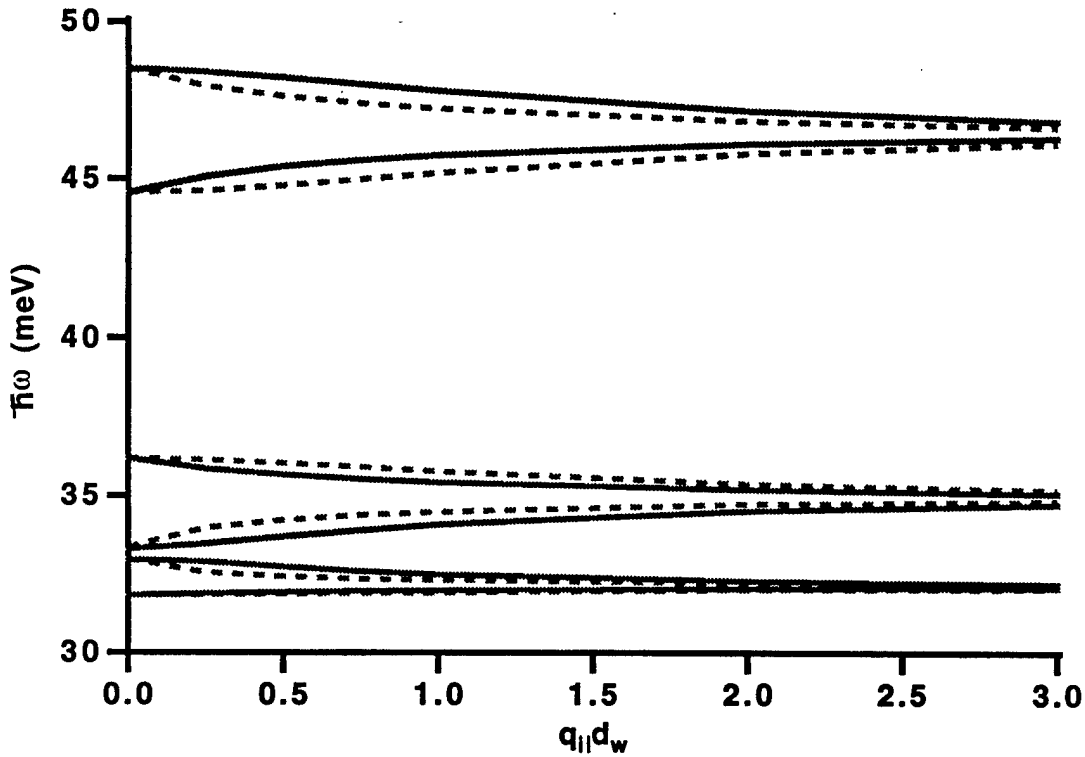


Figure 2.7: Dispersion relations for interface phonons in sample 263 calculated using modified mean field method. Solid lines are symmetric modes and dashed lines are antisymmetric modes. The four low energy modes are present only at aluminum concentrations $x < 1$.

interface modes [TT]. The interface modes of the mean dielectric function method and eight of the interface modes of the modified mean field method are present with pure AlAs barriers, with LO and TO energies given by the the bulk LO and TO energies in the long wavelength limit. Four of the modes given by the modified mean field method have energies below 33.3 meV and are not present with pure AlAs barriers.

Figure 2.7 illustrates the dispersion relation for sample 263 biased in the reverse direction. From Appendix B, we see that this sample nominally has an 80 Å GaAs well, a 62.2 Å emitter barrier, and a 45.6 Å collector barrier. The barriers consist of $\text{Al}_{0.7}\text{Ga}_{0.3}\text{As}$. The dispersion curves were calculated using

the modified mean field method and using a numerical root solving method to find the energies. As we can see from the figure, the eight high energy interface modes ($\hbar\omega > 33.3$ meV) have very similar dispersion relations as the eight interface modes of the DBS with pure AlAs barriers shown in Fig. 2.3. In the long wavelength limit, we have two modes each converging to the bulk energies of the LO-like and TO-like AlAs-like modes and to the bulk energies of the LO-like and TO-like GaAs-like modes. In the short wavelength limit, the modes converge to the solutions of $\epsilon_{\text{Al}_x\text{Ga}_{1-x}\text{As}} + \epsilon_{\text{GaAs}} = 0$ [MA89].

Figure 2.8 illustrates the LO-like phonon potentials calculated for the 263 sample with $q_{||}d_w = 0.75$ and using the modified mean field method. Since it is very difficult to obtain the analytical solutions, the potentials were found numerically using the technique described in Section 2.3.2. Indeed, this numerical method proves most efficient to find the phonon potentials when there is an asymmetrical structure or when we use $\text{Al}_x\text{Ga}_{1-x}\text{As}$ in the barriers. A glance at Fig. 2.4 reveals that the GaAs-like and the AlAs-like phonon potentials for sample 263 are very similar to the phonon potentials of the sample with pure Al barriers. In addition, we show the phonon potentials for the low energy phonons, and we can see that they are almost identical to the AlAs-like phonon modes.

2.4.4 Electron-Phonon Interaction

We have already presented the formula for the current, Eq. (2.31), due to each phonon mode. The current is directly related to the square of the coupling coefficient $\beta^2(q_{||})$ given by Eq. (2.24), and the square of the overlap integral $|\lambda(q_{||})|^2$, given by Eq. (2.28). The coupling coefficients for bulk $\text{Al}_x\text{Ga}_{1-x}\text{As}$ and some heterostructures with GaAs and $\text{Al}_x\text{Ga}_{1-x}\text{As}$ have been calculated [WL90,

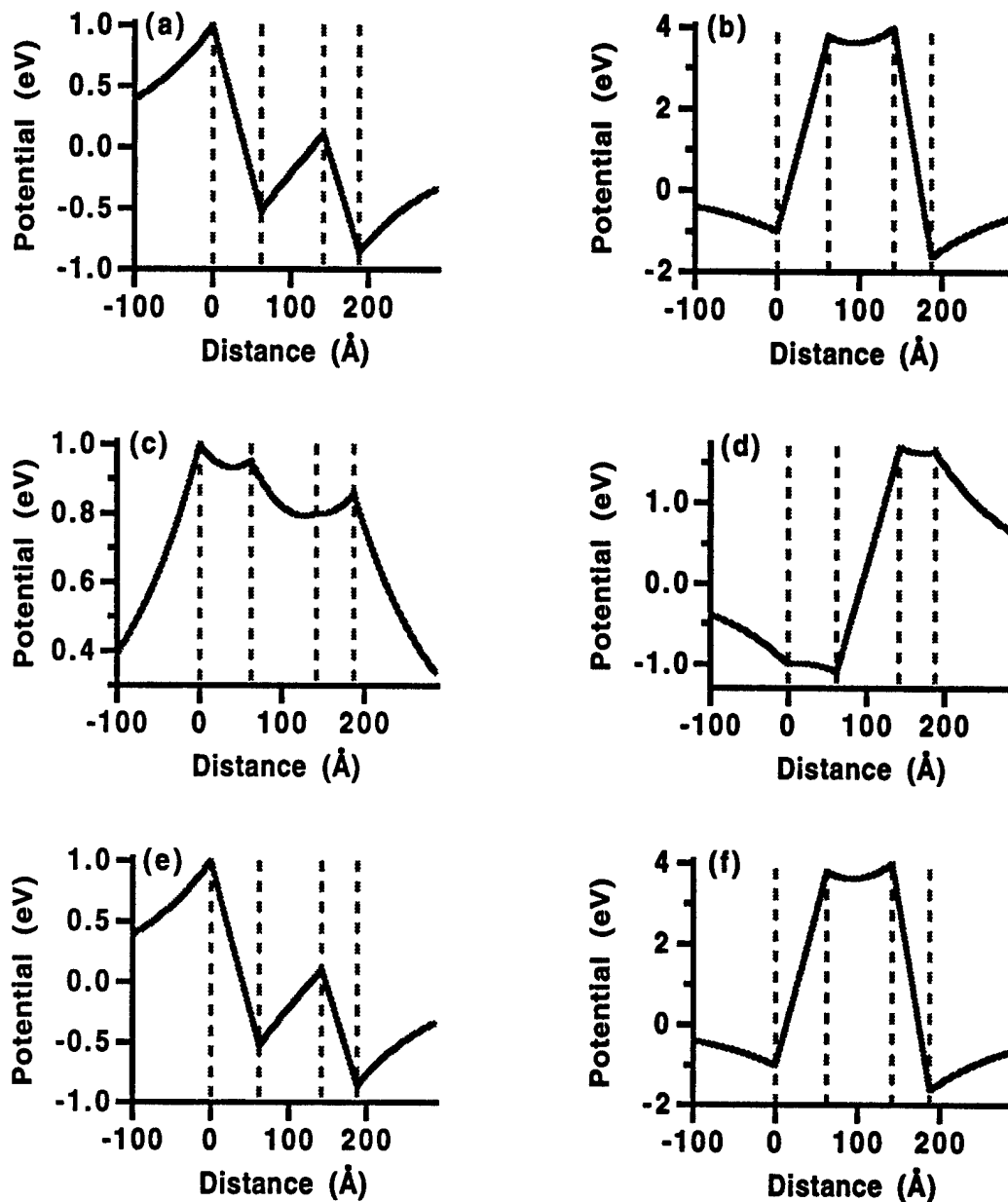


Figure 2.8: Potentials for LO-like phonon modes in sample 263 calculated by modified mean field method. Here, $q_{||}d_w = 0.75$. (a) Low energy anti-symmetric-like mode. (b) Low energy symmetric-like mode. (c) GaAs-like symmetric-like mode. (d) GaAs-like antisymmetric-like mode. (e) AlAs-like anti-symmetric-like mode. (f) AlAs-like symmetric-like mode. TO-like modes are almost identical.

KS90, GC91, TT], and often it is found that the coupling coefficients for the AlAs-like interface modes decrease and the coupling coefficients for the GaAs-like interface modes increase as the Al concentration decreases [WL90, KS90, TT]. Recent calculations of PAT currents of a DBS consisting of an 80 Å well, a 33 Å emitter barrier, and a 45 Å collector barrier with various concentrations of Al have found that the current due to the AlAs-like modes decreases relative to the current due to the GaAs-like modes as the aluminum concentration decreases [TT]. These same calculations have also shown that contributions from the TO-like GaAs-like interface modes also become more important as the Al concentration decreases. We find similar behavior for the asymmetric barrier structures described in Appendix B.

Figure 2.9(a) illustrates the current due to each phonon mode in sample 263 using the modified mean field method. We have labeled the ten highest contributing modes. Solid lines are due to the confined modes and the half space modes; gray lines are due to the LO-like phonons; dashed lines are due to the TO-like modes; and the dotted lines are due to the low energy modes. All the modes which contribute the most to sample 1863 in Fig. 2.5(a) also contribute significantly to the PAT current of this sample. These modes are the confined mode in the well ω_{cw} , the half space mode ω_{hs} , the LO-like interface modes, ω_{a1-} , ω_{s2-} , and ω_{a2+} and the TO-like interface mode ω_{a2-} at high voltages. However, comparing the two figures, we can see that the TO-like interface modes, ω_{s1-} and ω_{a1+} , for sample 263 contribute much more significantly than those same modes for sample 1863. In addition, we can see that the two LO-like low energy modes with $\hbar\omega < 33.3$ meV also make a small, but non-negligible contributions to the current. We have labeled these modes as ω_{a+} and ω_{s-} .

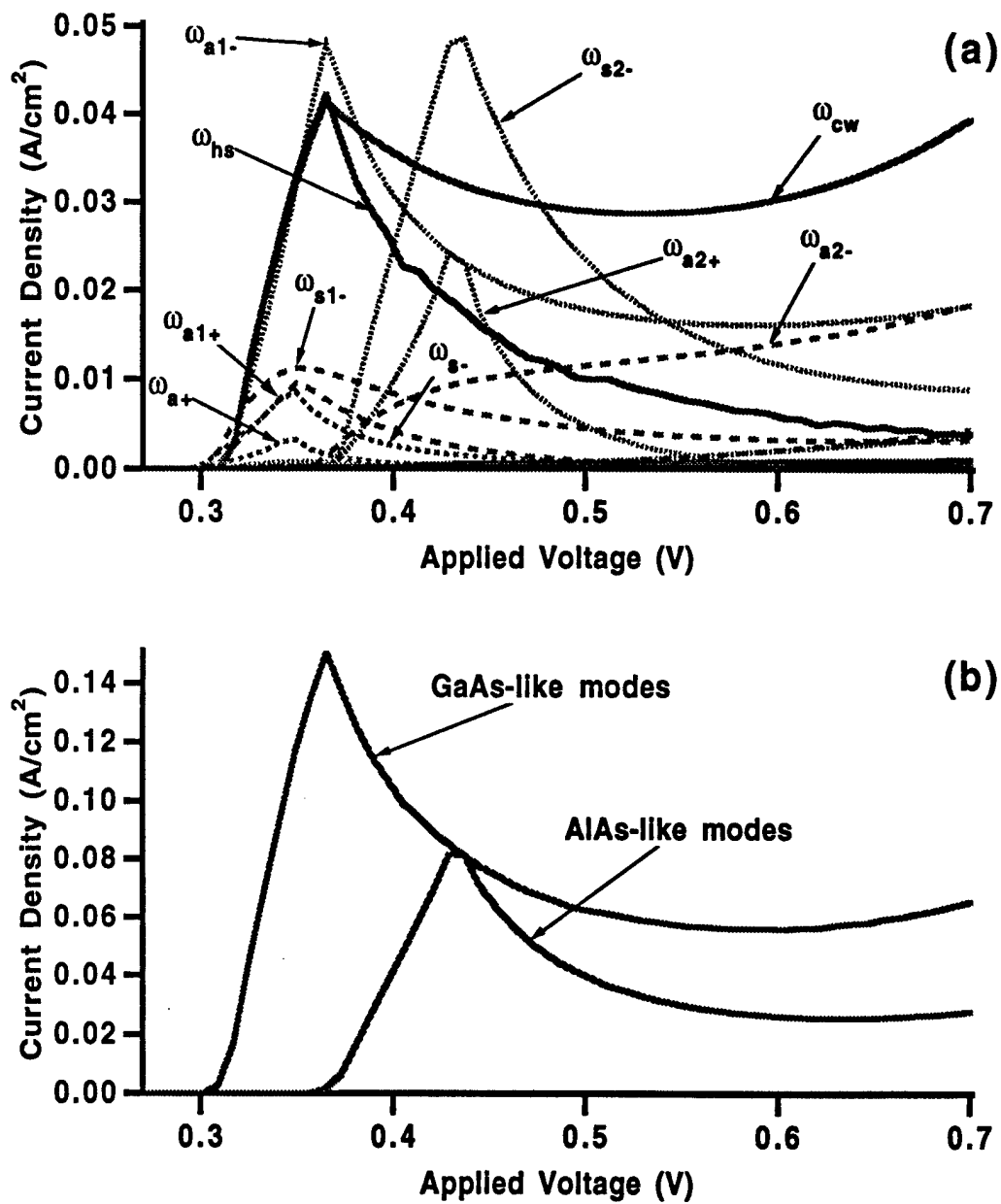


Figure 2.9: Calculated current densities for sample 263. Electronic broadening and charge build-up in well are not taken into account. (a) Current due to each phonon mode. (b) Current due to GaAs-like and AlAs-like modes. Five highest LO-like and TO-like modes are included in GaAs-like modes. Three highest LO-like and TO-like modes are included in AlAs-like modes. Ratio of peak currents is 0.543:1.

Another obvious difference between Figs. 2.5(a) and 2.9(a) is that the height of the AlAs-like modes relative to the GaAs-like modes are smaller for sample **263** with Al concentration $x = 0.7$ than for sample **1863** with pure AlAs barriers. This decrease is evident in Fig. 2.9(b) where we show the sum of the five highest GaAs-like modes and the sum of the three highest AlAs-like modes. The ratio of the current peak of the AlAs-like modes to the current peak of the GaAs-like modes is 0.543:1 compared to 0.67:1 for sample **1863**. This is not surprising because the Al concentration is lower in sample **263** than in sample **1863**.

We have also calculated the currents due to each of the phonon modes for sample **293** which has an 80 Å well, a 94.4 Å emitter barrier, and a 69.2 Å collector barrier. The barriers consist of $\text{Al}_{0.4}\text{Ga}_{0.6}\text{As}$. We plot these currents in Fig. 2.10(a), and we have labeled eight modes with the highest contributions. We can easily see a continuation of the trends described above. The TO-like interface modes, ω_{s1-} and ω_{a1+} , are now very significant and contribute almost as much as the confined mode in the well, the half space mode, and the AlAs-like interface modes. As we shall see in Chapter 6, this increase in the contribution from the TO-like modes is in good agreement with our experimental results, which shows strong evidence for a mode with a GaAs-like TO-like energy, and that this mode becomes stronger as the aluminum concentration decreases. The contributions from the low energy modes, however, are not as significant as they are for sample **263** and are not visible on this scale. From Fig. 2.10(a), we can also see that the AlAs-like phonons have a much smaller contribution to the current relative to the GaAs-like modes, but that the contribution from these modes should still be experimentally detectable. In Fig. 2.10(b), we plot the sum of the five highest GaAs-like modes and the sum of the three highest

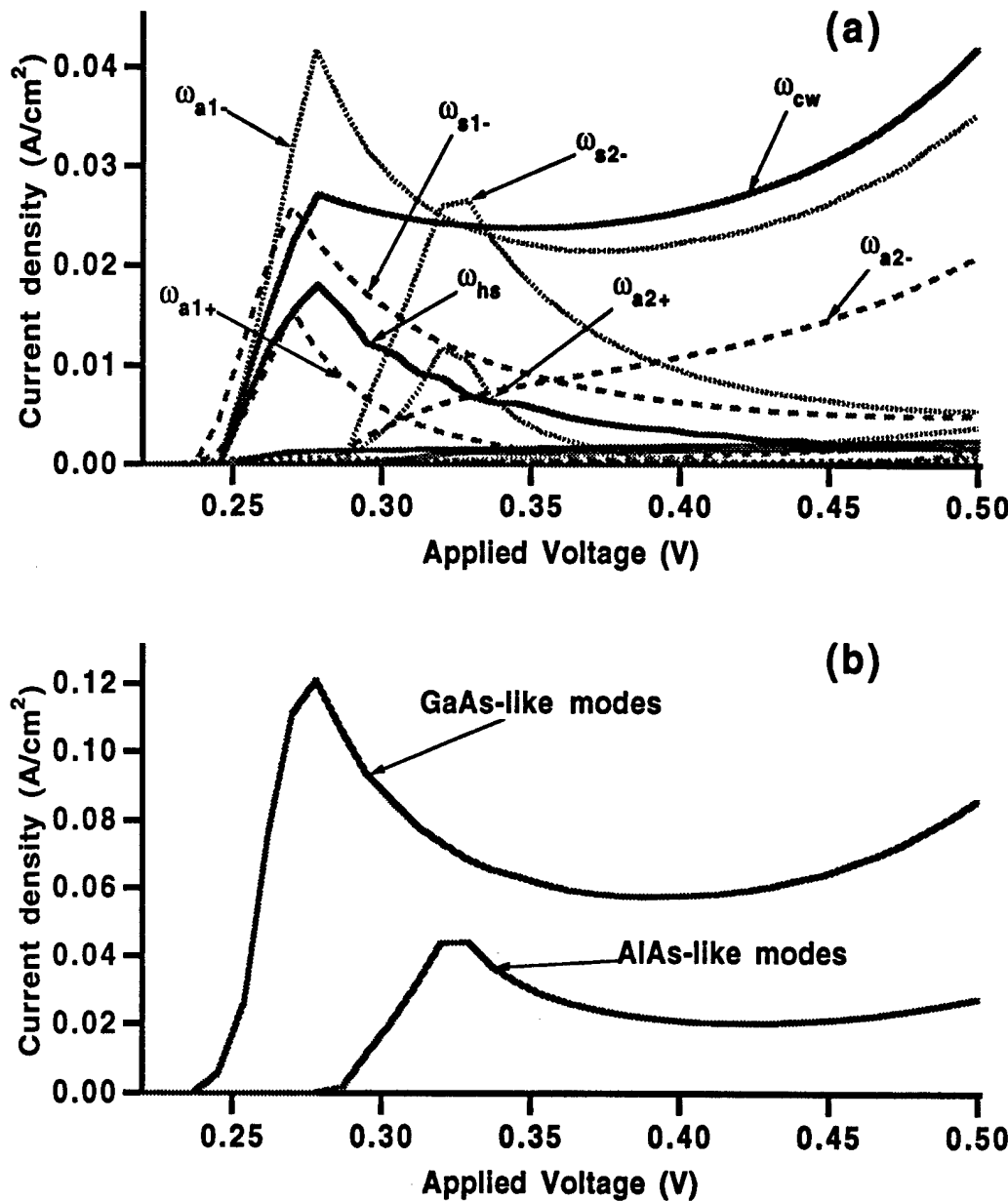


Figure 2.10: Calculated current densities for sample 293. Electronic broadening and charge build-up in well not taken into account. (a) Current due to each phonon mode. (b) Current due to GaAs-like and AlAs-like modes. Five highest LO-like and TO-like modes are included in GaAs-like modes. Three highest LO-like and TO-like modes are included in AlAs-like modes. Ratio of peak currents is 0.364:1.

AlAs-like modes. The ratio of the AlAs-like modes to the GaAs-like modes is 0.364:1 and is smaller than the corresponding ratios for samples **263** and **1863**.

We have calculated the currents due to all the asymmetric barrier samples described in Appendix B. To compare the relative contributions from the AlAs-like modes compared to the GaAs-like modes, we have summed for each sample the five highest contributing GaAs-like modes and the three highest contributing AlAs-like modes. We then found the ratio of the peak of the AlAs-like modes to the peak of the GaAs-like modes, and we have plotted this ratio as a function of the Al concentration x in Fig. 2.11. It is clear from the graph that this ratio decreases as a function of x . In Chapter 6, we will present preliminary results of a fitting routine to determine these ratios from the experimental current-voltage curves, and compare these ratios with Fig. 2.11.

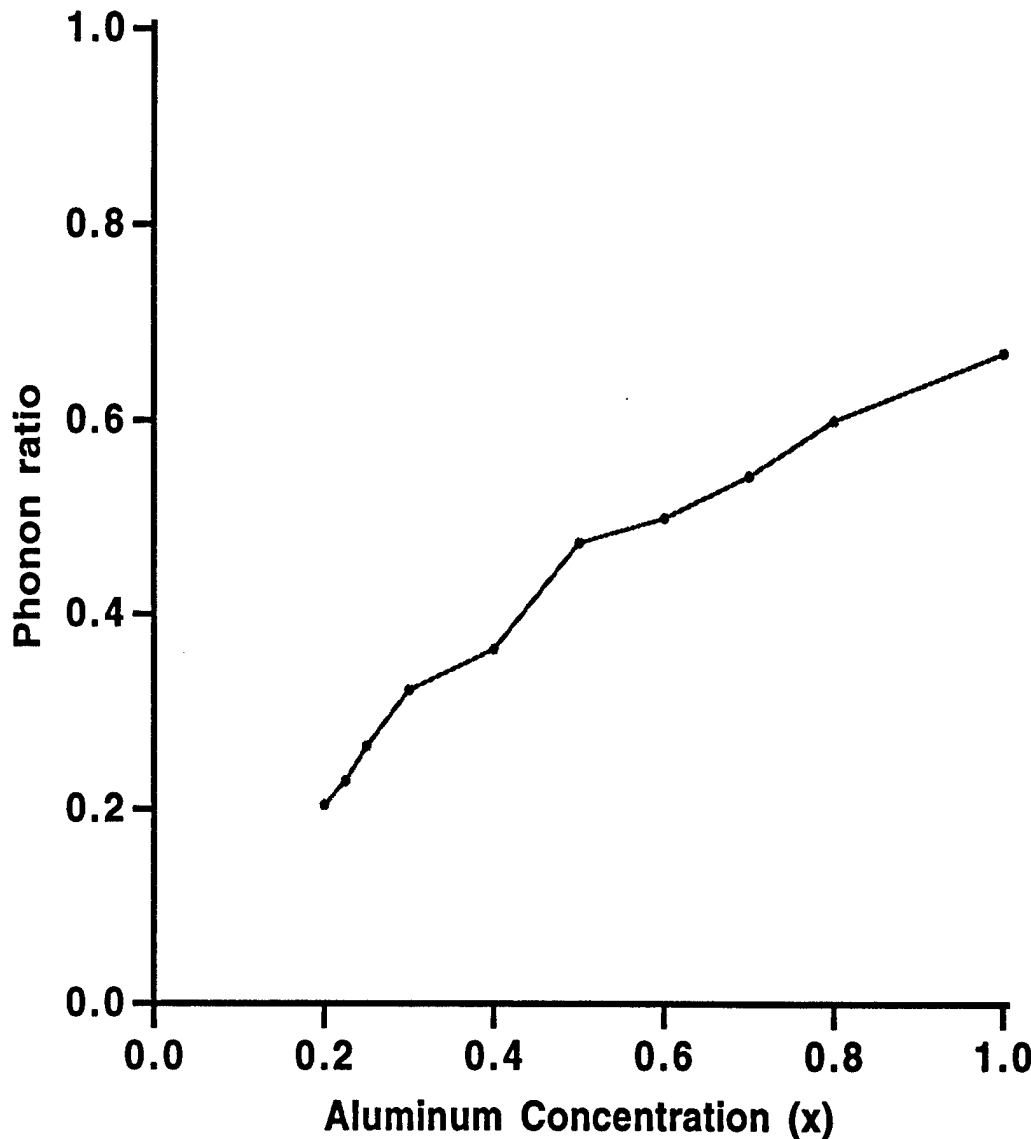


Figure 2.11: Ratios of calculated GaAs-like currents to calculated AlAs-like currents as a function of aluminum concentration for asymmetric barrier samples given in Appendix B.

Chapter 3

Theory of Circuits which Incorporate DBS's

3.1 Introduction

Experimental measurements of time-averaged current-voltage (I-V) curves of devices with negative differential resistance (NDR), such as double barrier structures, commonly reveal irregular structure, hysteresis, and bistability in that region [GTC87b, AEH⁺88, YWL⁺88, MLSE94]. This behavior has been attributed to both “intrinsic” mechanisms—such as the effects of space charge buildup in the resonant state of the well for double barrier structures [GTC87b, MSH89, JB91, ST92] as well as various “extrinsic” mechanisms associated with parasitic reactances in the circuit [Sol87, Liu88b, JK91, KMEH91]. In this chapter we will deal exclusively with extrinsic effects, although much of the analysis applies to systems with intrinsic bistability as well.

In Fig. 3.1(a) we show an example of an I-V curve of a sample, which we will later label as sample 1863, which shows irregular structure and hysteresis in the NDR region [TWT93]. Here we label I as the total measured current through the circuit and v as the measured voltage across the sample.

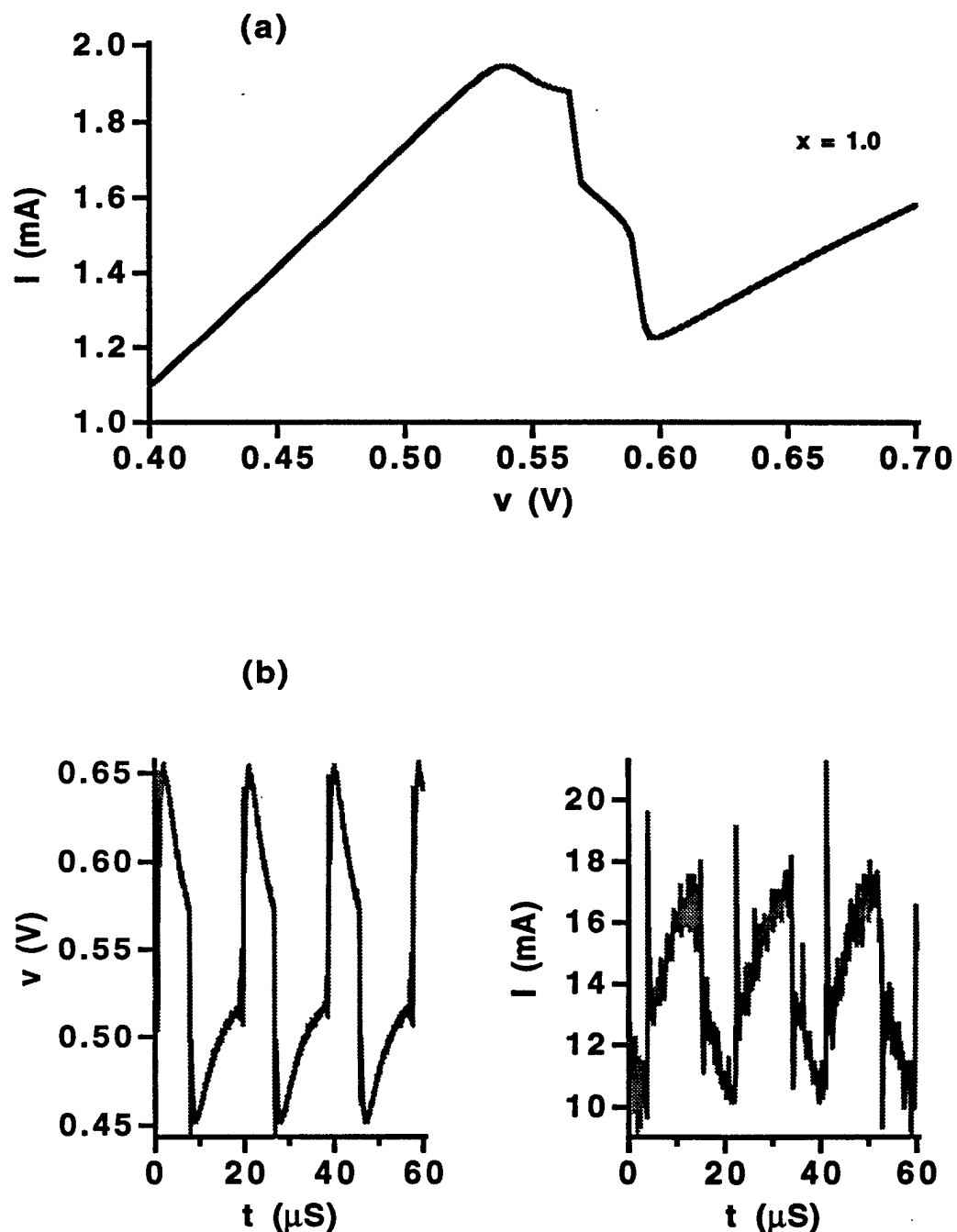


Figure 3.1: (a) Forward bias experimental I-V curve for asymmetric barrier sample with $x = 1.0$. Irregular structure in NDR region is due to spontaneous circuit oscillations. (b) Voltage and current oscillations for $V_{\text{ext}} = 0.62$ V.

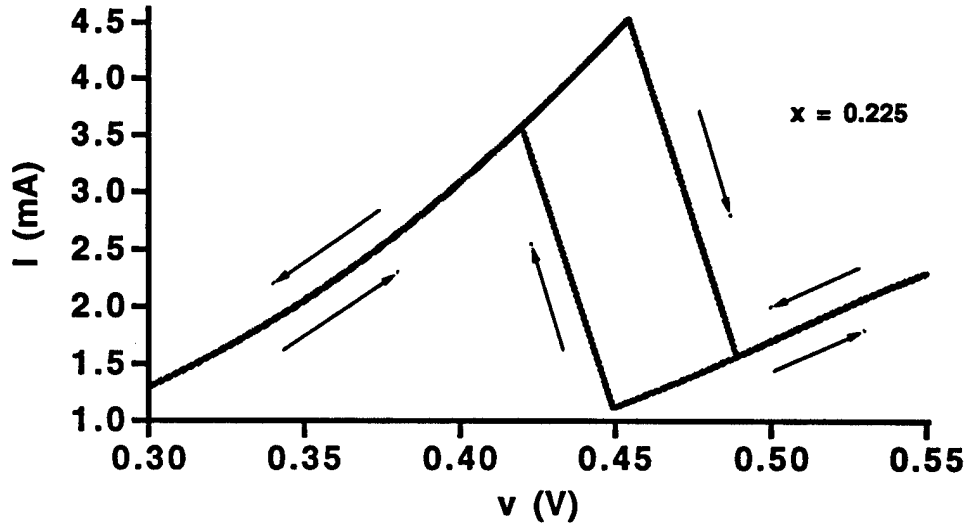


Figure 3.2: Forward bias experimental I-V curve for asymmetric barrier sample with $x = 0.225$. Curve is intrinsically bistable and no oscillations are observed and no points in the NDR region are measured.

All experimental data shown here was obtained using techniques described in Chapter 5. The irregular structure or the plateau evident in the NDR region is the time-averaged current and voltage of spontaneous oscillations caused by parasitic reactances in the measuring circuit. Examples of the voltage and current oscillations at some applied voltage are shown in Fig. 3.1(b). In Fig. 3.2 we show an example of an I-V curve with intrinsic bistability. This curve was measured from the sample we label the $x = 0.225$ asymmetric barrier sample. The resonant peak is offset to higher voltages due to charge in the well [ST92, MLSE94]. No point in the NDR region is seen, and no oscillations are associated with this curve. We are interested only in curves such as that in Fig. 3.1(a).

Figure 3.3 shows a typical biasing circuit with an applied dc voltage, V_{ext} across a DBS. This and related circuits have been the subject of extensive numerical simulations and small signal (linear stability) analysis [Liu88a, Liu88b,

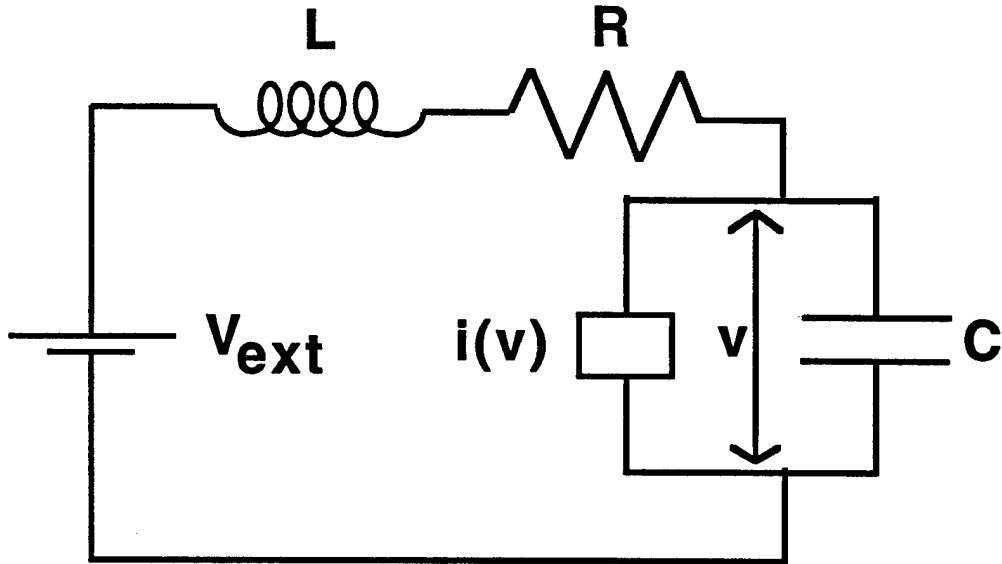


Figure 3.3: Typical biasing circuit for a DBS.

BMBA⁺90, JK91, KMEH91], and these circuits can also be used to model devices with NDR other than DBS's and circuits which incorporate these devices such as high frequency oscillators [BGS88]. The characteristic curve of the device, denoted $i(v)$, is modeled by some parametric curve. The series resistance R is due to parasitic resistance in the lead wires and contact regions or any resistors deliberately added [GCM⁺87, BGS88, JK91]. The inductance L models the self-inductance in the wires and contacts [GCM⁺87, JK91, KMEH91]. The capacitance C in parallel with the DBS is due, for example, to the charge layers that form on either side of the double barrier structure [GCM⁺87, JK91, KMEH91].

The large signal behavior of the circuit in Fig. 3.3 is governed by the following equations [Liu88b]

$$\frac{dI}{dt} = \frac{1}{L}(V_{ext} - IR - v) \quad (3.1)$$

$$\frac{dv}{dt} = \frac{1}{C} (I - i(v)) \quad (3.2)$$

where I is the total current through the circuit. Steady state solutions, which we denote I_0 and v_0 , of Eqs. (3.1) and (3.2) are obtained by setting the time derivatives to zero. Linear stability of the steady state of a particular V_{ext} is then determined from the eigenvalues from the linearized versions of Eqs. (3.1) and (3.2). These eigenvalues are given by [Liu88a]

$$\lambda = - \left(\frac{R}{2L} + \frac{i'(v_0)}{2C} \right) \pm \left[\left(\frac{R}{2L} - \frac{i'(v_0)}{2C} \right)^2 - \frac{1}{LC} \right]^{\frac{1}{2}} \quad (3.3)$$

where $i'(v_0)$ is the DBS steady state differential conductance. The steady state solution can be seen to be linearly unstable if $i'(v_0) < -RC/L$ or $i'(v_0) < -1/R$. The steady state is linearly stable otherwise.

If the circuit in Fig. 3.3 spontaneously oscillates, it can be shown analytically that the oscillations result from a Hopf bifurcation, and that there is a relationship between the bifurcation type and resulting dynamical behavior [WT93, WT94]. In this chapter we apply bifurcation theory to Eqs. (3.1) and (3.2) and discuss the analytic and numerical results. Section 3.2.1 reviews general bifurcation theory and presents the analytical results. Section 3.2.2 discusses the numerical results by numerically integrating Eqs. (3.1) and (3.2).

3.2 Bifurcation Analysis

3.2.1 Review of Bifurcation Theory and Analytical Results

In general, a Hopf bifurcation occurs when a steady state becomes unstable to periodic oscillations as we vary a control parameter into the unstable eigenvalue

region. For the circuit in Fig. 3.3, V_{ext} is the control parameter and the oscillations can be associated with a limit cycle in the I-V plane [GH83, BPV84]. The defining condition for a Hopf bifurcation is the point where the real part of the eigenvalue in Eq. (3.3) passes through zero with non-zero imaginary part as V_{ext} is varied. If we denote the voltage point of the intrinsic $i(v)$ curve at the instability threshold as v_c , then we can see from Eq. (3.3) that the conditions for a Hopf bifurcation for this system are given by two conditions [WT94]

$$i'(v_c) = -\frac{RC}{L} \quad (3.4)$$

$$\frac{L}{R} > RC. \quad (3.5)$$

Note that these conditions imply that current oscillations are observed only when $i'(v_c) > -1/R$. The condition $i'(v_c) < -1/R$ of linear instability mentioned above implies the existence of two new steady state solutions in the unstable region; the circuit may then exhibit bistability and hysteresis, but no time-dependent current oscillations. Furthermore, the imaginary part of the eigenvalue at v_c gives a close estimate of the frequency of oscillations near the bifurcation point [Liu88a]. This frequency is given by

$$\begin{aligned} \omega_{lc} &\approx \sqrt{\frac{1}{LC}} \sqrt{1 - \frac{RC}{L/R}} \\ &= \omega_0 \sqrt{1 - \frac{\tau_{RC}}{\tau_{LR}}}. \end{aligned} \quad (3.6)$$

All the following discussion assumes that Eqs. (3.4) and (3.5) are satisfied.

In general, in the neighborhood of a Hopf bifurcation, Eqs. (3.1) and (3.2) can be transformed into normal form which is given in polar coordinates

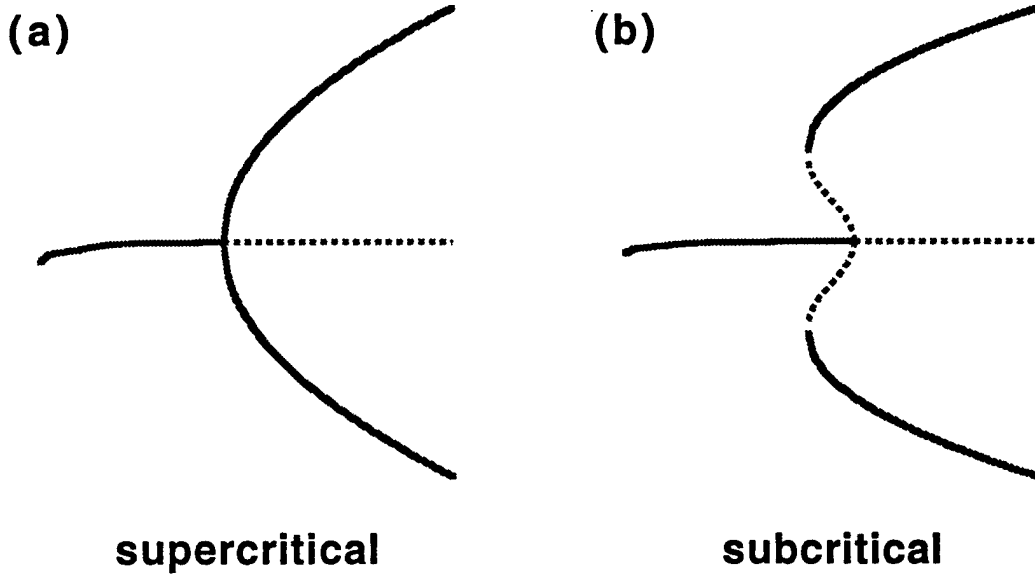


Figure 3.4: Illustration of Supercritical vs. Subcritical Hopf bifurcation ($f > 0$). Solid lines represent linearly stable steady state points or amplitude extremes of stable oscillations and dashed lines represent linearly unstable steady state points or amplitude extremes of unstable oscillations. (a) Supercritical Hopf bifurcation. Stable oscillations grow smoothly from zero as $(-f\mu/a)^{1/2}$. No hysteresis is expected. (b) Subcritical Hopf bifurcation. Unstable oscillations grow smoothly from zero as $(-f\mu/a)^{1/2}$. Discontinuity and hysteresis is now expected in the onset of oscillations and oscillations may be observed where the system is linearly stable.

by [GH83]

$$\frac{dr}{dt} = (f\mu + ar^2)r \quad (3.7)$$

$$\frac{d\theta}{dt} = (\omega + c\mu + br^2) \quad (3.8)$$

where f , a , ω , c , and b are constants in the particular system of interest, and μ is the control parameter scaled such that the bifurcation occurs at $\mu = 0$. The linear stability of the oscillations are determined by the sign of the parameter a . Therefore, there are two possible types of Hopf bifurcation which may be observed in the system and they are illustrated in Fig. 3.4. Solid lines in the figure represent linearly stable steady state solutions or amplitude extremes of

stable oscillations, while dashed lines represent linearly unstable solutions or amplitude extremes of unstable oscillations.

If $a < 0$, then the Hopf bifurcation is supercritical [BPV84]. As μ is increased (when $f > 0$) or μ decreased (when $f < 0$) through zero, small amplitude stable limit cycle oscillations grow from the steady state solution. Their amplitude grows smoothly from zero as $(-f\mu/a)^{1/2}$. For this bifurcation, no hysteresis is expected in the onset of oscillations.

If $a > 0$, then the Hopf bifurcation is subcritical. As μ is increased (when $f < 0$) or μ decreased (when $f > 0$) through zero, small amplitude unstable limit cycle oscillations grow from the steady state solution. Their amplitude grows smoothly from zero as $(-f\mu/a)^{1/2}$. For this case, there are (at least) two stable solutions, most typically the linearly stable solution and a large amplitude limit cycle oscillation. For this system, the amplitudes of the unstable limit cycle oscillations cannot grow indefinitely. Eventually, the current and voltage reach the region of positive differential resistance and damping occurs. The transition between the large amplitude current oscillations and steady state behavior is now expected to be discontinuous and hysteretic. We note here that the presence of a bifurcation can be important in determining the sensitivity of the device to noise. Random fluctuations can cause the circuit to switch between steady state and oscillatory behavior causing additional noise.

To determine the type of Hopf bifurcations in our system, we must perform a standard normal form calculation on Eqs. (3.1) and (3.2). We need only to determine the sign of the parameter a defined in Eq. (3.7). Details of this calculation are given in Appendix A. Therefore, we find that [WT94]

$$\text{sgn}(a) = \text{sgn} \left[\frac{RL(i''(v_c))^2}{L - R^2C} - i'''(v_c) \right] \quad (3.9)$$

where $i''(v_c)$ and $i'''(v_c)$ are the second and third derivatives of $i(v)$ evaluated at the Hopf bifurcation point of interest.

Equation (3.9) reveals that the bifurcation type is sensitively dependent on the detailed form of $i(v)$ as well as the circuit parameter values. We note that if $i'''(v_c)$ is negative, then $\text{sgn}(a)$ is always positive, and, hence, the bifurcation at that point will always be subcritical, regardless of the choice of parameters. However, if $i'''(v_c)$ is positive, then the bifurcation type will be determined by the circuit parameters. We have observed this type of behavior in many of the numerical simulations which are described in the next section.

3.2.2 Numerical Results for Circuit Model

We can numerically integrate Eqs. (3.1) and (3.2) if we know the precise form of $i(v)$ and all the circuit parameters. We have studied several functional forms of $i(v)$ and a typical example is shown in Fig. 3.5(a). If we also choose typical values of $R = 10\Omega$, $C = 0.1 \text{ pF}$, and $L = 1.0 \text{ nH}$, we can see that condition in Eq. (3.5) is satisfied and that $-RC/L = -1.0 \text{ mS}$. Figure 3.5(b) shows the differential conductance $i'(v)$ along with the instability condition of Eq. (3.4) for the chosen parameters above. Two Hopf bifurcation points are clearly evident at $v_{1c} = 0.207 \text{ V}$ (corresponding to $V_{\text{ext}} = 0.217 \text{ V}$) and $v_{2c} = 0.362 \text{ V}$ (corresponding to $V_{\text{ext}} = 0.367 \text{ V}$).

Defining $h(v)$ to be the bracketed term in Eq. (3.9), we plot in Fig. 3.5(c) $h(v)$ corresponding to the $i(v)$ curve in Fig. 3.5(a) and the circuit parameters chosen above. We can see that $h(v) < 0$ at $v_{1c} = 0.207 \text{ V}$ corresponding to a supercritical Hopf bifurcation and that the $h(v) > 0$ at $v_{2c} = 0.362 \text{ V}$ corresponding to a subcritical Hopf bifurcation. We numerically integrate Eqs. (3.1) and (3.2) using a fourth order Range Kutta method and plot the enve-

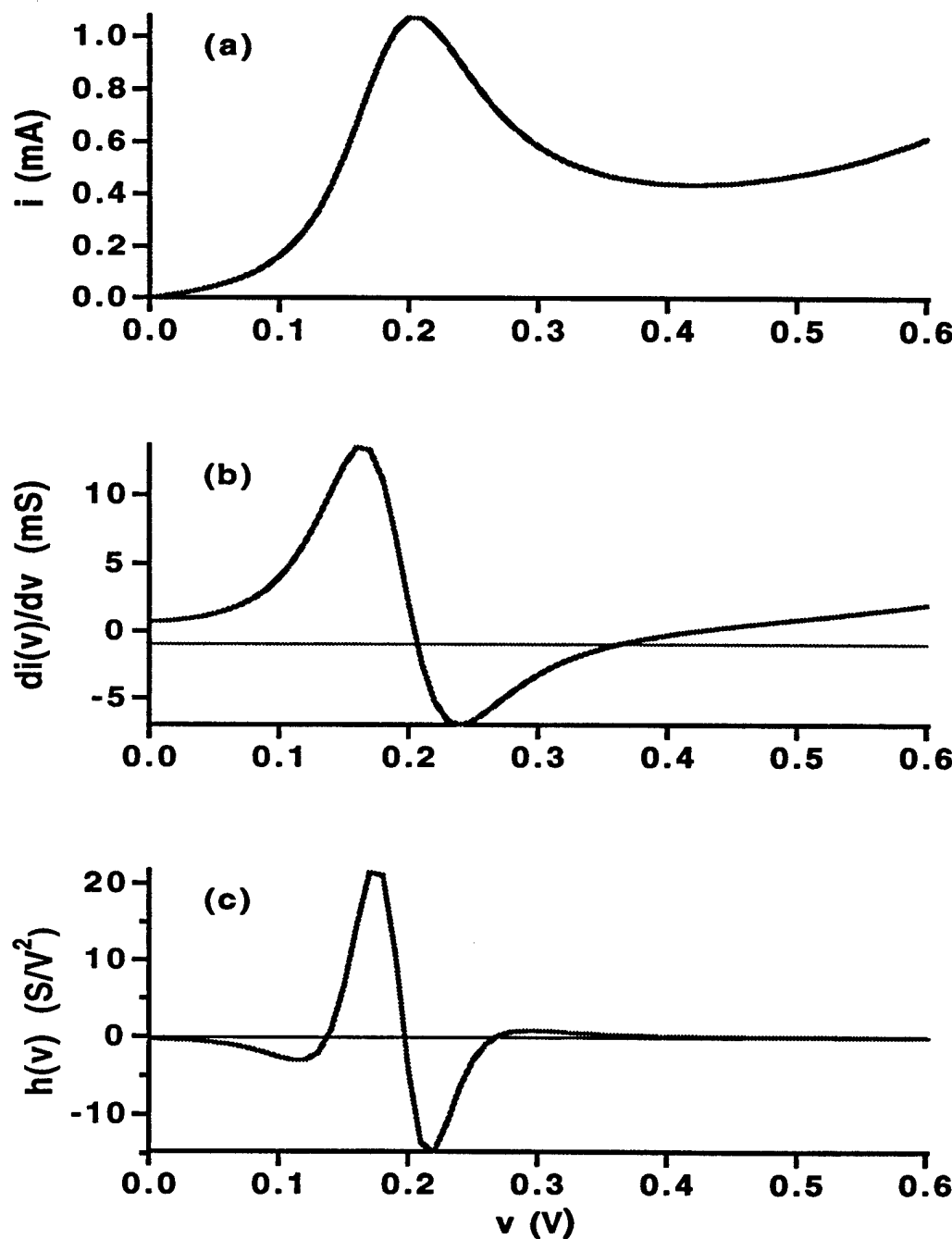


Figure 3.5: (a) Typical intrinsic device i-v characteristic used in numerical simulations. (b) Differential conductance curve $i'(v)$; intersections with horizontal line at $RC/L = -1\text{mS}$ indicate Hopf bifurcations at $v_{1c} = 0.207$ V and $v_{2c} = 362$ V. (c) $h(v)$ curve; $h(0.207) = -11.4$ indicates a supercritical bifurcation and $h(0.362) = 0.3$ indicates a subcritical bifurcation.

lope of time-dependent oscillations and time-averaged I-V curve in Fig. 3.6(a). Solid lines represent the time-averaged total current versus the applied voltage; dashed lines indicate the amplitude extremes of current oscillations for increasing applied voltage while dotted lines indicate amplitude extremes for decreasing applied voltage. Figure 3.6(a) clearly shows a supercritical bifurcation at $V_{\text{ext}} = 0.217$ V and a subcritical bifurcation at $V_{\text{ext}} = 0.367$ V in full agreement with the analytical results described above.

We should note that $i'''(v_{2c})$ is negative and hence any Hopf bifurcation that occurs at that point will always be subcritical. However, $i'''(v_{1c})$ is positive and the type of Hopf bifurcation at that point depends on the choice of circuit parameters [WT93]. For example, if we choose $R = 100\Omega$, $L = 50.0$ nH, and $C = 0.5$ pF instead, there are still two bifurcation points which occur at $v_{1c} = 0.207$ V (corresponding to 0.314 V) and at $v_{2c} = 0.362$ V (corresponding to 0.408 V). However, we have that $h(v_{1c})$ is now greater than zero indicating a subcritical bifurcation. Figure 3.6(b) shows the envelope of oscillations and time-averaged I-V curve for this system. The insert enlarges the area near this subcritical bifurcation point to clearly indicate the hysteretic region.

In addition to possibly determining the type of bifurcation, the value of the circuit parameters also determines the shape and frequency of the oscillations observed [Liu88a, KMEH91, Wal]. The current and voltage oscillations that give rise to the I-V curve in Fig. 3.6(a) are sinusoidal and examples of each at $V_{\text{ext}} = 0.22$ V is shown in Fig. 3.7(a). Their frequency is about 15.5 GHz and in good agreement with a theoretical value of 15.8 GHz given by Eq. (3.6). The frequency and shape of these oscillations vary only slightly as we vary the applied voltage throughout the NDR region. However, the current and voltage oscillations that give rise to the I-V curve in Fig. 3.6(b) are not sinusoidal

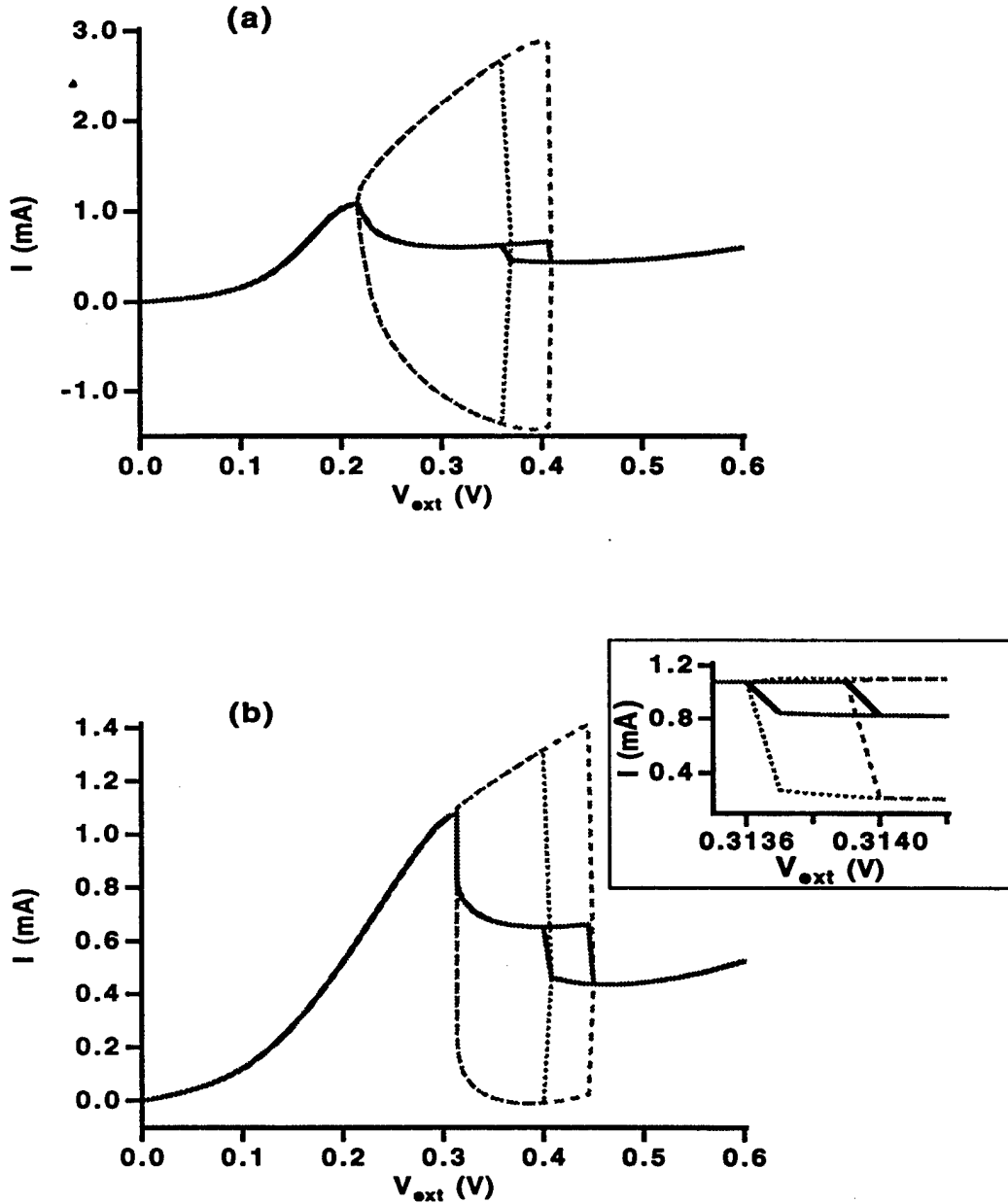


Figure 3.6: (a) Numerically determined I-V curve for $i(v)$ curve of Fig. 3.5(a), $L = 1 \text{ nH}$, $C = 0.1 \text{ pF}$, and $R = 10 \Omega$. Solid lines represent time-averaged total current; dashed lines indicate upper and lower limits of stable current oscillations for increasing applied voltage; dotted lines indicate limits of stable current oscillations for decreasing applied voltage. (b) Numerically determined I-V curve for $i(v)$ curve of Fig. 3.5(a), $L = 50.0 \text{ nH}$, $C = 0.5 \text{ pF}$, and $R = 100 \Omega$. Inset shows enlargement near bifurcation point, v_{1c} , corresponding to $V_{\text{ext}} = 0.3138 \text{ V}$.

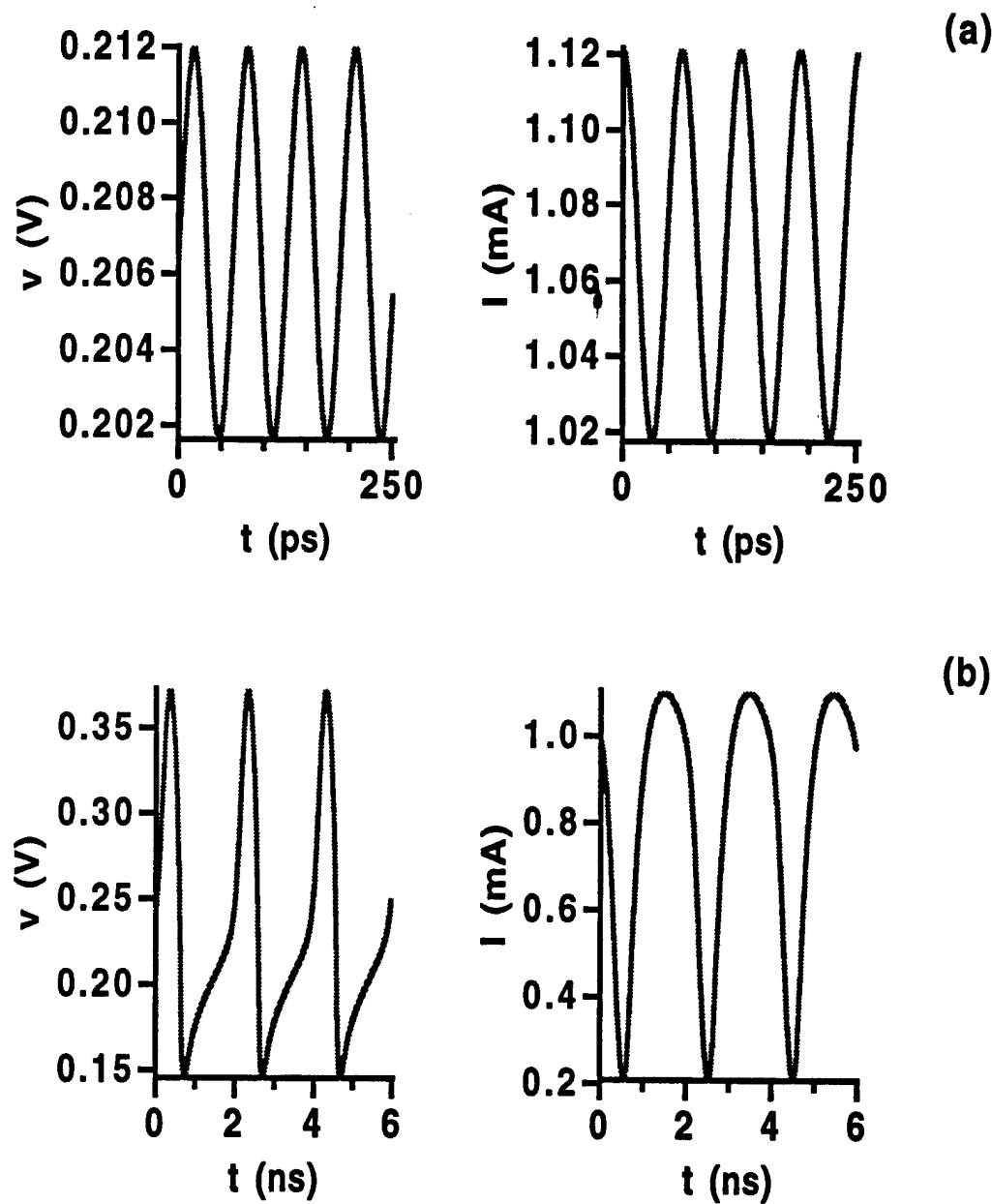


Figure 3.7: (a) Voltage and current oscillations for $L = 1 \text{ nH}$, $C = 0.1 \text{ pF}$, and $R = 10\Omega$ with $V_{\text{ext}} = 0.22 \text{ V}$. (b) Voltage and current oscillations for $L = 50.0 \text{ nH}$, $C = 0.5 \text{ pF}$, and $R = 100\Omega$ with $V_{\text{ext}} = 0.316 \text{ V}$.

and a large variation in the frequencies and shape for different applied voltages is observed. The current and voltage oscillations across the structure at $V_{\text{ext}} = 0.316$ V are shown in Fig. 3.7(b). They appear similar to relaxation oscillations [Cho64] and their frequency of 0.57 GHz is significantly less than 0.95 GHz, the frequency predicted by Eq. (3.6). An additional striking feature, shown clearly in the insert in Fig. 3.6(b), is the asymmetry of the amplitude extremes. This asymmetry results in part from the non-sinusoidal nature of the oscillations [Wal].

Relaxation oscillations tend to occur if the eigenvalue in Eq. (3.3) becomes real for some points in the NDR region [Liu88b, KMEH91]. This situation often occurs when we have a large resistance or a large value for the ratio of L/C. When the circuit is exhibiting this type of oscillation, the total current through the circuit follows the $i(v)$ curve in the positive slope region. When the current reaches the NDR region, the voltage tends to jump to the other positive slope region, while the total current remains fairly constant. This behavior is expected due to the relatively large inductance in the circuit as opposed to the capacitance of the device. As a result, relaxation oscillations tend to have large amplitudes and lower frequencies than would be expected if the oscillations were sinusoidal for those particular values of R, L, and C. In our numerical simulations, we found that the type of bifurcation is still determined by Eq. (3.9) regardless of the oscillation observed.

Finally, we note here that more complex circuit modes have been proposed to describe the behavior of circuits containing DBS samples [HLH88, BPS89, NJK93, MLSE94]. Our results described here should be relevant to these circuits, although it will be considerably more difficult to obtain analytical results such as Eq. (3.9).

Chapter 4

Experimental Techniques—Growth and Characterization

4.1 Introduction

In this chapter we discuss the details of the growth using molecular beam epitaxy (MBE) and characterizations of our samples. Section 4.2 gives a general overview of the samples which were grown. Section 4.3 discusses the MBE process and details of the growths, and section 4.4 discusses the characterization of the samples using the Transmission Electron Microscope (TEM).

4.2 Experimental Samples

We have designed and measured a total of twelve double barrier samples. All samples were grown by L. J. Blue and T. Daniels-Race at Duke University on a quarter or an eighth of a two-inch n^+ wafer using a Riber32 R&D MBE system. The detailed growth schematics are given in tables in Appendix B. All these samples may be classified into three general types; the asymmetric *spacer* sample, the notch samples, and the asymmetric *barrier* samples, and

examples of the potential profile in the Γ conduction band edge are shown in Fig. 4.1. The classification scheme is described below and depends on the width of spacer layers and composition of the barriers.

All three types of samples are undoped double barrier structures grown on a heavily doped n^+ substrate oriented in the (100) direction. The substrate temperature was 600 °C during GaAs growth and 635 °C during AlAs and $Al_xGa_{1-x}As$ growths. To ensure even growth across the substrate, the substrate was rotated during growth at about 20 revolutions/minute [CC81, Cho83]. The unintentional background doping is p-type with an estimated concentration of approximately 10^{14} cm^{-3} .

On either side of the double barrier in all samples, there are spacer regions consisting of GaAs layers with a graded doping profile. The spacers include an undoped region next to the barriers and successive layers with Si n-type doping, increasing in steps, to the contact regions which have a doping concentration of $2 \times 10^{18} \text{ cm}^{-3}$. Growth interrupts of two minutes between layers with different doping concentrations in the spacer region were used, except between the undoped GaAs layer and the GaAs layer doped to 10^{16} cm^{-3} . These spacer layers are grown to form a small barrier in the Γ point conduction band profile which ensures the separation of the 3D electron gas in the contacts and the 2D electron gas in the emitter region. The graded doping profile helps to keep the barrier small enough to allow a good flow of electrons from the 3D gas to the 2D gas [ELNT64, Tur94].

One sample is labeled the asymmetric *spacer* sample and is a symmetric double barrier structure with AlAs barriers and with asymmetric spacers. The potential profile is illustrated in Fig. 4.1. Growth interrupts of 75 seconds

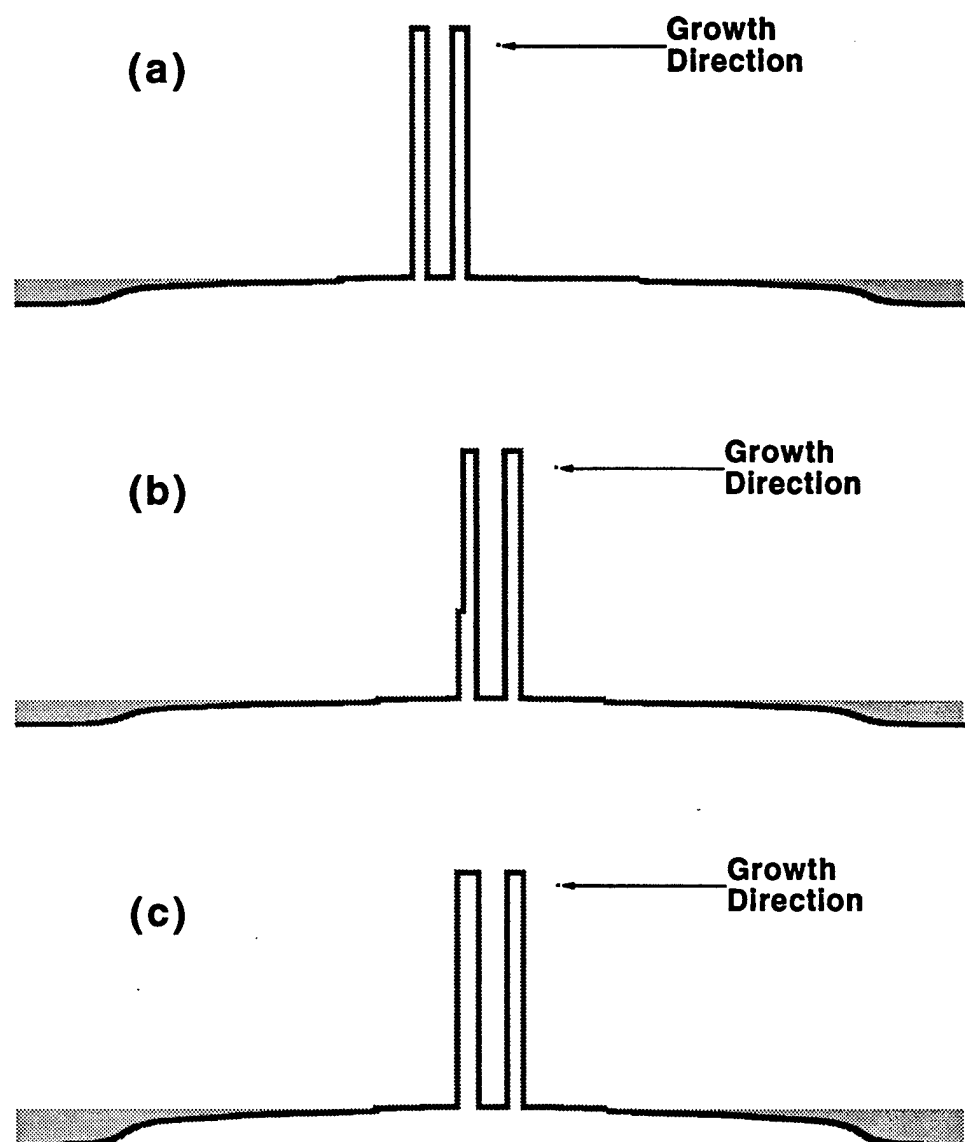


Figure 4.1: Examples of the potential profile in the Γ conduction band edge for (a) the asymmetric *spacer* sample, (b) the notch sample 250, and (c) the asymmetric *barrier* sample 263. See Appendix B for the detailed growth schematics of these samples.

from GaAs to AlAs and 90 seconds from AlAs to GaAs are used. On one side of the double barrier, the spacer contains an undoped layer of 350 Å and an undoped layer of 50 Å in the spacer on the other side. The spacers are otherwise symmetric with a 300 Å layer of GaAs doped to 10^{16} cm^{-3} , a 300 Å layer of GaAs doped to $4 \times 10^{16} \text{ cm}^{-3}$, and a 300 Å layer of GaAs doped to $2 \times 10^{17} \text{ cm}^{-3}$.

Two of the samples are labeled the notch samples and have symmetric spacer layers and an asymmetric double barrier structure. The example of the potential profile where the notch has an aluminum concentration $x = 0.45$ is illustrated in Fig. 4.1. The DBS consists of an AlAs barrier on one side of the well and a barrier consisting of a layer of AlAs and a layer of $\text{Al}_x\text{Ga}_{1-x}\text{As}$ on the other side, with the $\text{Al}_x\text{Ga}_{1-x}\text{As}$ layer grown next to the spacer. The spacers are symmetric with a 50 Å undoped layer of GaAs, a 300 Å layer of GaAs doped to 10^{16} cm^{-3} , a 300 Å layer of GaAs doped to $4 \times 10^{16} \text{ cm}^{-3}$, and a 300 Å layer of GaAs doped to $2 \times 10^{17} \text{ cm}^{-3}$. Growth interrupts of 75 seconds from GaAs to AlAs and 90 seconds from AlAs or $\text{Al}_x\text{Ga}_{1-x}\text{As}$ to GaAs and from the AlAs layer to the $\text{Al}_x\text{Ga}_{1-x}\text{As}$ layer are used. These samples are designed so that both barriers in the structure have approximately the same total transmission coefficient. Therefore, differences between direction in voltage bias in magnitude and shape of the phonon peaks should be due only to the variation of the Al concentration. We label these samples the notch samples because if the device is biased so that the electrons tunnel through the barrier with the $\text{Al}_x\text{Ga}_{1-x}\text{As}$ layer first, the $\text{Al}_x\text{Ga}_{1-x}\text{As}$ layer forms a 'notch' in the gamma point conduction band profile between the 2D electron gas in the emitter and AlAs barrier.

The final nine samples are labeled the asymmetric *barrier* samples and are

double barrier structures with asymmetric barriers of $\text{Al}_x\text{Ga}_{1-x}\text{As}$ and symmetric spacer layers. An example of the potential profile where the barriers have an aluminum concentration $x = 0.7$ is illustrated in Fig. 4.1. The spacers are symmetric with a 50 Å undoped layer of GaAs, a 300 Å layer of GaAs doped to 10^{16} cm^{-3} , a 300 Å layer of GaAs doped to $4 \times 10^{16} \text{ cm}^{-3}$, and a 300 Å layer of GaAs doped to $2 \times 10^{17} \text{ cm}^{-3}$. Growth interrupts of 30 seconds from GaAs to $\text{Al}_x\text{Ga}_{1-x}\text{As}$ and 30 seconds from $\text{Al}_x\text{Ga}_{1-x}\text{As}$ to GaAs are used. We vary the $\text{Al}_x\text{Ga}_{1-x}\text{As}$ composition of the barriers from $x = 0.2$ to $x = 0.8$, and the barrier widths for values of x between 0.3 and 0.8 are chosen so that the transmission coefficients of the barriers are approximately the same as those of a sample with pure AlAs barriers (also listed in Appendix B) which has been studied extensively both theoretically and experimentally [TTW⁺93, TWT93, TT94]. By keeping the transmission coefficients the same, we hope to be able to isolate the effect of varying the concentration of Al in the barriers, both on the energies of the localized phonons and the relative coupling constants of the phonons. The barrier widths of those samples with aluminum concentrations of $x = 0.2$, $x = 0.225$, and $x = 0.25$ are the same as the barrier widths of the sample with aluminum concentration $x = 0.3$. In this way, we hope to observe a possible transition between emission of localized modes and emission of propagating modes, which were seen in Raman data of superlattices [KBJ⁺92, JKB⁺94, FR94, KBJ⁺95].

4.3 MBE Growth

4.3.1 Introduction and Overview

All samples were grown using Molecular Beam Epitaxy (MBE) which is a process which involves growing crystals one atomic layer at a time by directing thermal beams of molecules at a heated substrate under ultra-high vacuum conditions ($P < 10^{-10}$ torr). Using this technique, a grower is capable of depositing very thin films and has near perfect control of layer thicknesses, layer compositions, and doping profiles. In addition, the samples exhibit excellent surface morphology [Sak89]. These advantages make the MBE technique ideal for the growth of $\text{GaAs}/\text{Al}_x\text{Ga}_{1-x}\text{As}$ DBS's.

A base vacuum pressure of approximately 10^{-11} to 10^{-10} torr is obtained in the growth chamber before our samples are loaded. These ultra-high vacuum conditions are necessary to control the background level of impurities which in the Duke system are composed primarily of water, oxygen, and carbon. Hence, undoped layers of GaAs and $\text{Al}_x\text{Ga}_{1-x}\text{As}$ have an unintentional p-type background doping of about 10^{14} cm^{-3} .

Proper substrate preparation and mounting before growth is crucial for good quality devices [Cho83]. The substrate surface is cleaned using solvent rinses and acid etches to remove organic and metal contaminants. The surface is then passified with a thin oxide layer before mounting. After the substrate has been prepared, it is mounted using In solder onto a Mo block preheated to 160 °C. The substrate is then placed into a sample exchange chamber which can be evacuated to about 10^{-9} torr. The substrate is then transferred into the growth chamber using a transfer rod with a magnetic coupling mechanism. This two step loading process ensures that there is minimal contamination of

the growth chamber. In the growth chamber, the temperature of the Mo block is measured by either a thermocouple or pyrometer.

The MBE system at Duke is equipped with six effusion cells containing Ga, Al, As, Si, Be, or In. The effusion cells are resistively heated to produce the beam of molecules, and the flux of the beams is related to the effusion cell temperature, which is measured by a thermocouple. Ionization gauges are used to measure the flux of each beam before every growth and the effusion cell temperature is adjusted accordingly for that run. There are also shutters in front of the effusion cells so that by opening or closing the shutters, abrupt layers of material can be grown and doping and alloy composition can be rapidly changed.

In the case of GaAs or AlAs growth, growth rates are determined by the incident Ga or Al flux. The sticking coefficient, defined as the ratio of the number of atoms incorporated into the crystal to the incident beam flux, is nearly one for Ga and Al. However, since As has a very low sticking coefficient above 500 °C, most As is desorbed from the surface unless combined with a Ga or Al atom [Cho83, Sak89]. Therefore, a constant overpressure of As must be maintained during the entire growth. Typical growth rates are between 1 and 2 $\mu\text{m}/\text{hour}$ or about one atomic layer per second.

During growth, the substrate is normally heated to an optimal temperature between 600 and 640 °C [Cho83, Sak89]. The temperature must first be raised above 580 °C to desorb the thin oxide layer from the surface and to prevent further incorporation of oxygen. The temperature must also be less than the congruent sublimation temperature of 640 °C. These temperatures also allow good incorporation of the dopants Be and Si, and they help to control impuri-

ties and defects which may result at lower substrate temperatures.

Doping of samples can be obtained by incorporating either Be for p-type doping or Si for n-type doping. Sticking coefficients for both Be and Si are nearly one. Hence, doping levels are a function of the incident flux and are calibrated beforehand by growing a series of modulated doped samples. The dopant concentrations of these samples are then determined by Hall measurements.

4.3.2 RHEED

All MBE systems incorporate Reflection High Energy Electron Diffraction (RHEED). RHEED is a process which involves a beam of high energy electrons, typically 12 keV, reflecting off the substrate surface at an angle of about 1 or 2 degrees and forming diffraction streaks on a phosphorous screen. This process is useful for several reasons. By observing the streaks, RHEED can be used to determine when the oxide has been desorbed from the surface and the general smoothness of the surface [Cho71a, PFK79]. RHEED can also be used to determine the growth rate and the composition of the materials being grown by observing the oscillations in intensity [NJDN83, STY85, JDNZ86, Sak89].

Typically RHEED is used during two phases before the actual growth of the device. First, RHEED is used to monitor the desorption of the thin oxide layer on the surface as the substrate is heated above 580 °C. After the oxide layer is removed, a heavily doped GaAs layer is grown for about 5 minutes to smooth the surface. This layer must be heavily doped to minimize the thickness of undoped material before the desired structure is grown. A thick undoped layer can dramatically affect device performance, by adding a large nonlinear resistance in series with the structure [Wal]. After this smoothing

layer is grown, RHEED then is used to calibrate the growth rates of GaAs and $\text{Al}_x\text{Ga}_{1-x}\text{As}$. These calibration layers are undoped.

RHEED is used to determine growth rates by observing the oscillations in intensity of the diffracted electron beam. The layers grown while observing these RHEED oscillations are undoped and the sample is not rotated. Before a layer begins to grow, the surface is smooth and the diffracted beam is very bright. However, as the growth starts and continues, the surface becomes more rough and the intensity of the diffracted beam decreases to a minimum. As growth further continues and a layer nears completion, the surface becomes mostly smooth again, and the intensity increases to a maximum. Thus, a complete oscillation in intensity corresponds to a monolayer of growth, and these oscillations may be monitored by an oscilloscope. In this way, the growth rates may be determined by given fluxes and adjusted accordingly.

4.3.3 Growth of Alloy Barriers

To grow a layer of $\text{Al}_x\text{Ga}_{1-x}\text{As}$, the growth rate and mole fraction are determined by the individual fluxes of Ga and Al arriving at the substrate. The growth rate of $\text{Al}_x\text{Ga}_{1-x}\text{As}$ is simply the sum of the growth rates of GaAs and AlAs, and the mole fraction x of Al in the alloy is determined by the following relation [Cho83]:

$$x = \frac{G(\text{Al}_x\text{Ga}_{1-x}\text{As}) - G(\text{GaAs})}{G(\text{Al}_x\text{Ga}_{1-x}\text{As})}, \quad (4.1)$$

where $G(\text{Al}_x\text{Ga}_{1-x}\text{As})$ and $G(\text{GaAs})$ are the growth rates of $\text{Al}_x\text{Ga}_{1-x}\text{As}$ and GaAs respectively. Typically, for small Al concentrations, the growth rate of GaAs is fixed at $0.8 \mu\text{m}/\text{hour}$, and the growth rate of $\text{Al}_x\text{Ga}_{1-x}\text{As}$ is adjusted during RHEED oscillations to achieve the desired mole fraction.

Growth rates of $\text{Al}_x\text{Ga}_{1-x}\text{As}$ must be less than $2 \mu\text{m}/\text{hour}$. A higher growth rate is avoided to ensure that growth is occurring evenly layer by layer and not in clumps throughout the substrate. As can be seen from Eq. (4.1), with a nominal growth rate for GaAs of about $0.8 \mu\text{m}/\text{hour}$, a growth rate for $\text{Al}_x\text{Ga}_{1-x}\text{As}$ is less than $2 \mu\text{m}/\text{hour}$ for Al concentrations with $x < 0.6$. Therefore, in growing the asymmetric spacer sample, notch samples, and samples with alloy barriers with $x < 0.6$, the growth rates of GaAs and AlAs remained constant and the temperature of the effusion cells containing Ga and Al were not changed during the growth. However, during the growth of samples containing barriers with $x \geq 0.6$, it was necessary to change the growth rates during the growth of the double barrier structure itself.

Most layers of the asymmetric barrier samples with alloy barriers with $x \geq 0.6$ are grown exactly like the samples with alloy barriers with $x < 0.6$, with growth rates of GaAs given by $0.8 \mu\text{m}/\text{hour}$. However, 75 seconds before the end of the growth of the 300 \AA lightly doped ($N_D = 10^{16} \text{ cm}^{-3}$) GaAs layer in the spacer before the barriers, the Ga effusion cell's temperature is lowered so that the growth rate of $\text{Al}_x\text{Ga}_{1-x}\text{As}$ is about $1 \mu\text{m}/\text{hour}$. The actual growth rates are $G(\text{GaAs}) = 0.48 \mu\text{m}/\text{hour}$ and $G(\text{Al}_x\text{Ga}_{1-x}\text{As}) = 1.2 \mu\text{m}/\text{hour}$ for $x = 0.6$, $G(\text{GaAs}) = 0.32 \mu\text{m}/\text{hour}$ and $G(\text{Al}_x\text{Ga}_{1-x}\text{As}) = 1.07 \mu\text{m}/\text{hour}$ for $x = 0.7$, and $G(\text{GaAs}) = 0.185 \mu\text{m}/\text{hour}$ and $G(\text{Al}_x\text{Ga}_{1-x}\text{As}) = 0.905 \mu\text{m}/\text{hour}$ for $x = 0.8$. For these samples with large mole fractions, the undoped layers in the spacer regions and the double barrier are all grown at these lower rates. We also employ a 30 second growth interrupt between the GaAs to $\text{Al}_x\text{Ga}_{1-x}\text{As}$ interface and a 30 second interrupt between the $\text{Al}_x\text{Ga}_{1-x}\text{As}$ to GaAs interface. As soon as the lightly doped layer ($N_D = 10^{16} \text{ cm}^{-3}$) in the spacer after the double barrier structure starts to grow, the Ga effusion cell temperature

begins to rise so that the rest of the growth occurs with a GaAs growth rate of $0.8 \mu\text{m}/\text{hour}$.

4.3.4 Growth Interrupts Between GaAs and $\text{Al}_x\text{Ga}_{1-x}\text{As}$ Layers

Photoluminescence studies have shown that the photoluminescence peak intensity in GaAs wells tends to be larger when the growth is interrupted for a time when the layer changes from $\text{Al}_x\text{Ga}_{1-x}\text{As}$ to GaAs, suggesting smoother interfaces [STY85, FN85]. This growth interrupt is achieved by closing the shutter to the Al and Ga beams while retaining the As beam to avoid desorption of As from the surface. It is thought that the growth interrupt allows the atoms on the surface to migrate about the surface, allowing for a smoother interface.

It is important that the growth interrupt not be too long especially between layers of undoped material. During the interrupt, there is the possibility that a greater concentration of background impurities may be incorporated on the surface, forming deep level traps which may affect device performance, especially at high voltage biases [CKC⁺88]. The asymmetric spacer sample and the notch samples incorporated a 75 second growth interrupt from GaAs to AlAs and a 90 second growth interrupt from AlAs to GaAs or $\text{Al}_x\text{Ga}_{1-x}\text{As}$ and $\text{Al}_x\text{Ga}_{1-x}\text{As}$ to GaAs. Trapping-like behavior was observed in many of these samples, often permanently affecting the device characteristic.

Figure 4.2 illustrates this trapping-like behavior. Figure 4.2(a) illustrates the I-V characteristic at 4 K for the notch sample with an $\text{Al}_x\text{Ga}_{1-x}\text{As}$ layer with mole fraction $x = 0.45$ at low applied voltage biases before higher voltage biases were applied and the trapping behavior was observed. Figure 4.2(b)

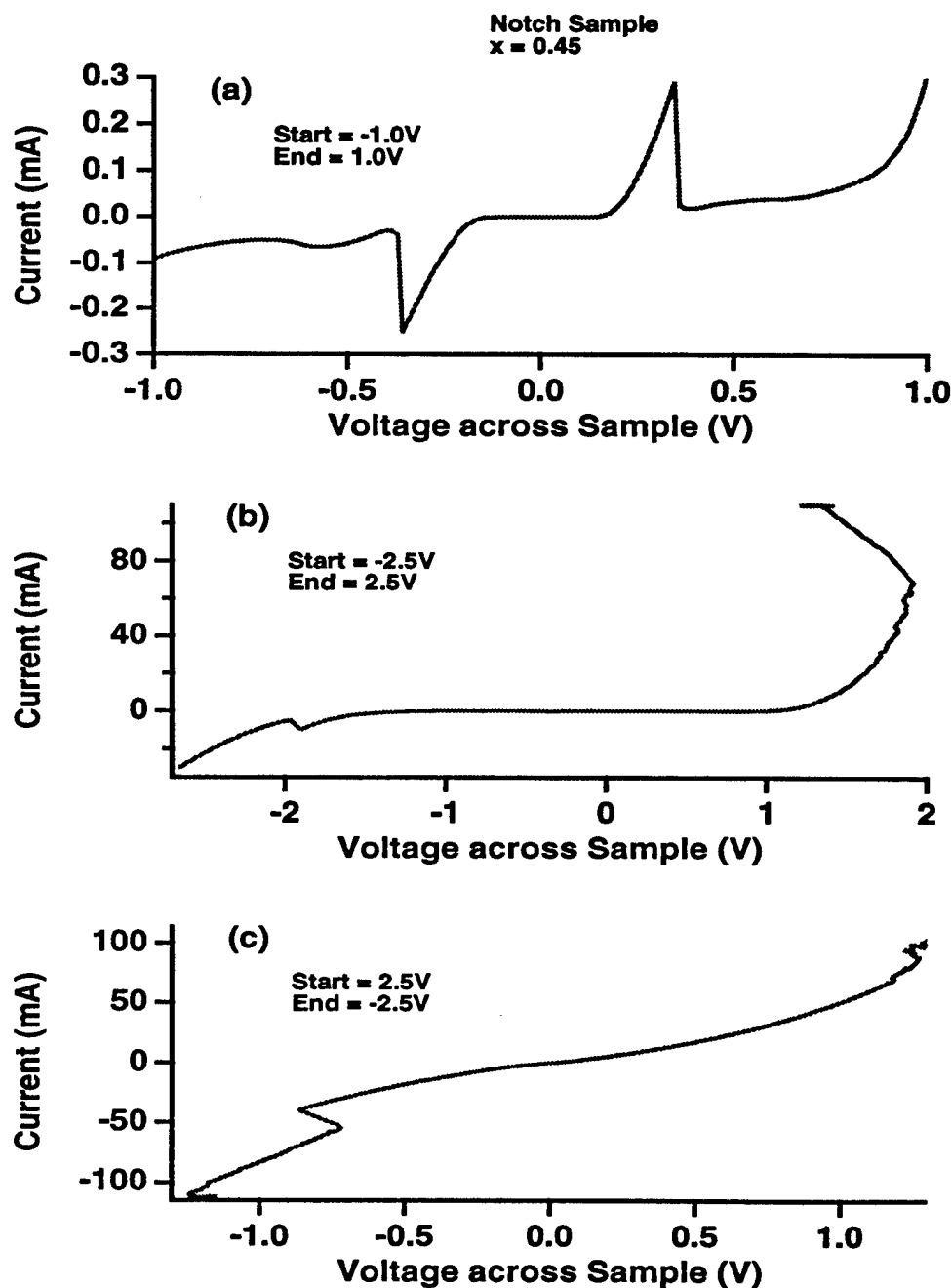


Figure 4.2: Example of trapping behavior in a sample with long growth interrupts. (a) Current-voltage characteristic at 4 K with low applied voltages before any higher voltages were applied. (b) Current switch during a high voltage sweep. Note that current through sample increases abruptly above a certain voltage. (c) Current-voltage characteristic after the high voltage sweep in (b). Although current still varies, characteristic has been permanently changed.

illustrates the trapping-like behavior during a high voltage sweep at a temperature of 4 K. At a sufficiently high voltage, the current jumps suddenly to very high levels, very often reaching the current compliance of the voltage source. This behavior suggests that populated deep-level traps are being depopulated at a certain applied voltage which produces the excess current. Many times, these large currents would permanently affect the I-V characteristics, effectively destroying the usefulness of the device. Figure 4.2(c) illustrates the I-V characteristic of the device after the high voltage sweeps. Current levels are much higher than the original characteristic, and we observe little evidence for resonant tunneling.

The device is not always permanently changed, however. Sometimes the device would return to an I-V curve similar to its original characteristic after it is heated and then recooled, suggesting that the high power flowing through the structure does not always permanently destroy the structure. The heating allows the traps to be repopulated and hence the resonant tunneling to reappear. This trapping behavior is similar to a switching phenomenon associated with deep level traps [CKC⁺87, CKC⁺88, CKB⁺89].

It should be noted here that the long growth interrupts between heavily doped layers of GaAs in the spacer regions should not present much of a problem because the background p-type doping is of the order 10^{14} cm^{-3} while the doped layers with an interrupt at the interface is at least of the order 10^{16} cm^{-3} . Indeed, the asymmetric *barrier* samples which have these long growth interrupts between differently doped layers, but short interrupts at the GaAs/Al_xGa_{1-x}As interfaces show a marked decrease in the number of devices on the sample exhibiting the trapping behavior compared with the number on the asymmetric *spacer* sample and notch samples which have long growth

interrupts at the GaAs/Al_xGa_{1-x}As interfaces.

4.4 TEM Characterization

4.4.1 TEM Equipment

Transmission electron microscopy (TEM) is a powerful technique of imaging that uses electrons accelerated through a potential difference to probe very thin samples and focuses these electrons with magnetic lenses to form the image [Rei89]. This technique is widely used and can provide high resolution images typically on the order of angstroms. All TEM images presented in this section are cross sections of DBS's and were taken by Sopa Chevacharoenkul using a JEOL JEM200CX HRTEM operated at 200 KV accelerating voltage capable of 2.6 Å resolution. This TEM machine and all sample preparation and darkroom facilities are located in the Analytical Lab of the Microelectronics Center of North Carolina (MCNC).

4.4.2 Sample Processing

To obtain a good image of the cross section of the DBS, it is very important that the thickness of the sample in the vicinity of the DBS be very uniform and very thin, typically less than 100 Å. The procedure to obtain these thicknesses is illustrated in Fig. 4.3 and discussed in more detail below. The general procedure involves forming a stack by gluing Si pieces to either side of the sample. The stack is then cut, ground, and polished to about 75 μ m thick. The middle of the stack near the DBS is then dimpled and then ion milled to thin the area to be imaged to the required thickness. Most of this procedure described below is discussed elsewhere [BS84, MC90].

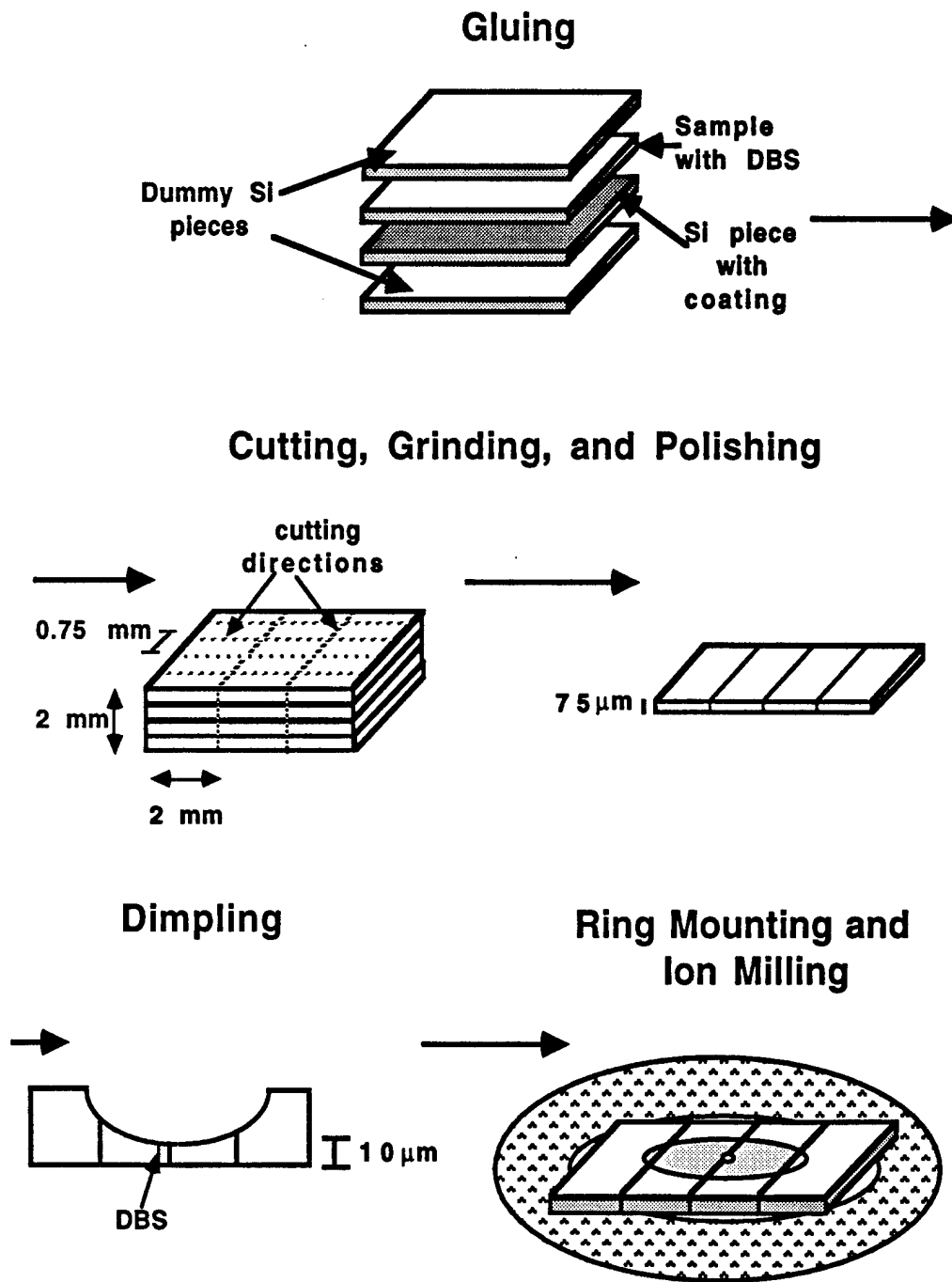


Figure 4.3: Schematic diagram for steps in processing samples for a TEM cross section.

Before the samples are processed at MCNC, they are cleaved into squares about 1 cm² and the indium solder on the substrate or back side is removed. We follow the procedure for removing the indium described in more detail in the next chapter. The general procedure involves mounting the samples epitaxial side down with crystal bond 509, which is a wax-like substance that is resistant to acids, but dissolves in organic solvents such as acetone. Crystal bond is also hard at room temperature but melts at approximately 120 °C which allows easy application and removal of samples. We etch most of the indium from the back of the sample in concentrated HCl and then lap the sample using a mixture of 5.0 μ m grit alumina powder and DI water to smooth the back side surface. The samples are then removed from the

Since the cross sections of these samples are very thin, typically about 0.5 mm or less, the first step in processing the sample for TEM imaging is to build a stack from four pieces of wafers. This step ensures that the final sample to be imaged is much easier to handle. All slabs to be glued together to form the stack are first cleaned on both sides with a cotton swab soaked in acetone and then with a cotton swab soaked in methanol to remove any grease or dirt from the surfaces. We then place a small amount of M-bond 610 adhesive onto the coated side of a Si slab and carefully place the GaAs sample epitaxial side down onto the Si slab. Two dummy Si slabs are then glued face to face on each side of the two center slabs in the same way. In this arrangement, the DBS is very close to the center of the stack. The stack is then placed in a vise with two Teflon pieces placed on the top and bottom of the stack to prevent the glue from sticking to the vice during the glue-curing step. The vise is tightened carefully to squeeze out any excess glue from between the slabs, and the whole apparatus is placed in a furnace with the temperature set at 145 °C for at least

45 minutes.

The next step of the procedure is to cut, grind and polish the stack so that the cross section thickness is about $75 \mu\text{m}$ thick. The stack is first mounted onto a glass slide with crystal bond and with the (110) direction parallel to the glass-slide edge. The stack is then cut into smaller rectangular pieces 2 mm long and 0.75 mm wide using a low speed diamond saw (Bueler "Isomet"). These pieces are then removed from the slide and rinsed in acetone. Three of these sample pieces are then mounted with crystal bond in an equilateral triangle on a glass stub, which then fits into the cavity of a Gatan Model 623 disc grinder and a Gatan Model 656 dimple grinder. The sample pieces are mounted such that the cross sections of all four slabs are face up, and care is taken to ensure that a minimal amount of crystal bond is between the sample and glass stub. The pieces are then ground to a thickness of about $300 \mu\text{m}$ using 600 grit SiC paper on a rotating wheel with running water. The thickness is measured with a micrometer. This side of the samples is then polished with a soft polishing cloth on the rotating wheel and with $0.3 \mu\text{m}$ alumina thin slurry.

After the samples have been polished, they are cleaned with soap and water, and then they are dismounted from the glass stub and cleaned with acetone. They are then turned over and remounted onto the glass stub polished side down. They are then ground with the 600 grit SiC paper until the samples are about $75 \mu\text{m}$ thick. No polishing is needed for this side. The stub and samples are then cleaned with soap and water before dimpling.

Dimpling specimens, which involves grinding a depression in the center of the stack near the area to be imaged, helps to reduce ion milling time by as much as 50 to 60 minutes per sample piece. The glass stub is placed on

the stage of the Gatan Model 656, and one of the stacks is centered in the middle at the interface between the coated Si slab and GaAs sample using the cross hair of a low powered microscope provided with the dimpler. The stage and grinding wheel start to rotate and the grinding wheel is lowered onto the sample. The sample is then dimpled at the center with $1 \mu\text{m}$ diamond paste till the bottom of the crater is about $10 \mu\text{m}$ thick. The proper thickness is determined when a transmitting light through the crater appears reddish. The stub is then removed and cleaned with soap and water and recentered on the same sample. The sample is then polished with $0.03 \mu\text{m}$ alumina slurry to remove any scratches which may have resulted from the grinding. Afterward, the samples are then cleaned again with soap and water, and the procedure is repeated for the other two stacks on the stub.

Since the samples are now extremely thin, extraordinary care must be taken in handling them. We need to remove them from the stub and mount them onto a supporting ring which can then be safely handled with tweezers. The glass stub is first heated on a hot plate to melt the crystal bond. The samples are then slid to the edge of the stub and removed with a toothpick and very carefully placed in a beaker of acetone. The samples are then rinsed in a beaker of methanol. We usually use vacuum tweezers to handle the sample now before mounting onto the ring.

The samples are now ready to be mounted onto a $50 \mu\text{m}$ thick Ta ring about 3 mm in diameter. This ring is placed on a piece of filter paper and a drop of M-bond 610 is put on the ring. Using the vacuum tweezers, the sample is carefully placed in the center of the ring. This mounted sample is then placed on a piece of teflon on a hot plate heated to 150°C for about one minute to cure the glue. The sample can now be safely handled with regular tweezers

since we can now grip the Ta ring.

The final step in processing is thinning the sample to electron transparency in an ion mill. We use a Gatan Model 660 dual-ion miller. The sample mounted on the ring is placed on the platform, covered with a clamping plate, and lowered into the chamber which has been cooled to 77 K. The sample is then milled from dual Ar ion beams set at 5 kV at about a 10° to 12° angle of incidence. A laser terminator which is equipped with the ion mill is set to terminate the milling when a 100 μm hole has formed. The hole should be formed slightly off center of the stack with most of the hole forming in the middle Si slab. Typical times for milling are about 50 minutes to an hour.

4.4.3 Results

In this section we present images taken from two samples using TEM. These samples were grown by MBE using a Varian GEN II at the University of Michigan by W. Li and P. K. Bhattacharya. Additional details of the growth and the electronic properties are discussed elsewhere [TTW⁺93, TWT93, Tur94]. Both samples are asymmetric barrier samples with AlAs barriers. The proposed structures, as determined by RHEED calibration, contain either an 80 Å or a 100 Å well and 33 Å and 45 Å barriers. The growth schematic of the structure with the 80 Å well is given in Appendix B.

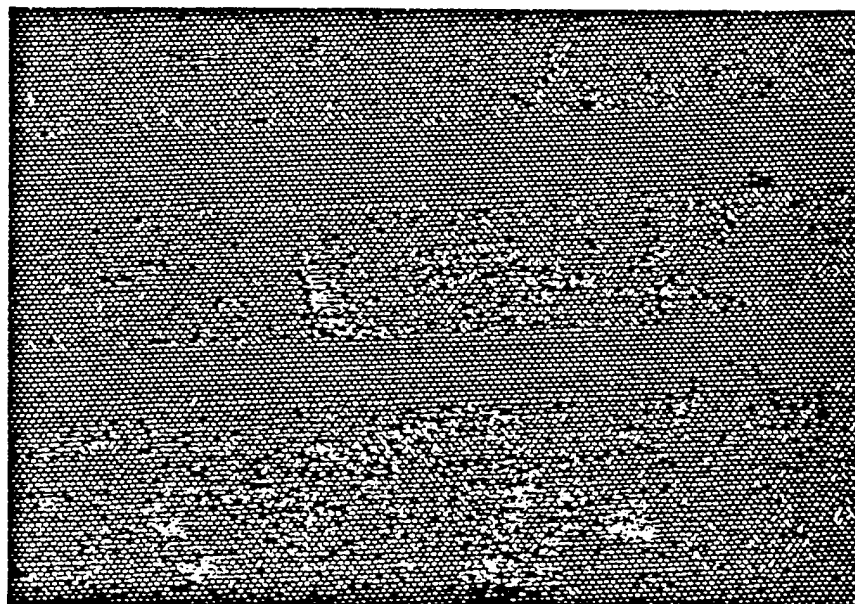
Both samples were observed in cross section [HHN⁺65, Rei89]. The samples were tilted such that the incident electron beam is incident in the (110) direction of each sample. Bright field images, images which include the main nondiffracted electron beam, were formed and photographed. Dark field images use diffracted beams only and are not shown here. The objective aperture

is positioned carefully so that the eight diffracted beams included in the image are positioned symmetrically about the main beam. The image includes the (002) beam which shows the most contrast between GaAs and AlAs. According to Petroff et. al. [Pet77, PGWS78], the diffraction beam in the (002) direction for GaAs and AlAs are proportional to $(f_{\text{Ga}} - f_{\text{As}})^2$ and to $(f_{\text{Al}} - f_{\text{As}})^2$ respectively, where f_{Ga} , f_{Al} , and f_{As} are the atomic scattering factors for Ga, Al, and As respectively. The atomic scattering factors for Ga and As are nearly identical, so that GaAs appears darker than AlAs in the corresponding TEM images.

Figure 4.4(a) shows the TEM image for the cross section of the sample with an 80 Å well with a magnification of 690 K. The growth direction is given from bottom to top. Although the lattice image is visible, it is difficult to make out the image very clearly. Sample thickness nonuniformity, where thicker parts of the sample would be darker than thinner parts, and sample orientation are suspected to be the main causes of the image blurriness [HHN⁺65]. However, one can still see clearly rows of dots and the distance between dots in the growth direction is the lattice constant of GaAs or AlAs of 2.8 Å. Hence, by counting rows we find that the well is about (80 ± 3) Å wide and the two barriers are about (33 ± 3) Å and (45 ± 3) Å wide as proposed by the RHEED calibration.

Figure 4.4(b) shows the TEM image for the second sample with a 100 Å well with a magnification of 690 K. The growth direction again is given from bottom to top. This image clearly shows the contrast between AlAs and GaAs. As determined by the RHEED calibrations, the well has a width of 100 Å and the barriers have widths of 33 Å and 45 Å. However, we can clearly see that although the well is about (100 ± 3) Å, the barriers are both much smaller with widths of (23 ± 3) Å and (33 ± 3) Å. Thus, TEM is clearly a good way

(a)



(b)

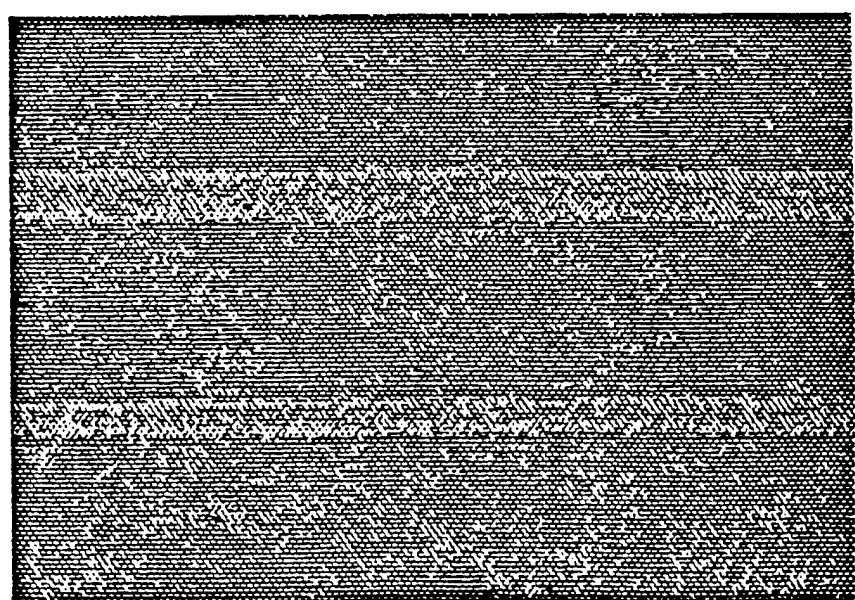


Figure 4.4: (a) TEM image with magnification of 690 K of DBS sample with 80 Å well and 33 Å and 45 Å barriers. (b) TEM image with magnification of 690 K of DBS sample with 100 Å well and 23 Å and 33 Å barriers.

of independently determining the exact DBS's grown.

Due to the expense and time involved with obtaining a TEM image of any sample, only these two samples were imaged. The other samples discussed in this thesis are assumed to be the proposed structures as grown by MBE and calibrated with RHEED at Duke.

Chapter 5

Experimental Techniques—Processing and Measurement

5.1 Introduction

In the chapter we discuss the general processing and measurement techniques. Section 5.2 discusses the processing techniques necessary to make electrical contact with the structures. Section 5.3 discusses the low temperature systems and hardware used to make the measurements. Section 5.4 discusses the electronics and data collection.

5.2 Processing

In order to perform electrical measurements on our samples, it is necessary to remove the indium left over after the MBE growth from the substrate and to make ohmic contact on both sides of the sample. After the samples are grown, they are cleaved into smaller pieces about 0.25 cm^2 . The general procedure, discussed in detail below, involves first evaporating a pattern of dots of varying size of gold, nickel, and germanium onto the epitaxial or front side of the

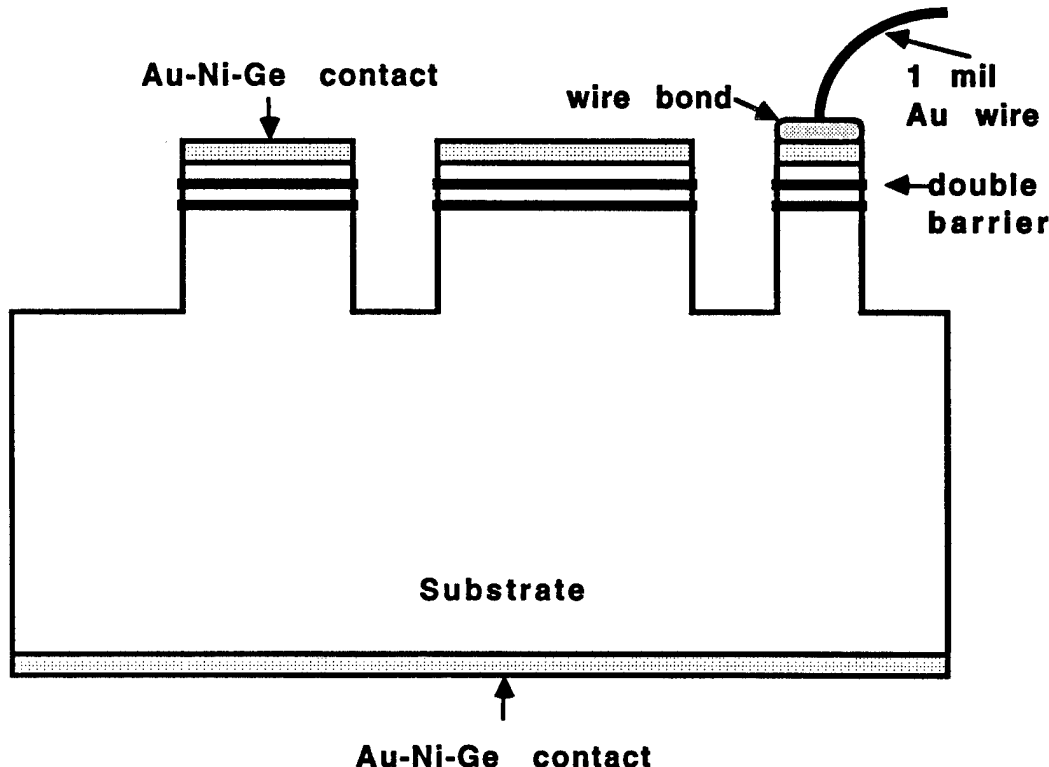


Figure 5.1: Illustration of the finished processed sample with Au-Ni-Ge contacts. Front side has several mesas of four different sizes, 500 μm , 250 μm , 125 μm , and 62.5 μm . Wirebonds are usually used for measurements at liquid He temperatures.

sample. The excess indium is then removed from the substrate or back side, and then we evaporate the metals onto the entire backside surface. The samples are then annealed to form the ohmic contact, and then finally, the pattern on the front side is used as a mask for an etch to form separate devices. To perform measurements at 4 K, the contacts are then wirebonded with one mil. gold wire. Figure 5.1 illustrates the finished processed sample.

5.2.1 Evaporation and Indium removal

Before the samples are loaded into the evaporation chamber, they must be cleaned with etches to ensure that few impurities exist on the surface before

depositing the metals used as contacts. All GaAs etches used in processing are mixtures of DI water, phosphoric acid, and hydrogen peroxide. This particular mixture of compounds etches GaAs because the hydrogen peroxide oxidizes the GaAs, and the acid then dissolves the oxide. All etches have also been calibrated beforehand. This procedure involved depositing a protective layer of photoresist on half of a GaAs wafer using standard photolithography techniques, then etching the unprotected GaAs for a fixed amount of time, and then using a Tencor Instruments Alpha-Step 100 surface profiler to measure the amount etched away.

The procedure to clean the samples before any evaporation involves first etching each sample in a solution of 100 mL of DI water, 12 mL of phosphoric acid, and 4 mL of hydrogen peroxide for 30 seconds, which etches away about 1000 Å of GaAs [Wil84]. The samples are then rinsed twice in beakers full of DI water. The samples are then etched in a solution of 50 mL of DI water and 50 mL of hydrochloric acid to remove any remaining oxides on the surface. The samples are then rinsed three times in beakers full of DI water and then blown dry with nitrogen gas.

For the front side evaporation, the samples are then placed back side down onto a holder and the front side is covered with a shadow mask. The samples are immediately placed into the evaporation chamber which is then evacuated as quickly as possible. It is important to minimize the exposure of the front side surface of the sample to air to avoid contamination.

The deposition takes place in an Edwards Model 306 vacuum coater. The evaporation chamber is evacuated to about 10^{-6} torr before the evaporation. The shadow mask covering the samples have drilled circular holes that are

500 μm , 250 μm , 125 μm , and 62.5 μm in diameter. During evaporation, the metals are deposited through the holes onto the uncovered parts of the GaAs. In this way, we first deposit approximately 400 \AA of germanium, then approximately 300 \AA of nickel, and finally about 1800 \AA of gold. Deposition rates are typically between 2 \AA and 4 $\text{\AA}/\text{second}$. Gold is deposited last so that it can be used as a mask during the final etch of the sample. After the evaporation, the samples are allowed to cool for about two hours before removing them from the evaporator.

After the front side evaporation, we then must remove the indium from the back side of the sample. Recall that indium solder was used to adhere the substrate to the Mo block during the MBE growth. The samples are first bonded front side down in an equilateral triangle onto a lapping block. The adhesive we use is crystal bond 509, which is a wax-like substance that is resistant to acids, but dissolves in organic solvents such as acetone. Crystal bond is also hard at room temperature but melts at approximately 120 $^{\circ}\text{C}$ which allows easy application and removal of samples. After the samples have been mounted onto the lapping block, they are then placed in concentrated hydrochloric acid until most of the indium is etched away. This process usually takes approximately an hour or more depending on the amount of indium present. After the samples have been rinsed, they are then lapped with 5.0 micron grit alumina powder to remove any additional indium and smooth the back side surface which allows a better deposition during the back side evaporation. Usually, samples are lapped for approximately two or three minutes.

After the lapping is complete, the block is then heated and the samples removed and rinsed in acetone. We then rinse the samples for five minutes in acetone, five minutes in methanol, and twice in beakers full of DI water. We

repeat this procedure twice for each sample to ensure no crystal bond remains before the evaporation onto the back side. After the rinses, the samples are dried with nitrogen gas.

After the samples have been removed from the lapping block, they are then mounted front side down onto a microscope with crystal bond. The samples are then cleaned using the etches and procedure described above for the front side deposition. Before loading the samples into the evaporation chamber, a small block of aluminum is clipped onto the microscope slide to help conduct heat away and prevent the crystal bond from melting during the evaporation. We again deposit, at a rate between 2 Å and 4 Å/second, 400 Å of germanium, then 300 Å of nickel, and finally 1800 Å of gold onto the entire back side of the samples under a pressure of about 10^{-6} torr. After the evaporation, the microscope slide is then heated and the samples removed and rinsed in acetone. We then rinse the samples twice for five minutes each in acetone, methanol, and DI water.

5.2.2 Annealing

Immediately following the evaporation, the metal forms a Schottky barrier contact with the GaAs. This type of contact conducts current in one direction only and has very non-linear characteristics. In order to make ohmic contact, we must heat the sample for a brief period of time. Although it is not known exactly why annealing the sample in this way works, it is believed that during the annealing process, the Ge is imbedded into the GaAs, forming a very heavily doped n^+ layer near the contact. There are still many areas of this reaction which are not clearly understood, and this process is still being investigated [Bra81, Wil84, San89].

Before the anneal, we clean a piece of GaAs approximately the same size as the sample. This piece of GaAs is used as a cap and placed on top of the sample to help prevent the GaAs on the surface of the sample from sublimating during the anneal. We first etch the GaAs cap in the solution of 100 mL of DI water, 12 mL of phosphoric acid and 4 mL of hydrogen peroxide for 60 seconds and rinse with DI water twice. We then etch the GaAs cap in the solution of 50 mL of DI water and 50 mL of hydrochloric acid for 15 seconds and rinse in DI water twice and dry the cap off with nitrogen gas. We then place the sample back side down on a four inch silicon substrate and cap on top of the sample in an AG Associates Heatpulse 410 rapid thermal processor (RTP) and allow the system to purge with nitrogen gas for two minutes before the anneal.

The sample is heated in the RTP by lamps in an atmosphere of nitrogen gas with a flow rate of about two liters per minute. We have programmed the RTP to use a two step annealing process to help prevent temperature overshoot. The sample is first heated to 340 °C for 10 seconds, and immediately following, the sample is then brought up to 380 °C for 60 seconds. The temperature is measured using a thermocouple, and, since the thermocouple's temperature calibration seems to drift over time, a trial run on a test sample is usually done first. After the anneal the lamps disengage and the sample is allowed to cool to below 100 °C before removing from the RTP.

We must take care to find the correct temperatures and times for the anneal. If the temperature is not high enough or the time of the anneal not long enough, we find that the contacts are either nonlinear or have a very high contact resistance or both. However, at the same time, we must be careful not to overanneal the sample by raising the temperature too high or by annealing too long. If we overanneal the sample, too much nickel and germanium can be

brought to the surface of the contact and mix with the gold. It is crucial that we avoid this situation since the metal contacts on the front side are used as a mask for the final GaAs etch described in the next section. Gold is resistant to this etch but nickel and germanium are not. If we overanneal the sample, the final etch often dissolves much of the contact away and, in many cases, lifting the contact completely off the surface. Overannealing can also make it difficult to properly wirebond onto the contact later since we must have a gold surface. Finding the proper anneal temperature and time is done mainly by trial and error.

We can measure the effects of the anneal by placing two probes onto two separate contacts and taking an I-V measurement with a Hewlett Packard 4741 Semiconductor Parameter Analyzer. Before the anneal, we find that the resistance due to the contacts is very nonlinear and on the order of $M\Omega$. This characteristic is expected since we are measuring the current between two reversed Schottky contacts. After the anneal, we find the contacts to be ohmic and usually we measure a resistance between $5\ \Omega$ and $10\ \Omega$. Although, we cannot be sure how much the resistance is due to the actual contact and how much is due to the resistance of the epitaxial GaAs between the contacts, we can say with confidence that our contact resistance is $5\ \Omega$ or less.

5.2.3 Final Etch

After the samples have been annealed, we need to wet etch the samples using the front side metal contacts as a mask to define the devices. We first mount the samples back side down to a microscope slide with crystal bond to help protect the back side contact. We then etch any remaining oxide on the front side by etching the samples in a solution of 50 mL of DI water and 50 mL

of hydrochloric acid for 15 seconds and rinsing twice in DI water. We then etch the front side using a solution of 70 mL of DI water, 10 mL of phosphoric acid, and 20 mL of hydrogen peroxide for 2 minutes and 45 seconds. The etch rate for this solution has also been calibrated, and the above procedure etches approximately $5 \mu\text{m}$ from the surface [Wil84] which is plenty to etch through the double barrier structures and spacers to define the devices. It has also been found that this faster etch does much less undercutting of the contacts than the slower etch used in the cleaning procedures. After the etch, the samples are rinsed three times in DI water and dried with nitrogen gas. The samples are then removed from the microscope slide and rinsed in acetone, methanol and DI water.

5.3 Low Temperature Systems

After we finish processing a sample, we may use a phosphor bronze wire set-up to take preliminary current-voltage measurements at room temperature and at 77 K to test the quality of the sample. We find that measurements at 77 K closely resemble measurements at 4 K and, hence, the measurements at 77 K which are easy to do are a good indication of the quality of the devices. Figure 5.2 shows a schematic of this set-up which can be immersed into a small dewar of liquid nitrogen. A small piece of insulated circuit board with copper on top is placed insulated side down on a large block of copper and is held in place by a ceramic spacer and plastic screw. Two separate leads of coax wire which carry current and voltage signal for the back side of the sample are placed in direct contact to the copper piece of circuit board. On top of the ceramic spacer anchored by a screw are the phosphor bronze wire and two separate

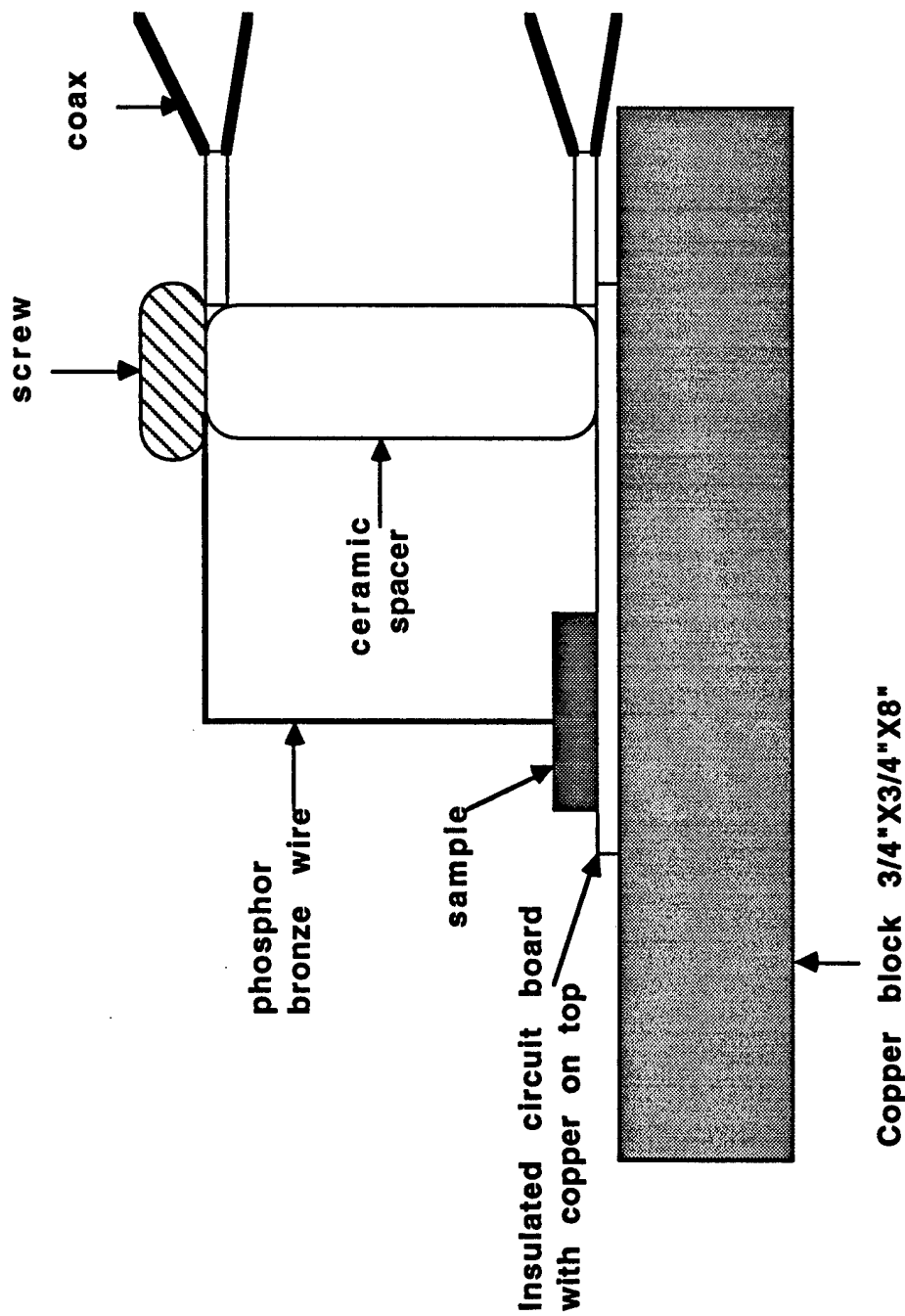


Figure 5.2: Schematic of measurement set-up (not to scale) using phosphor bronze wire to contact devices on sample. Set-up is dunked into a dewar of liquid nitrogen.

leads of coax wire carrying the current and voltage signal to one of the front side contacts. Both the copper on the circuit board and the end of the wire are sanded to remove any residual oxides and the sample is then slipped under the phosphor bronze wire which is placed on one of the gold contacts. This arrangement is flexible enough to easily allow a large number of contacts to be individually measured, but the phosphor bronze wire is strong enough to hold the sample in place while the apparatus is immersed in liquid nitrogen. The current and voltage leads are then used to take a four-terminal current-voltage measurement by the parameter analyzer or the four-terminal current-voltage measurement described in Section 5.4.

The measurements at 4 K are taken in an Oxford instruments SMD8 liquid helium dewar. A simplified version is illustrated in Fig. 5.3. This dewar is equipped with a NbTi superconducting magnet which can reach fields as high as 7.2 T. Helium is allowed into the sample chamber from the magnet space via a needle valve. All measurements described in this thesis are made at atmospheric pressure, although the He bath in the sample chamber may be pumped on to make measurements at lower temperatures. The temperatures of the sample is monitored by carbon glass resistors placed near the sample and connected to an ITC4 Temperature Controller. Measurements at temperatures higher than 4 K may also be taken since resistive heaters are also placed near the sample. A small amount of He gas is allowed to flow through the needle valve, and the gas is thus heated near the sample. The temperature of this gas is controlled by the temperature controller through a feedback loop.

For reliable electrical measurements in the liquid helium dewar, we have found that using wirebonds to measure the contacts is the best technique. We first mount the sample onto a transistor outline (TO) gold plated header back

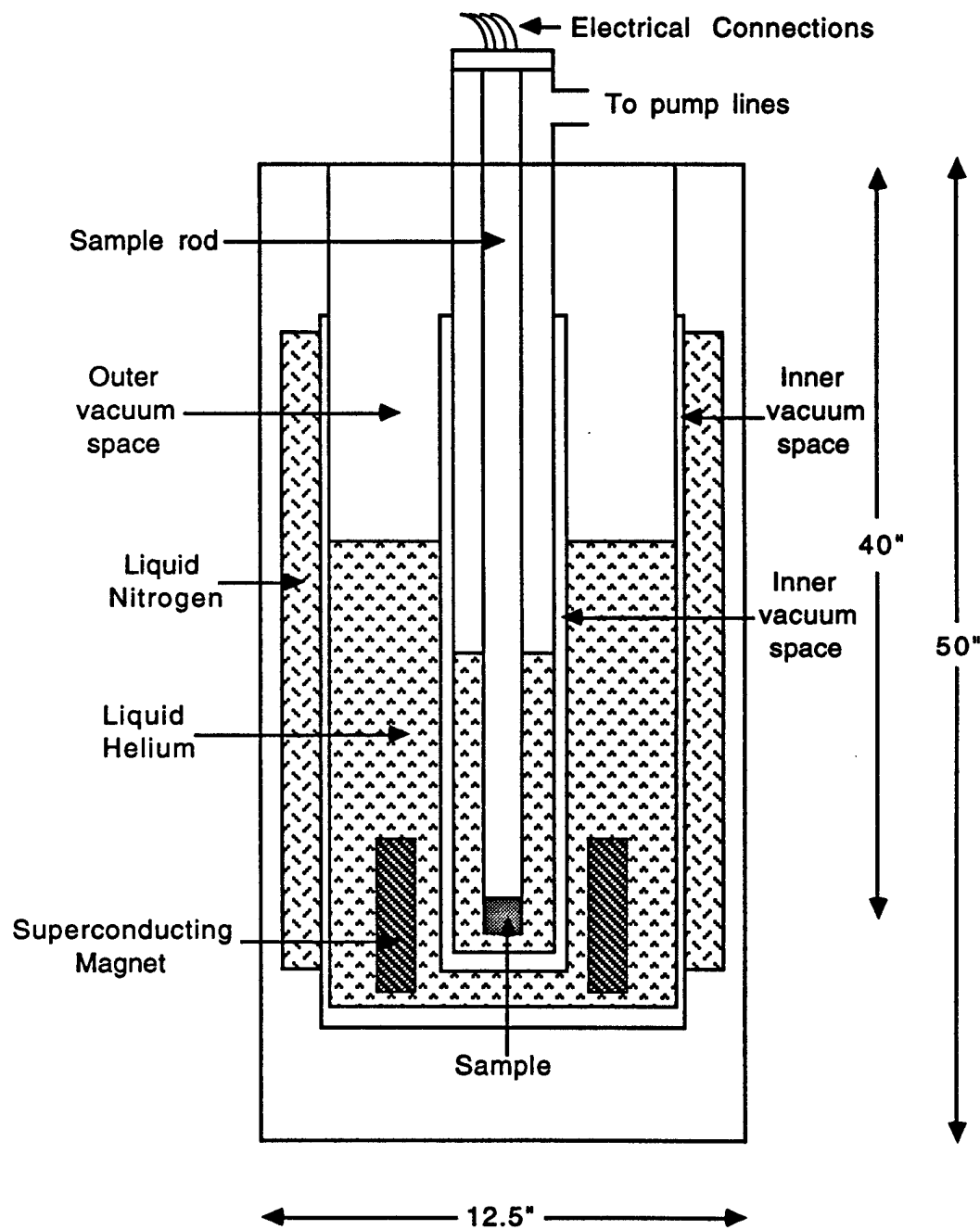


Figure 5.3: Schematic of helium dewar.

side down using silver paint. Most headers used contain 12 hermetically sealed pins. The header and sample is then placed onto a heating block and clamped into place. The heating block is then raised to 100 °C for the wirebonding.

We use a Hybond model 572 ultrasonic wire-bonder to bond 1 mil. gold wire from the sample to a pin on the header. The settings for the force, power of the ultra sound, and time the ultra sound is applied for each bond are all determined by trial and error. If the force, time and power are too long, the contact may not stick to the sample after the bond. If the force, time and power are too short, then the wire may not bond to the contact at all. The first bond is made to a pin on the header and the second is made to the appropriate contact. Finally, in order to contact the back side, a bond is made from a pin to the header itself.

After the bonding is finished, the TO header is fixed to a circular disk of oxygen free high conductivity copper with GE varnish and cigarette paper which effectively insulates the header from the mount [Tur94]. This piece of copper is then mounted onto the end of the sample probe which is placed inside the liquid helium dewar.

Three different pins from the header can then be connected to the leads wired onto the sample probe to make the four-terminal measurement. This set-up allows two different contacts to be measured at 4 K without taking the sample probe out of the dewar when the system is cold. Each pin is connected to two leads, one to carry the current, and one to measure the voltage. The voltage leads are made of 40Ω steel coax (Lake Shore Ultra miniature Coax, type S1) provided with the dewar. The voltage signal from these coax wires are then transferred to regular 50Ω coax within a shielded box outside the dewar.

Since all signals in our measurements are below 1 kHz, impedance matching is not a problem.

The steel coax is very resistive, however, with 1.1Ω per foot, and is much too resistive to carry the current for our samples. Such large series resistances cause large hysteresis and bistability in the NDR region of the current-voltage curve as noted in Chapter 3. Therefore, we use low resistive copper wires as the current leads. The only shielding for these wires is provided by the dewar itself. However, we have found this shielding to be adequate for our measurements.

5.4 Electronics and Data Collection

We take four different types of measurements on samples in the liquid helium dewar. These measurements are schematically illustrated in Figs. 5.4, 5.5, 5.6, and 5.7. All instruments are connected to a MacIntosh II computer with GPIB cables. These instruments are then controlled by Labview programs which also take and store the appropriate data. Labview is a graphical interface software and most of the programs used to take the measurements described in this thesis were written by Peter Turley [Tur94], except for the measurements of oscillations with the digital oscilloscope. This particular program was included with the Labview software and modified accordingly to take the appropriate measurements.

Figure 5.4 illustrates the four terminal current-voltage measurement. The output voltage across the circuit is supplied by a Keithley 230 programmable voltage source. The voltage at the front side contact is measured using a Keithley 175 digital multimeter (DMM) and the voltage at the back side contact is measured by a Keithley 197 DMM. The d.c. voltage across the sample is simply

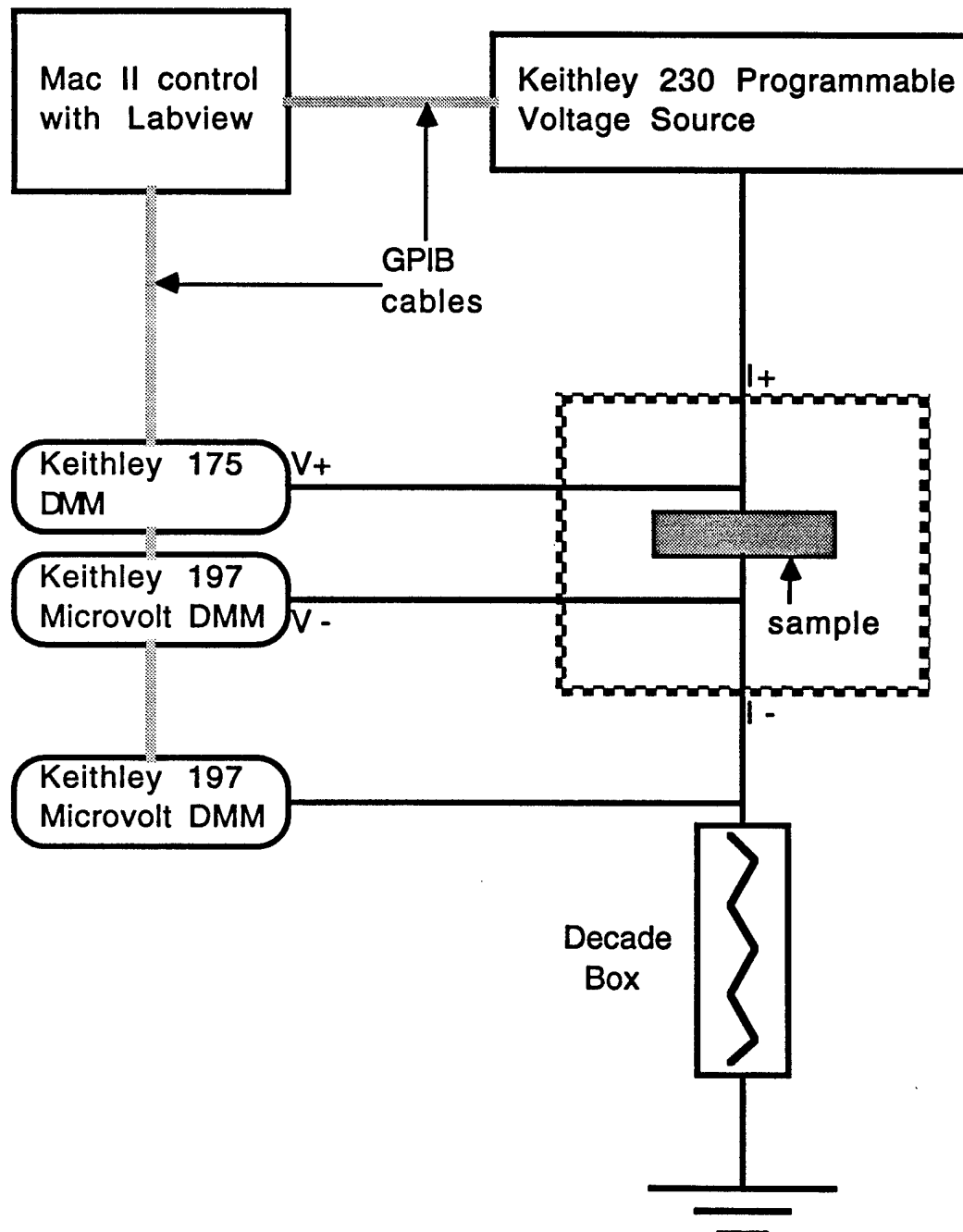


Figure 5.4: Schematic of four terminal Current-voltage measurement.

the difference between these voltage signals. The current through the sample is found by measuring the voltage with a Keithley 197 DMM across a known resistance. This resistance is set by a decade box and the value depends on the current flowing through the circuit. Usually, we use a higher resistance for lower currents to obtain greater accuracy. However, we must be careful not to set the resistance too high to avoid hysteresis in the NDR region. Typical values of resistance are about $10.0\ \Omega$ for about a mA of current and about $1\ K\Omega$ to $2\ K\Omega$ for about a μA of current.

Figure 5.5 illustrates the conductance-voltage measurement using lock-in amplifiers. The d.c. voltage signal from the Keithley 230 programmable voltage source is added to a small sinusoidal a.c. signal with typical frequencies of 500 Hz or 1 KHz from a Wavetek model 132. We add these signals using a Teledyne 4253 Low Noise FET instrumentation amplifier. This total signal is then applied across the circuit. The d.c. voltage across the sample is monitored using the two Keithley 197 DMM's. The a.c. voltage amplitude is measured using a Stanford Instruments model SR-510 lock-in amplifier and the a.c. voltage amplitude across the decade box is measured using a Stanford Instruments model SR-530 lock-in amplifier. The conductance of the sample is then directly proportional to the ratio of these two amplitudes.

Figure 5.6 illustrates the set-up for the Shubnikov-de Haas measurements. A constant voltage is applied across the circuit from the Keithley 230 programmable voltage source. As in the current-voltage measurement, the voltage across the sample is monitored by the Keithley 175 and Keithley 197 DMM's and the current is found by measuring the voltage across the decade box using a Keithley 197 DMM. The labview program also controls the magnetic field by supplying an appropriate voltage from the analog output board in the computer

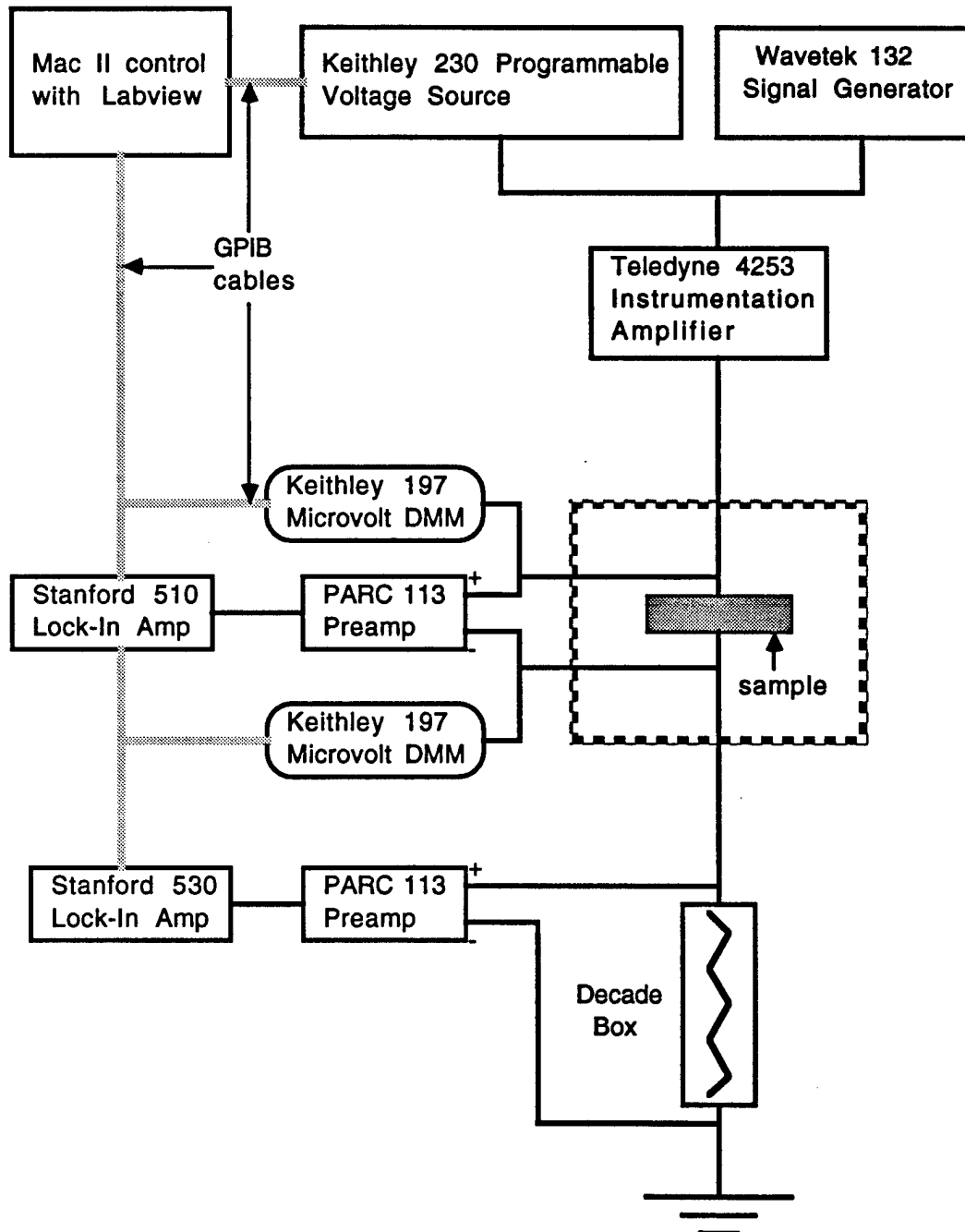


Figure 5.5: Schematic of Conductance-voltage measurement using Lock-In Amplifiers.

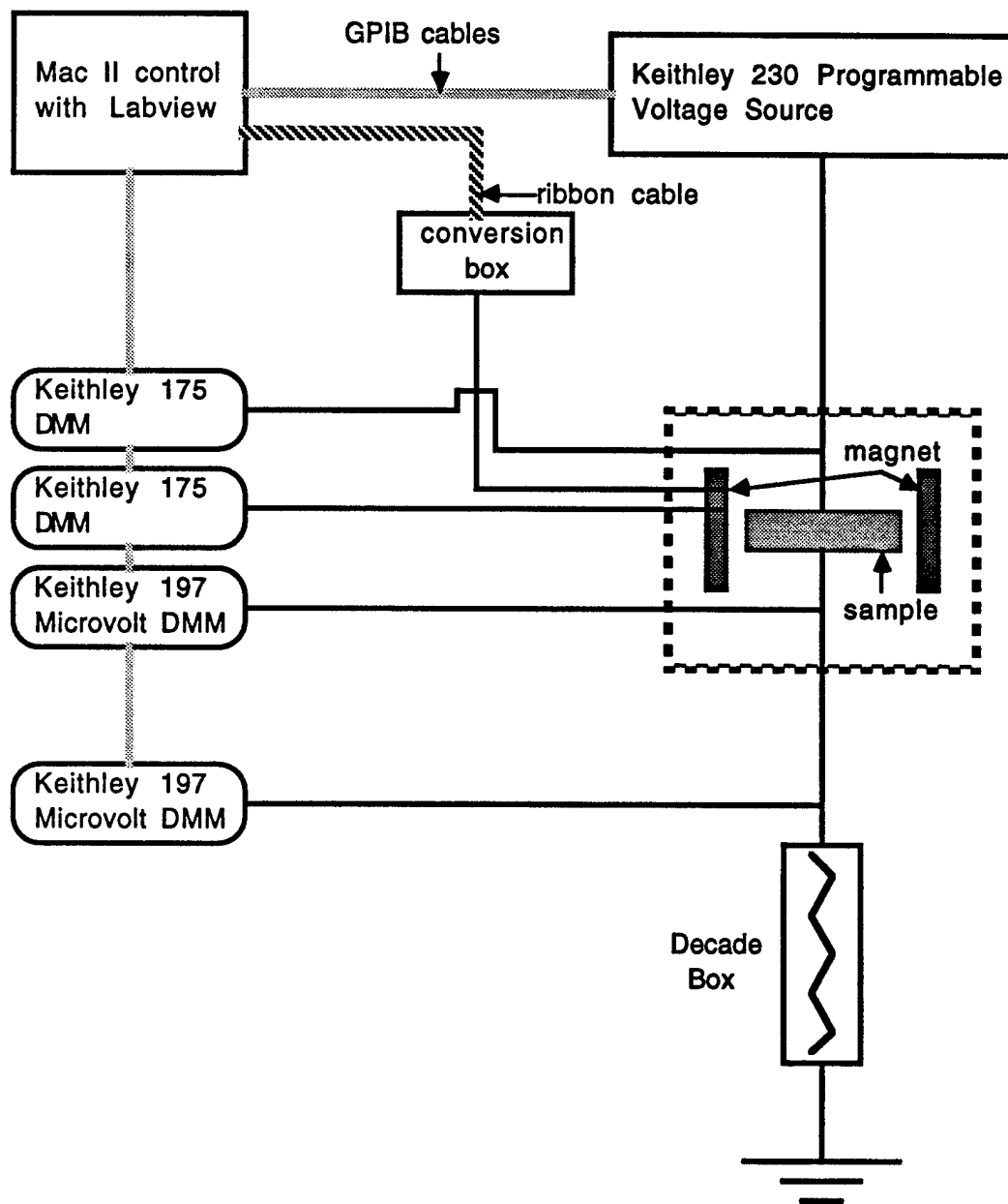


Figure 5.6: Schematic of set-up for Shubnikov de Haas measurements.

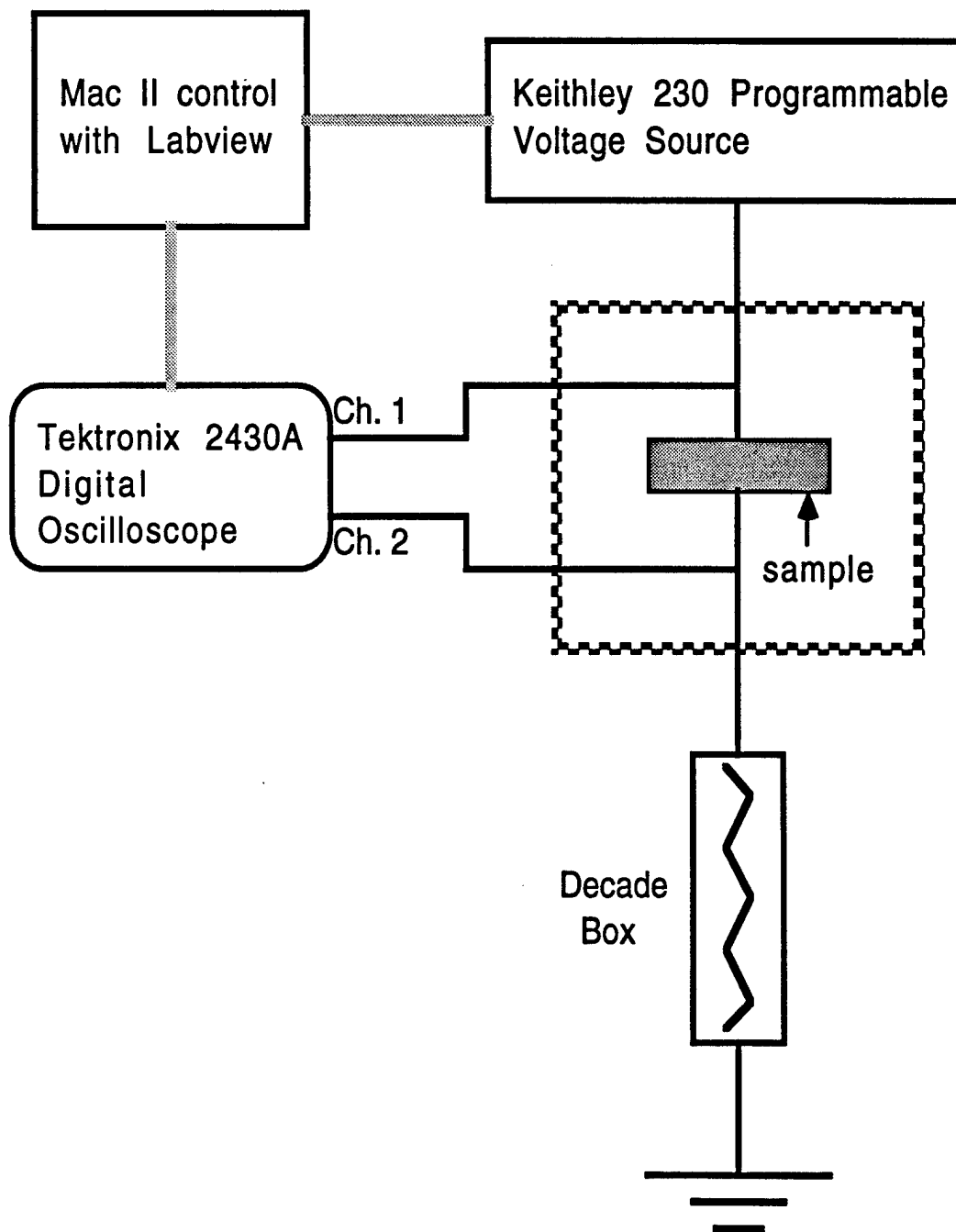


Figure 5.7: Schematic of oscillations data measurements with digital oscilloscope. Examples are shown in Chapter 3.

to the magnet power supply. The current through the magnet which is directly proportional to the magnetic field is monitored by a Keithley 175 DMM.

Figure 5.7 illustrates the set-up to measure spontaneous current and voltage oscillations with a Tektronix 2430A digital oscilloscope. The voltage, supplied by the Keithley 230 programmable voltage source, across the circuit is tuned manually to an unstable point in the NDR region. The voltage at the front and back side contacts are then sent to the two channels in the oscilloscope. The Labview program then takes the resulting time traces. The voltage oscillation across the sample is simply the difference of the two signals, and the current oscillation is directly proportional to the signal from the low voltage oscillation.

5.5 Digital Filters

To determine the position of peaks and inflections in the current-voltage and conductance-voltage curves in the phonon peaks of all our samples, we looked for minima in the second derivative of the current-voltage curves or minima in the first derivative of the conductance-voltage curves. To accomplish the task of taking low frequency derivatives without magnifying the high frequency noise, we use numerical nonrecursive digital filters as prescribed by Hamming [Ham89].

Any nonrecursive filter can be written in the form:

$$y_n = \sum_{k=-\infty}^{\infty} c_k u_{n-k} \quad (5.1)$$

where u_{n-k} are the original data points, c_k are constants of the filter, and y_n are the filtered data. To determine the coefficients c_k for a particular filter, it

is useful to consider the Fourier transform of Eq. (5.1):

$$Y(\omega) = H(\omega)U(\omega) \quad (5.2)$$

where $U(\omega)$ is the Fourier transform of the original data series, $Y(\omega)$ is the Fourier transform of the filtered data series, and $H(\omega)$ is the Fourier transform of the constants of the filter and is also known as the transfer function.

To simply take a derivative of the data, the transfer function is simply given as $H(\omega) = i\omega$. However, to avoid magnifying high frequency noise, while retaining the low frequency derivatives, we set $H(\omega) = 0$ above some frequency ω_c called the cutoff frequency. The transform function can therefore be written as:

$$H(\omega) = \begin{cases} i\omega & \text{if } |\omega| < \omega_c \\ 0 & \text{if } |\omega| > \omega_c. \end{cases} \quad (5.3)$$

Hence, we can now take a reverse Fourier transform to find the constants c_k which are given by:

$$c_k = \frac{2i}{\pi} \left(\frac{\sin(k\omega_c)}{k^2} - \frac{\omega_c \cos(k\omega_c)}{k} \right). \quad (5.4)$$

Unfortunately, any data series is finite, and the sum in Eq.(5.1) must be truncated at some finite N :

$$y_n = \sum_{k=-N}^N c_k u_{n-k}. \quad (5.5)$$

Because of Gibb's phenomenon, this truncation will produce unwanted ripples in the transform function $H(\omega)$ at high frequencies. There are many ways to smooth these ripples, but one of the easiest is to use Lancos smoothing, which

involves multiplying each of the c_k in Eq.(5.4) by the sigma factors $\sigma(N, k)$ given by:

$$\sigma(N, k) = \frac{\sin(\pi k/N)}{\pi k/N}. \quad (5.6)$$

It should be noted that there is usually a normalization constant to ensure that the filter has the proper low frequency limit. However, because we are not interested in the absolute value of the derivatives and are looking only for maxima and minima, we ignore the normalization of the filter.

Choosing the optimal values of N and ω_c is done by trial and error. The exact values depend on how closely spaced the original data points are and how fast we expect the data series to oscillate. A closely spaced series of data requires a higher value of N and a lower value of ω_c . Typically, we use either 10 or 15 points for N , and a cutoff frequency between 0.1 s^{-1} and 0.3 s^{-1} .

Chapter 6

Experimental Results

This chapter presents the experimental results of all samples described in Appendix B. Most of the data were collected for the asymmetric *barrier* samples since they are the most similar to the AlAs asymmetric *barrier* sample which was extensively studied both theoretically and experimentally in earlier works of Turley, Teitsworth, and Wallis [TTW⁺93, TWT93, TT94]. Section 6.1 presents the preliminary data of the notch and asymmetric *spacer* samples. Section 6.2 presents results of the asymmetric *barrier* samples. These results include data and analysis with and without an applied magnetic field and also explore temperature dependence. We are able to determine the energy dependence of the phonon modes as a function of the alloy concentration in the barriers and present a fitting routine to determine the relative contribution to the PAT current from the AlAs-like phonons compared to the relative contribution to the PAT current from the GaAs-like phonons as a function of the alloy concentration in the barriers.

6.1 Experimental Results of Asymmetric Spacer and Notch Samples

6.1.1 Asymmetric Spacer Sample

For this sample, we took measurements only at 77 K. We used the Nitrogen Dewar set-up described in Chapter 5, and four terminal measurements were taken with the 4145A Semiconductor Parameter Analyzer. Figure 6.1 shows the current-voltage characteristic of this sample at 77 K. Figure 6.1(a) shows the current-voltage characteristic under forward bias where the electrons tunnel through the thicker spacer layer first (i.e. the front side contact is biased with a higher voltage, so electrons flow from the back of the sample to the front) and Fig. 6.1(b) shows the current-voltage characteristic under reverse bias where the electrons tunnel through the thinner spacer layer first. The contact size is 500 μm in diameter.

Comparing the voltage positions of the resonant peaks between forward and reverse bias, we can see that the current peaks at a much higher voltage at -0.5 V under reverse bias than under forward bias which occurs at 0.34 V. When the double barrier structure is symmetrical, the resonant currents should peak at approximately the same electric field across the DBS. However, the undoped collector region under reverse bias is much larger (350 \AA) compared to the undoped collector region under forward bias (50 \AA). Hence, the voltage drop under reverse bias should be larger for the same electric field across the DBS than the voltage drop under forward bias.

It should also be noted that the current under forward bias does seem to be slightly limited by the size of the hump separating the 3D gas in the contact

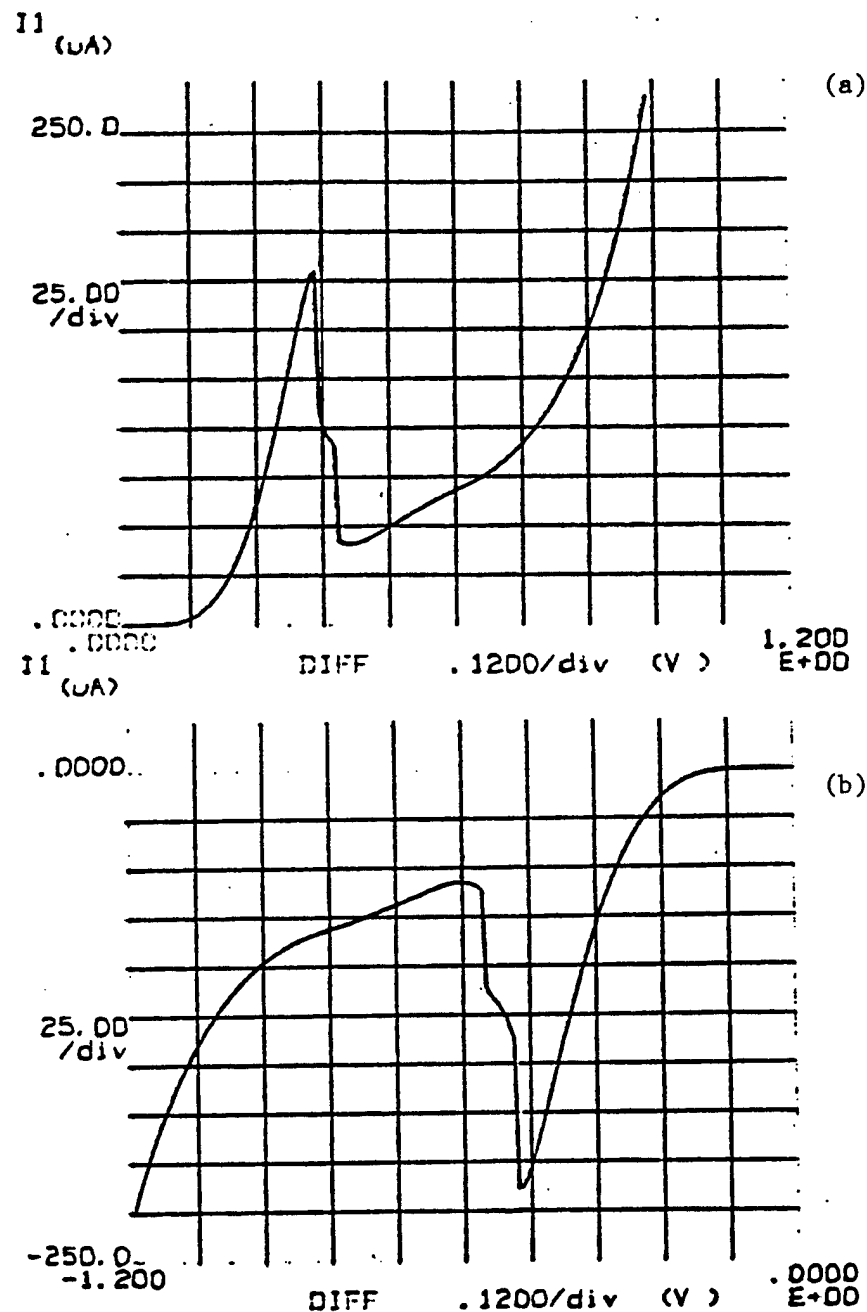


Figure 6.1: (a) Current versus applied voltage under forward bias for the asymmetric spacer sample. (b) Current versus applied voltage under reverse bias for the asymmetric spacer sample.

from the 2D gas in the emitter region. The current peak which occurs at $-213 \mu\text{A}$ under reverse bias is about 19% larger than the current peak under forward bias at $177 \mu\text{A}$. In addition, the peak to valley current ratio (PVCR), defined as the maximum current of the resonant peak to the minimum current in the valley, under reverse bias is 3.7:1 and is slightly smaller than the PVCR under forward bias which is 4.3:1. This asymmetry could partly be due to the interface roughness in the emitter for reverse bias, since the interface of GaAs grown on AlAs tends to be rougher than the interface of AlAs grown on GaAs as mentioned in Chapter 4 [STY85, FN85].

As can be seen for both forward and reverse bias, the phonon peaks appear mostly as inflections in the current-voltage curve instead of an actual peak in the current. The PAT peak seems to be masked by other sources of valley current. Possible sources of this valley current include elastic scattering [LC88, LM90, CV93a, WLP⁺88, CH89, LRF92], Γ to X conversion in the AlAs barrier [Liu87, MCW86, MFE⁺91, SR95] and onset of the first excited state. Because the phonon peaks are just inflections and trapping behavior is prevalent in this sample, we did not take any measurements of this sample at 4 K.

6.1.2 Notch Samples

The notch samples give somewhat better results. One reason to include the notch is to reduce the valley current due to Γ to X conversion in the barrier [CH90]. Another reason we designed the notch samples is to study the effects of screening of the phonons by the electron gas in the emitter. Since optical phonons create an electric field as they propagate, electrons may act to screen this field. The most likely places for this screening to occur is the

well, the heavily doped parts of the contact regions in the emitter and collector, and the accumulation layer next to the emitter barrier. It is unlikely that the phonon potentials are screened much in the well. Because the well widths are narrow in these samples, the electrons in the well occupy the ground state. Hence, the electron gas in the well acts like a 2D gas, and a 2D electron gas does not screen an electric field as efficiently as a 3D electron gas. Hence, it is a good approximation to ignore the screening in the well altogether [AFS82, Tur94]. However, the electron gas in the heavily doped contact regions far from the DBS itself is 3D, and it is likely that the the half space modes and the long wavelength interface modes that penetrate far into the contacts are screened in those regions [KDS78]. To determine the effects of screening in the accumulation layer is far more difficult. Calculations indicate that a small fraction of the electrons in the accumulation layer occupy the first excited state, and the electron gas in the emitter is neither 2D nor 3D. The theoretical treatment of screening of phonon modes by such an electron gas is not easy [Wen88]. By putting a 'notch' of $\text{Al}_x\text{Ga}_{1-x}\text{As}$ between the AlAs barrier and the electron gas in the emitter, we hope to spatially separate much of the potential of the phonon modes, at least the interface modes, in the emitter barrier from the electron gas in the accumulation layer. The notch samples are designed so that the transmission coefficient in each barrier is approximately the same. In this way, we hope to directly see the difference in coupling to different modes which may be affected by screening in the emitter by observing the differences in the phonon peaks for different biases.

Since the results are similar for both notch samples, we show the results for sample 250 only. Figure 6.2(a) shows an example of the current-voltage characteristic of the 250 notch ($x = 0.45$) sample in the forward bias direc-

tion, and Fig. 6.2(b) plots the characteristic in the reverse bias direction. All measurements described in this section were taken at 4 K using a 250 μm diameter contact. From Appendix B, we see that when the sample is under reverse bias, the electrons tunnel through the notch first. The current-voltage characteristics are similar for both bias directions. The currents below 0.15 V are too small to be seen on this scale. The currents then quickly rise to a peak corresponding to resonance. These peaks occur at 272 μA at 0.339 V in the forward bias direction and at -310 μA at -0.386 V in the reverse bias direction. The characteristic in both curves are slightly hysteretic, although the hysteresis in the characteristic in the reverse bias direction is somewhat greater. Above resonance, the currents fall quickly to a minimum of 19.2 μA at 0.39 V under forward bias, and to -29.7 μA at -0.390 V under reverse bias. The PVCRs are 14.2:1 in the forward bias direction and 10.4:1 in the reverse bias direction. The phonon-assisted tunneling process above resonance then forms a strong inflection under forward bias, and a peak in the current of -65.3 μA at -0.571 V under reverse bias. Above these voltages, the currents continue to rise. We note here that this sample exhibits substantial trapping behavior as discussed in Chapter 4, so measurements at high voltages are avoided in this sample.

Figure 6.3 shows the enlargement of the phonon peaks under both forward and reverse bias. It can be seen at these scales that this sample exhibits trapping-like behavior even at low voltages. Figure 6.3(a) shows that under forward bias and at voltages above the phonon feature, the current measured with increasing applied voltage is a little higher than the current measured with decreasing applied voltage. However, the currents at voltages below the phonon peak are about the same for both increasing and decreasing applied voltages. Figure 6.3(b) illustrates that under reverse bias, the current in the phonon peak

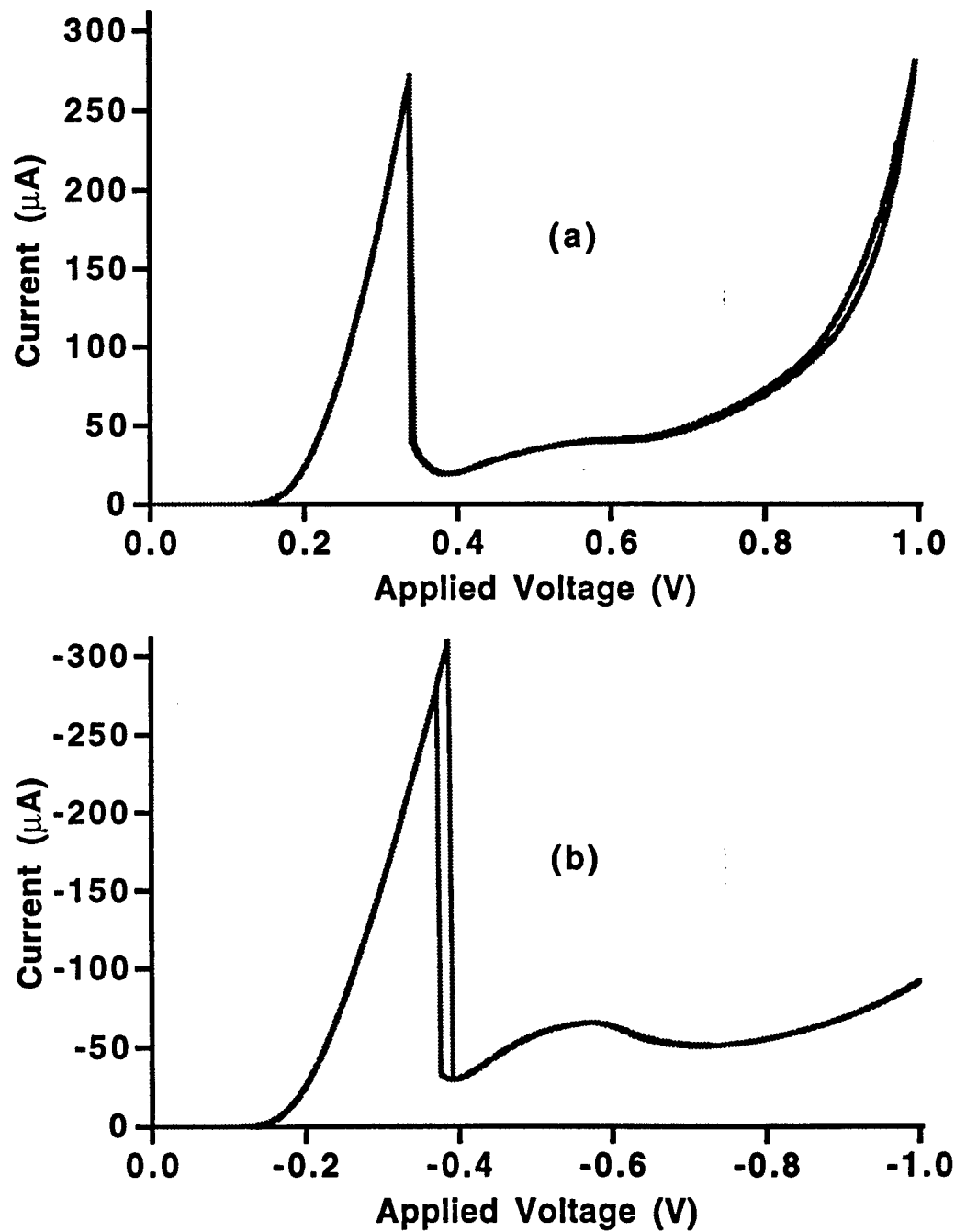


Figure 6.2: (a) Current versus applied voltage under forward bias for sample 250. (b) Current versus applied voltage under reverse bias for sample 250.

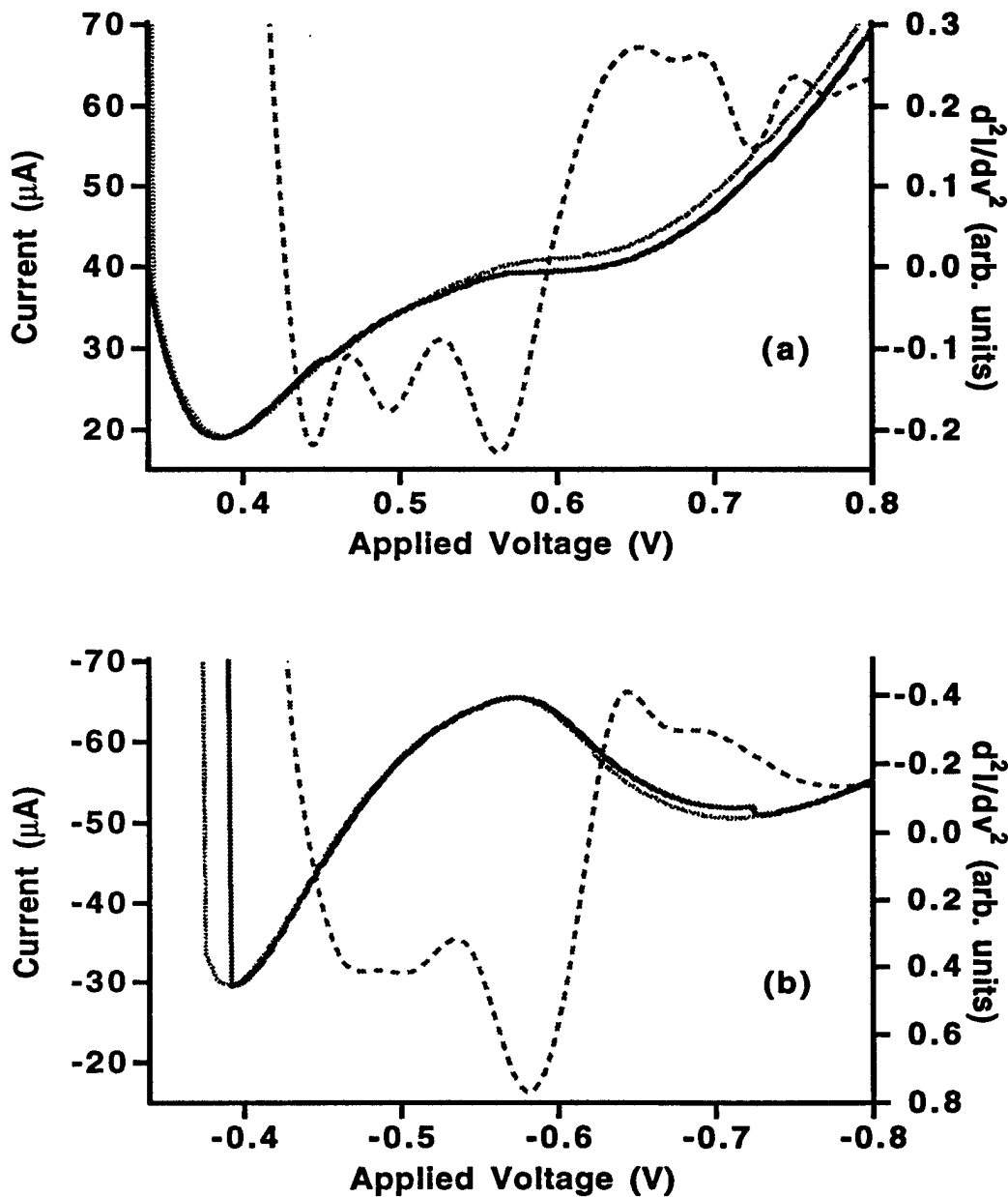


Figure 6.3: Enlargement of phonon peaks of sample 250. Solid lines plot current versus applied voltage with increasing applied voltage. Gray lines plot current versus applied voltage with decreasing applied voltage. Dashed lines plot second derivatives of current versus applied voltage. (a) Phonon peak of sample 250 under forward bias. (b) Phonon peak of sample 250 under reverse bias.

measured with increasing applied voltage is larger than the current measured with decreasing applied voltage. However, at -0.725 V, the current measured with increasing applied voltage suddenly switches to coincide with the current measured with decreasing applied voltage. Some, but not all, other contacts in this sample exhibit similar trapping behavior.

To observe features in the phonon peaks more clearly, we also plot in Fig. 6.3 the second derivatives of the current versus the applied voltage. Different features show up in the second derivative as minima. Under forward bias, there are three features in the phonon peak. These features occur at 0.562 V, 0.494 V, and 0.444 V. The phonon peak under reverse bias also exhibits three features in the second derivative, and these features occur at -0.581 V, -0.501 V, and -0.476 V. The features at 0.562 V and at -0.581 V probably correspond to emission of a phonon with the energy of a bulk AlAs LO phonon. The features at 0.494 V and at -0.501 V probably correspond to emission of a phonon with the energy of a bulk GaAs LO phonon. It is uncertain what the features at 0.444 V and at -0.476 V correspond to. Perhaps they correspond to emission of a phonon with the energy of a bulk GaAs TO-like energy.

We note here that the resonant peak and the features in the phonon peak for reverse bias occur at slightly higher voltages than the resonant peak and the features in the phonon peak for forward bias. The occurrence of features at higher voltages and the greater hysteretic behavior in the resonant peak under reverse bias suggests that there is some space charge build-up in the well when the sample is under reverse bias [ZGTC88, LAS⁺89, ST92]. The notch barrier probably has a slightly larger transmission coefficient than the barrier consisting of pure AlAs. As explained in Chapter 2, charge-build up may deflect features to higher voltages. Although charge build-up in the well

tends to reduce the tunneling current, this current also depends heavily on the width of the emitter barrier. Therefore, a smaller emitter barrier (higher transmission coefficient) means a higher tunneling current.

Although we can see features in the phonon peaks in Fig. 6.3 quite clearly, features become more prominent when we apply a magnetic field B parallel to the direction of the current. As explained in Chapter 2, the energies of the electrons parallel to the interfaces now are quantized into Landau levels, and the phonon peak splits into several peaks corresponding to the emission of a phonon and a possible change in Landau level. By plotting a sample's fan diagram—a plot of the applied magnetic field versus the voltages where the current peaks or minima in the second derivative occur—we can usually observe fans converging to voltages corresponding to the emission of a phonon with no change in Landau level. We also note here that the resonant tunneling peak shows only a weak effect on applied magnetic field.

Figure 6.4(a) illustrates the fan diagram of sample 250 under forward bias. The dots are all minima of the second derivatives of the current-voltage characteristics. Unfortunately, this fan does little to illuminate the processes which are occurring. There are few points, partially because the magnetic field has only a small effect on the phonon peak and is much less than expected. There is one relatively straight vertical line, corresponding to emission of a phonon with no change in Landau level, which occurs at about 0.483 V. This feature does not correspond to any of the features seen with $B = 0$. It is too difficult to tell to what voltages any of the other fans may converge.

The fan for the reverse bias shown in Fig. 6.4(b) has more points, because the dependence of the phonon peak on the magnetic field is fairly strong. There

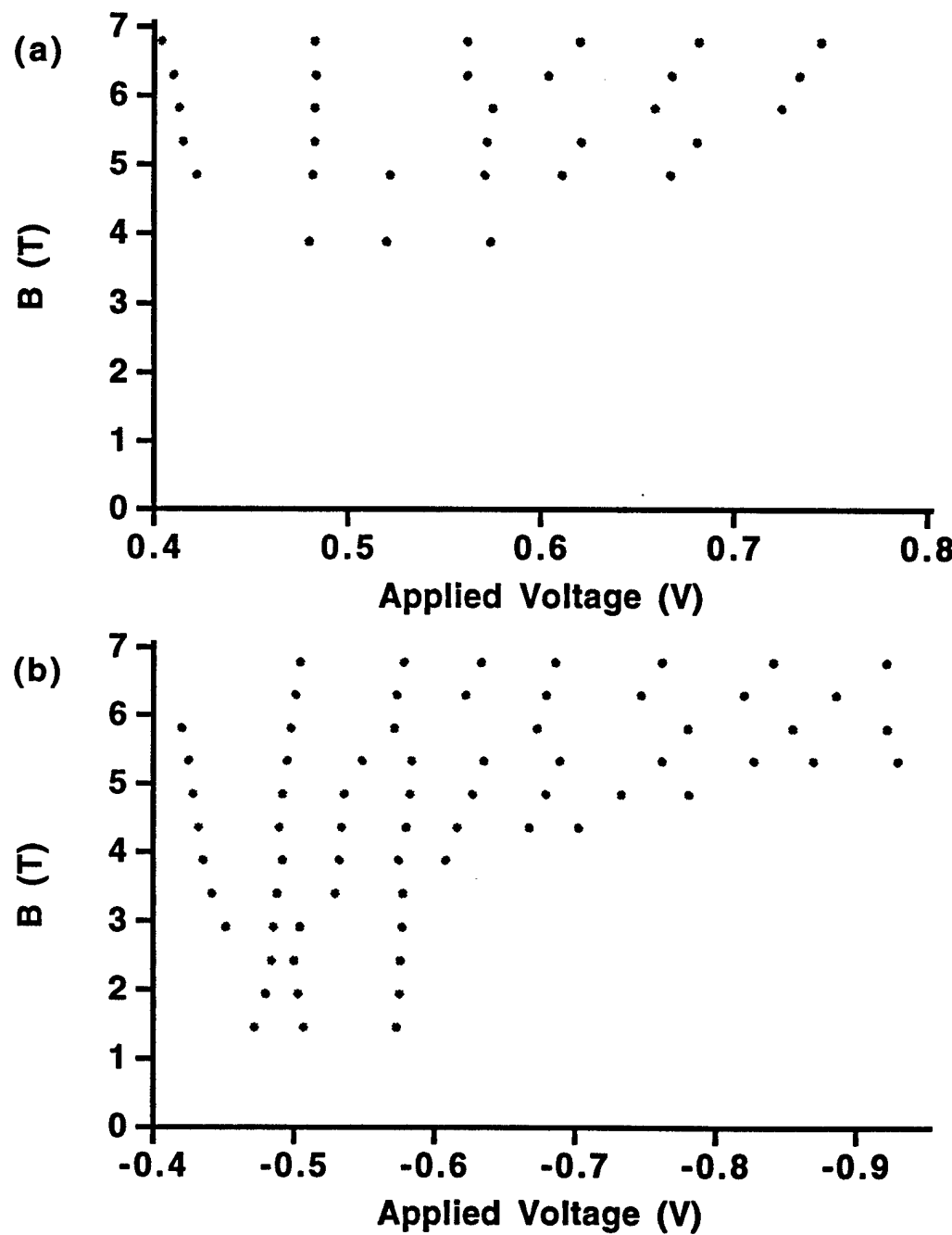


Figure 6.4: (a) Fan diagram for sample 250 under forward bias. (b) Fan diagram for sample 250 under reverse bias.

seem to be two fans, although not well developed, converging at voltages of approximately -0.573 V and at -0.48 V, and some of the lines seem to converge at entirely different voltages. In addition, the vertical lines corresponding to emission of a phonon with no change in Landau level seem to be deflected to higher voltages at high magnetic fields. This is expected if there is considerable charge build-up in the well [TT91a, Tur94]. Because of the large charge build-up, it is not feasible to obtain an energy scale from this fan, and it is also uncertain if the energies obtained would be reliable because of the extensive trapping this sample exhibits. However, the data presented thus far are intriguing, especially since we have seen three features in the phonon peaks as illustrated in Fig. 6.3. Another sample should be grown without the big growth interrupts to minimize the effects of the trapping behavior. Measurements on such a sample could corroborate whether there are three such features in the phonon peak and possibly determine the energies.

6.2 Experimental Results of Asymmetric Barrier Samples

In this section, we will present extensive studies on the asymmetric *barrier* samples, specifically the dependence of the phonon properties such as energies and relative coupling strengths as a function of alloy concentration in the barriers. Since there is a considerable amount of data to present, we will focus on three specific samples, which illustrate quite clearly, some of the trends and properties of all the samples. We will refer to samples by the MBE growth number as given in Appendix B. These samples are the **263** sample whose barriers have an alloy concentration of $x = 0.7$, the **293** sample whose barriers

have an alloy concentration of $x = 0.4$, and the **291** sample whose barriers have an alloy concentration of $x = 0.225$. Section 6.2.1 will discuss results of sample **263** under forward bias, and the remaining sections will discuss all asymmetric *barrier* samples under reverse bias. Section 6.2.2 will discuss the results of the current-voltage and conductance-voltage characteristics with no external magnetic field. Section 6.2.3 will discuss some of the results with an applied external magnetic field. Sections 6.2.4 and 6.2.5 will present analysis of the energy dependence of the phonon modes and dependence of the relative contributions from modes with different energies, respectively, as a function of alloy concentration. Finally, Section 6.2.6 will present some temperature dependent data and analysis.

6.2.1 Data Under Forward Bias

Most of the data and analysis in this chapter is obtained under reverse bias in which the electrons tunnel through the thicker barrier first. In this way, we hope to minimize the effects of charge build up in the well. This subsection will present some data obtained under forward bias, in which the electrons tunnel through the thinner barrier first, to illustrate the effects of space charge build-up in the well. This data is for sample **263**, but the general conclusions apply to all the samples.

Figure 6.5(a) shows the current-voltage characteristic of the sample under forward bias with no applied magnetic field. The dotted lines give the curve for increasing applied voltage, and the dashed lines give the curve for decreasing applied voltage. For applied voltages of less than about 0.15 V, the current is too small to be seen on this scale. The current then increases almost linearly till it peaks at resonance. With increasing applied voltage, the resonant peak oc-

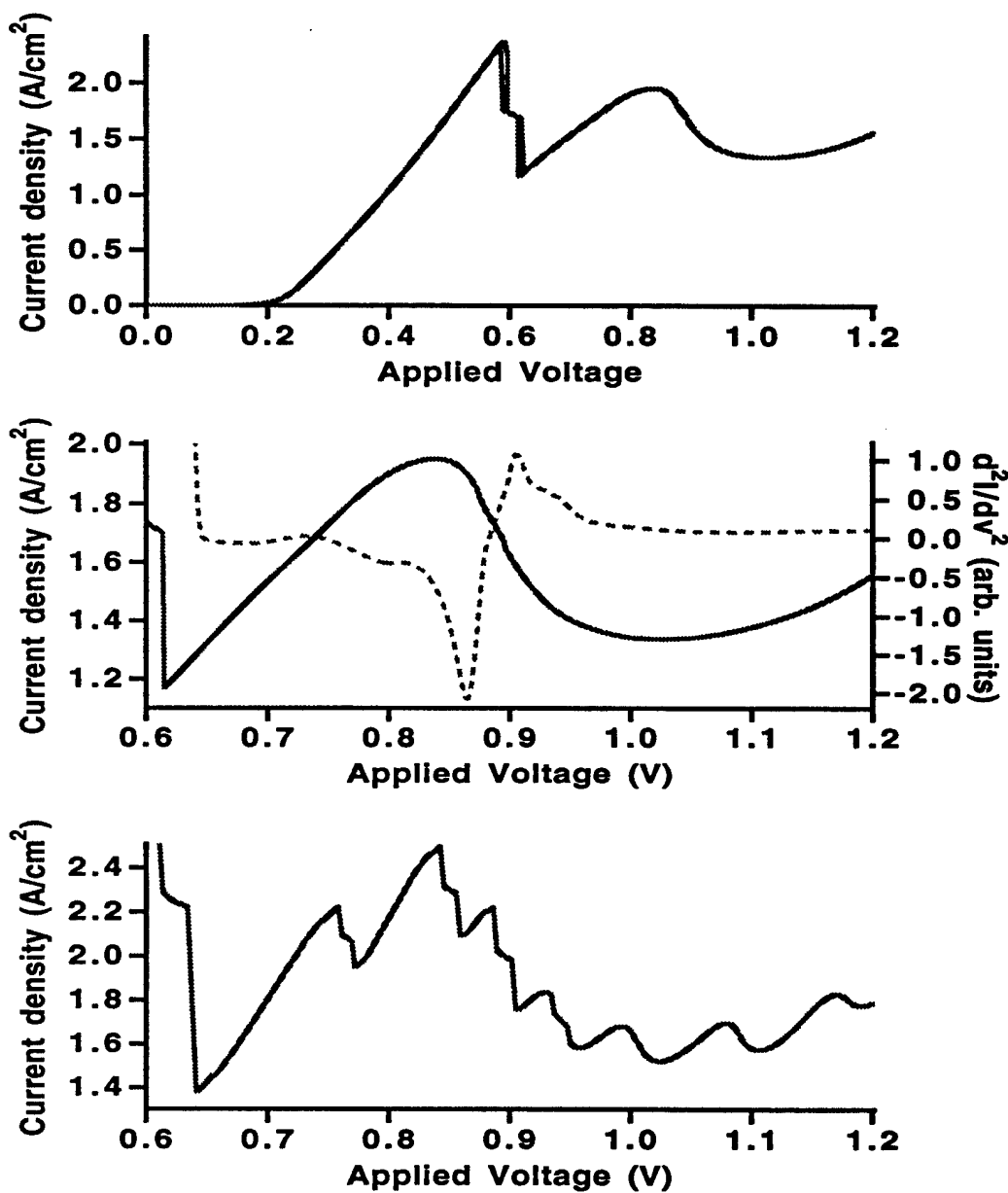


Figure 6.5: (a) Current versus applied voltage across sample under forward bias for sample 263. (b) Solid line is current in phonon peak versus applied voltage across sample. Dashed line is second derivative of the current versus applied voltage across sample. (c) Current versus voltage of phonon peak with an applied magnetic field of 6.8 T.

curs at 0.595 V with a current of 2.37 A/cm^2 . The current then drops suddenly, but the NDR region above resonance is masked by spontaneous circuit oscillations. Since the current-voltage characteristic is hysteretic in two different regimes, we note that there are two subcritical Hopf bifurcation points in the NDR region [WT94]. Sample 262 ($= 0.6$) also exhibits current oscillations in the NDR region of the forward bias resonant peaks. All the other asymmetric *barrier* samples, however, exhibit no oscillations in this region, but, instead, are intrinsically bistable, where the current simply switches from the high current region to the lower current region. Intrinsic bistability is somewhat expected in all these samples due to charge build-up in the well [ZGTC88, LAS⁺89, ST92]. See also Chapters 2 and 3. However, all samples exhibit other clear evidence of space charge build-up, especially in the phonon peaks with an applied magnetic field, and in the fan diagrams like the data for sample 263 presented below.

Above the resonant tunneling peak, the current again rises to a peak of 1.94 A/cm^2 at 0.844 V, corresponding to the phonon-assisted tunneling peak. The current then falls to a minimum of 1.33 A/cm^2 at 1.0 V and then rises again beyond the compliance of our instruments. The phonon peak does not exhibit hysteresis or oscillations in the NDR region. Figure 6.5(b) shows an enlargement of the phonon-assisted tunneling peak. In order to distinguish features in the phonon peak more clearly, we also plot in Fig. 6.5(b) the second derivative of the current versus the applied voltage. We can see three minima in the phonon peak which occur at 0.864 V, 0.800 V, and 0.684 V.

By applying a magnetic field parallel to the current, we can observe the splitting of the phonon peak into several peaks corresponding to emission of a phonon and a possible change in Landau level. Figure 6.5(c) plots the phonon peak versus the applied voltage with an applied field of 6.8 T. In addition

to the splitting into very sharp peaks, we also observe that the current of the phonon peak has increased significantly as well. The tallest peak has a current of 2.48 A/cm^2 . It is important to note that the resonant peak is only weakly affected by the applied magnetic field.

Figure 6.6 plots the fan diagram for this sample under forward bias. It can be seen that we have a well developed fan converging to about 0.715 V. This voltage is a little higher than the feature seen with $B = 0$, which occurs at 0.684 V. Another less developed fan seems to converge to the feature at 0.864 V. There seems to be no fan corresponding to the feature at 0.800 V. However, there is an additional well developed fan which seems to converge at about 1.095 V, which may indicate the emission of two phonons. Fan diagrams in the forward bias in all samples indicate the possibility of emission of two phonons.

Space charge effects are very evident in this sample under forward bias. Although this sample does not exhibit magnetic-field-enhanced bistability, other samples, such as sample 280 does [LE91, GMC94]. The space charge effects for sample 263 are most evident in the fan. The features at higher magnetic fields are deflected to higher voltages which is an indication of charge build-up in the well [TT91a, Tur94]. Some of the fan lines also seem to converge to voltages lower than the resonant tunneling peak. Because of such large space charge effects, we do not expect to be able to determine an energy scale from this fan, or from the fan of any sample biased in the forward direction.

We note here some general observations and trends in all the samples under forward bias. Samples 264 ($x = 0.8$) and 262 ($x = 0.6$) both have resonant peaks which consist of two separate current peaks which are close in their

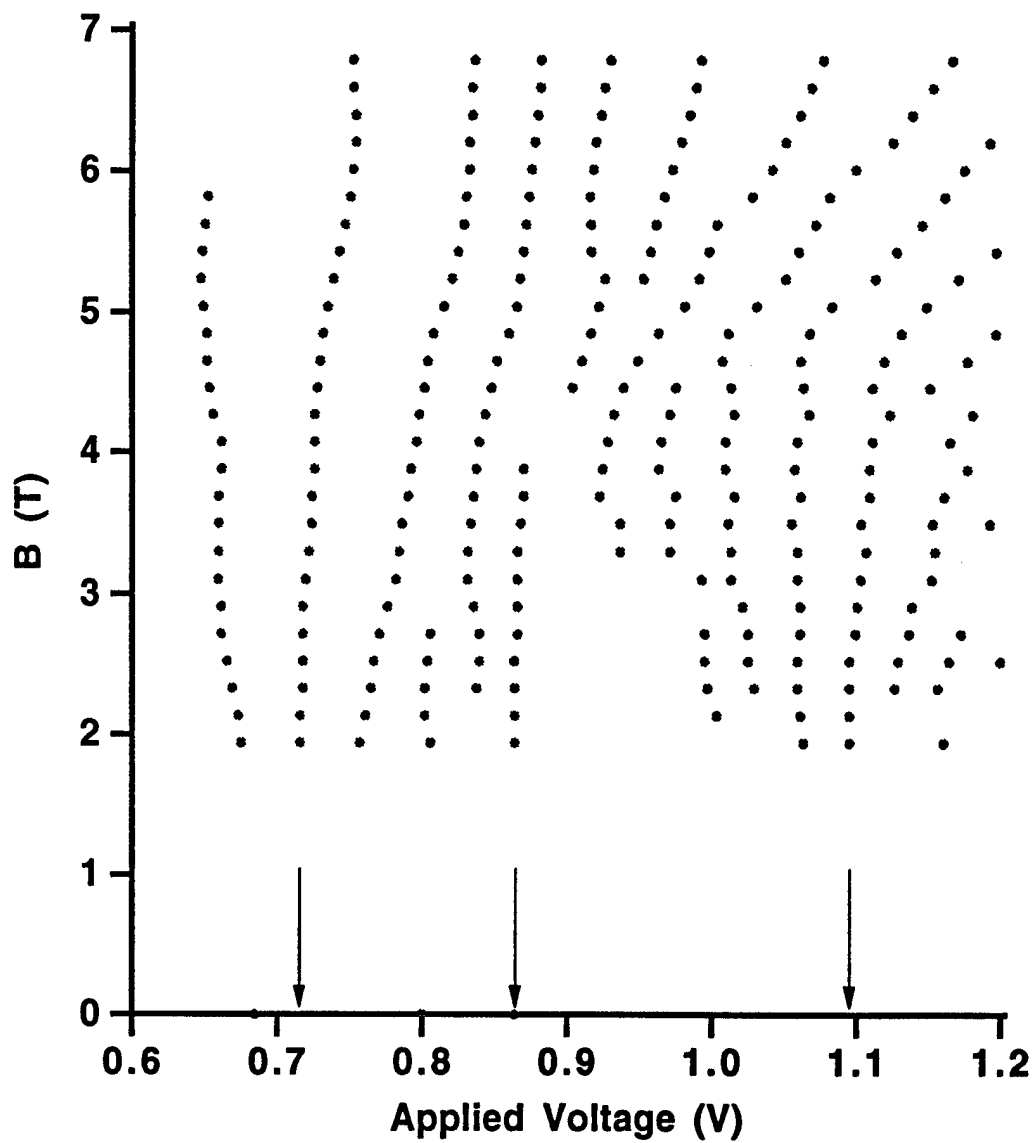


Figure 6.6: Fan diagram for sample 263 under forward bias. Fans seem to converge to 0.715 V, 0.864 V, and 1.095 V.

voltage values. The resonant current peak of sample **278** ($x = 0.3$) is similar and consists of an inflection point and a current peak which are close in their voltage values. These two separate peaks in the resonant peak suggest that there may be considerable interface roughness in these samples, resulting in two wells of different sizes and with different resonant energies. All the other samples exhibit only one peak at resonance. The variation in voltage where these resonant peaks occur appears to be random, and within about 16 % of a mean value of 0.54 V. The voltages of the resonant peak vary from 0.454 V for sample **291** ($x = 0.225$) to 0.631 V for sample **278** ($x = 0.3$). This is not surprising since the doping levels are expected to be within only 20 % of the nominal values. However, the voltage difference ΔV between the voltage where the phonon peak occurs and the voltage where the resonance occurs decreases as the aluminum concentration in the barriers decreases. This ΔV is maximum for sample **264** ($x = 0.8$) with a value of 0.288 V, and decreases to a value of 0.155 V for sample **291** ($x = 0.225$). The phonon feature for sample **279** ($x = 0.2$) is only an inflection in the current-voltage curve.

The overall current levels (which include both resonant and phonon peaks) appear to be less random. The current density levels for samples **292** ($x = 0.5$), **293** ($x = 0.4$), and **280** ($x = 0.3$) are less than the current levels for samples **264** ($x = 0.8$), **263** ($x = 0.7$), and **226** ($x = 0.6$). The differences in current levels may be due to fluctuations in the barrier thicknesses. Samples **280** ($x = 0.25$), **291** ($x = 0.225$), and **279** ($x = 0.2$) have the largest overall current densities which is to be expected since they have the same barrier widths as sample **278** but lower aluminum concentrations.

Finally, we compare peak to current valley ratios (PVCR) as a function of the aluminum concentration x . We define two PVCRs. One, which we label

as PVCRmin is the ratio of the maximum current in the resonant peak to the minimum current in the valley above resonance. The other PVCR, which we label as PVCRph is the ratio of the maximum current in the resonant peak to the maximum current in the phonon peak. Both of these PVCRs follow the same pattern as a function of the aluminum concentration. The highest PVCRs occur in sample **291** ($x = 0.225$) which has a value of 4.07 for PVCRmin and 1.65 for PVCRph. The value of PCVRmin in sample **279** ($x = 0.2$) is about 2.70. As the aluminum concentration in the barriers increases from 0.225, both PVCRs decrease. They reach a minimum for sample **292** ($x = 0.5$) which has a value of 1.61 for PVCRmin and 0.81 for PVCRph. The phonon peaks in samples **264** ($x = 0.8$) and **293** ($x = 0.4$) are also higher than the resonant peaks. As we increase the aluminum concentration in the barriers above 0.5, the PVCRs increase to a value of 1.99 for PVCRmin and a value of 1.22 for PVCRph in sample **263** ($x = 0.7$). The PVCRs in sample **264** ($x = 0.8$) are slightly smaller, with a value of 1.61 for PCVRmin and 0.965 for PVCRph. The fact that both PVCRs follow the same pattern suggests that most of the excess current in the valley is due to PAT.

6.2.2 Reverse Bias Data with $B = 0$

Figure 6.7(a) illustrates the current-voltage curve for sample **263** under reverse bias taken on a device 125 μm in diameter. This curve clearly shows that the current is very small at low voltages, and that it quickly rises to a peak of -0.924 A/cm^2 at -0.237 V corresponding to resonance. At voltages above this peak, the current falls, but some of this NDR region is masked by spontaneous current oscillations, and only the average current and voltage is plotted here in this region. We observe two subcritical Hopf bifurcations in this

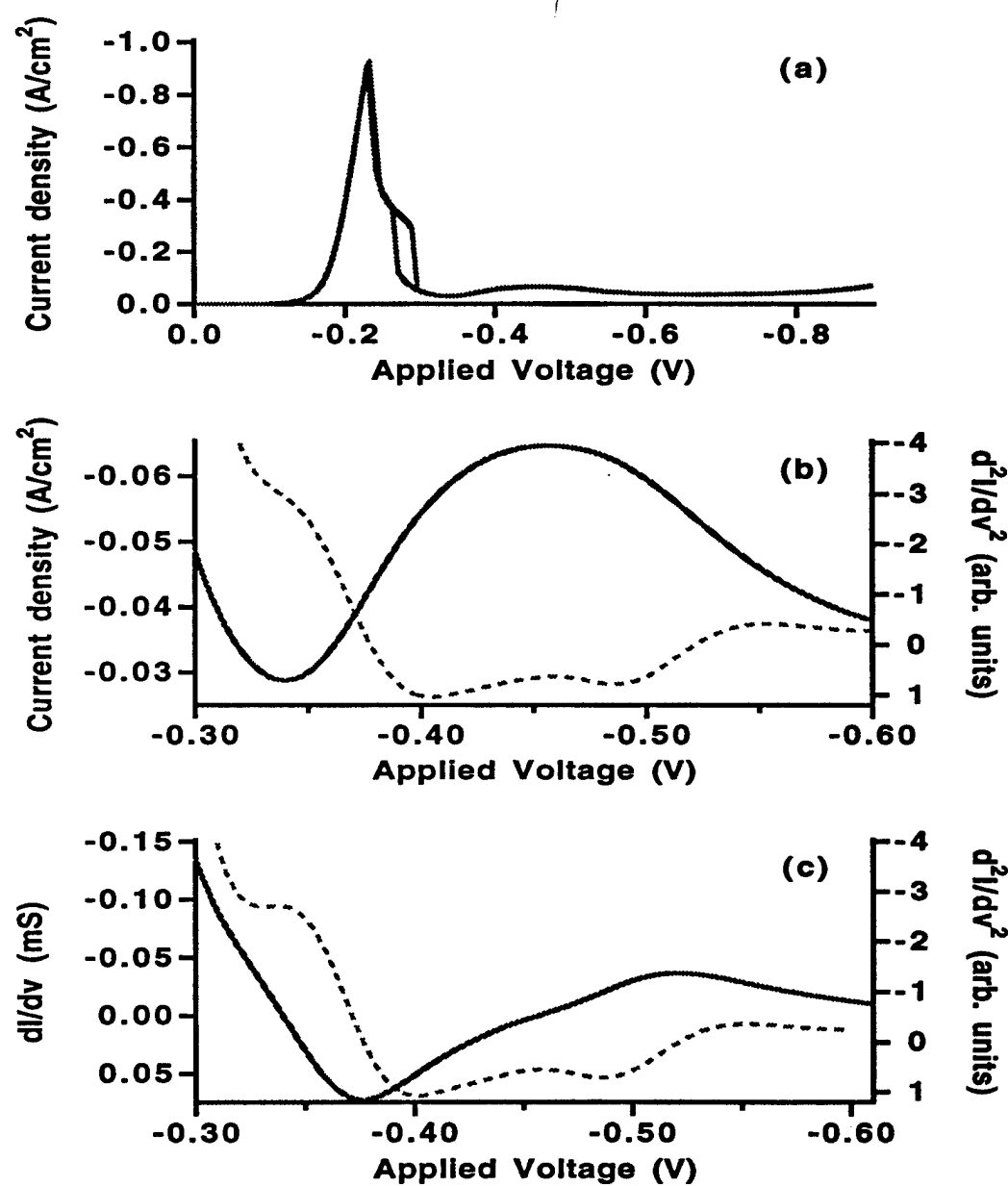


Figure 6.7: (a) Current versus applied voltage across sample under reverse bias for sample 263. (b) Solid line is current in phonon peak versus applied voltage across sample. Dotted line is second derivative of the current versus applied voltage across sample. (c) Solid line is conductance versus applied voltage across sample with data taken from lock-in amplifiers. Dotted line is first derivative of conductance versus applied voltage across sample.

regime [WT94]. The current reaches a minimum of -0.029 A/cm^2 at -0.339 V . The current then peaks again at -0.457 V with a current of -0.065 A/cm^2 corresponding to the phonon peak. The current then reaches a minimum of -0.035 A/cm^2 at -0.671 V before rising again to current levels above this scale.

Figure 6.7(b) shows a close-up of the phonon peak. In order to see features in this peak more clearly, we also plot the second derivative as a function of the applied voltage and search for minima. This second derivative is the dashed line in Fig. 6.7(b). The second derivative plot of the current-voltage curve clearly shows two features in the phonon peak corresponding to the emission of phonons with two separate energies. The first minima occurs at -0.405 V and the second occurs at -0.485 V . As an independent and probably more accurate measurement, we also plot the conductance versus applied voltage in Fig. 6.7(c). We obtained this curve using the lock-in amplifiers setup shown in Fig. 5.5. We also plot in Fig. 6.7(c) the first derivative of the conductance versus applied voltage which appears as the dashed line. Again, there are two minima in the phonon peak, one occurring at -0.401 V and the other occurring at -0.486 V , which is in good agreement with the minima found directly from the current-voltage curve. However, Fig. 6.7(c) clearly shows that there is a third minimum occurring just above resonance at -0.332 V . This feature in the conductance-voltage data corresponds to a feature in the current-voltage curve which is manifested only as a strong inflection in the second derivative of the current-voltage characteristic. In fact, all the features from the lock-in data appear sharper and are probably more accurate than the features found directly from the current-voltage characteristic, showing that the data obtained from the lock-in amplifiers is more sensitive.

We have ascertained two possibilities which may explain the third feature

just above resonance. One possibility includes the emission of a third phonon with very low energies. The second and more likely possibility is that this feature is an artifact of the sudden turn-on in phonon emission, which occurs when the energy of the electrons at the Fermi edge in the emitter is above the energy in the well by exactly a phonon energy. Both of these possibilities will be discussed in much more detail in the Section 6.2.6, when we discuss the Shubnikov-de Haas oscillations and temperature dependence of this peculiar feature. We note here that this feature appears in most of our samples.

Figures 6.8(a) and 6.9(a) illustrate the current-voltage curves for the **293** ($x = 0.4$) and **291** ($x = 0.225$) samples. Data for the **293** sample are taken with a device $500 \mu\text{m}$ in diameter and data for the **291** sample are taken with a device $250 \mu\text{m}$ in diameter. The resonant peak for the **293** sample occurs at -0.18 V with a current of -0.119 A/cm^2 and the minimum above resonance occurs at -0.300 V with a current of -0.004 A/cm^2 . There is a small region of instability in the NDR region, but no hysteresis. Hence, we note the existence of two supercritical Hopf bifurcations in the NDR region [WT94]. The phonon peak for this sample occurs at -0.412 V with a current of -0.013 A/cm^2 .

The resonant peak for sample **291** occurs at -0.191 V with a current of -0.963 A/cm^2 and the minimum above resonance occurs at -0.258 V with a current of -0.059 A/cm^2 . Part of the NDR region is masked by spontaneous current oscillations. However, there is only one region of hysteresis which occurs at high voltages in the NDR region. Hence, we have a supercritical Hopf bifurcation at low voltages and a subcritical Hopf bifurcation at high voltages in the NDR region [WT94]. The current in the phonon peak in sample **291** does not achieve a maximum which is quite clearly illustrated in Fig. 6.9(b). There is only a strong inflection where the phonon peak would occur since the

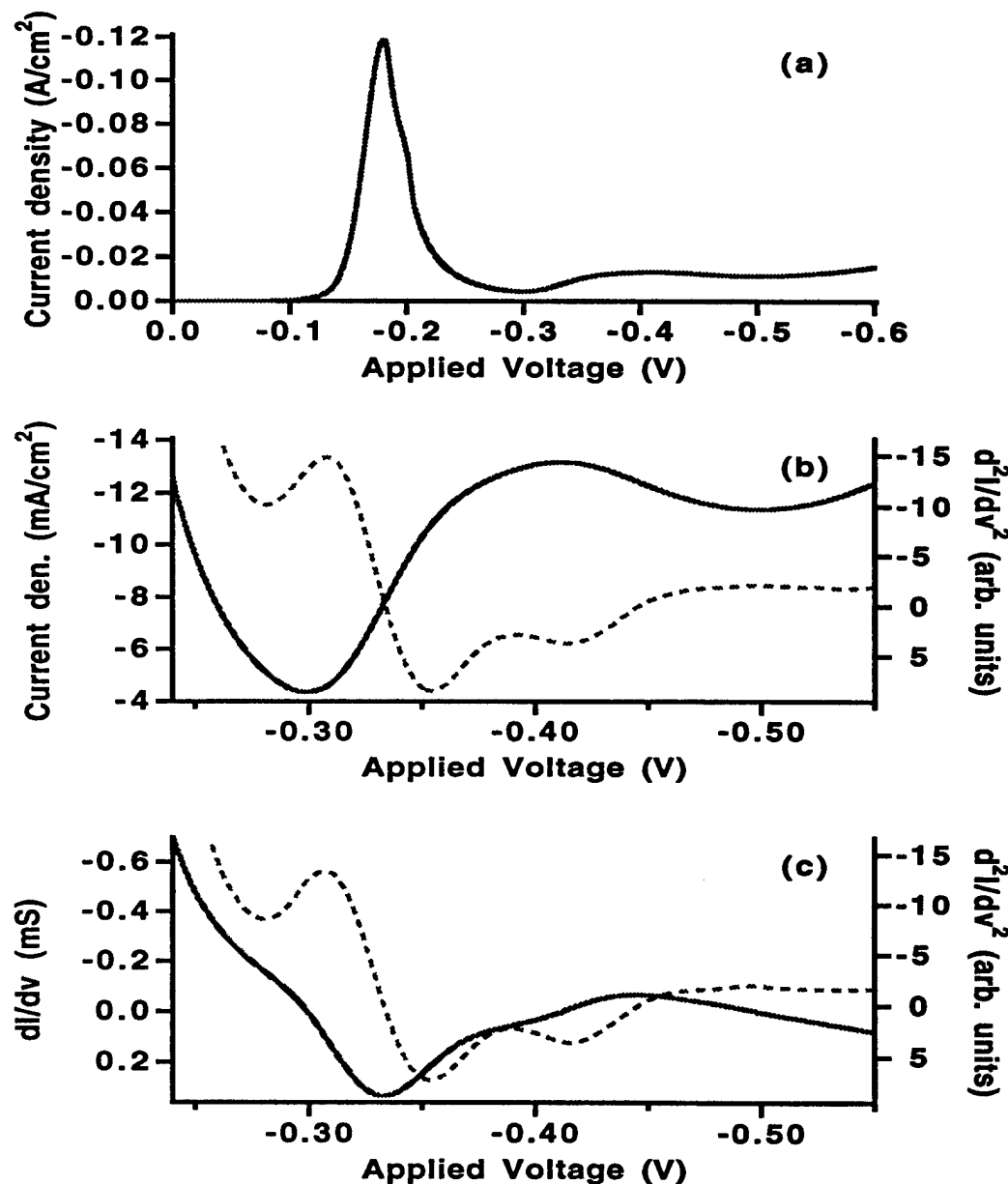


Figure 6.8: (a) Current versus applied voltage across sample under reverse bias for sample 293. (b) Solid line is current in phonon peak versus applied voltage across sample. Dotted line is second derivative of the current versus applied voltage across sample. (c) Solid line is conductance versus applied voltage across sample with data taken from lock-in amplifiers. Dotted line is first derivative of conductance versus applied voltage across sample.

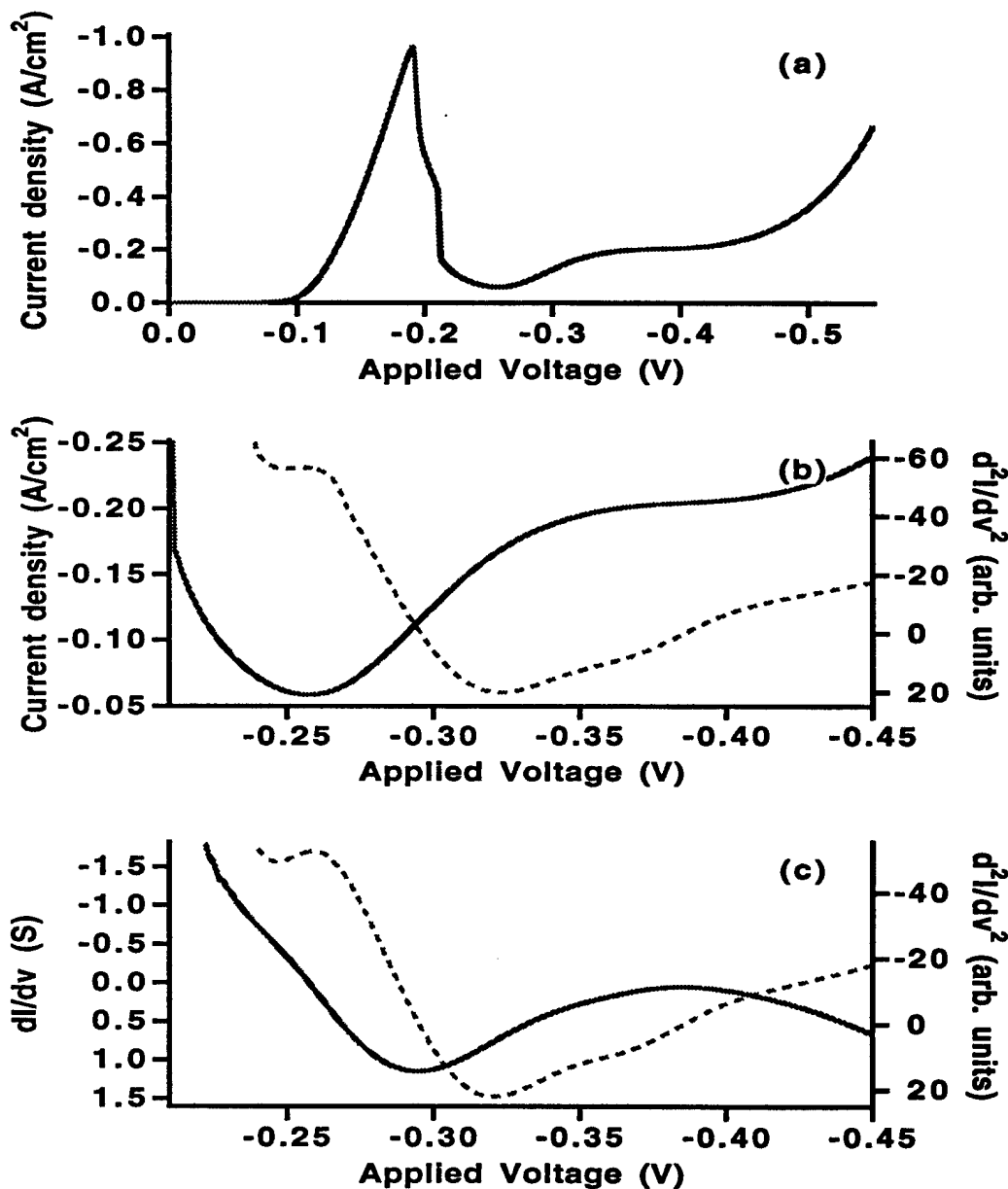


Figure 6.9: (a) Current versus applied voltage across sample under reverse bias for sample 291. (b) Solid line is current in phonon peak versus applied voltage across sample. Dotted line is second derivative of the current versus applied voltage across sample. (c) Solid line is conductance versus applied voltage across sample with data taken from lock-in amplifiers. Dotted line is first derivative of conductance versus applied voltage across sample.

current rises quickly at low voltages due to onset of the second resonant peak.

To see features in the phonon assisted tunneling regions in samples **293** and **291** clearly, we again plot both the current as a solid line and its second derivative as a dashed line versus applied voltage in Figs. 6.8(b) and 6.9(b). We also plot the conductance-voltage characteristics and their first derivatives in Figs. 6.8(c) and 6.9(c). The phonon peak of sample **293**, like the phonon peak of sample **263**, shows two different minima corresponding to emission of phonon with two different energies. These minima occur at -0.354 V and -0.414 V for the current-voltage measurements and occur at -0.354 V and -0.416 V for the conductance-voltage measurements. Both the current-voltage and conductance-voltage characteristics for the **293** sample show a low energy feature just above resonance occurring at -0.281 V for the current-voltage measurement and -0.280 V for the conductance-voltage measurement.

The phonon inflection in sample **291**, however, shows strong evidence of emission of phonons with only one energy. There are two minima in the second derivative versus applied voltage, and one of the minima corresponds to the low energy feature which occurs at just above resonance. This minimum occurs at -0.254 V for the current-voltage measurement and at -0.247 V for the conductance-voltage measurement. There is only one additional minimum in the phonon inflection. This minimum occurs at -0.323 V for the current-voltage measurement and at -0.321 V for the conductance-voltage measurement. These measurements of sample **291** clearly show that the dominant phonons emitted in the phonon assisted tunneling process either have only one energy or energies which are very close together.

Without showing all the data here, we note some general characteristics of

current-voltage and conductance-voltage data with no applied magnetic field from all samples. Some of these trends are clearly shown in the data with applied magnetic fields and these trends are also discussed in the next section. There are clearly two minima in the second derivatives in the phonon peaks for samples with barriers having aluminum concentrations $x \geq 0.3$. There is only one minimum in the phonon peak for samples 291 ($x = 0.225$) and 279 ($x = 0.2$). In sample 280 ($x = 0.25$) there is one minimum and an inflection in the second derivative of the current-voltage data of the phonon peak. Minima in the second derivative corresponding to the low energy feature occur in most of our samples. However, in samples 264 ($x = 0.8$), 278 ($x = 0.3$), 279 ($x = 0.2$), there is only an inflection in the second derivative where the low energy feature would occur.

The overall current levels and voltages of the resonant and phonon peaks under reverse bias follow similar patterns as a function of the aluminum concentration as the samples under forward bias. The variation in voltages where the resonances occur appears to be random, and within about 16 % of a mean value of -0.204 V. The only exception is sample 279 ($x = 0.2$) whose resonant peak occurs at -0.254 V. The voltages where the resonant peak occurs range from -0.18 V for sample 293 ($x = 0.4$) to -0.237 V for sample 263 ($x = 0.6$). These differences are probably due to the uncertainty in the doping profile. Unlike the forward bias case, however, the difference in voltage ΔV between the resonant peak and phonon peak does not necessarily decrease as the concentration of aluminum in the barriers decreases, although that is the general overall trend. The largest value for ΔV is 0.241 V for sample 262 ($x = 0.6$) and the smallest value is 0.154 V for sample 278 ($x = 0.3$).

The overall current levels of the resonant and phonon features of these

samples under reverse bias follow the same pattern as those of the samples under forward bias. The current density levels for samples **292** ($x = 0.5$), **293** ($x = 0.4$), and **280** ($x = 0.3$) are less than the current levels for samples **264** ($x = 0.8$), **263** ($x = 0.7$), and **226** ($x = 0.6$). The differences in current levels may be due to fluctuations in the barrier thicknesses. Samples **280** ($x = 0.25$), **291** ($x = 0.225$), and **279** ($x = 0.2$) have the largest overall current densities which is to be expected since they have the same barrier widths as sample **278** but lower aluminum concentrations.

The PVCRs for reverse bias do not follow the same patterns for the samples under reverse bias as under forward bias. Both PVCRs appear to have random variations around well defined mean values, although a sample with a high value of PVCR_{min} also tends to have a high value of PVCR_{ph}. The highest value of PVCR_{min} 31.86 occurs in sample **263** ($x = 0.7$) which also has the highest value of PVCR_{ph} of 14.22. The lowest values of PVCR_{min} occur for samples **291** ($x = 0.225$), with a value of 16.32, and **279**, with a value of 15.37. We could not calculate PVCR_{ph} for either of these samples because the PAT current does not peak for either of these samples, but shows only an inflection in the current-voltage data.

In the next section, we will show how we can use data obtained with an applied magnetic field to determine the energies of the phonons observed in the data with no applied magnetic field. In Section 6.2.4, we will present these energies as a function of the alloy concentration in the barrier. In Section 6.2.5, we will present a fitting routine to determine the relative coupling strengths of phonon modes with different energies.

6.2.3 Data with $B \neq 0$

Although we can clearly see features in the phonon peaks with $B = 0$, we have no way of determining the energies of these phonons from these curves alone. As explained in Chapter 2, these minima are quite broad since electrons can lose or gain energy in the direction parallel to the interfaces during the phonon-assisted tunneling process [Tur94]. In addition, most of the voltage drop in the device comes from the voltage drop in the collector region. Since we expect little charge build-up in the well under reverse bias for these samples, we expect a nearly linear relationship between ΔE_z , the energy in the z direction lost by the electron tunneling from the emitter into the well, and ΔV , the difference between the voltage position of the resonant peak and the voltage position of the phonon features above the resonant peak. In order to determine this relationship, we apply a series of magnetic fields parallel to the current flow. With an applied magnetic field, the electronic energy levels parallel to the interfaces are now quantized into Landau levels whose energies are given by Eq. (2.8). In the current-voltage curve, the phonon peak splits into several peaks, corresponding to emission of a phonon and a possible change in Landau level. It is important to note here that the resonant peaks show only a weak dependence on magnetic field. Electrons may change Landau level during resonant tunneling if there is a mechanism for elastic scattering such as interface roughness. Other researchers have reported such findings [YYK89, LAE⁺89, BLSR⁺90, GCB91, CYYW91]. However, we observe little such behavior, testifying to the generally high quality of these devices.

Figures 6.10 and 6.11 illustrate the effects of applied magnetic fields on the phonon peak of sample 263 under reverse bias. The effects are quite

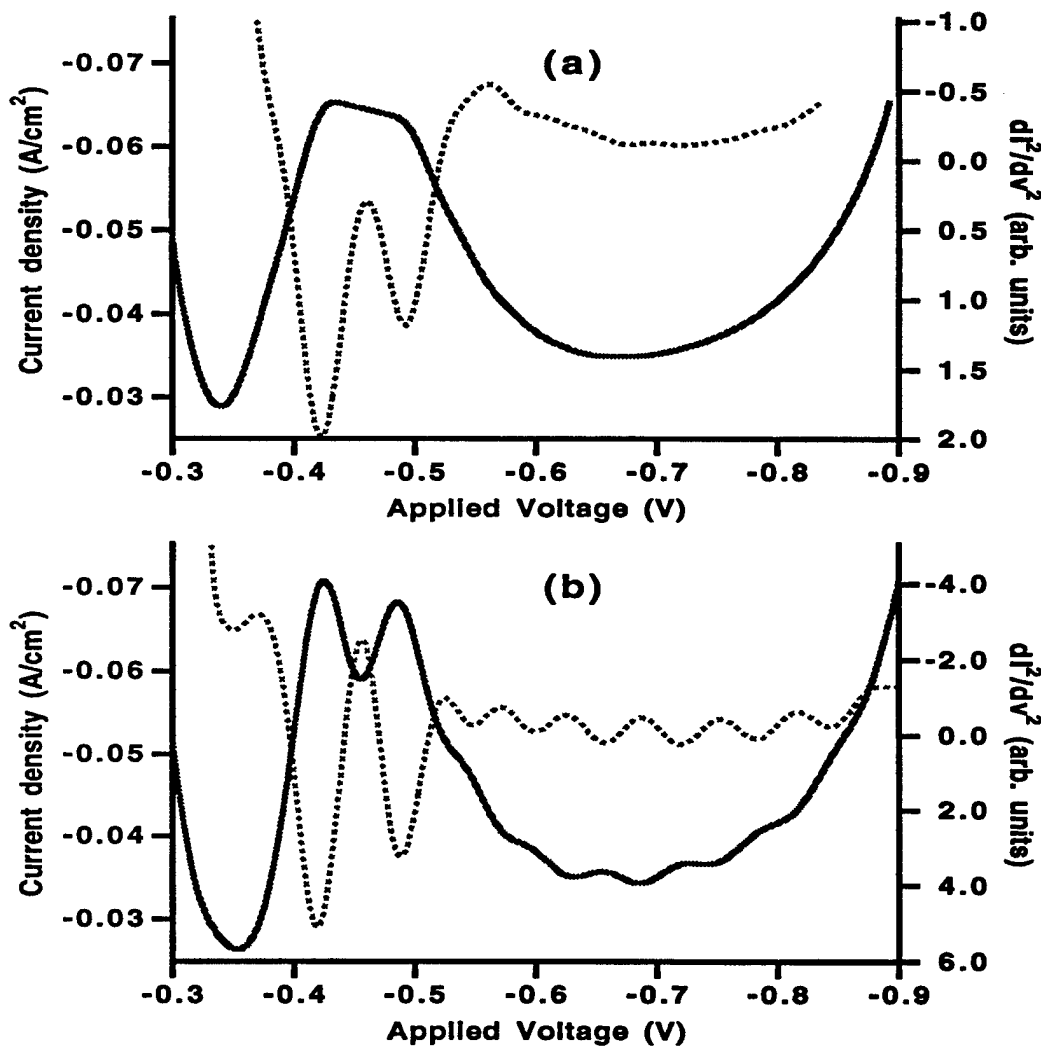


Figure 6.10: Current-voltage curves of sample 263 under reverse bias with an applied magnetic field of (a) 4.85 T and (b) 6.79 T. Solid lines plot the current-voltage data and dotted lines plot the second derivative versus applied voltage across sample.

pronounced at high magnetic fields. The solid line in Fig. 6.10(a) plots the current-voltage data with an applied magnetic field of 4.85 T, and the dotted line plots the second derivative of the current versus the applied voltage. It is clear that there are two minima in the second derivative in the phonon peak at voltages which are approximately those where the minima occur in the data with no applied magnetic field as seen in Fig. 6.7(b). There are additional minima at higher voltages, but they are difficult to see on this scale. These minima become more pronounced at higher magnetic fields as clearly illustrated in Fig. 6.10(b) which plots the current and the second derivative versus the applied voltage across the sample with an applied magnetic field of 6.79 T.

For smaller magnetic fields, the effects of the magnetic field on the phonon peak are most easily seen in the conductance-voltage data. Figure 6.11(a) plots the conductance and the first derivative of the conductance (second derivative of current) versus applied voltage for sample **263** under reverse bias with an applied magnetic field of 2.91 T. The minima in the second derivative are more pronounced than the minima in the data with no applied magnetic field as seen in Fig. 6.7(c). Figure 6.11(b) plots the conductance-voltage data with an applied magnetic field of 3.88 T. There are now three minima in the phonon peak. The two minima which occur at -0.405 V and at -0.48 V correspond to the minima in the conductance-voltage data with no applied magnetic field. An additional minimum has developed at a voltage of -0.425 V.

Current-voltage and conductance-voltage curves for the other asymmetric *barrier* samples under reverse bias with an applied magnetic field generally follow the pattern described above. The features tend to be very sharp, and separate features can usually be distinguished from each other at fields of about

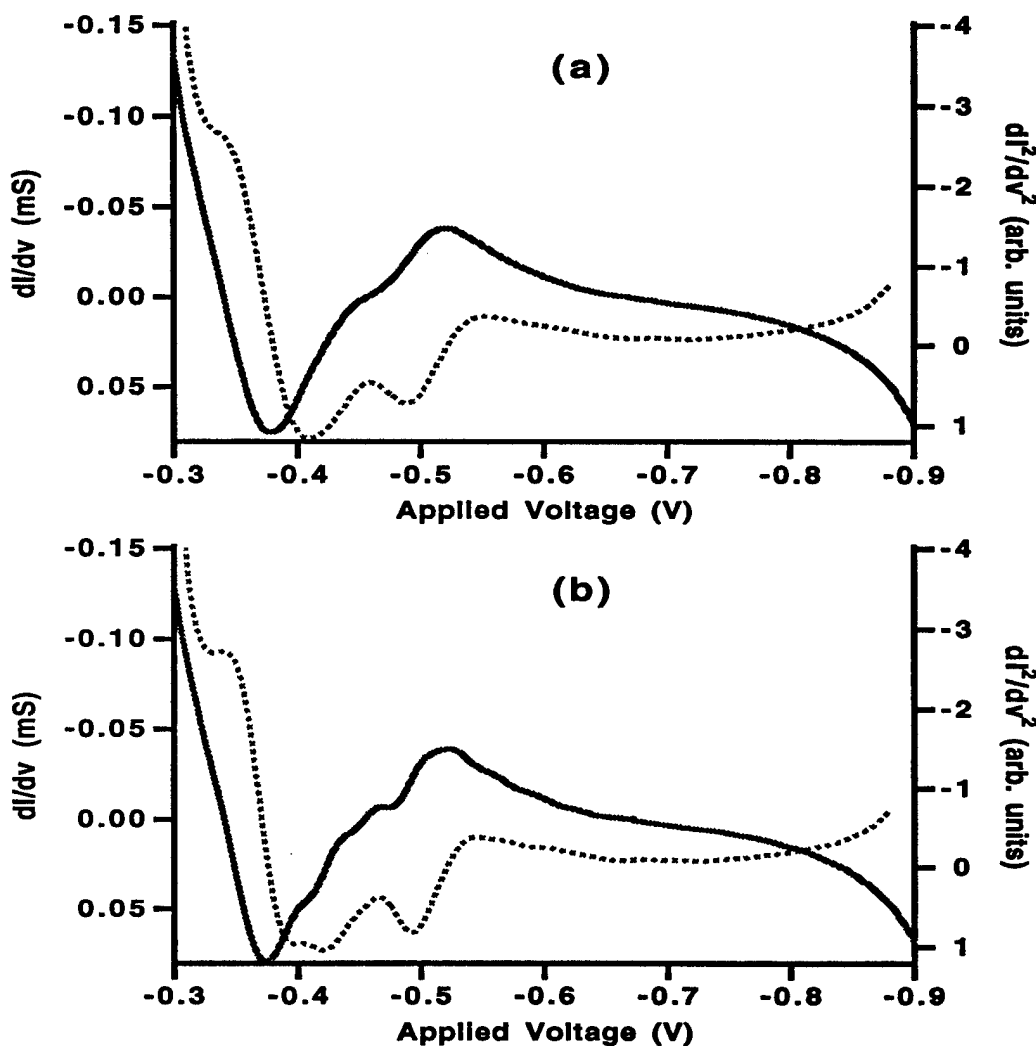


Figure 6.11: Conductance-voltage curves of sample 263 under reverse bias with an applied magnetic field of (a) 2.91 T and (b) 3.88 T. Solid lines plot the conductance-voltage data and dotted lines plot first derivative of conductance versus applied voltage across sample.

5.5 T and above. In addition, the current-voltage curves at fields of about 4 T and above are usually visibly different and distinguishable from the curves with no applied magnetic field. The only notable exception is sample 264 ($x = 0.8$). In this sample, the features were not very sharp, even at high magnetic fields. The most apparent difference is that there are fewer minima in the second derivative compared to the other samples and the minima are much less pronounced.

By plotting the magnetic field versus the minima of the second derivatives, we create the sample's fan diagram. Figure 6.12 shows the fan diagram for the reverse bias for sample 263. All these minima occur above the resonance peak, and here solid circles plot the minima of the second derivatives of the current-voltage data, and the open circles plot the minima of the first derivatives of the conductance-voltage data. Though not exact, there is good agreement between the current-voltage and conductance-voltage data.

It is evident that the sample has well-developed fans that converge to features at four separate voltages, -0.332 V, -0.405 V, -0.425 V, and -0.48 V. The lines have been drawn to indicate the best fit. Vertical lines in the fans correspond to an emission of a phonon with no change in Landau level. Except for the feature at -0.425 V, all these voltages correspond exactly to minima in the current-voltage curves with $B = 0$. However, most of the fans converge to the feature at -0.425 V, which forms a vertical line only above 3.1 T. The feature at -0.405 V is not seen at fields above 3.1 T, but is evident at lower fields. The low energy feature corresponding to -0.332 V behaves similarly. This feature is seen only at fields below 4.2 T. Finally, the vertical line corresponding to the feature at -0.485 V is not entirely vertical, although the feature is still fairly evident.

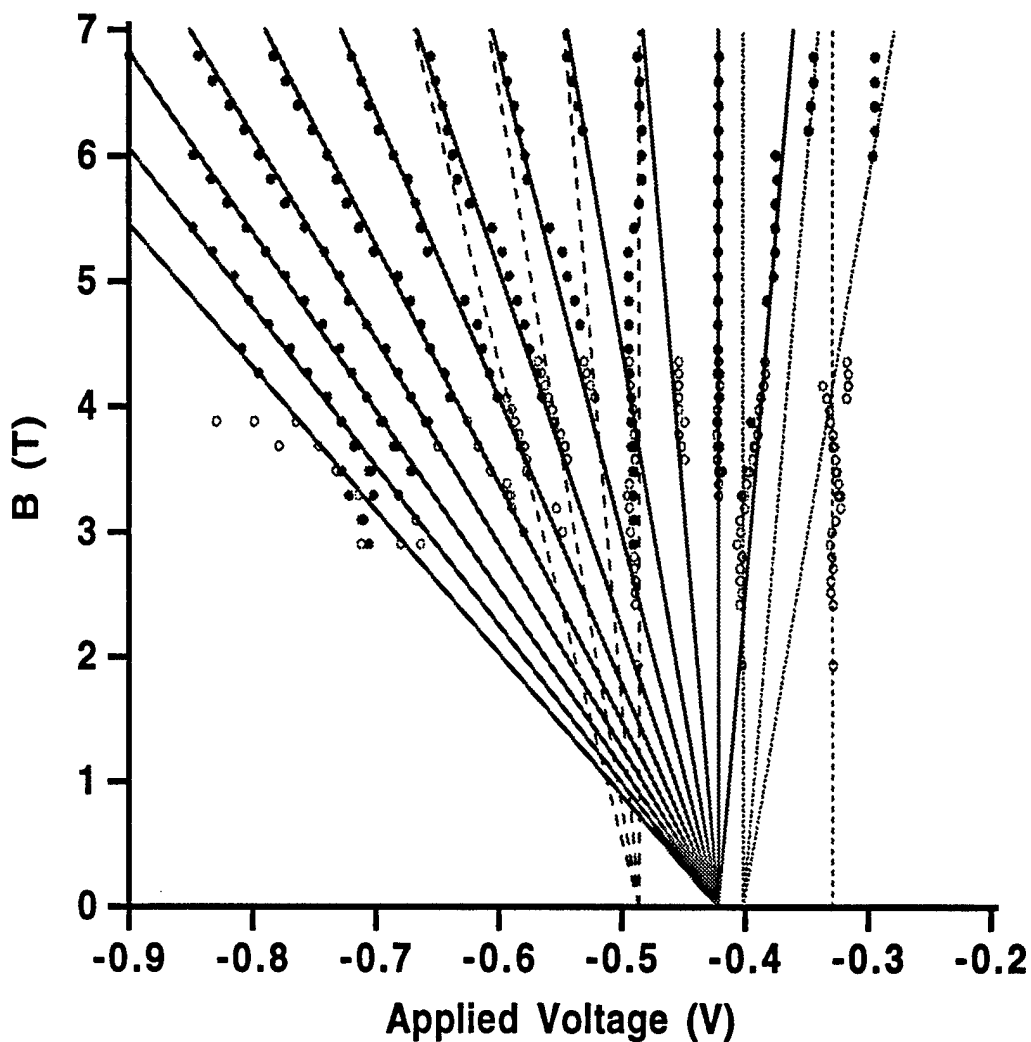


Figure 6.12: Fan diagram for sample 263 sample under reverse bias. Solid circles plot the minima of the second derivatives of the current-voltage data, and the open circles plot the minima of the first derivatives of the conductance-voltage data. Lines show best fit to features in phonon peak.

Other lines with finite slope correspond to emission of a phonon with an integral change in Landau level. By determining the best fit of the slopes of the lines, we can then determine an energy scale. Using this method, we have calculated that $\Delta V = (5.06 \pm 1.8) \Delta E_z$. The error bars are determined by adding the uncertainty from the slope, determined by the standard deviation, to the uncertainty in determining the location of the intercepts. Errors are added by using fractional uncertainties. Given this scale, we have the emission of three phonons; one with an energy (32.6 ± 1.4) meV corresponding to a GaAs-like TO-like energy, one with an energy of (36.5 ± 1.5) meV corresponding to a GaAs-like LO-like energy, and one with an energy of (49.2 ± 2.0) meV corresponding to an AlAs-like LO-like energy. The low energy feature has an energy of (18.2 ± 1.3) meV. The lines drawn in Fig. 6.12 are the fan fit for this energy scale. Solid lines show best fit to phonon mode with energy 36.5 meV. Dashed lines show best fit to phonon mode with energy 49.2 meV. Dotted lines show best fit to phonon mode with energy 32.6 meV. The other dotted line shows a low energy feature corresponding to about 18.2 meV. The fit is quite good.

It appears from this fan that the phonons with GaAs-like TO-like energies dominate at low magnetic fields, while the phonons with GaAs-like LO-like energies dominate at higher magnetic fields. The only exceptions are the minima that occur at low voltages above 6 T, where it appears that the TO-like modes again dominate. The transition between these modes appears to be rather abrupt, occurring in a range of less than 0.2 T. Such abrupt changes in the dominant processes in the fan diagram were reported for an (InGa)As/Al(InAs) DBS [CCP⁸⁹]. It also appears that the AlAs-like LO-like phonons fail to dominate at any place in the fan, but they appear to interact with electrons strongly

enough to "deflect" some of the fans from the GaAs-like LO-like mode.

We also plot the fan diagrams for samples **293** and **291** under reverse bias. Figure 6.13 plots the fan diagram for sample **293**. Again, closed circles are minima of second derivative of current-voltage data and open circles are minima of first derivative of conductance-voltage data, and lines are drawn corresponding to the best fit energy scale. Fans show at least two distinct modes in the phonon peak, with energies determined to be (34.6 ± 2.0) meV and (46.5 ± 2.5) meV. The low energy feature is also very prominent and has an energy of about (20.0 ± 1.5) meV. It is difficult to tell from this fan diagram whether, like sample **263**, there is a split between phonon with energy of the GaAs-like TO-like mode and the phonon with energy of the GaAs-like LO-like mode. It is possible that these energies are so close that the features blend together.

There are other significant features to note from this fan diagram of sample **293**. It is clear that the vertical line for the 46.5 meV phonon which corresponds to the AlAs-like LO-like interface phonon is significantly affected by the fans from the other phonon, since this vertical line contains substantial wiggles, especially where another fan crosses this feature. These wiggles are more apparent for sample **293** than they are for sample **263**. We also note that the vertical lines corresponding to the AlAs-like phonons in both the **263** and **293** samples have more wiggles than the vertical line corresponding to the AlAs-like phonon reported in the sample with pure AlAs barriers, sample **1863** [TWT93]. An additional interesting feature in the fan for the **293** sample is the possibility of two higher energy modes as indicated by the data from the lock-in amplifiers. These modes have energies of (70.6 ± 3.0) meV and (76.1 ± 3.0) meV, and could very well correspond to emission of two phonons.

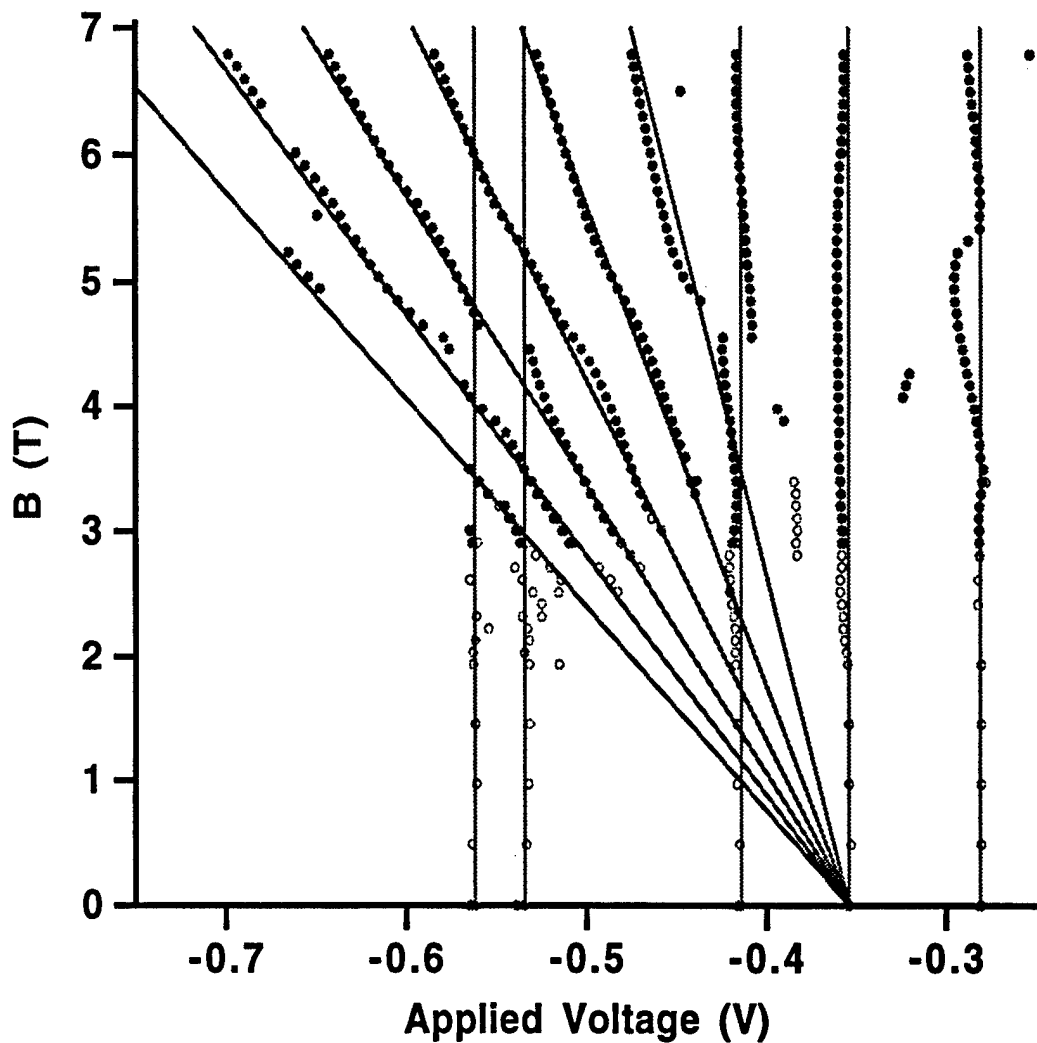


Figure 6.13: Fan diagram for sample 293 under reverse bias. Solid circles plot the minima of the second derivatives of the current-voltage data, and the open circles plot the minima of the first derivatives of the conductance-voltage data. Lines show best fit to features in phonon peak.

We also plot the fan diagram for the 291 sample in Fig. 6.14. Closed circles are minima of second derivative of current-voltage data and open circles are minima of first derivative of conductance-voltage data. Here, there is only one clearly distinct mode in the phonon peak as indicated by the one minimum in the phonon peak with $B = 0$. The energy of this phonon is calculated to be (31.9 ± 3.7) meV. The low energy feature is also quite prominent in this sample with an energy of (13.7 ± 2.0) meV. The difficulty in fitting slopes to the fan lines accounts for the large uncertainties as can be seen from the lines showing the best fit to minima at lower fields. The minima at high voltages seem to be deflected into still higher voltages for large magnetic fields. Our assumption of the linear relationship between the change in voltage corresponding to the change in z energy may not be appropriate for this sample.

There are several possible reasons for this deflection. One possibility is charge build-up in the well which tends to deflect peaks to higher voltages, especially at higher magnetic fields [TT91a, Tur94]. This seems unlikely since this sample is biased so that the electrons tunnel through the thicker barrier first, and preliminary calculations based on a simultaneous solution of Schroedinger's equation and Poisson's equation indicate no such significant effect [Wal]. However, the large amounts of current, which are probably due to the onset of the first excited state, in these voltage regions could play a role in altering the potential profile of the structure [Tur94]. Another possible reason for this deflection is the possibility of a high resistance in series with the DBS such that the voltage difference across the sample includes the voltage drop across this resistance. This resistance would include the contact resistance and possibly any resistance due to the barrier which separates the 3D gas in the heavily doped contact from the 2D gas in the accumulation layer. To get a feel for such an

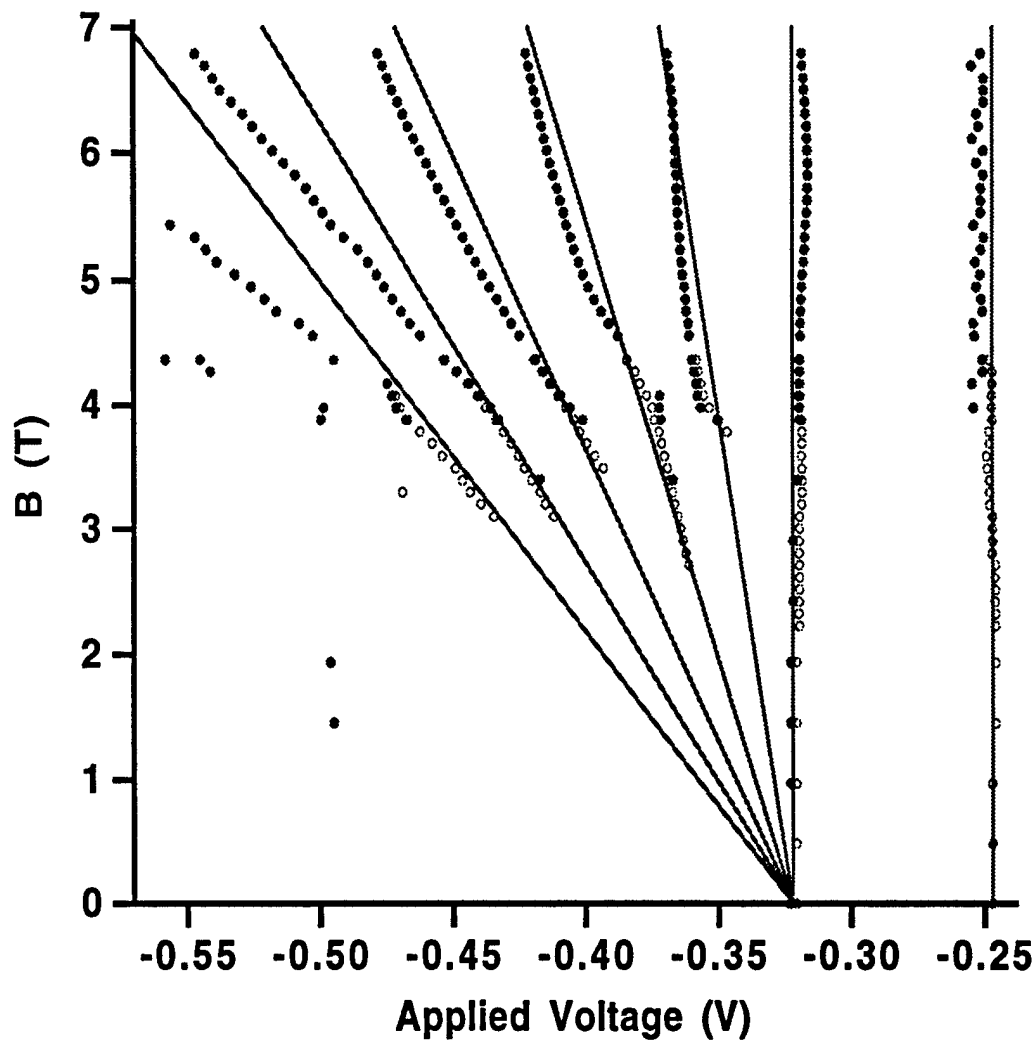


Figure 6.14: Fan diagram for sample 291 under reverse bias. Solid circles plot the minima of the second derivatives of the current-voltage data, and the open circles plot the minima of the first derivatives of the conductance-voltage data. Lines show best fit to features in phonon peak.

effect, note that for an applied voltage of about 0.32 V, we have about $70 \mu\text{A}$ of current. With a series resistance of 100Ω , this would give an extra voltage drop of only 0.007 V. However, at an applied voltage of about 0.54 V, the current is about $300 \mu\text{A}$, which would give an extra voltage drop of about 0.03 V. The resistance of 100Ω assumed here seems rather high since the contact resistances of this sample were measured at less than 10Ω each at room temperature. One last possible reason for this deflection could be that these barriers are thin enough and the concentration of Al low enough to allow possible propagating modes through the structure [KBJ⁺92, JKB⁺94, FR94, KBJ⁺95]. These propagating modes would have significantly different properties and produce a significantly different current-voltage profile. Phonon emission by propagating modes is an interesting subject that warrants further study.

Finally, for completeness, we show in Fig. 6.15 the fans for all the rest of the asymmetric barrier samples. As in previous fan diagrams, we plot the minima of the second derivative of the current-voltage characteristics as solid dots, and the minima of the first derivative of the conductance-voltage characteristics as open dots. From these fans and those of samples **263**, **293**, and **291**, we note a few general characteristics. Firstly, there is clear evidence of emission of an AlAs-like LO-like phonon in samples **264**, **263**, **262**, **292**, **293**, and **278**, or in samples with aluminum concentration $x \geq 0.3$. It appears that in samples **279** ($x = 0.2$) and **291** ($x = 0.225$) there are emission of phonons with only one energy. It is unclear whether there is emission of phonons with one or two energies in sample **280**. Secondly, in samples **264**, **263**, **262**, and **292**, or in samples with aluminum concentration $x \geq 0.5$, there is a clear separation of the minima due to emission of the modes with GaAs-like LO-like energies and emission of the modes with GaAs-like TO-like energies. Different fans converge

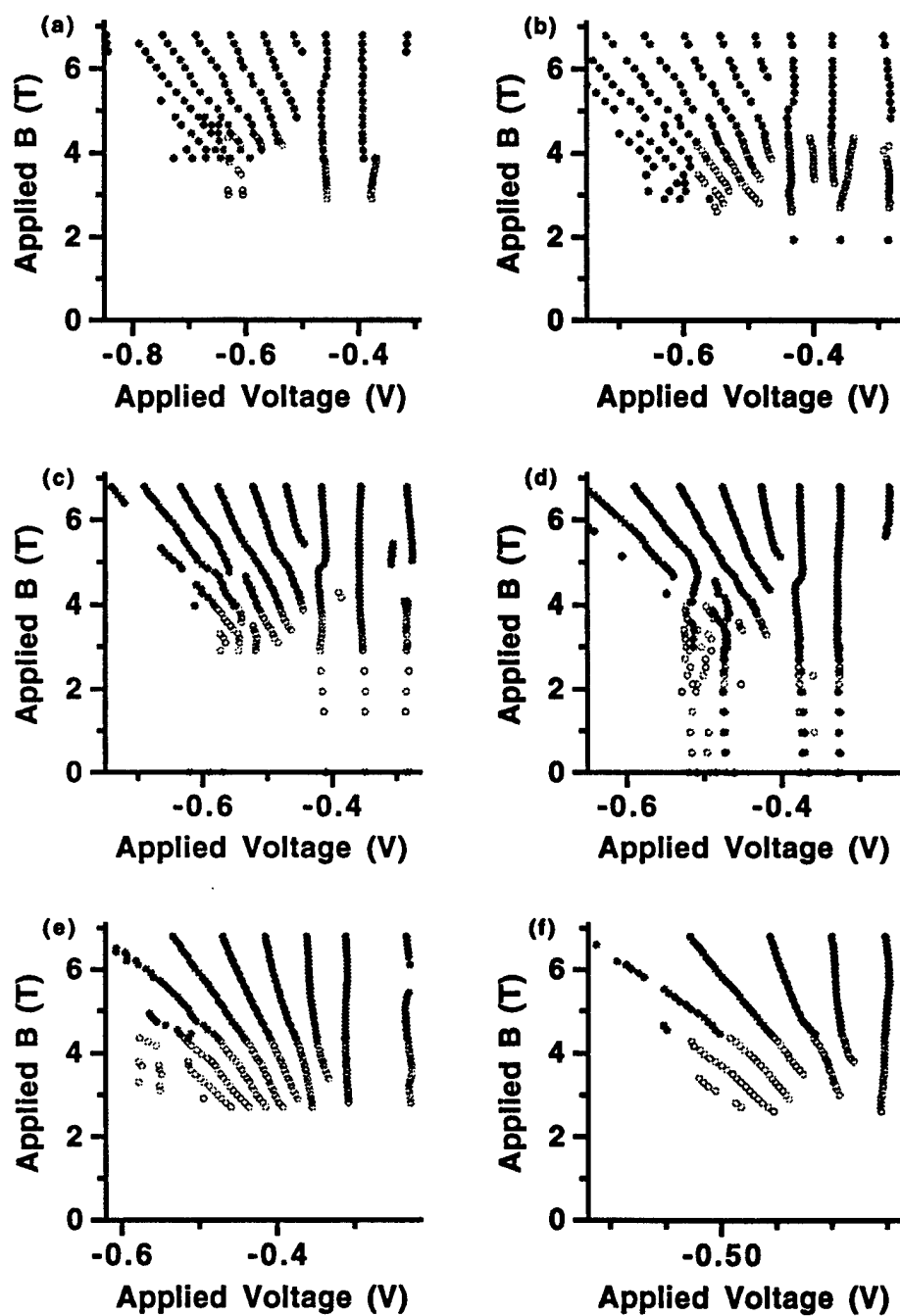


Figure 6.15: (a) Fan diagram for sample 264, $x = 0.8$. (b) Fan diagram for sample 262, $x = 0.6$. (c) Fan diagram for sample 292, $x = 0.5$. (d) Fan diagram for sample 278, $x = 0.3$. (e) Fan diagram for sample 280, $x = 0.25$. (f) Fan diagram for sample 279, $x = 0.2$.

to each of these energies, and these are especially apparent in samples **263**, **262**, and **292**. Thirdly, there is clear evidence that sample **278** ($x = 0.3$) exhibits evidence of emission of two higher energy phonons at two different voltages like sample **293**. We measure these energies to be (58.7 ± 2.9) meV and (67.9 ± 3.6) meV. Lastly, we note that the low energy is prominent in samples **263**, **262**, **292**, **293**, **280**, and **291**. However, they are not very prominent in samples **264**, **278**, and **279**. More will be said on this subject in Section 6.2.5.

6.2.4 Energy Dependence of Modes on Alloy Concentration

Using the methods described in the last section, we can determine from the fan diagrams the energies of the emitted phonons in all the asymmetric *barrier* samples. Figure 6.16 illustrates the energies of emitted phonons obtained in such a manner versus the alloy concentration in the barriers. The energies of the emitted phonons in the asymmetric *barrier* sample with $x = 1.0$ has been included for completeness. The solid squares indicate the highest energy phonons corresponding to the AlAs-like LO-like phonons. The solid triangles indicate energies corresponding to GaAs-like LO-like phonons, and the solid circles indicate the energies of the phonons corresponding to the emission of the GaAs-like TO-like phonons. The solid lines are from Fig. 2.6 showing a straight line fit to the Raman data of bulk AlGaAs phonons [MS87]. The extra modes at $x = 0.3$ is discussed later in this section.

There are a few things to note from this energy diagram. First of all, the energies of the phonons in samples **1863** ($x = 1.0$), **263** ($x = 0.7$), **262** ($x = 0.6$), **292** ($x = 0.5$), **293** ($x = 0.4$), **291** ($x = 0.225$), and **279** ($x = 0.2$) are all within experimental error of the energies of the corresponding bulk $\text{Al}_x\text{Ga}_{1-x}\text{As}$

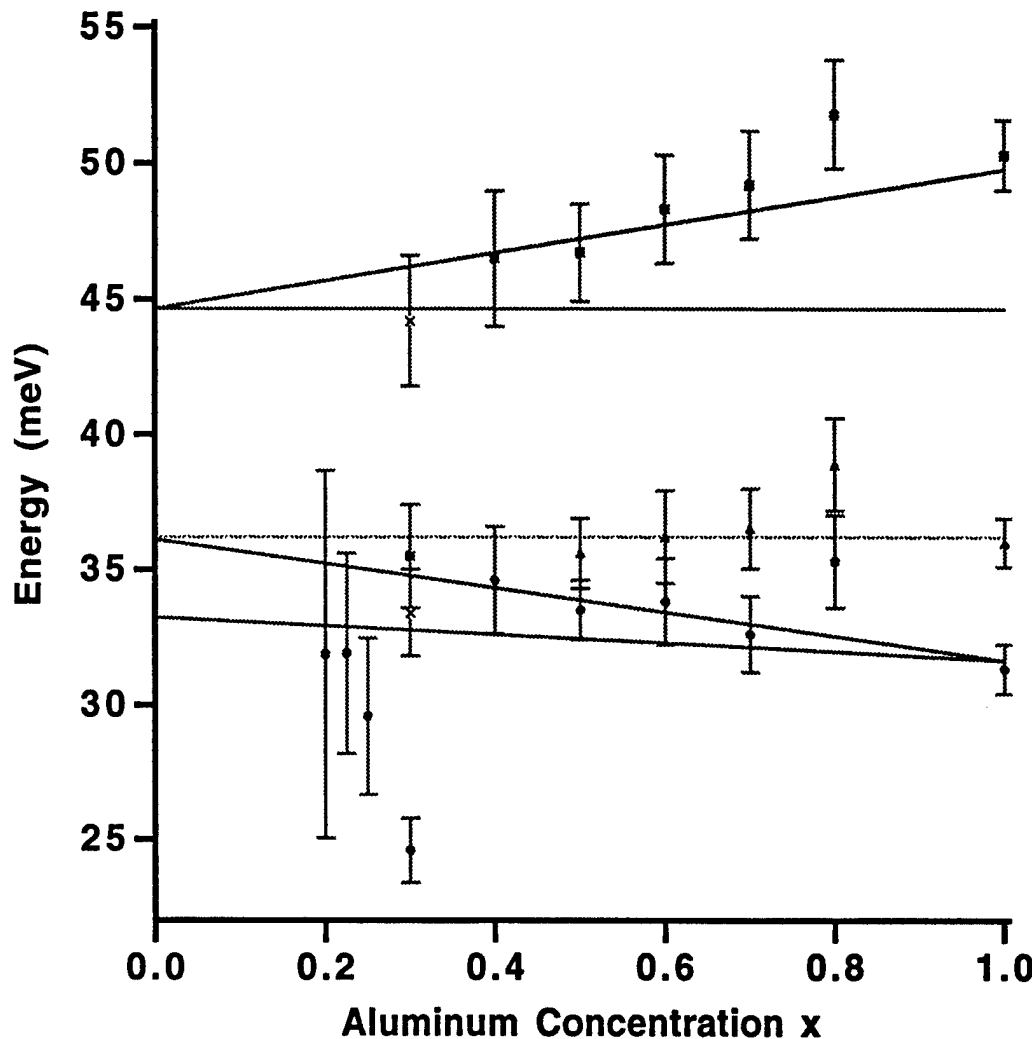


Figure 6.16: Energy dependence of modes with error bars on alloy concentration as determined by the fan diagrams. AlAs-like LO-like modes given by solid squares; confined modes in well given by triangles; GaAs-like TO-like interface phonons given by circles. Solid lines indicate fit to Raman data of bulk modes given in Fig. 2.6 [MS87]. Extra modes at $x = 0.3$ shown as x are energies of modes if resonant peak of sample 278 were located at -0.18 V.

phonons. The energies of the phonons for sample **264** ($x = 0.8$) are all consistently higher than what would be expected from bulk $\text{Al}_{0.8}\text{Ga}_{0.2}\text{As}$, and the energies of the phonons for samples **278** ($x = 0.3$) and **280** ($x = 0.25$) are both consistently lower than what would be expected from the corresponding bulk $\text{Al}_x\text{Ga}_{1-x}\text{As}$ energies. For sample **264** ($x = 0.8$), one possible explanation is that there is an additional structure within the heavily doped contact region consisting of various layers of undoped $\text{Al}_x\text{Ga}_{1-x}\text{As}$ with various concentrations of Al. This structure, which is a result of the RHEED calibrations, has a much larger thickness for sample **264** than for other samples, due to the difficulty in obtaining the necessary high Al concentration. This structure would be a complicated superlattice structure with possible quantized levels and could cause a small series nonlinear characteristic within the contact resistance not evident in the measurements determining the contact resistance.

For the samples with consistently low readings, there exist a few possible explanations. One could include the possibility of a large contact resistance or a nonlinear characteristic in series with the double barrier structure. Such a characteristic or resistance could result from problems with overall doping, or result from a large undoped layer between heavily doped layers, such as what could occur during RHEED calibrations. Since the peak current under reverse bias of the resonant peak in sample **278** ($x = 0.3$) is more than 20 times the peak current in the phonon peak, a large series resistance could have a significant effect in making the resonance peak at a higher voltage while having only a little or an insignificant effect on the positions of the phonon peaks themselves. A large series nonlinear characteristic may even cause the resonant peak appear to be intrinsically bistable, especially if the PVCR is large. This effective series resistance could cause the difference in

voltage between the resonant peak and the phonon features to be significantly less than if the series resistance did not exist, thereby causing the phonon energies measured to be less than they actually are. For example, we measure the resonant peak for sample **278** to occur at -0.218 V. In the fan diagram for sample **278** in Fig. 6.15, there is evidence for the emission of two phonons. If we assume that the feature at -0.473 V corresponds to the emission of two GaAs-like TO-like phonons, and that the feature at -0.513 V corresponds to the emission of a GaAs-like TO-like and an AlAs-like LO-like phonon, then the resonant peak must occur at approximately -0.18 V in order for all the energies to be consistent. The energies would therefore become (33.4 ± 1.6) meV, (44.2 ± 2.4) meV, (67.5 ± 3.1) meV, and (76.7 ± 3.8) meV, which are more consistent with the energies of the bulk phonon modes. The two lower energies are plotted as crosses in Fig. 6.16. Also, the low energy feature would have an energy of (18.7 ± 1.0) meV.

Another possibility for consistently low phonon energies is charge buildup in the well. Samples **279** and **280** are intrinsically bistable under reverse bias, but charge buildup in the well does seem to be somewhat unlikely, since under reverse bias, the electrons are tunneling through the thicker layer first, minimizing the likelihood that there would be charge buildup in the well. We also did some simulations involving simultaneous solution of Schrödinger's and Poisson's equations, and there were no indications of charge build-up in the well [Wal]. One last possibility, especially for sample **278**, is the chance that these are the actual energies of the phonons. This possibility would indicate that there is no evidence for the AlAs-like phonons in sample **278**, and the phonons measured at 35.5 meV corresponds to emission of GaAs-like LO-like or TO-like phonons.

6.2.5 Dependence of Relative Coupling Constants of AlAs-like Phonons

In this section, we present a fitting routine to determine the relative strengths of the AlAs-like phonons compared to the GaAs-like phonons in the experimental phonon peak. We make several assumptions. Firstly, the current in the phonon peak is due entirely to the emission of phonons with one of only two distinct energies. This is reasonable for many of the samples because theoretical calculations show that most of the current for some samples is due to phonons with only two energies [TT, Wal]. However, as we have seen in the fan diagrams for many of the samples, the phonons emitted may have more than two energies. As for now, we wish to keep the fitting routine as simple as possible. Secondly, we assume that the tail of the resonant peak is Gaussian. Again, this is reasonable because we have found that the turn-on of the resonant peak fits a Gaussian rather well [Wal].

The boldest assumption involves the form of the phonons. We assume that the current due to each phonon can be modeled effectively by the following form:

$$i_{ph} = c(0) \left(1 - \frac{1}{1 + \exp \left(\frac{v - c(1)}{c(2)} \right)} \right) \left(\frac{\exp(vc(3)) - 1}{c(4)^2 + (v - c(5))^2} \right) \quad (6.1)$$

where i is the current due to a phonon mode, v is the applied voltage across the sample, and $c(n)$ are constants to be determined by a least squares fit. We chose this form because it fits the theoretical calculations rather well. We also expect that the turn-on for the phonons to resemble a Fermi function, since phonons begin to be emitted when the Fermi energy in the emitter is one phonon energy above the bottom of the energy in the well. We also assume Lorentzian broad-

ening of the phonon peak [TWT93, Tur94]. Lorentzian broadening also fit the best to the theoretical calculations. Finally, the theoretical calculations show that the phonons have a tail at higher voltages [TWT93, TT94]. We model this by multiplying by an exponential with a turn-on at rather high voltages.

To fit the data to this form, we choose a range of voltages where it is reasonably expected that most of the current in the phonon peak measured in the experiment consists of the tail from the main resonant peak and contributions from the emission of the phonons themselves. In order to choose reasonable initial values for the $c(n)$, we use information from both experimental data and calculated curves. We expect the current due to each phonon to peak at approximately the voltages where the minima in the second derivative occur in the experimental data. These voltages give the initial values for each $c(5)$. In addition, since we expect that the abrupt turn on in the current due to the GaAs-like phonons to occur at approximately the voltage where we observe the low energy feature, we use that voltage for $c(1)$ for the GaAs-like phonons in the fit. To find the corresponding voltage for $c(1)$ for the AlAs-like phonons, we note that the difference between $c(1)$ and $c(5)$ for the AlAs-like phonons should be approximately the same as the difference between $c(1)$ and $c(5)$ for the GaAs-like phonons. We also note that $c(2)$ should have a value on the order of $k_b T$, where k_b is the Boltzmann constant. We choose $c(4)$ so that the PAT current peaks in our fit have approximately the same widths as the PAT current peaks in the theoretical calculations. We also choose $c(3)$ so that the tail of the PAT currents at higher voltages also approximate the theoretical calculations. Finally, we choose values for $c(0)$ so that the sum of the PAT currents is approximately the total current in the experimental data and the ratio of the current peaks are approximately the same as the ratio of the cur-

rent peaks in the theoretical calculations. After choosing all constants, we then allow the fit to relax.

Figure 6.17(a) illustrates this fit, which we refer to as the phonon fit, for sample 263 for the range of applied voltages between 0.28 V and 0.8 V. The solid curve indicates the actual current-voltage data for the sample. The gray line indicates the Gaussian tail of the main resonant peak; the dotted lines indicate the currents of the phonons found from the fit to the experimental curve; and the dashed line indicates the sum of the two phonon peaks plus the Gaussian tail. The fit is too close to be distinguished from the experimental curve on this scale. The value for the reduced χ^2 is 0.003. As we can see the fit is remarkably good considering this is an empirical formula. The peak current density for the sum of the GaAs-like modes is 0.048 A/cm^2 and occurs at a voltage of -0.419 V. The peak current density for the sum of the AlAs-like modes is 0.028 A/cm^2 and occurs at a voltage of -0.488 V. The voltages of these peaks compare well with the voltages of the minima of the second derivatives in this sample, which occur at -0.405 V and -0.485 V. We can easily find the ratio of the current of the sum of the AlAs-like phonons and the sum of the GaAs-like phonons, which we will refer as the phonon ratio, and we find the phonon ratio of this sample to be 0.58:1.

To easily compare the experimental characteristics with the theory, we plot the theoretical calculation of the total currents due to the phonon modes in Fig. 6.17(b). The theoretical currents due to the GaAs-like and AlAs-like modes are also plotted in Fig. 2.9(b). Here, we have added the five highest phonons with GaAs LO- and TO-like energies and plotted the sum and have also added the three highest phonons with AlAs LO- and TO-like energies and plotted the sum. We have also plotted the total current due to these modes which can be

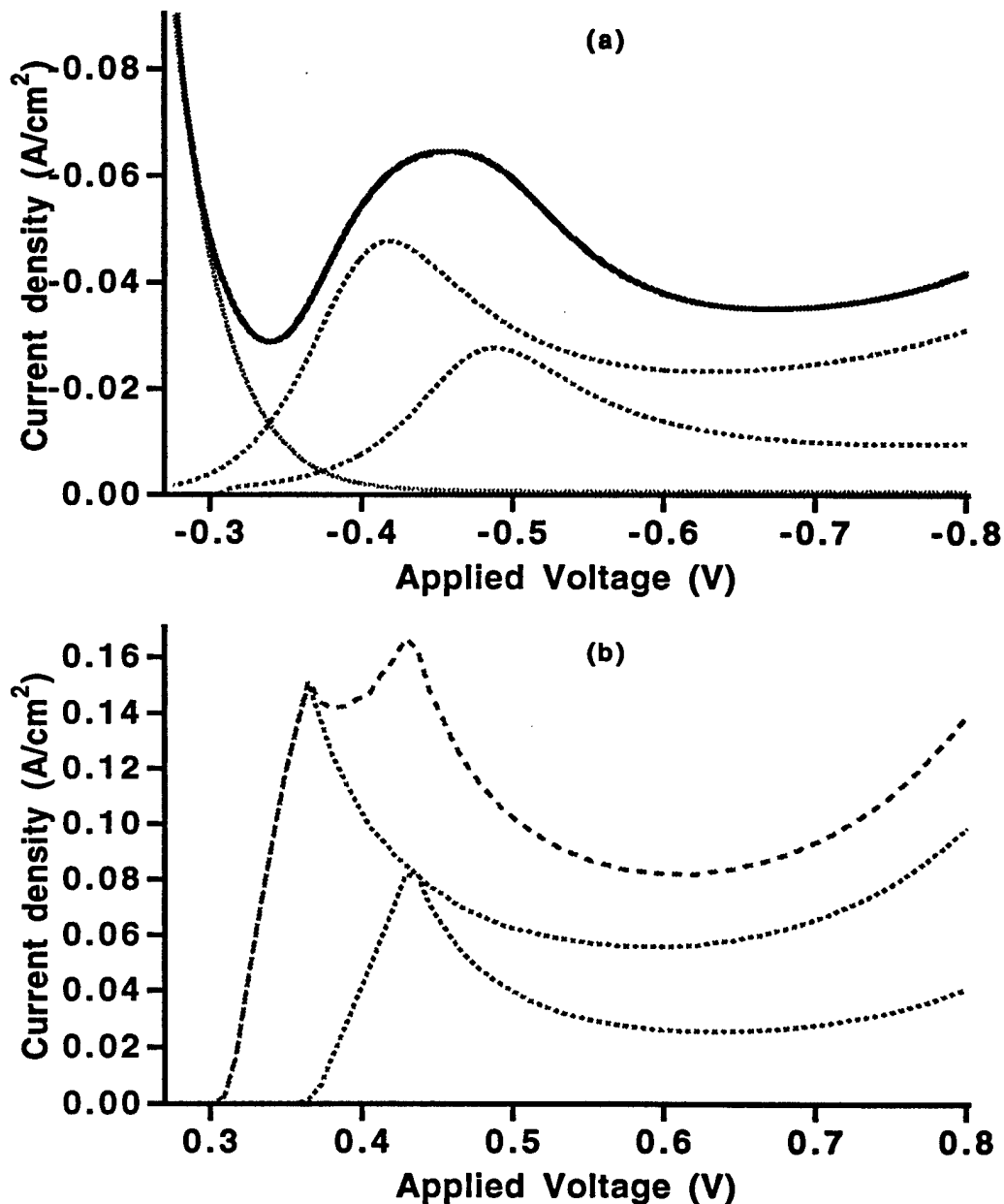


Figure 6.17: (a) Phonon Fit to experimental curve of sample 263. Gray line is Gaussian tail to model resonant peak. Dotted lines are current densities due to GaAs-like phonons and AlAs-like phonons. Dashed curve is sum of current densities from phonons. Solid line is experimental data. (b) Theoretical calculation of current densities due to phonons of sample 263. Broadening and charge build-up in the well are not included. Dotted lines are current densities due to GaAs-like phonons and AlAs-like phonons. Dashed curve is sum of current densities of these phonons.

compared to the experimental data in Fig. 6.17(a). The peak current density for the sum of the GaAs-like modes is 0.150 A/cm^2 and occurs at a voltage of 0.365 V. The peak current density for the sum of the AlAs-like modes is 0.815 A/m^2 and occurs at a voltage of 0.429 V. The phonon ratio is calculated to be 0.54:1. The calculated voltages of the peak are rather low, but this is probably due to our incomplete knowledge of the exact doping profile of the spacer layers. This doping is only expected to be within 20 % of the nominal value. The calculated currents are much higher than the experimental curves. We found that the theoretically calculated currents are consistently high for all the samples. This may be due to the uncertainty of the barrier widths. The barriers may be larger by a few monolayers each, but the only way to be sure is to image the samples using TEM. The phonon ratios for this sample, however, are in rather good agreement, considering that we fit the curves to an empirical formula. Discrepancies are due to the fact that the phonon currents probably are not given exactly by this form and the fact that we completely ignored other possible scattering mechanisms.

We can repeat the phonon fit for all other samples and calculate the corresponding phonon ratio. We can then plot the phonon ratio as a function of the aluminum concentration, and this plot is shown in Fig. 6.18. We did the phonon fits for all samples except for samples 279 ($x = 0.2$) and 291 ($x = 0.225$). The phonon ratios for these samples are set to zero since there is little evidence for emission of phonons with two energies in either of these samples. Although this plot is not very accurate, it does show a general decline in the importance of the AlAs-like phonons compared to the GaAs-like phonons as the aluminum concentration is decreased in the barriers. This decline is expected from theoretical calculations which is clearly shown in Fig.

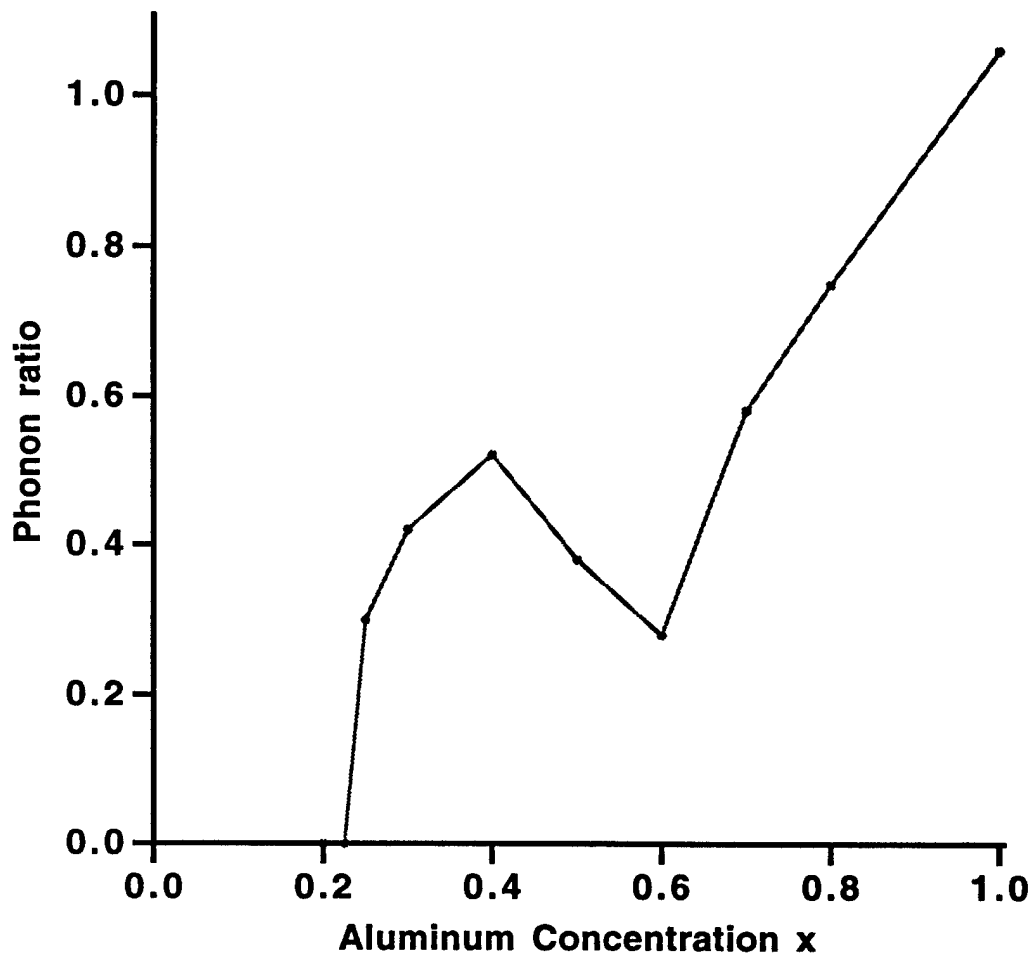


Figure 6.18: Phonon ratios of asymmetric barrier samples under reverse bias versus the aluminum concentration x . Phonon ratios for samples 279 ($x = 0.2$) and 291 ($x = 0.225$) are set to zero.

MBE #	(x)	energy (meV)
264	0.8	
263	0.7	18.2 ± 1.3
262	0.6	19.0 ± 1.3
292	0.5	19.8 ± 1.0
293	0.4	20.0 ± 1.0
278	0.3	9.9 ± 0.5
280	0.25	11.9 ± 1.5
291	0.225	13.7 ± 2.0
279	0.2	

Table 6.1: Energies corresponding to low energy features of asymmetric *barrier* samples.

2.11. It is interesting to note from Fig. 6.18 that the phonon ratios for samples **262** ($x = 0.6$) and **292** ($x = 0.5$) seem abnormally low compared with the phonon ratios for the other samples. In sample **262**, this is not surprising since the experimental current-voltage characteristic seems to contain an additional smooth background current which was added into the phonon fit. It is uncertain why the phonon ratio found for sample **292** is so much lower than the rest of the samples.

6.2.6 Low Energy Feature

As discussed in previous sections, we observe a minimum in the second derivative of the current versus the applied voltage corresponding to low energies for many of the asymmetric barrier samples. Table 6.1 gives the values for these energies for each of the asymmetric *barrier* samples. These features occur in the NDR region of the resonant tunneling peak for voltages just below the minimum in the current. We note that for samples **264** ($x = 0.8$) and **279** ($x = 0.2$) there isn't much evidence for this feature in the fans. This low energy feature suggests either the possibility of a scattering mechanism with

an energy of about 10 to 20 meV, or it may be an indication of the sudden turn on in current of the phonon-assisted tunneling process. In this case, this feature would give a measurement of the Fermi energy in the emitter state. These Fermi energies would range from 13.7 meV to 14.7 meV in samples **263** ($x = 0.7$), **262** ($x = 0.6$), **292** ($x = 0.5$), **293** ($x = 0.4$), and **278** ($x = 0.3$). The Fermi energies would be much higher for samples **280** ($x = 0.25$) giving an energy of 17.7 meV and sample **291** ($x = 0.225$) giving an energy of 18.2 meV. However, because it appears that the relationship between ΔE_z and ΔV is nonlinear for samples **280** and **291**, it is highly unlikely that these energies would be correct. We will explore this low energy feature in this section by considering temperature dependent data and oscillations in the current as a function of magnetic field. We will focus our attention on sample **293** since the low energy feature in this sample is very prominent, and has a typical energy of about 20 meV above resonance.

We begin by looking at temperature dependent data. Figure 6.19(a) plots the current versus the applied voltage for sample **293** near the low energy feature for four different temperatures. These curves illustrate that the maximum current in the phonon peak changes slightly as we increase the temperature from 4 K to 40 K. However, the increase in the valley current between the resonant and phonon peaks is more dramatic. This should be expected because of the thermal broadening of the Fermi energy. Figure 6.19(b) plots the second derivative of the current versus the applied voltage, and we can see that the increase in temperature significantly reduces the prominence of the low energy feature, becoming just an inflection at 30 K. The increase in temperature, however, does not significantly reduce the curvature of the two features in the phonon peak. The large dependence of the low energy feature on tempera-

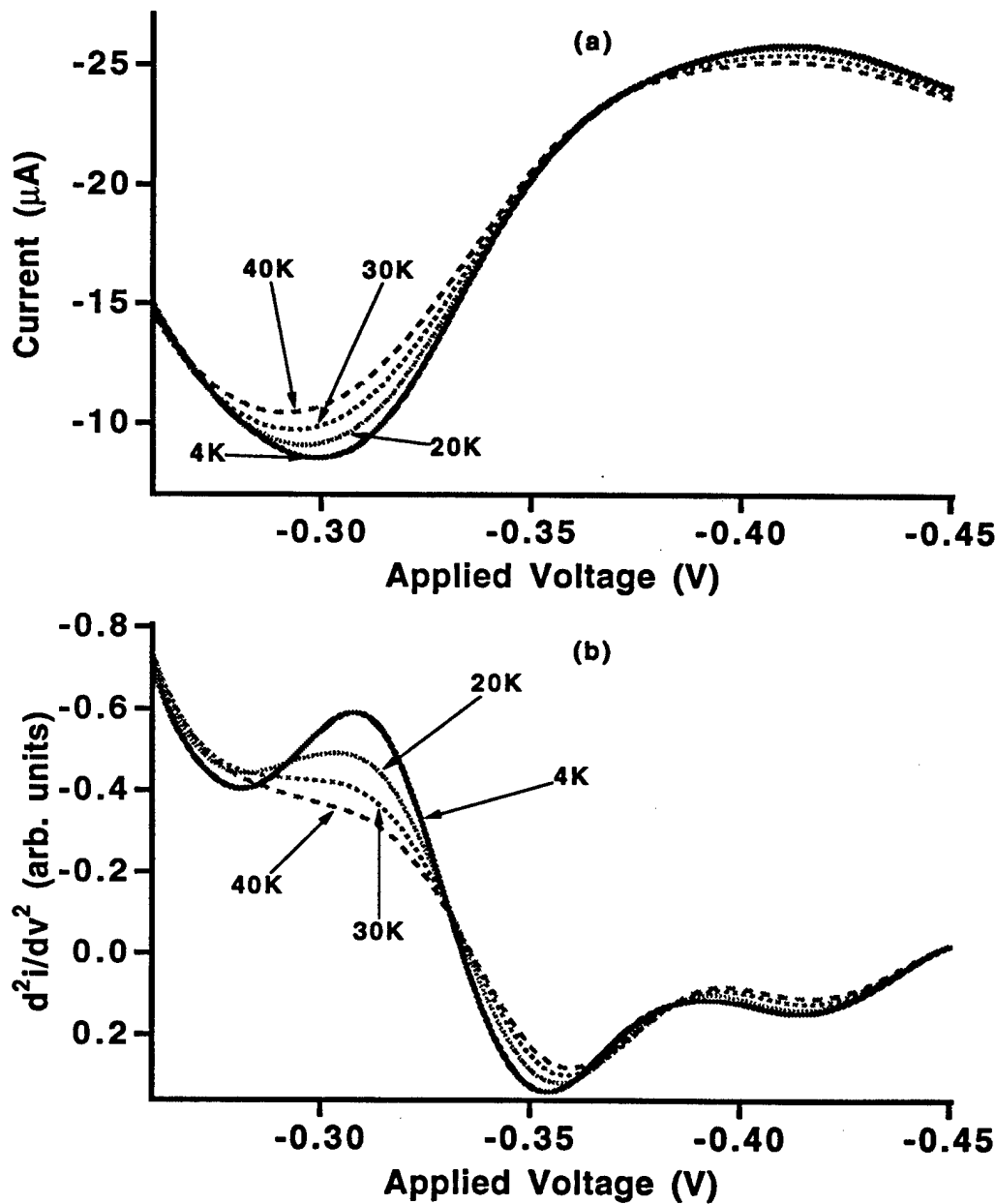


Figure 6.19: (a) Current versus applied voltage for sample 293 near low energy feature and phonon peak for temperatures 4 K, 20 K, 30 K and 40 K. (b) Second derivative of current versus applied voltage for temperatures 4 K, 20 K, 30 K, and 40 K. Curves focus on minima corresponding to phonons and minimum corresponding to low energy feature.

ture suggests that it may be an indication of the Fermi turn on of the phonon currents.

There is an independent way to measure the Fermi energy in the emitter. If we keep the applied voltage constant and vary the magnetic field, the current will oscillate with some definite period $\Delta(1/B)$ proportional to $1/B$. These oscillations are a result of the modulation of charge when the Landau levels pass through the Fermi level [ELH⁺89, LAE⁺89]. The Fermi energy E_f for a degenerate 2D electron gas can be found by noting that

$$E_f = \frac{\hbar e B_f}{m^*}, \quad (6.2)$$

where B_f is defined by the frequency in oscillations in $1/B$ and m^* is the effective mass. We can also determine the density n of the 2D electron gas by its relationship to the Fermi energy

$$E_f = \frac{\hbar^2 \pi n}{m^*}. \quad (6.3)$$

Figure 6.20 illustrates a typical plot of the current oscillations as a function of the applied magnetic field. This trace was taken with an applied voltage of -0.281 V where the low energy feature occurs. Current-field plots at other applied voltages are similar. We use a cubic spline interpolation [PFTV86] to obtain current points evenly spaced in $1/B$. We then take a standard numerical Fast Fourier Transform to obtain the frequency distribution of the current in B , and this distribution is plotted in Fig. 6.20(b). The maximum amplitude occurs at a frequency $B_f = 4.2$ T. From Eq. 6.2 this magnetic field gives a Fermi energy in the accumulation layer of about 7.3 meV, which is about half of the difference between the low energy feature and the feature corresponding

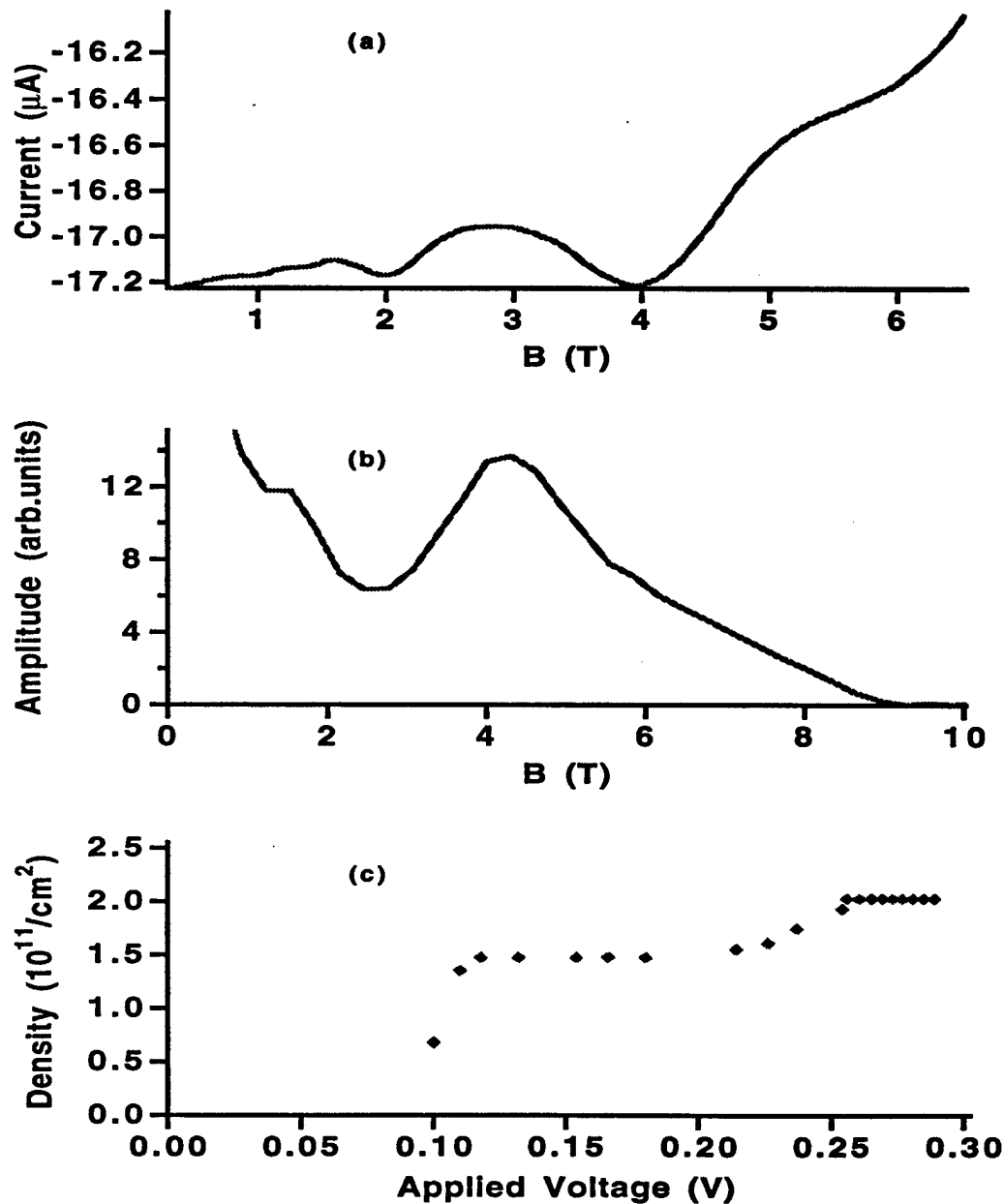


Figure 6.20: (a) Typical current oscillation versus applied magnetic field. Trace is taken at an applied voltage of -0.281 V where the low energy feature occurs. (b) Amplitude of frequency distribution versus frequency of oscillations found by taking Fast Fourier Transform of current trace in $1/B$. Maximum amplitude occurs at 4.2 T. (c) Measured electronic density of accumulation layer versus applied voltage.

to the GaAs-like TO-like mode, which is about 14.6 meV. It is unclear yet as to why there is this discrepancy.

Having obtained the Fermi energy, we use Eq. 6.3 to obtain an electronic density of about $2 \times 10^{11} \text{ cm}^{-2}$ at the voltage where the low energy feature occurs. By taking similar current traces at different applied voltages, we can find the density in the accumulation layer as a function of the applied voltage, and we plot this in Fig. 6.20(c). The density is fairly low before the onset of the resonant peak. During onset, the density quickly rises and reaches a plateau value of about $1.48 \times 10^{11} \text{ cm}^{-2}$ throughout the rise in current in the resonant peak. This value is on the same order of accumulation layer densities found by others [ELH⁺89, LAE⁺89, GMC94]. We do not observe an additional peak in the frequency distribution that would correspond to the density of charge in the well as other researchers have seen [LAE⁺89]. However, they used magneto-oscillations in the differential capacitance which they claim to be more sensitive. Above the resonant peak, the accumulation layer electronic density begins to rise again to another plateau level of $2 \times 10^{11} \text{ cm}^{-2}$. This plateau begins at an applied voltage of about -0.255 V. This suggests that during the rise of the resonant peak, there is a small charge build-up in the well, and as the voltage rises above the resonant peak, the current in the well begins to slowly fall as less charge tunnels into the well.

Other possible explanations for the low energy feature include an additional scattering mechanism. One possibility could be an additional phonon, perhaps a disorder activated longitudinal optical phonon seen in Raman data of bulk $\text{Al}_x\text{Ga}_{1-x}\text{As}$, which has an energy of about 20 meV [JS81, Bon81]. This scattering seems unlikely since, in the Raman data, these peaks are very small, and much larger peaks occur from the longitudinal acoustical (LA) phonons

which have a cutoff frequency of about 25 meV, and the transverse acoustical (TA) phonons which have an energy of about 11 meV at the edge of the Brillouin Zone. However, we see no evidence whatsoever for the emission of these phonons [Sir]. Another possible explanation involving phonons is second order processes [Sir, Str], involving emission of a phonon of one energy and the absorption of another phonon of another energy. This is very unlikely, since these measurements are done at 4 K, and there would be very few optical phonons for the electrons to absorb. This scattering process would be weaker at lower temperatures, and as we have seen above, the feature becomes more prominent at lower temperatures.

One last possibility is the scattering due to plasmons, but this is extremely unlikely in this sample, especially under reverse bias. Zhang et. al. [ZLM⁺94] have seen a peak in the NDR region which they have attributed to scattering by plasmons. This peak, however, was seen with samples that were intrinsically bistable because of large amount of charge in the well. They were able to see the peak because the biasing circuit they used resulted in an effective negative resistance [MLSE94]. This allowed them to probe the NDR region normally hidden in more common biasing circuits. In addition, this peak corresponded to only a few meV. Since the plasmon energy of a 2D gas is directly related to its density, the electronic densities in our sample would have to be much larger than the densities they assumed, which was $2 \times 10^{11} \text{ cm}^{-2}$ [ZLM⁺94].

Chapter 7

Conclusions

In this thesis, we have presented a systematic experimental study of localized phonon interactions with electrons in $\text{GaAs}/\text{Al}_x\text{Ga}_{1-x}\text{As}$ DBS samples as a function of the alloy concentration in the barrier. Specifically, we have measured the energies of the localized phonons using magnetotunneling data, and presented results of a fitting routine to experimentally measure the relative contributions to the PAT current assuming contributions from phonons with two separate energies. We have found that phonons with at least three different energies, corresponding to GaAs-like LO-like, AlAs-like LO-like and GaAs-like TO-like modes, contribute to the current for samples with $x \geq 0.5$ and phonons with at least two separate energies contribute to the current for samples with $x \leq 0.4$. We did no measurements of samples with $0.4 < x < 0.5$, and a study of such samples in the future would be useful. In addition, both the fan diagrams and phonon fitting routines suggest that with decreasing alloy concentration in the barriers, the contribution from the AlAs-like phonons decreases while the contribution from the GaAs-like TO-like phonons increases. These observations compare well qualitatively with theoretical calculations which use the modified

dielectric continuum model to estimate the localized phonon potentials.

In order to make detailed quantitative comparisons between theory and experiment, these experimental samples need to be characterized using TEM images. The current densities of the theoretical PAT currents are considerably higher than the experimentally measured PAT currents, and this suggests that the actual barrier widths are larger by at least a few monolayers than the nominal values given. The theoretically calculated voltages of the phonon peaks are also somewhat different from the experimental values, which is probably due to variations in doping profile.

Theoretical calculations should also be modified to make detailed quantitative comparisons with our experimental results. Taking into account broadening of the electronic states is very important, and has been done for GaAs/AlAs DBS samples [TWT93, Tur94]. In addition, taking into account possible screening of phonons in the emitter could also improve the fit. Other sources which may contribute to the valley current should also be included. These mechanisms include Γ to X conversion in the barriers [MCW86, Liu87, MFE⁺91, SR95], second order processes such as magnetopolarons [BLSR⁺90, CYYW91] and multiphonon processes which were observed in samples **293** and **278** and in other works [BLSR⁺90], onset of the first excited state, and elastic scattering mechanisms such as interface roughness. Propagating phonon modes may also contribute to the current in samples **279**, **280**, and **291**. Such propagating modes have been seen in superlattices in Raman scattering experiments [KBJ⁺92, JKB⁺94], and theoretical calculations suggest that propagating modes may be a possible scattering mechanism in our experimental samples with low Al concentrations [FR94]. Theoretical calculations of PAT current including these propagating modes may help to explain some of the

data seen in these samples.

Knowing the relative contributions from the different phonon modes would help to experimentally determine the corresponding electron-phonon coupling coefficients, and the role of screening of the modes in the emitter state. The results from our fitting routine suggests that these relative contributions can be experimentally determined. Some phonon modes have large potentials in the emitter, and the electron gas in the accumulation layer may screen these potentials. Thus, some modes may not contribute to the current as much as the theoretical calculations may imply. More extensive studies of this and other fitting routines on our experimental samples need to be done to better determine the relative contributions from the GaAs-like and AlAs-like phonons.

The notch samples also provide an opportunity to experimentally determine the role of screening. These samples are also interesting because the small $\text{Al}_x\text{Ga}_{1-x}\text{As}$ layer in the notch sample reduces the current in the valley due to Γ to X conversion in the barriers [CH90]. These types of samples may thus prove useful in applications, especially those requiring a large PVCR. However, as the preliminary results from our samples have suggested, the addition of the notch may significantly affect the phonon potentials and their energies, and experimental and theoretical studies need to be done to determine how these phonons are affected. It would be interesting to see if the third feature results from the GaAs-like TO-like interface phonon mode or whether introducing the notch also introduces a new phonon mode.

We have also presented the results of a calculation which determines whether extrinsic bistability and hysteresis in the onset of oscillations is observed in a simple and typical equivalent circuit which incorporates a device with NDR

such as a DBS. This calculation can help to determine if extra noise due to switching between bistable states may be introduced if the device with NDR is used as an oscillator or logic device. A study determining the effects of such noise would be useful.

GaAs/Al_xGa_{1-x}As heterostructures are important in possible device applications since the lattice constants of GaAs and Al_xGa_{1-x}As are very similar and therefore little strain at the interfaces is introduced. Most applications require large PVCR's, and therefore, the PAT current should be minimized in such devices. However, there have been some suggestions to use the electron-phonon interaction in practical devices. One application involves using the PAT current as a source of NDR [LK93], and the other involves using triple barrier structures as phonon detectors [KR94]. In any of these situations, it is useful to have detailed experimental information on the electron-localized phonon interaction in semiconductor heterostructures.

Appendix A

Calculational Details of Hopf Bifurcation

Suppose that we have a set of two coupled first order nonlinear differential equations that are in the following form

$$\begin{pmatrix} \dot{x} \\ \dot{y} \end{pmatrix} = \begin{pmatrix} 0 & -\omega \\ \omega & 0 \end{pmatrix} \begin{pmatrix} x \\ y \end{pmatrix} + \begin{pmatrix} F(x,y) \\ G(x,y) \end{pmatrix} \quad (A.1)$$

where $F(x,y)$ and $G(x,y)$ are functions which have the properties such that at the bifurcation point

$$F(0) = G(0) = 0 \quad (A.2)$$

$$D F(0) = D G(0) = 0 \quad (A.3)$$

where $D F(0)$ denotes the partials of F evaluated at $x = y = 0$. It can be shown using the near identity transformation that Eqs. (A.1) can be transformed into normal form given by Eqs. (3.7) and (3.8) in Chapter 3 [GH83]. The parameter a defined in Eq. (3.7) is found to be

$$a = \frac{1}{16} \{ F_{xxx} + F_{yyx} + G_{xxy} + G_{yyy} \} +$$

$$\frac{1}{16\omega} \left\{ -2G_{xx}F_{xx} + 2G_{yy}F_{yy} - 2G_{xy}(G_{xx} + G_{yy}) + 2F_{xy}(F_{xx} + F_{yy}) \right\} \quad (A.4)$$

where F_{xxx} is the third partial of $F(x,y)$ with respect to x evaluated at bifurcation point and all other terms in Eq. (A.4) defined similarly.

Equations (3.1) and (3.2) are clearly not in the form of Eq. (A.1). To obtain the necessary form, we define the following new variables

$$x = \sqrt{\omega_0 - \frac{R}{L}} [\sqrt{L}(I - I_c) - \sqrt{C}(v - v_c)] \quad (A.5)$$

$$y = \sqrt{\omega_0 + \frac{R}{L}} [\sqrt{L}(I - I_c) + \sqrt{C}(v - v_c)] \quad (A.6)$$

where $\omega_0 = \sqrt{\frac{1}{LC}}$, and I_c and v_c are the total current in the device and voltage across the structure at the bifurcation point. Note that $\sqrt{L}(I - I_c)$ and $\sqrt{C}(v - v_c)$ are in the same units. Substituting these variables into Eqs. (3.1) and (3.2) we find that the equations are now in the proper form

$$\dot{x} = -\omega_{lc}y + F(x,y) \quad (A.7)$$

$$\dot{y} = \omega_{lc}x + G(x,y) \quad (A.8)$$

where

$$\omega_{lc} = \sqrt{\omega_0^2 - \frac{R^2}{L^2}} \quad (A.9)$$

is the limit cycle frequency in Eq. (3.6) and $F(x,y)$ and $G(x,y)$ are given by:

$$F(x,y) = -\sqrt{\omega_0 - \frac{R}{L}} \left\{ \frac{I_c}{\sqrt{C}} - \frac{i(v)}{\sqrt{C}} - \frac{R\sqrt{C}}{L}(v - v_c) + \zeta(V_{ext}) \right\} \quad (A.10)$$

$$G(x,y) = \sqrt{\omega_0 + \frac{R}{L}} \left\{ \frac{I_c}{\sqrt{C}} - \frac{i(v)}{\sqrt{C}} - \frac{R\sqrt{C}}{L}(v - v_c) + \zeta(V_{ext}) \right\}, \quad (A.11)$$

where $\zeta(V_{\text{ext}}) = \frac{1}{\sqrt{L}}(V_{\text{ext}} - RI_c - v_c)$. It can be seen that Eqs. (A.10) and (A.11) satisfy the conditions of Eqs. (A.2) and (A.3).

Finally, if we calculate all the partials given in Eq. (A.4), we find that

$$a = \frac{\omega_0}{32C^2 \left(\omega_0^2 - \frac{R^2}{L^2} \right)} \left[\frac{RL(i''(v_c))^2}{L - R^2C} - i'''(v_c) \right] \quad (\text{A.12})$$

where $i''(v_c)$ and $i'''(v_c)$ are the second and third derivatives of the intrinsic $i(v)$ curve evaluated at the bifurcation point. Moreover, since $\omega_0 > R/L$ is a defining condition for a Hopf bifurcation (see Eq. (3.5)), it can be seen that the term outside the brackets in (A.12) is always positive, and, hence, only the term in brackets is needed to determine $\text{sgn}(a)$ as given by Eq. (3.9).

Appendix B

Epilayer Schematics

B.1 Asymmetric Spacer Sample

layer	thickness	doping level
GaAs cap	1 μm	Si doped $2 \times 10^{18} \text{ cm}^{-3}$
GaAs spacer	300 \AA	Si doped $2 \times 10^{17} \text{ cm}^{-3}$
	300 \AA	Si doped $4 \times 10^{16} \text{ cm}^{-3}$
	300 \AA	Si doped $1 \times 10^{16} \text{ cm}^{-3}$
	50 \AA	undoped
AlAs emitter barrier	45 \AA	undoped
GaAs well	80 \AA	undoped
AlAs collector barrier	45 \AA	undoped
GaAs spacer	350 \AA	undoped
	300 \AA	Si doped $1 \times 10^{16} \text{ cm}^{-3}$
	300 \AA	Si doped $4 \times 10^{16} \text{ cm}^{-3}$
	300 \AA	Si doped $2 \times 10^{17} \text{ cm}^{-3}$
GaAs buffer	2 μm	Si doped $2 \times 10^{18} \text{ cm}^{-3}$
GaAs substrate		n^+ (100) direction

Table B.1: Epilayer schematic of asymmetric spacer sample.

B.2 Notch Samples

layer	thickness	doping level
GaAs cap	1 μm	Si doped $2 \times 10^{18} \text{ cm}^{-3}$
GaAs spacer	300 \AA	Si doped $2 \times 10^{17} \text{ cm}^{-3}$
	300 \AA	Si doped $4 \times 10^{16} \text{ cm}^{-3}$
	300 \AA	Si doped $1 \times 10^{16} \text{ cm}^{-3}$
	50 \AA	undoped
$\text{Al}_x\text{Ga}_{1-x}\text{As}$ $x = 0.45$ $x = 0.3$	14.2 \AA 19.8 \AA	undoped
AlAs emitter barrier	36.7 \AA	undoped
GaAs well	80 \AA	undoped
AlAs collector barrier	45.3 \AA	undoped
GaAs spacer	50 \AA	undoped
	300 \AA	Si doped $1 \times 10^{16} \text{ cm}^{-3}$
	300 \AA	Si doped $4 \times 10^{16} \text{ cm}^{-3}$
	300 \AA	Si doped $2 \times 10^{17} \text{ cm}^{-3}$
GaAs buffer	2 μm	Si doped $2 \times 10^{18} \text{ cm}^{-3}$
GaAs substrate		n^+ (100) direction

Table B.2: Epilayer schematics of notch samples.

B.3 Asymmetric Barrier Samples

layer	thickness	doping level
GaAs cap	1 μm	Si doped $2 \times 10^{18} \text{ cm}^{-3}$
GaAs spacer	300 \AA	Si doped $2 \times 10^{17} \text{ cm}^{-3}$
	300 \AA	Si doped $4 \times 10^{16} \text{ cm}^{-3}$
	300 \AA	Si doped $1 \times 10^{16} \text{ cm}^{-3}$
	50 \AA	undoped
$\text{Al}_x\text{Ga}_{1-x}\text{As}$ emitter barrier	see table (B.4)	undoped
GaAs well	80 \AA	undoped
$\text{Al}_x\text{Ga}_{1-x}\text{As}$ collector barrier	see table (B.4)	undoped
GaAs spacer	50 \AA	undoped
	300 \AA	Si doped $1 \times 10^{16} \text{ cm}^{-3}$
	300 \AA	Si doped $4 \times 10^{16} \text{ cm}^{-3}$
	300 \AA	Si doped $2 \times 10^{17} \text{ cm}^{-3}$
GaAs buffer	2 μm	Si doped $2 \times 10^{18} \text{ cm}^{-3}$
GaAs substrate		n^+ (100) direction

Table B.3: General epilayer schematic of asymmetric barrier samples. Emitter and collector barrier widths are given in table (B.4)

MBE #	aluminum concentration (x)	emitter barrier (\AA)	collector barrier (\AA)
1863	1.0	45.0	33.0
264	0.8	55.4	40.6
263	0.7	62.2	45.6
262	0.6	70.6	51.8
292	0.5	81.0	59.4
293	0.4	94.4	69.2
278	0.3	115.4	84.7
280	0.25	115.4	84.7
291	0.225	115.4	84.7
279	0.2	115.4	84.7

Table B.4: Asymmetric barrier sample emitter and collector barrier widths for values of aluminum concentration x in $\text{Al}_x\text{Ga}_{1-x}\text{As}$

Appendix C

Properties GaAs, AlAs, and $Al_xGa_{1-x}As$

Conduction band offset between GaAs and $Al_xGa_{1-x}As$	$0.75x$ if $x \leq 0.45$ [CP78] $0.75x + 0.69(x - 0.45)^2$ if $x > 0.45$.
Effective mass of electrons in GaAs	$0.067 m_0$ [Ada85]
Effective mass of electrons in AlAs	$0.09 m_0$ [BdAeSS ⁺ 90, LAW92]
Effective mass of electrons in $Al_xGa_{1-x}As$	$(0.067 + 0.023x) m_0$
TO phonon energy in GaAs	33.3 meV [MA89]
LO phonon energy in GaAs	36.2 meV [MA89]
TO phonon energy in AlAs	44.8 meV [Ada85]
LO phonon energy in AlAs	50.1 meV [Ada85]
Phonon energies in $Al_xGa_{1-x}As$	see Fig. 2.6 [MS87]
κ_∞ in GaAs	10.9 [MA89]
κ_∞ in AlAs	8.16 [MA89]
κ_∞ in $Al_xGa_{1-x}As$	10.9 - 1.94x
κ_0 in GaAs	13.1 [CP78]
κ_0 in AlAs	10.1 [CP78]
κ_0 in $Al_xGa_{1-x}As$	10.1 + 3x

Appendix D

List of Symbols Used in this Thesis

D.1 List of Symbols Used in Electron-Phonon Interaction: Chapter 2 and Chapter 6

$a(\mathbf{q}_{ })$	Annihilation operator for phonons
$a^\dagger(\mathbf{q}_{ })$	Creation operator for phonons
A	Cross sectional area of device
A_i	Normalization constant
B	Magnitude of applied magnetic field
B_i	Normalization constant
$c(n)$	Constants in least squares fit
d_w	Width of well
D_z	Electric displacement in z direction
E	Total energy of the electron
E_a	Total energy of initial electronic state in emitter
E_f	Fermi energy
E_w	Total energy of initial electronic state in well
E_{za}	z component of electronic state in emitter
E_{zj}	z energy of jth bound state in emitter
E_{zw}	z component of electronic state in well
e_{Al}	Effective charge of Al ion
e_{As}	Effective charge of As ion
e_{Ga}	Effective charge of Ga ion
$ f\rangle$	Total final state

i_{ph}	Current due to phonon
$f_a(k_{ })$	Fermi distribution of electrons in emitter
$f_w(k_{ })$	Fermi distribution of electrons in well
$g_a(k_{ })$	2D density of electronic states in emitter
$g_w(k'_{ })$	2D density of electronic states available in well
$f(q_{ })$	phonon potential in z direction
H_{e-ph}	Electron-optical phonon Hamiltonian
$ i\rangle$	Total initial state
$J(V)$	Current density as a function of voltage
$k_{ }$	Momentum of electron in x-y direction in emitter state
$K_{ }$	x-y component of electron in emitter in current integral
$k'_{ }$	x-y component of momentum in emitter state
$K'_{ }$	x-y component of electron momentum in emitter in current integral
$k'_{ min}$	Lower integration limit for $k_{ }$
m_0	Bare electron mass
m_{Al}	Effective mass of Al ion
m_{As}	Effective mass of As ion
m_{Ga}	Effective mass of Ga ion
$m^*(z)$	Effective mass of electron in DBS
$q_{ }$	x-y component of phonon momentum
$Q_{ }$	x-y component of phonon momentum in current integral
$r_{ }$	position vector in x-y direction
$U(z)$	Conduction band potential
u_{Al}	Displacement of Al ion
u_{As}	Displacement of As ion
u_{Ga}	Displacement of Ga ion
$W(i \rightarrow f)$	Scattering rate of electrons from optical phonon
z	Direction parallel to the current and perpendicular to the interfaces
β_1	Nearest-neighbor force constant between Al and As ions
β_2	Nearest-neighbor force constant between Ga and As ions
$\beta(q_{ })$	Electron-phonon coupling constant
ΔE_z	Difference in z energy between emitter and well state
ΔV	Voltage difference between resonant peak and feature in phonon peak

ϵ_0	Permitivity of free space
$\epsilon(\omega)$	Dielectric function in layer
ε_c	Electric field in collector barrier
η_w	Charge density in well
η_j	Charge density of bound state in emitter
κ_0	Static dielectric constant
κ_∞	High frequency dielectric constant
$\lambda(q_{ })$	Overlap integral in z direction
ϕ	Scattering angle between electron and phonon
$\phi(q_{ })$	phonon potential in x-y direction
$\Phi(\mathbf{r})$	Three dimensional phonon potential
$\varphi_a(z)$	z component of electronic wavefunction in emitter
$\varphi_w(z)$	z component of electronic wavefunction in well
$\rho(z)$	Space charge density in z direction
$\Psi_a(\mathbf{r})$	Three dimensional electronic wavefunction in emitter
$\Psi_w(\mathbf{r})$	Three dimensional electronic wavefunction in well
ω_c	Cyclotron frequency
ω_{LA}	Frequency of bulk LO phonon in AlAs
ω_{LG}	Frequency of bulk LO phonon in GaAs
ω_{LO}	Bulk longitudinal optical frequency
ω_{ph}	Angular frequency of emitted phonon
ω_{TA}	Frequency of bulk TO phonon in AlAs
ω_{TG}	Frequency of bulk TO phonon in GaAs
ω_{TO}	Bulk transverse optical frequency
$\omega(q_{ })$	Localized optical phonon frequency

D.2 List of Symbols Used in Equivalent Circuit and Hopf Bifurcation Calculation: Chapter 3 and Appendix B

a	Constant in Hopf bifurcation normal form equation
b	Constant in Hopf bifurcation normal form equation
c	Constant in Hopf bifurcation normal form equation
f	Constant in Hopf bifurcation normal form equation
$F(x,y)$	Function in normal form calculation
$G(x,y)$	Function in normal form calculation
I	Total current in circuit
I_c	Total current in circuit at bifurcation point
$i(v)$	Intrinsic current-voltage characteristic
C	Parallel capacitance
L	Series inductance
r	Normal form coordinate for Hopf bifurcation
R	Series resistance
v	Voltage across DBS
v_0	Steady state voltage of equivalent circuit model
v_c	Voltage across DBS at bifurcation point
V_{ext}	Applied external voltage
x	Variable used in normal form calculation
y	Variable used in normal form calculation
λ	Eigenvalues of equivalent circuit model
θ	Normal form coordinate for Hopf bifurcation
μ	Control parameter
ω	Constant in Hopf bifurcation normal form equation
ω_{lc}	Limit cycle frequency
ω_0	Resonant frequency of capacitor and inductor

D.3 List of Symbols Used in Experimental Techniques: Chapter 4

f_{Al}	Atomic scattering form factor for Al
f_{As}	Atomic scattering form factor for As
f_{Ga}	Atomic scattering form factor for Ga
$G(GaAs)$	MBE growth rate of GaAs
$G(Al_xGa_{1-x}As)$	MBE growth rate of $Al_xGa_{1-x}As$
x	Aluminum concentration in $Al_xGa_{1-x}As$

D.4 List of Symbols Used in Digital Filter: Chapter 5

c_k	Constants of filter
$H(\omega)$	Transfer function
N	Number of points in filter
u_{n-k}	Unfiltered data
$U(\omega)$	Fourier transform of unfiltered data points
y_n	Filtered data
$Y(\omega)$	Fourier transform of filtered data points
ω_c	Cutoff frequency of filter

Bibliography

[Ada85] Sadao Adachi. GaAs, AlAs, and $Al_xGa_{1-x}As$: Material parameters for use in research and device applications. *J. Appl. Phys.*, 58:R1, 1985.

[AEH⁺88] E. S. Alves, L. Eaves, M. Henini, O. H. Hughes, M. L. Leadbeater, F. W. Sheard, G. A. Toombs, G. Hill, and M. A. Pate. Observation of intrinsic bistability in resonant tunnelling devices. *Electron. Lett.*, 24:1190, 1988.

[AES93] Ali Abou-Elnour and Klaus Schuenemann. A comparison between different numerical methods used to solve Poisson's and Schrödinger's equations in semiconductor heterostructures. *J. Appl. Phys.*, 74:3273, 1993.

[AFS82] Tsuneya Ando, Alan B. Fowler, and Frank Stern. Electronic properties of two-dimensional systems. *Rev. Mod. Phys.*, 54:437, 1982.

[AMR⁺89] S. Ben Amor, K. P. Martin, J. J. L. Rascol, R. J. Higgens, R. C. Potter, A. A. Lakhani, and H. Hier. Magnetotransport studies of

charge accumulation in an AlInAs/GaInAs tunneling structure. *Appl. Phys. Lett.*, 54:1908, 1989.

[BD66] D. J. BenDaniel and C. B. Duke. Space-charge effects on electron tunneling. *Phys. Rev.*, 152:683, 1966.

[BdAeSS⁺90] G. Brozak, E. A. de Andrada e Silva, L. J. Sham, F. DeRosa, P. Miceli, S. A. Schwarz, J. P. Harbison, L. T. Florez, and S. J. Allen, Jr. Tunneling cyclotron resonance and the renormalized effective mass in semiconductor barriers. *Phys. Rev. Lett.*, 64:471, 1990.

[BGS88] E. R. Brown, W. D. Goodhue, and T. C. L. G. Sollner. Fundamental oscillations up to 200 GHz in resonant tunneling diodes and new estimates of their maximum oscillation frequency from stationary-state tunneling theory. *J. Appl. Phys.*, 64:1519, 1988.

[BH54] M. Born and K. Huang, editors. *Dynamical Theory of Crystal Lattices*. Clarendon Press, Oxford, 1954.

[BL94] Paolo Bordone and Paolo Lugli. Effect of half-space and interface phonons on the transport properties of $\text{Al}_x\text{Ga}_{1-x}\text{As}$ heterostructures. *Phys. Rev. B.*, 49:8178, 1994.

[BLSR⁺90] G. S. Boebinger, A. F. J. Levi, S. Schmitt-Rink, A. Passner, L. N. Pfeiffer, and K. W. West. Direct observation of two-dimensional magnetopolarons in a resonant tunnel junction. *Phys. Rev. Lett.*, 65:235, 1990.

[BMBA⁺90] C. Y. Belhadj, K. P. Martin, S. Ben Amor, J. J. L. Rascol, R. J. Higgins, R. C. Potter, H. Hier, and E. Hempfling. Bias circuit effects on the current-voltage characteristic of double-barrier tunneling structures: Experimental and theoretical results. *Appl. Phys. Lett.*, 57:58, 1990.

[Bon81] R. Bonneville. Local-field effects and their optical properties of ternary semiconductor alloys. *Phys. Rev. B.*, 24:1987, 1981.

[BPS89] E. R. Brown, C. D. Parker, and T. C. L. G. Sollner. Effect of quasibound-state lifetime on the oscillation power of resonant tunneling diodes. *Appl. Phys. Lett.*, 54:934, 1989.

[BPV84] P. Berge, Y. Pomear, and C. Vidal. *Order Within Chaos*. Wiley, New York, 1984.

[Bra81] N. Braslau. Alloyed ohmic contacts to GaAs. *J. Vac. Sci. Tech.*, 19:803, 1981.

[BS84] J. C. Bravman and R. Sinclair. The preparation of cross-section specimens for transmission electron microscopy. *J. Electron Micro. Tech.*, 1:53, 1984.

[BSP⁺89] E. R. Brown, T. C. L. G. Sollner, C. D. Parker, W. D. Goodhue, and C. L. Chen. Oscillations up to 420 GHz in GaAs/AlAs resonant tunneling diodes. *Appl. Phys. Lett.*, 55:1777, 1989.

[BSP⁺91] E. R. Brown, J. R. Söderström, C. D. Parker, L. J. Mahoney, K. M. Molvar, and T. C. McGill. Oscillations up to 712 GHz

in InAs/AlSb resonant tunneling diodes. *Appl. Phys. Lett.*, 58:2291, 1991.

[CA75] A. Y. Cho and J. R. Authur. Molecular beam epitaxy. *Prog. Solid State Chem.*, 10:157, 1975.

[CC81] A. Y. Cho and K. Y. Cheng. Growth of extremely uniform layers by rotating substrate holder with molecular beam epitaxy for applications to electro-optic and microwave devices. *Appl. Phys. Lett.*, 38:360, 1981.

[CCP⁺89] A. Celeste, L. A. Cury, J. C. Portal, M. Allovon, and D. K. Maude. AlAs and InAs mode LO phonon emission assisted tunneling in (InGa)As/(AlIn)As double barrier structures. *Solid-State Electron.*, 32:1195, 1989.

[CET74] L. L. Chang, L. Esaki, and R. Tsu. Resonant tunneling in semiconductor double barriers. *Appl. Phys. Lett.*, 24:593, 1974.

[CH89] P. Cheng and J. S. Harris, Jr. Effect of Si doping in AlAs barrier layers of AlAs-GaAs-AlAs double-barrier resonant tunneling diodes. *Appl. Phys. Lett.*, 55:572, 1989.

[CH90] Peng Cheng and James S. Harris, Jr. Improved design of AlAs/GaAs resonant tunneling diodes. *Appl. Phys. Lett.*, 56:1676, 1990.

[Cho64] W. F. Chow. *Principles of Tunnel Diode Circuits*. Wiley, New York, 1964.

- [Cho71a] A. Y. Cho. Film deposition by molecular-beam techniques. *J. Vac. Sci. Tech.*, 8:S31, 1971.
- [Cho71b] A. Y. Cho. Growth of periodic structures by the molecular-beam method. *Appl. Phys. Lett.*, 19:467, 1971.
- [Cho83] A. Y. Cho. Growth of III-V semiconductors by molecular beam epitaxy and their properties. *Thin Solid Films*, 100:291, 1983.
- [CKB⁺89] A. C. Campbell, V. P. Kesan, T. R. Block, G. E. Crook, D. P. Neikirk, and B. G. Streetman. Influence of MBE growth temperature on GaAs/AlAs resonant tunneling structures. *J. Electron. Mater.*, 18:585, 1989.
- [CKC⁺87] A. C. Campbell, V. P. Kesan, G. E. Crook, C. M. Maziar, D. P. Neikirk, and B. G. Streetman. Impedance switching effects in GaAs/AlAs barrier structures. *Electron. Lett.*, 23:926, 1987.
- [CKC⁺88] A. C. Campbell, V. P. Kesan, G. E. Crook, C. M. Maziar, D. P. Neikirk, and B. G. Streetman. Capacitive hysteresis effects in 5.0 nm single and double barrier AlAs/GaAs tunneling structures grown by molecular beam epitaxy. *J. Vac. Sci. Tech.*, B6:651, 1988.
- [CM71] I. F. Chang and S. S. Mitra. Long wavelength optical phonons in mixed crystals. *Adv. Phys.*, 20:359, 1971.
- [CP78] H. C. Casey and M. B. Panish, editors. *Heterostructure Lasers*. Academic, New York, 1978.

- [CV88] F. Chevoir and B. Vinter. Calculation of phonon-assisted tunneling and valley current in a double-barrier diode. *Appl. Phys. Lett.*, 55:1859, 1988.
- [CV93a] F. Chevoir and B. Vinter. Scattering-assisted tunneling in double-barrier diodes: Scattering rates and valley current. *Phys. Rev. B.*, 47:7260, 1993.
- [CV93b] François Chevoir and Borge Vinter. Scattering-assisted tunneling in double-barrier diodes: Scattering rates and valley current. *Phys. Rev. B.*, 47:7260, 1993.
- [CYYW91] J. G. Chen, C. H. Yang, M. J. Yang, and R. A. Wilson. Observation of two-dimensional resonant magnetopolarons and phonon-assisted resonant tunneling in double-barrier heterostructures. *Phys. Rev. B.*, 43:4531, 1991.
- [DRY95] T. Daniels-Race and S. Yu. Effect of spacer layer thickness on tunneling characteristics in asymmetric AlAl/GaAs/AlAs double barrier structures. *Solid-State Electron.*, 38:1347, 1995.
- [DS91] S. Das Sarma. Quantum many-body aspects of hot carrier relaxation in semiconductor microstructures. In J. Shah, editor, *Hot Carriers in Semiconductor Microstructures: Physics and Applications*, chapter II.2. Academic Press, Boston, 1991.
- [ELH⁺89] L. Eaves, M. L. Leadbeater, D. G. Hayes, E. S. Alves, F. W. Sheard, G. A. Toombs, P. E. Simmonds, M. S. Skolnick, M. Henini, and O. H. Hughes. Electrical and spectroscopic

studies of space-charge buildup, energy relaxation, and magnetically enhanced bistability in resonant tunneling structures. *Solid-State Electron.*, 32:1101, 1989.

[ELNT64] O. V. Emel'yanenko, T. S. Lagunova, D. N. Nasledov, and G. N. Talalakin. Investigation of transport effects in $A^{III}b^V$ type compounds. *Bull. Acad. Sci. USSR Phys. Ser.*, 28:855, 1964.

[FK65] R. Fuchs and K. L. Kliewer. Optical modes of vibration in an ionic crystal slab. *Phys. Rev.*, 140:A2076, 1965.

[FN85] K. L. T. Fukunaga, T. Kobayashi and H. Nakashima. Photoluminescence from AlGaAs-GaAs single quantum well with growth interrupted heterointerfaces grown by molecular beam epitaxy. *Jpn. J. Appl. Phys.*, 24:L510, 1985.

[FR94] H. A. Fertig and T. L. Reinecke. Localization and diffusion of energy via confined phonon modes in semiconductor superlattices. *Phys. Rev. B.*, 50:7443, 1994.

[GC91] C. Guillemot and F. Clerot. Model for longitudinal-optical phonons and electron-phonon coupling in GaAs-Ga_{1-x}Al_xAs multilayer structures. *Phys. Rev. B.*, 44:6249, 1991.

[GCB91] Y. Galvao Goboto, F. Chevoir, and J. M. Berroir. Magnetotunneling analysis of the scattering processes in a double-barrier structure with a two-dimensional emitter. *Phys. Rev. B.*, 43:4843, 1991.

- [GCM⁺87] J. M. Gering, D. A. Crim, D. G. Morgan, P. D. Coleman, W. Kopp, and H. Morkoç. A small-signal equivalent-circuit model for GaAs-Al_xGa_{1-x}As resonant tunneling heterostructures at microwave frequencies. *J. Appl. Phys.*, 61:271, 1987.
- [GH83] J. Guckenheimer and P. Holmes. *Nonlinear Oscillations, Dynamical Systems, and Bifurcations of Vector Fields*. Springer, New York, 1983.
- [GMC94] C. J. Goodings, H. Mizuta, and J. R. A. Cleaver. Electrical studies of charge build-up and phonon-assisted tunneling in double barrier materials with very thick spacer layers. *J. Appl. Phys.*, 75:2291, 1994.
- [GRE93] C. H. Grein, E. Runge, and H. Ehrenreich. Phonon-assisted transport in double-barrier resonant-tunneling structures. *Phys. Rev. B.*, 47:12590, 1993.
- [GTC87a] V. J. Goldman, D. C. Tsui, and J. E. Cunningham. Evidence for LO-phonon-emission-assisted tunneling in double-barrier heterostructures. *Phys. Rev. B.*, 36:7635, 1987.
- [GTC87b] V. J. Goldman, D. C. Tsui, and J. E. Cunningham. Observation of intrinsic bistability in resonant-tunneling structures. *Phys. Rev. Lett.*, 58:1256, 1987.
- [GTC87c] V. J. Goldman, D. C. Tsui, and J. E. Cunningham. Resonant tunneling in magnetic fields: Evidence for space-charge buildup. *Phys. Rev. B.*, 35:9387, 1987.

- [Ham89] R. W. Hamming. *Digital Filters*. Prentice-Hall, Inc., Englewood Cliffs, New Jersey, third edition, 1989.
- [HHN⁺65] P. B. Hirsch, A. Howie, R. B. Nicholson, D. W. Pashley, and M. J. Whelan. *Electron Microscopy of Thin Crystals*. Butterworth, Washington, 1965.
- [HLH88] E. S. Hellman, K. L. Lear, and J. S. Harris, Jr. Limit cycle oscillation in negative differential resistance devices. *J. Appl. Phys.*, 64:2798, 1988.
- [HZ88] Kun Huang and Bangfen Zhu. Dielectric continuum model and Fröhlich interaction in superlattices. *Phys. Rev. B.*, 38:13377, 1988.
- [JB91] K. L. Jensen and F. A. Buot. Numerical simulation of intrinsic bistability and high-frequency current oscillations in resonant tunneling structures. *Phys. Rev. Lett.*, 66:1078, 1991.
- [JDNZ86] B. A. Joyce, P. J. Dobson, J. H. Neave, and J. Zhang. In situ study of MBE growth mechanisms using RHEED techniques—some consequences of multiple scattering. In G. Bauer, F. Kuchar, and H. Heinrich, editors, *Two-Dimensional Systems: Physics and New Devices*, pages 42–51. Springer-Verlag, Berlin, 1986.
- [JK91] B. Jogai and E. T. Koening. A parametric study of extrinsic bistability in the current-voltage curves of resonant tunneling diodes. *J. Appl. Phys.*, 69:3381, 1991.

[JKB⁺94] J. M. Jacob, D. S. Kim, A. Bouchalkha, , J. J. Song, J. F. Klem, H. Hou, C. W. Tu, and H. Morkoç. Spatial characteristics of GaAs, GaAs-like and AlAs-like LO phonons in GaAs/Al_xGa_{1-x}As superlattices: The strong x dependence. *Solid State Comm.*, 91:721, 1994.

[JS81] Bernard Jusserand and Jacques Sapriel. Raman investigation of anharmonicity and disorder-induced effects in Ga_{1-x}Al_xAs epitaxial layers. *Phys. Rev. B.*, 24:7194, 1981.

[KBJ⁺92] Dai-Sik Kim, Abdellatif Bouchalkha, J. M. Jacob, J. F. Zhou, J. J. Song, and J. F. Klem. Confined-to-propagating transition of LO phonons in GaAs/Al_xGa_{1-x}As superlattices observed by picosecond Raman scattering. *Phys. Rev. Lett.*, 68:1002, 1992.

[KBJ⁺95] D. S. Kim, A. Bouchalkha, J. M. Jacob, J. J. Song, J. F. Klem, H. Hou, C. W. Tu, and Morkoç. Hot-phonon generation in GaAs/Al_xGa_{1-x}As superlattices: Observations and implications on the coherence length of LO phonons. *Phys. Rev. B.*, 51:5449, 1995.

[KBS⁺92] K. W. Kim, A. R. Bhatt, Michael A. Stroscio, P. J. Turley, and S. W. Teitsworth. Effects of interface phonon scattering in multiheterointerface structures. *J. Appl. Phys.*, 72:2282, 1992.

[KDS78] M. E. Kim, A. Das, and S. D. Senturia. Electron scattering interaction with coupled plasmon–polar-phonon modes in degenerate semiconductors. *Phys. Rev. B.*, 18:6890, 1978.

[KHJ90] E. T. Koenig, C. I. Huang, and B. Jogai. Independence of peak current from emitter spacer layer width in AlGaAs/GaAs resonant tunneling diodes. *J. Appl. Phys.*, 68:5905, 1990.

[KMEH91] C. Kidner, I. Mehdi, J. R. East, and G. I. Haddad. Bias circuit instabilities and their effect on the d.c. current-voltage characteristics of double-barrier resonant tunneling diodes. *Solid-State Electron.*, 34:149, 1991.

[KR94] V. I. Kozub and A. M. Rudin. Three-barrier tuned structure as a phonon-spectroscopy device. *Phys. Rev. B.*, 49:5710, 1994.

[KS90] K. W. Kim and M. A. Stroscio. Electron-optical-phonon interaction in binary/ternary heterostructures. *J. Appl. Phys.*, 68:6289, 1990.

[LAE⁺89] M. L. Leadbeater, E. S. Alves, L. Eaves, M. Henini, O. H. Hughes, A. Celeste, J. C. Portal, G. Hill, and M. A. Pate. Magnetic field studies of elastic scattering and optic phonon emission in resonant tunneling devices. *Phys. Rev. B.*, 39:3438, 1989.

[LAS⁺89] M. L. Leadbeater, E. S. Alves, F. W. Sheard, L. Eaves, M. Henini, O. H. Hughes, and G. A. Toombs. Observation of space-charge build-up and thermalization in an asymmetric double-barrier resonant tunneling structure. *J. Phys. Condens. Matt.*, 1:10605, 1989.

[LAW92] D. Landheer, G. C. Aers, and Z. R. Wasilewski. Effective mass in the barriers of GaAs/AlAs resonant tunneling double barrier diodes. *Superlatt. Microstruct.*, 11:55, 1992.

[LC87] H. C. Liu and D. D. Coon. Heterojunction double-barrier diodes for logic applications. *Appl. Phys. Lett.*, 50:1246, 1987.

[LC88] H. C. Liu and D. D. Coon. Interface-roughness and island effects on tunneling in quantum wells. *J. Appl. Phys.*, 64:6785, 1988.

[LE77] J. L. Licari and R. Evard. Electron-phonon interaction in a dielectric slab: Effect of the electronic polarizability. *Phys. Rev. B.*, 15:2254, 1977.

[LE91] M. L. Leadbeater and L. Eaves. Sequential tunneling and magnetically enhanced bistability in double-barrier resonant tunneling structures. *Physica Scripta*, T35:215, 1991.

[Liu87] H. C. Liu. Resonant tunneling through single layer heterostructures. *Appl. Phys. Lett.*, 51:1091, 1987.

[Liu88a] H. C. Liu. Circuit simulation of resonant tunneling double-barrier diode. *J. Appl. Phys.*, 64:4792, 1988.

[Liu88b] H. C. Liu. Simulation of extrinsic bistability of resonant tunneling structures. *Appl. Phys. Lett.*, 53:485, 1988.

[LKB70] A. A. Lucas, E. Kartheuser, and R. G. Badro. Electron-phonon interaction in dielectric films. application to electron energy loss and gain spectra. *Phys. Rev. B.*, 2:2488, 1970.

[LKD93] R. Lake, G. Klimeck, and S. Datta. Rate equations from the Keldysh formalism applied to the phonon peak in resonant-tunneling diodes. *Phys. Rev. B.*, 47:6427, 1993.

[LM90] J. Leo and A. H. MacDonald. Disorder-assisted tunneling through a double-barrier structure. *Phys. Rev. Lett.*, 64:6785, 1990.

[LMR91] P. Lugli, E. Molinari, and H. Rücker. Electron-phonon interaction in two-dimensional systems: A microscopic approach. *Superlatt. Microstruct.*, 10:471, 1991.

[LRF92] F. Laruelle, A. Ramdane, and G. Fain. Experimental investigation of ionized impurity scattering in double barrier resonant tunneling diodes. *Surf. Sci.*, 267:396, 1992.

[MA89] N. Mori and T. Ando. Electrical-optical-phonon interaction in single and double heterostructures. *Phys. Rev. B.*, 40:6175, 1989.

[MC90] G. H. Ma and S. Chevacharoenkul. A technique for preparing two-in-one cross sectional TEM specimens. Technical report, MCNC, July 1990.

[MCW86] E. E. Mendez, E. Calleja, and W. I. Wang. Tunneling through indirect-gap semiconductor barriers. *Phys. Rev. B.*, 34:6026, 1986.

[Men89] J. Menéndez. Phonons in $\text{GaAs}-\text{Al}_x\text{Ga}_{1-x}\text{As}$ superlattices. *J. Luminescence*, 44:285, 1989.

[MFE⁺91] D. K. Maude, T. J. Foster, L. Eaves, M. Davies, O. H. Henini, M. Hughes, and M. Heath. High pressure studies of resonant tunneling and superlattice phenomena. *Semicon. Sci. Technol.*, 6:422, 1991.

[MH88] R. K. Mains and G. I. Haddad. Time-dependent modeling of resonant-tunneling diodes from direct solution of the Schroedinger equation. *J. Appl. Phys.*, 64:3564, 1988.

[MLSE94] A. D. Martin, M. L. Lerch, P. E. Simmonds, and L. Eaves. Observation of intrinsic tristability in a resonant tunneling structure. *Appl. Phys. Lett.*, 64:1248, 1994.

[MOEW91] E. E. Mendez, H. Ohno, L. Esaki, and W. I. Wang. Resonant interband tunneling via landau levels in polytype heterostructures. *Phys. Rev. B.*, 43:5196, 1991.

[MS87] O. Madelung and M. Scholz, editors. *Landolt-Bornstein 1987 New Series*, volume 22. Springer-Verlag, Berlin, 1987.

[MSH89] R. K. Mains, J. P. Sun, and G. I. Haddad. Observation of intrinsic bistability in resonant tunneling diode modeling. *Appl. Phys. Lett.*, 55:371, 1989.

[NJDN83] J. H. Neave, B. A. Joyce, P. J. Dobson, and N. Norton. Dynamics of film growth of GaAs by MBE from RHEED observations. *Appl. Phys. A*, 31:1, 1983.

[NJK93] H. J. M. F. Noteborn, H. P. Joosten, and K. Kaski. Alternative for the quantum inductance model in double-barrier resonant tunneling. *Superlatt. Microstruct.*, 13:153, 1993.

[Pet77] P. M. Petroff. Transmission electron microscopy of interfaces in III-V compound semiconductors. *J. Vac. Sci. Tech.*, 14:973, 1977.

- [PFK79] K. Ploog, A. Fischer, and H. Kunzel. Improved p/n junctions in Ge-doped GaAs grown by molecular beam epitaxy. *Appl. Phys.*, 18:353, 1979.
- [PFTV86] William H. Press, Brian P. Flannery, Saul A. Teukolsky, and William T. Vetterling, editors. *Numerical Recipes*. Cambridge University Press, Cambridge, 1986.
- [PGWS78] P. M. Petroff, A. C. Gossard, W. Wiegmann, and A. Savage. Crystal growth kinetics in $(\text{GaAs})_n\text{-}(\text{AlAs})_m$ superlattices deposited by molecular beam epitaxy. *J. Crystal Growth*, 44:5, 1978.
- [RB91] B. K. Ridley and B. Baibaker. Continuum theories of optical phonons and polaritons in superlattices: A brief critique. *Phys. Rev. B.*, 43:9096, 1991.
- [Rei89] L. Reimer. *Transmission Electron Microscopy*. Springer Verlag, Berlin, second edition, 1989.
- [Rid89] B. K. Ridley. Electron scattering by confined LO polar phonons in a quantum well. *Phys. Rev. B.*, 39:5282, 1989.
- [RL93] Patrick Roblin and Wan-Rone Liou. Three-dimensional scattering-assisted tunneling in resonant-tunneling diodes. *Phys. Rev. B.*, 47:2146, 1993.
- [RLGL92] H. Rücker, P. Lugli, S M. Goodnick, and J. E. Lary. Intersubband relaxation of photoexcited carriers in asymmetric coupled quantum wells. *Semicon. Sci. Technol.*, 7:B98, 1992.

[RRB⁺93] F. Rossi, L. Rota, C. Bungaro, P. Lugli, and E. Molinari. Phonons in thin GaAs quantum wires. *Phys. Rev. B.*, 47:1695, 1993.

[Sak89] H. Sakaki. Molecular beam epitaxy. In F. F. Y. Wang, editor, *Materials Processing Theory and Practices*, volume 7, chapter 5, pages 217–330. North Holland, New York, 1989.

[San89] T. Sands. Compound semiconductor contact metallurgy. *Materials Science and Engineering*, B1:289, 1989.

[SGT⁺83] T. C. L. G. Sollner, W. D. Goodhue, P. E. Tannenwald, C. D. Parker, and D. D. Peck. Resonant tunneling through quantum wells at frequencies up to 2.5 THz. *Appl. Phys. Lett.*, 43:588, 1983.

[Sir] Yuri Sirenko. private communication.

[Sol87] T. C. L. G. Sollner. Comment on "Observation of intrinsic bistability in resonant-tunneling structures". *Phys. Rev. Lett.*, 59:1622, 1987.

[SPGW85] Jagdeep Shah, A. Pinczuk, A. C. Gossard, and W. Weigmann. Energy-loss rates for hot electrons and holes in GaAs quantum wells. *Phys. Rev. Lett.*, 54:2045, 1985.

[SR95] Paul Sotirelis and Patrick Roblin. Intervalley scattering in GaAs/AlAs resonant-tunneling diodes. *Phys. Rev. B.*, 51:13381, 1995.

[ST88] F. W. Seard and G. A. Toombs. Space-charge buildup and bistability in resonant-tunneling double-barrier structures. *Appl. Phys. Lett.*, 52:1228, 1988.

[ST92] F. W. Sheard and G. A. Toombs. Theory of resonant tunneling between 2D electron systems. *Semicon. Sci. Technol.*, 7:B460, 1992.

[Str] Michael A. Stroscio. private communication.

[STY85] H. Sakaki, M. Tanaka, and J. Yoshino. One atomic layer heterointerface fluctuations in GaAs/AlAs quantum well structures and their suppression by insertion of smoothing period in molecular beam epitaxy. *Jpn. J. Appl. Phys.*, 24:L417, 1985.

[TJM93] K. T. Tsen, R. Joshi, and H. Morkoç. Direct measurements of electron-optical photon scattering rates in ultrathin GaAs-AlAs multiple quantum well structures. *Appl. Phys. Lett.*, 62:2073, 1993.

[TT] P. J. Turley and S. W. Teitsworth. unpublished.

[TT91a] P. J. Turley and S. W. Teitsworth. Effect of localized phonon modes on magnetotunneling spectra in double-barrier structures. *Phys. Rev. B.*, 44:12959, 1991.

[TT91b] P. J. Turley and S. W. Teitsworth. Phonon-assisted tunneling due to localized modes in double-barrier structures. *Phys. Rev. B.*, 44:8181, 1991.

- [TT92] P. J. Turley and S. W. Teitsworth. Theory of localized phonon modes and their effects on electron tunneling in double-barrier structures. *J. Appl. Phys.*, 72:2356, 1992.
- [TT94] P. J. Turley and S. W. Teitsworth. Phonon-assisted tunneling from a two-dimensional emitter state. *Phys. Rev. B.*, 50:8423, 1994.
- [TTW⁺93] S. W. Teitsworth, P. J. Turley, C. R. Wallis, W. Li, and P. K. Bhattacharya. Magnetotunneling measurements of localized optical phonons in GaAs/AlAs double barrier structures. *Semicon. Sci. Technol.*, 9:508, 1993. Hot Carriers in Semiconductors 1993.
- [Tur94] P. J. Turley. *Tunneling Measurements of Localized Phonons in Semiconductor Heterostructures*. PhD thesis, Duke University, 1994.
- [TWS⁺93] W. I. E. Tagg, C. R. H. White, M. S. Skolnick, L. Eaves, M. T. Emeny, and C. R. Whitehouse. Elastic and inelastic tunneling in a strained-layer double-barrier resonant-tunneling structure. *Phys. Rev. B.*, 48:4487, 1993.
- [TWT93] P. J. Turley, C. R. Wallis, and S. W. Teitsworth. Tunneling measurements of symmetric-interface phonons in GaAs/AsAs double barrier structures. *Phys. Rev. B.*, 47:12640, 1993.
- [Wal] C. R. Wallis. unpublished.
- [Wen85] L. Wendler. Electron-phonon interaction in dielectric bilayer system. *Phys. Stat. Sol.*, B129:513, 1985.

- [Wen88] L Wendler. Landau damped collective excitations of the quasi-two-dimensional polaron gas in double heterostructures. *Solid State Comm.*, 65:1197, 1988.
- [Wil84] Ralph E. Williams. *Gallium Arsenide Processing Techniques*. Artech House, Dedham, MA, 1984.
- [WJW88] Ned S. Wingreen, Karsten W. Jacobsen, and John W. Wilkins. Resonant tunneling with electron-phonon interaction: An exactly solvable model. *Phys. Rev. Lett.*, 61:1396, 1988.
- [WL90] Xu Wang and Xi Xia Liang. Electron-phonon interaction in ternary mixed crystals. *Phys. Rev. B.*, 42:8915, 1990.
- [WLP⁺88] E. Wolack, K. L. Lear, P. M. Pinter, E. S. Hellman, B. G. Park, T. Weil, J. S. Harris, and D. Thomas. Elastic scattering centers in resonant tunneling diodes. *Appl. Phys. Lett.*, 53:201, 1988.
- [WT93] C. R. Wallis and S. W. Teitsworth. Conditions for current oscillations and hysteresis in resonant tunneling diode circuits. In *Proceedings of the 1993 International Semiconductor Device Research Symposium*, 1993.
- [WT94] C. R. Wallis and S. W. Teitsworth. Hopf bifurcations and hysteresis in resonant tunneling diode circuits. *J. Appl. Phys.*, 76:4443, 1994.
- [YCSLW85] C. H. Yang, Jean M. Carson-Swindle, S. A. Lyon, and J. M. Worlock. Hot-electron relaxation in GaAs quantum wells. *Phys. Rev. Lett.*, 55:2359, 1985.

[YGA90] H. M. Yoo, S. M. Goodnick, and J. R. Arthur. Influence of spacer layer thickness on the current-voltage characteristics of AlGaAs/GaAs and AlGaAs/InGaAs resonant tunneling diodes. *Appl. Phys. Lett.*, 56:84, 1990.

[YWA⁺88] J. F. Young, B. M. Wood, G. C. Aers, R. L. S. Devine, H. C. Liu, D. Landheer, M. Buchanan, A. J. SpringThorpe, and P. Mandeville. Determination of charge accumulation and its characteristic time in double-barrier resonant tunneling structures using steady-state photoluminescence. *Phys. Rev. Lett.*, 60:2085, 1988.

[YWL⁺88] J. F. Young, B. M. Wood, H. C. Liu, M. Buchanan, D. Landheer, A. J. SpringThorpe, and P. Mandeville. Effect of circuit oscillations on the dc current-voltage characteristics of double barrier resonant tunneling structures. *Appl. Phys. Lett.*, 52:1398, 1988.

[YYK89] C. H. Yang, M. J. Yang, and Y. C. Kao. Magnetotunneling spectroscopy in double barrier heterostructures: Observation of incoherent resonant tunneling processes. *Phys. Rev. B.*, 40:6272, 1989.

[ZC92] Nanshi Zou and K. A. Cho. Inelastic electron resonant tunneling through a double-barrier nanostructure. *Phys. Rev. Lett.*, 69:3224, 1992.

[ZGTC88] A. Zaslavsky, V. J. Goldman, D. C. Tsui, and J. E. Cunningham. Resonant tunneling and intrinsic bistability in asymmetric double-barrier heterostructures. *Appl. Phys. Lett.*, 53:1408, 1988.

[ZLM⁺94] C. Zhang, M. L. F. Lerch, A. D. Martin, P. E. Simmonds, and L. Eaves. Plasmon assisted resonant tunneling in a double barrier heterostructure. *Phys. Rev. Lett.*, 72:3397, 1994.

[ZYC90] Hou-zhi Zheng, Fu-hua Yang, and Zong-gui Chen. Nonresonant magnetotunneling in asymmetric GaAs/AlAs double-barrier structures. *Phys. Rev. B.*, 42:5270, 1990.

Biography

Personal: Born in Meadville, PA, August 28, 1967

Education: High School Diploma, Maplewood High School
Guys Mills, PA, May 1985

B.S., Physics, Mathematics, Allegheny College, *summa cum laude*
Meadville, PA, June 1989

M.A., Physics, Duke University
Durham, NC, May 1992

Candidate for Ph.D. in Physics, Duke University
Durham, NC, January 1996

Positions: Research Assistant, Duke University
1991-present

Teaching Assistant, Duke University
1989-1990

NDSEGF Research Internship, Air Force Academy
Summer, 1990

Teaching Assistant, Allegheny College
1986-1988

Research Internship, Argonne National Laboratory
Summer, 1988

Affiliations: Member, American Physical Society
1993-present

Member, American Association of Physics Teachers
1995-present

Honors: National Defense Science and Engineering Graduate Fellow
1989-1992

Publications:

C. R. Wallis and S. W. Teitsworth, "Hopf bifurcations and hysteresis in resonant tunneling diode circuits", *J. Appl. Phys.* **76**, 4443 (1994).

S. W. Teitsworth, P. J. Turley, and C. R. Wallis, W. Li, P. K. Bhattacharya, "Magnetotunneling measurements of localized optical phonons in GaAs/AsAs double barrier structures", *Hot Carriers in Semiconductors* 1993, *Semicon. Sci. Technol.* **9**, 508 (1994).

C. R. Wallis and S. W. Teitsworth, "Conditions for current oscillations and hysteresis in resonant tunneling diode circuits", *Proc. of the 1993 Int. Semiconductor Device Research Symposium*.

P. J. Turley, C. R. Wallis, and S. W. Teitsworth, "Magnetocurrent oscillations in resonant tunneling structures", *Proc. of the 1993 Int. Semiconductor Device Research Symposium*.

P. J. Turley, C. R. Wallis, S. W. Teitsworth, W. Li, and P. K. Bhattacharya, "Tunneling measurements of symmetric-interface phonon in GaAs/AlAs double-barrier structures", *Phys. Rev. B* **47** 12460 (1993).

Stephen W. Teitsworth, Peter J. Turley, Corinne R. Wallis, Weiqi Li, and Pallab Bhattacharya, "Electron-localized phonon interactions in GaAs/AlAs double barrier structures", *Proc. of the 1991 Int. Semiconductor Device Research Symposium*.